DEVELOPMENT OF DOUBLE-SIDED INTERIOR PERMANENT MAGNET FLAT LINEAR BRUSHLESS MOTOR AND ITS CONTROL USING LINEAR OPTICAL POTENTIOMETER

A Dissertation

by

YOUNG SHIN KWON

Submitted to the Office of Graduate and Professional Studies of
Texas A&M University
in partial fulfillment of the requirements for the degree of

DOCTOR OF PHILOSOPHY

Chair of Committee,	Won-jong Kim
Committee Members,	Hamid A. Toliyat
	Alexander Parlos
	Bryan Rasmussen
Head of Department,	Andreas A. Polycarpou

August 2016

Major Subject: Mechanical Engineering

ABSTRACT

A new 6/4 double-sided interior permanent-magnet (IPM) flat linear brushless motor (IPM-FLBM) and novel optical potentiometer mechanism for a linear motion-control system are presented in this dissertation.

For this purpose, new detent-force-minimization methodologies for the IPM-FLBM are studied on the basis of the superposition principle. The end-effect force is reduced by a new two-dimensional optimization using the step-shaped end frames. The cogging force is minimized through a destructive interference using the slot-phase shift between the upper and lower stators. A base model prototype with the detent force of only 1.5% of the maximum thrust force is developed using the electrical solid steel. Analytic modeling techniques of the base model prototype with slot-phase shift and alternate teeth windings are investigated. A variable winding function is newly developed to evaluate the inductances of the salient motor with the alternate teeth windings. The steady-state thrust force is modeled for this linear brushless AC (BLAC) motor. Their validities are demonstrated experimentally. The electromagnetic and steady-state performance analyses of a new prototype using a soft magnetic composite (SMC) material are also studied using a simplified nonlinear magnetic equivalent circuit (MEC) analysis. Its iron and copper losses are investigated in terms of the thermal limitation. The feasibility of the IPM-FLBM using the SMC material is demonstrated through the comparisons of the average steady-state thrust and ripple forces for these two prototype linear motors.

A novel low-cost high-precision absolute displacement-sensing mechanism using optoelectronic components is developed. The working principle that is based on the change of the optical power that is reflected off the monotone-colored pattern track from a light emitting diode (LED) to a red-green-blue (RGB) photo diode (PD) is presented. The performance of the proposed optical potentiometer (OP) mechanism is verified by the bandwidth (BW) of 4.42 kHz and nonlinearity of 2.8% are achieved.

A novel low-ripple 12-step current control scheme using a single current sensing resistor is developed using the six Hall-effect sensors for the force control of the IPM-FLBM. Its performances are experimentally verified and compared with a conventional field-oriented control (FOC) scheme. In the end, the position-control loop, which includes the 12-step current control loop, double-sided IPM-FLBM, and linear optical potentiometer (LOP), is designed using a proportional controller with a lead compensator. The performances of the linear motion-control system are demonstrated through the various experiments in the time and frequency domains.

ACKNOWLEDGMENTS

First and foremost, I would like to express my sincere gratitude towards my advisor, Prof. Won-jong Kim, for his support, encouragement, and patience during my Ph.D. career. I enjoyed working with him, for all his considerate, thoughtful principles, and learning from him, for his vast knowledge about design and development of electromechanical systems.

I am grateful to Profs. Hamid Toliyat, Alexander Parlos, and Bryan Rasmussen for serving as my committee members. I especially thank Prof. Toliyat for all his invaluable lectures on electric machine design and control.

Thanks also go to my friends and colleagues in the Precision Mechatronics Lab for their support. I am very thankful to Mr. Eunseok Kim and Minsuk Kong for being such a good friend in this school.

I would certainly be remiss to mention and sincerely thank my friend, Hyeong-rae, and former colleague Jun-ki. Without their essential helps in hardware construction, this research and dissertation would not be complete.

Finally, I can never thank my wife, Soo-jung, and my son, Jung-woo, enough for their patience and understanding. They have always been great friends and wonderful counselors of mine. I would like to thank my parents, Tae-yong Kwon and Jung-hee Baik, and Soo-jung's parents Byung-in Choi and Young-hee Jun. Without their player and support, this level of doctoral work would not have been successful.

TABLE OF CONTENTS

Page

ABSTRACT ii

ACKNOWLEDGMENTS iv

TABLE OF CONTENTS v

LIST OF FIGURES viii

LIST OF TABLES xviii

CHAPTER I INTRODUCTION 1

1.1 Background 1
1.2 Literature Survey 3
1.2.1 Electromagnetic Linear Motors 3
1.2.2 Linear Displacement Sensors 7
1.2.3 Linear Motor Control Techniques 9
1.2.4 Dissertation Overview 10
1.2.5 Contribution of Dissertation 12

CHAPTER II DESIGN AND ANALYSIS OF IPM-FLBM 13

2.1 Conceptual Design of IPM-FLBM 14
2.1.1 Conventional Rotary Brushless Motors 14
2.1.2 6 /4 IPM Brushless Motor with Alternate Teeth Windings 15
2.1.3 6-Slot/4-Pole IPM FLBM 16
2.1.4 Design Parameters of Double-Sided 6/4 IPM-FLBM 17
2.2 Detent Force Minimization of Double-Sided 6/4 IPM-FLBM 19
2.2.1 Steady-State Thrust and Detent Forces of Base Model 20
2.2.2 End-Effect Force Minimization 21
2.2.3 Cogging Force Minimization 31
2.2.4 Detent Force-Free Stator 35
2.2.5 Total Detent- and Steady-state Thrust Force Measurements 37
2.3 Steady-State Modeling and Analysis of Double-Sided IPM-FLBM 40
2.3.1 Detent Force-Free Base Model Description 43
2.3.2 Simplified Magnetic Equivalent Circuit 45
2.3.3 No-Load Flux Density and Stator Relative Permeance 48
2.3.4 DC Resistance of Armature Winding 50

2.3.5 No-Load Flux Linkage and Back-EMF Voltage 52
2.3.6 Inductance Calculations 56
2.3.7 Thrust Force Calculation 63
2.3.8 Steady-State Force Validation 65
2.4 IPM-FLBM Using SMC 70
2.4.1 Inductance Calculations 72
2.4.2 No-Load Flux Linkage and Back-EMF Voltage 74
2.4.3 Simplified Nonlinear Magnetic Equivalent Circuit 75
2.4.4 Magnetic Field Analysis 79
2.4.5 Loss Analysis and Thermal Consideration 83
2.4.6 Steady-State Performance Validation 86

CHAPTER III OPTICAL POTENTIOMETER 92

3.1 Light and Its Terminologies 92
3.1.1 Light 92
3.1.2 Radiometry and Photometry 93
3.2 Optoelectronic Devices 96
3.2.1 Light-Emitting Diodes (LEDs) 96
3.2.2 Photo Diodes (PDs) 102
3.3 Optical Potentiometer Concept and Dynamic Model 107
3.3.1 Position-Sensing Mechanism Using Indirect Light 107
3.3.2 Dynamic Model of Optical Potentiometer 108
3.4 Rotary Optical Potentiometer 111
3.4.1 Mechanical Geometry Configuration 111
3.4.2 Steady-State Propagation Model in Color Coded Track 112
3.4.3 Steady-State Propagation Model in V-Shaped Track 118
3.5 Design Parameter Optimization and Calibration 120
3.5.1 Design Parameter Optimization 120
3.5.2 Calibration of Colored-Coded Track and Sensing Constant 122
3.5.3 Calibration of V-Shaped Track and Angle-Sensing Constant 125
3.6 Performance Validation 127
3.6.1 Hardware Implementation and Controller 127
3.6.2 Experimental Results 129

CHAPTER IV SYSTEM MODELING AND ITS CONTROL 133

4.1 Current Control of Double-Sided IPM-FLBM 134
4.1.1 Electromechanical Specification 134
4.1.2 12-Step Current Control 136
4.1.3 Field-Oriented Control 149
4.1.4 Performance Comparisons 153
4.2 Linear Motion System Model 159
4.2.1 Lumped-Parameter Model 159

4.2.2 Identification of Equivalent Stiffness 160
4.2.3 Simplified Model of Linear Motion Platform..... 164
4.2.4 Dynamic Friction Model..... 167
4.3 Position Loop Design and Performance..... 169
4.3.1 Frequency Response of Uncompensated System 170
4.3.2 Design of Proportional Controller and Lead Compensator 172
4.3.3 Performance Validation and Comparisons 176

CHAPTER V CONCLUSIONS AND SUGGESTIONS..... 183

5.1 Conclusions 183
5.2 Suggestions for Future Work 185

REFERENCES..... 186

APPENDIX A MECHANICAL ENGINEERING DRAWINGS..... 196

APPENDIX B ELECTRICAL ENGINEERING SCHEMATICS 209

APPENDIX C PROGRAM CODES 222

LIST OF FIGURES

Page

Fig. 1. Linear motion-control system using LOP. 2

Fig. 2. Magnetization curves of various soft iron-core materials. 6

Fig. 3. PM rotor configurations: (a) surface-mounted magnets and (b) buried PMs with circumference magnetization. 15

Fig. 4. 6/4-IPM brushless motors: (a) all teeth and (b) alternate teeth windings. 16

Fig. 5. 6/4 IPM-FLBM with all teeth windings 16

Fig. 6. 6/4 IPM-FLBM with all teeth windings and additional end frames 17

Fig. 7. 6/4 IPM-FLBM with alternate teeth windings. 17

Fig. 8. Base model of the double-sided 6/4 IPM-FLBM with alternate teeth windings. 18

Fig. 9. FEA results for the thrust and detent forces of the base model according to the mover positions. 20

Fig. 10. Left end-effect force measurement using the slotless rectangular prim iron-core stator when the mover's position is at zero. 22

Fig. 11. Measured left end-effect force according to mover positions when the pole pitch is 0.018 m, and the magnet length is 0.006 m. 23

Fig. 12. Measured end-effect forces according to the slotless stator's overall lengths and mover positions: slotless stators (top) and end-effect forces (bottom). 24

Fig. 13. (a) Optimal stator length analysis according to mover positions with respect to the peak-to-peak end-effect forces, (b) rms end-effect force according to the stator lengths. 24

Fig. 14. Dimension definition of the slotless stator with two different lengths. 26

Fig. 15. Measured end-effect forces according to the mover positions with respect to the stack depths of the long-length portion. 28

Fig. 16. Effective stack width ratio according to the mechanical stack width ratio of the long-length portion in the stator when $L_{ss} - L_s = 0.009$ m and $\delta = 0.001$ m. 30

Fig. 17. End-effect force comparison of the one-dimensional optimization (L_s = 0.0788) and two-dimensional optimization ($L_{ss} = 0.0835$ m, $L_s = 0.0745$ m, $D_s = 0.02$ m and $D_{ss} = 0.006$ m). 31

Fig. 18. Infinite-length stator model for the cogging force analysis. 32

Fig. 19. FEA results for cogging forces of the infinite-length stator model according to the mover positions with respect to the stator's tooth widths. 33

Fig. 20. Concept of the slot-phase shift configuration in the double-sided IPM-FLBM, where α_s is the slot-phase shift. 34

Fig. 21. FEA results for the stator with the slot-phase shift of $T_p/6$ between the upper and lower stators. (a) Total cogging forces and (b) the rms cogging force according to the tooth widths. 35

Fig. 22. Comparison of two different arrangements for double-sided stators: (a) non-slot-phase-shift configuration, and (b) slot-phase-shift configuration. 36

Fig. 23. Photograph of the experimental setup to measure the total detent- and steady-state thrust forces. 37

Fig. 24. Comparison of the predicted and measured thrust forces (top), and comparison of the predicted cogging and measured detent forces (bottom) when $T_t = 0.0076$ m. 38

Fig. 25. Maximum thrust force and detent force comparison (top), and magnified view of the detent force from the top figure (bottom). 39

Fig. 26. 3-D rendering for the proposed double-sided 6/4 IPM-FLBM with slot-phase shift and alternate teeth windings. 40

Fig. 27. Analysis flowchart for the double-sided 6/4 IPM-FLBM with the slot-phase shift and alternate teeth windings. 42

Fig. 28. Cross-sectional dimensions and coordinates of the double-sided 6/4 IPM-FLBM prototype using the electrical solid steel SS400. 43

Fig. 29. (a) Flux paths of the single-sided model when the *d*-axis is aligned with the stator reference axis under no-load condition. (b) Simplified MEC model with slot leakage reluctance under no-load condition. 46

Fig. 30. FE flux density vector paths in the mid-cross-section plane when the d-axis is aligned with the stator reference axis under the no-load condition. 50

Fig. 31. Predicted air-gap flux density distributions (the top and bottom plots are for the upper- and lower-side air gaps) when the *d*-axis is aligned with the stator reference axis under the no-load condition 50

Fig. 32. Uniformly concentrated rectangular winding: (a) the dimension definitions of the armature winding and (b) a photograph of the armature winding. 51

Fig. 33. Superposed winding functions of phases *a*, *b,* and *c* when a coil has the number of turns of 85. 54

Fig. 34. Analytic and FEA results of the no-load flux linkages for each phase according to the mover positions. 55

Fig. 35. Analytic and FEA results of the phase-to-neutral back-EMFs for each phase when the mover has the linear speed of 0.5 m/s. 56

Fig. 36. Variable winding function model in the IPM-FLBM: flux paths when the *d*-axis is aligned with the winding tooth center (top) and when the *q*-axis is aligned with the winding tooth center (bottom). 58

Fig. 37. Variable winding function of phase *b* in the upper and lower sides when the *d*-axis is aligned with the stator reference axis (top) and when the *q*-axis is aligned with the stator reference axis (bottom). 59

Fig. 38. Self-inductance distributions of each phase according to the mover positions. 62

Fig. 39. Mutual inductance distributions of each phase according to the mover positions. 62

Fig. 40. Photograph of the experimental setup to measure the inductances and steady-state thrust force. 66

Fig. 41. Thrust force components accordin to the current phase angle γ when the magnitude of the current vector I_s of 10 A is applied. 67

Fig. 42. Force-to-current ratios in the MFC and FOC scheme. 68

Fig. 43. Steady-state force and detent force according to the mover positions when I_{qs} and I_{ds} are controlled as 10 A and 0 A, respectively. 70

Fig. 44. Photograph of the stator core with the phase coils (right) and mover with PMs (left). 71

Fig. 45. The air-gap permeance models when the phase *b* is an armature MMF source: (a) the *q*-axis is aligned with the tooth center of phase *b*, (b) the *d*-axis is aligned with the tooth center of phase *b*. 72

Fig. 46. Flux paths of the single-sided models due to (a) PM and (b) armature current when the *d*-axis is aligned with the stator tooth centerline of phase *b*. Corresponding simplified nonlinear MEC models under (c) the no-load condition and (d) the electrical load condition. 76

Fig. 47. B-H curves of the SS400 and SPM. 76

Fig. 48. Stator-tooth flux curves (top) and air-gap flux density curves (bottom) according to the armature current. 79

Fig. 49. Stator-tooth flux Φ_3 (mWb) contour plot according to the PM and stator tooth widths when I_a = 10 A. 80

Fig. 50. Air-gap flux density curves according to the PM height for the three different load conditions when T_m = 0.006 m and T_t = 0.0076 m. 81

Fig. 51. Air-gap flux density curves according to the air-gap size for the three different load conditions when T_m = 0.006 m and T_t = 0.0076 m. 82

Fig. 52. Air-gap flux density variation curve in the mover core according to the back-iron height under the 10-A electrical load condition when T_m = 0.006 m and T_t = 0.0076 m. 82

Fig. 53. Steady-state temperature responses (top) and iron loss ratios (bottom) of the stator-winding assembly according to the phase current and operating frequency under the natural convection condition when A_{es} = 0.0079 m^2 and m_s = 0.0936 kg. 86

Fig. 54. Analytic and measurement results of the back-EMFs for each phase when the mover has the linear speed of 0.2 m/s. 86

Fig. 55. Self-inductance distributions of the SPM prototype according to positions 87

Fig. 56. Mutual inductance distributions of the SPM prototype according to positions. 88

Fig. 57. Steady-state thrust forces of the SPM and base model (SS400) prototypes according to the mover positions when I_a = 8.66 A, I_b = 0 A and I_c = –8.66 A. 89

Fig. 58. Steady-state forces (top) and detent forces (bottom) of the SPM and base model (SS400) prototypes according to the mover positions when I_{qs} and I_{ds} are controlled as 10 A and 0 A, respectively. 90

Fig. 59. Temperature responses in the end winding of the stator-winding assembly according to the magnitude of the phase current. 91

Fig. 60. Light emitting diodes and photo diodes: (a) Precision optical Performance Red color LED (HLMP-EG08_YZ000, Avago Technology), (b) High power Tri-Color LED (Moonstone, Avago Technology), (c) Red-green-blue (RGB) Photodiode (S7505-5, Hamamatsu, and (d) Gap Photodiode (FGAP71, ThorLabs. 96

Fig. 61. LED electroluminescene mechanism: (a) standard structure and (b) point source. emitter structure. 97

Fig. 62. Forward diode voltage versus bandgap energy of various LEDs using materials. 98

Fig. 63. (a) Definition of the critical angle. (b) Area element of calotte-shaped surface of the sphere defined by radius r and the critical angle. 99

Fig. 64. (a) Viewing angle, (b) Emission spectrum and FWHM. 102

Fig. 65. Photoelectric current mechanism (left) and symbol of PD (right) 102

Fig. 66. (a) Equivalent circuit model of PD. (b) Steady-state model of PD. 104

Fig. 67. Responsivity of silicon diode (OPA 101). 104

Fig. 68. Photoconductive mode (PC) and Photovoltaic Mode (PV). 106

Fig. 69. Optical potentiometer sensing mechanism: (a) RGB coded track. (b) V-shaped track. 108

Fig. 70. Dynamic analysis between LED and RGB: (a) Test scheme. (b) Time responses. 108

Fig. 71. 2-D cross-sectional view of the rotary optical potentiometer 111

Fig. 72. (a) Normalized 3-D Lambertian radiant intensity pattern of the LED. (b) Normalized radiant intensity according to the angle displacement of the LED (HLMP-EG08-Y2000). 113

Fig. 73. Expected normalized reflected power density on the tangential surface ($\rho(E_{ts}(\theta_v)+E_{ss}(\theta_i,\theta_r,0))/E_{ts}(0)$ with $\rho = 0.2$, $k_s = 0.4$, and $\sigma_s = 10°$)..... 114

Fig. 74. Power densities due to the red RGB colored track and the incident area illuminated by the LED. 116

Fig. 75. V-shaped track and the rectangular mask for linearization of the received optical power. 120

Fig. 76. Diameter of the incident-beam area and the visible viewing angle of the LED according to the displacement of d_{LS} when I_F is 20 mA..... 121

Fig. 77. (a) Experiment photo for optimal distance (d_{SR}). (b)The output voltages of the red color channel of the RGB sensor according to circular white-colored area and distance (d_{SR}). 122

Fig. 78. Non-compensated and compensated angle of the optical potentiometer in color-coded Track. (when $I_F = 20$ mA, $d_{LS} = 0.015$ m, $d_{SR} = 0.0065$ m, and the physical cell size of each color code on the cylinder is 0.0005236×0.1 m^2). 124

Fig. 79. Output voltage of the differential OP-amp with gain of 4.5..... 125

Fig. 80. Optical potentiometer angle vs. resistive potentiometer angle in V-shaped Track (when $I_F = 20$ mA, $d_{LS} = 0.015$ m, $d_{SR} = 0.0065$ m)..... 127

Fig. 81. Hardware block diagram of the rotary-position control system. 128

Fig. 82. Rotary position-control system with ROP..... 129

Fig. 83. Step responses of the position-control loop using the ROP with the CCT for various reference commands (±10°, ±20°, ±40°, and ±80°)..... 130

Fig. 84. Step responses of the position-control loop using the ROP with the VST for various reference commands (±10°, ±20°, ±30°, and ±60°)..... 131

Fig. 85. Sinusoidal response to a 1-Hz sinusoidal reference input with the magnitude of 60° and the period of 1 s (Position control using RRP (Top figure), position control using ROP with CCT (middle figure), and position control using ROP with VST (bottom). 132

Fig. 86. Photograph of the new double-sided 6/4 IPM-FLBM prototype 134

Fig. 87. Coordinate definitions of the double-sided 6/4 IPM-FLBM: (a) 3-D cross-sectional view of the mechanical model, (b) electrical angle model using the current vector coordinates with slot-phase shift, and (c) simplified equivalent electrical angle model using the resultant current vector coordinates. 135

Fig. 88. Measured Hall-effect sensor outputs (top) and back-EMF voltages (bottom) according to the mover positions when the mover moves at 0.2 m/s. 137

Fig. 89. Predicted 12-step quasi-sinusoidal phase current waveforms according to the electrical angles when I_m = 10.0 A. 138

Fig. 90. Predicted ripple forces according to the commutation schemes and electrical angle when the phase current of 10 A is applied. 138

Fig. 91. Hardware block diagram of the 12-step current control for the double-sided IPM-FLBM with slot-phase shift. 139

Fig. 92. 12-Step commutation sequence during one electrical angle cycle. 141

Fig. 93. Actual phase, measured, and corrected dc-link currents according to the duty cycle variation in the switching modes when the dc-link voltage of 30 V is applied. 143

Fig. 94. Block diagram of the 12-step current control using the dc-link current. 146

Fig. 95. Open-loop frequency responses of the phase current I_ϕ for the current command I^*_{dc} in the two-phase conduction mode (a) and three-phase conduction mode (b) when the dc-link voltage is 30.0 V, and the proportional gain K_p and integral gain W_i are 0.7 Duty Cycle/A and 754 rad/s, respectively. 148

Fig. 96. Control block diagram of the indirect FOC scheme for the double-sided IPM-FLBM with the slot-phase shift. 149

Fig. 97. (a) A representation of the space vectors V_1 to V_6, and a voltage vector V_{ref}. (b) The space vector modulation of the three-phase voltages in sector I. 151

Fig. 98. The dc-link current (top) and phase current waveforms (bottom) with respect to the mover positions when the step current command of 1.0 A is applied in the 12-step current control scheme 154

Fig. 99. The measured q- and d-axis current (top) and phase current waveforms (bottom) according to the mover positions when the step current command of 1.0 A is applied in the FOC scheme. 155

Fig. 100. The current vector trajectories in the stationary αβ-reference frame: (a) 12-step current control scheme and (b) FOC scheme. 155

Fig. 101. Thrust forces of the 12-step current control and FOC schemes according to the sinusoidal current command of 1.0 A and 3.0 Hz: thrust forces (top), current command I^*_{dc} and dc-link current $I_{dc\text{-}link}$ (middle), and current command I^*_q, q-axis current I_q, and d-axis current $I_d = 0$ (bottom)..... 156

Fig. 102. Pulsating forces (top), detent force (middle), and ripple forces (bottom) of the 12-step current control and FOC schemes when the mover moves at the constant speed of 0.1 m/s..... 158

Fig. 103. (a) Thrust force versus current command (K_f = 6.05 and 6.18 N/A for the 12-step current control and FOC schemes, respectively). (b) Electric power consumption comparison according to the thrust force. 158

Fig. 104. Lumped-parameter model concept for linear motion platform. 159

Fig. 105. Isometric view of the FEA model to evaluate the equivalent stiffness. 161

Fig. 106. Static deformation of the mover assembly when the x-directional loading force of 100 N is applied. 162

Fig. 107. X-directional deformation according to the applied forces and the mover positions. 163

Fig. 108. Equivalent spring constant of the mover assembly according to the mover positions. 164

Fig. 109. Parameters and variables in the lumped-parameter model. 164

Fig. 110. Simplified pure mass model with a friction model..... 166

Fig. 111. Velocity control loop to measure the friction coefficients. 168

Fig. 112. Measured and modeled frictions..... 168

Fig. 113. Current loop model of the linear motion system. 169

Fig. 114. Simplified open-loop model for the linear motion system. 170

Fig. 115. Open-loop frequency responses of the uncompensated system. 171

Fig. 116. Closed-loop control block diagram of the linear motion system. 172

Fig. 117. Open-loop frequency responses of the uncompensated and compensated systems when K_d = 3.5, A = 10.7, ω_1 = 26.4 rad/s, and ω_1 = 282.6 rad/s. 175

Fig. 118. Photograph of the experimental setup to measure the performances of the linear motion platform. 176

Fig. 119. Step responses of the same position-control loops according to the two different current control schemes. 177

Fig. 120. The responses of the same position-control loops according to the two different current control schemes for the ramp input command of 10 mm/s. 178

Fig. 121. The responses of two position-control loops using the different current control schemes for the sinusoidal input command of 15 mm at 1 Hz. 179

Fig. 122. Responses for various step inputs in the position-control loop using the 12-step current control and LOP. 180

Fig. 123. The responses of the position-control loops using the FOC and LOP for the ramp input command of 10 mm/s. 181

Fig. 124. The responses of the position-control loops using the FOC and LOP for the sinusoidal input command of 15mm with 1 Hz. 182

Fig. 125. The linear motion platform with LOP sensor module. 196

Fig. 126. High level components of the linear motion platform. 197

Fig. 127. Components of the double-sided IPM-FLBM assembly. 198

Fig. 128. Components of the dummy load assembly. 199

Fig. 129. Stator housing part 1. 200

Fig. 130. Stator housing part 2. 201

Fig. 131. SMC stator. 202

Fig. 132. Armature coil holder. 203

Fig. 133. Mover frame front. 204

Fig. 134. Mover core. 205

Fig. 135. Permanent magnet. 206
Fig. 136. Mover frame side. 207
Fig. 137. Mover loader. 208
Fig. 138. Photograph of the controller assembly for the linear-motion control. 209
Fig. 139. Photograph of the DSP breakout board 210
Fig. 140. Photograph of the digital interface board. 212
Fig. 141. Digital interface board schematic (1/2). 213
Fig. 142. Digital interface board schematic (2/2). 214
Fig. 143. Photograph of the analog interface board. 215
Fig. 144. Electric circuit schematic of the analog interface board (1/3). 216
Fig. 145. Electric circuit schematic of the analog interface board (2/3). 217
Fig. 146. Electric circuit schematic of the analog interface board (3/3) 218
Fig. 147. Photograph of the PWM amplifier board. 219
Fig. 148. Electric circuit schematic of the PWM amplifier board. 220
Fig. 149. Wiring diagram of the linear control system. 221

LIST OF TABLES

Page

Table 1. Possible topologies and configurations of linear motors [1], [2]..... 3

Table 2. Linear displacement sensors [25]. 8

Table 3. Driving methods for the LBM [35]–[42]..... 10

Table 4 Mechanical design specifications of the base model 18

Table 5 Estimated Fourier coefficient of the left end-effect force..... 23

Table 6. Final design parameter of the stator..... 36

Table 7 Mechanical specifications of the base model prototype 44

Table 8. Average values of the inductances..... 63

Table 9. Iron loss per kilogram of the SPM [57]. 84

Table 10. Average inductances of the SPM and base model prototypes. 88

Table 11. Performance comparison of the SS400 and SPM prototypes. 90

Table 12. Thermal conductivity and material thickness. 91

Table 13. Photometric and corresponding radiometric unit..... 93

Table 14. Performance parameters of LED, RGB Sensor, and PD. 110

Table 15. Statistic performance of uncompensated and compensated tracks in the range of −60° to 60°. 124

Table 16. Statistical performance analysis between −60° and 60° for printer DPI. 126

Table 17. Specification of the double-sided IPM-FLBM 135

Table 18. Phase current measured according to switching states. 142

Table 19. Coefficients of the error function according to switching modes..... 144

Table 20. Open-loop performance of 12-step current control scheme 147

Table 21. Open-loop performance of FOC scheme 153

Table 22. Material properties used in FEA 162

Table 23. Simulation parameters 170

Table 24. Open-loop frequency response characteristics of the uncompensated systems 171

Table 25. Open-loop frequency-response characteristics in two different current control schemes 175

Table 26. Pin descriptions of CN9100 and CN9101 headers 211

Table 27. Pin description of CN9200 and CN9201 headers 211

CHAPTER I

INTRODUCTION

1.1 Background

Linear motion-control systems are found in many industrial applications and are extensively used in machine-tool sliding tables, semiconductor fabrication, biomedical equipment, and precision factory automation. Many of them often use a conventional linear platform driven by electric rotary actuators with rotary or linear displacement sensors for linear position-control. Such linear motion-control systems have been combined with gear reducers and ball or lead screws to increase force capability for generating linear motion. This approach, although effective in many applications, requires the added complexity of a speed reducer as well as causes backlash. Moreover, it may be too sluggish for the applications that require rapid responses and maneuvering. Therefore, the demands replacing rotary magnetic actuators with direct-driven linear actuators increase faster than ever before. Many researchers have been seeking for the way to develop the cost-effective direct-driven linear motor that can generate high force density within a confined volume. A decade ago, it was a significant challenge to construct a commercially viable linear motor that can provide fast dynamic responses, exact positioning, and long life with less maintenance. Recently, thanks to the advancement of key technologies such as rare-earth magnets, high permeable soft-core materials, high-precision linear displacement sensors, and low-cost high performance digital signal processors, the linear motors having the mover directly connected to the

load without backlash and elasticity are being developed. This leads to the improvement of the dynamic behavior of linear motors and results in the higher accuracy.

The objective of this research is to develop a precision linear position-control system using a double-sided IPM-FLBM and a cost-effective novel LOP. For this purpose, this research addresses five parts: (1) detent force minimization of the double-sided IPM-FLBM with 6/4 configuration (two 6-pole stators having three active coils and a 4-pole mover), (2) optimal design and fabrication of the IPM-FLBM using the SMC material, (3) design and development of the high-precision absolute LOP, (4) new current control scheme for the new proposed linear motor, and finally, (5) development and performance validation of the linear motion-control system using the 12-step current control and LOP. Fig. 1 shows the drawing for the linear motion-control system using the LOP.

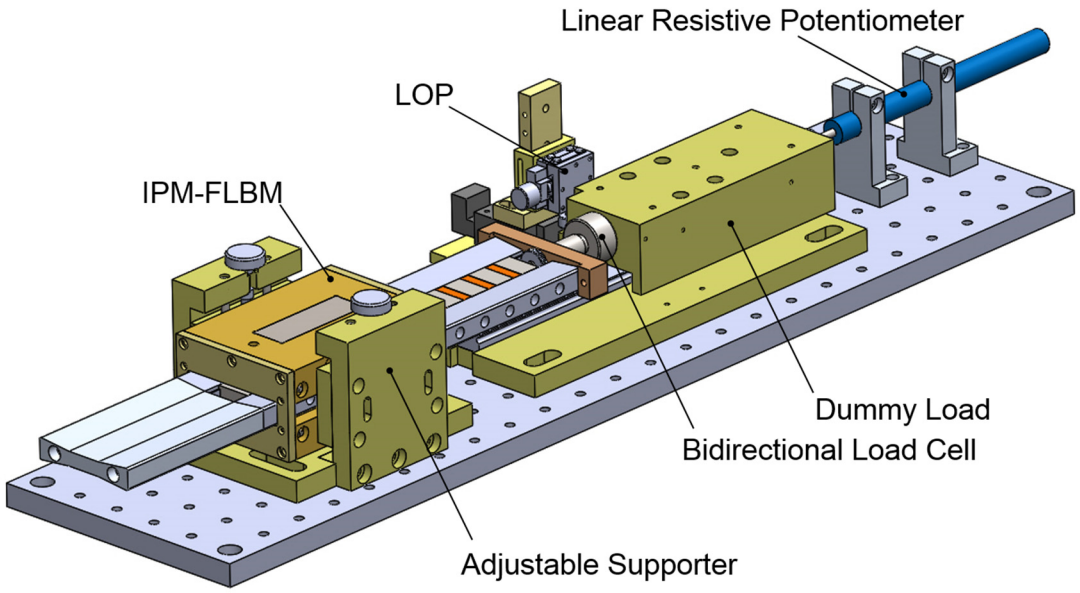

Fig. 1. Linear motion-control system using LOP.

1.2 Literature Survey

1.2.1 Electromagnetic Linear Motors

Since the first working model for linear motors was invented by Laithwaite in the 1960s [1], the linear motor fabrication and control techniques have been remarkably developed. The linear motor becomes an indispensable component in linear motion-control systems [1], [2]. As shown in Table 1, linear motors can be classified in three types according to their operating principles, such as linear induction motor (LIM), linear reluctance motor (LRM), and linear synchronous motor (LSM).

Table 1. Possible topologies and configurations of linear motors [1], [2].

Type	Shape	Number of Stator	Type of Stator	Mover core	Permanent Configuration	Force Density	Detent Force
Linear induction motor (LIM)	tubular	single	slotted	iron	none	medium	none
	flat	single				low	none
		double				medium	none
Linear synchronous motor (LSM) or Linear brushless motor (LBM)	tubular	single	slotted	iron	SPM or IPM	high	high
			none (air coil)	none	longitudinal stack on mover	low	none
	flat	single	slotted	iron	SPM or IPM	high	high
			slotless	iron	SPM on stator	medium	low
				air	SPM on stator	low	none
		double	slotted	iron	SPM or IPM	high	high
			slotless	air	SPM on stator	medium	none
Linear reluctance motor (LRM)	tubular	single	slotted	iron	none	medium	high
	flat	single				low	high
		double				medium	high

* SPM is the abbreviation of the surface-mounted permanent magnet.

The LIM is mainly employed in constant-speed applications or long travel applications. The LRM has no permanent magnet, and also has an advantage that can control motion with no position sensor, but its force density is not high because its thrust force is mainly generated by the variable reluctance. In contrast, the LSM can perform precision position control as well as generate high force density due to the advancement of rare-earth permanent magnet (PM) with high remanence. Especially, the linear brushless motor (LBM), which is one of the specialized LSMs, has several advantages: (1) easy to install the armature coils, (2) easy to assemble the unit modules, (3) easy to adjust the air-gap, (4) shorter end-winding length, and (5) smaller armature DC resistance. In this sense, the LBM can be the best candidate as an actuator of the linear motion-control system.

Since the slotted iron-core linear motors using the SPM or interior IPM configurations listed in Table 1 can produce much larger force than other types of linear motors, they are suitable in high-force density applications. However, their detent forces such as the end-effect force due to stator's finite length and the cogging force are drawbacks in the high-precision motion control in low-speed applications. Thus, air-core linear motors without such detent forces have been used as an alternative in precision linear motion-control systems that do not require high-force density, but their lower force density become another disadvantage. For these reasons, many researchers and industries have attempted to minimize the detent forces of the iron-core PM linear motor on the basis of the studies of the cogging force of the conventional rotary PM motors. Due to the advancement of the numerical analysis based on FEA tools, however, various detent-

force-minimization techniques such as skewed PM placement [3], semi-closed slots [3], [4], stator having auxiliary teeth [4], [5], overall length extension of stator [6], alternative fractional slot-pole structure [7], and asymmetric PM placement [8], [9] were developed previously. Although these techniques reduced the detent forces effectively, some methods increased fabrication difficulties such as oversized magnet, elaborated winding process, post-optimization for additional teeth, excessively lengthy stator, and various sized iron-cores [3]–[9]. Recently, a PM pole-shift method useful for mass production was introduced for a double-sided SPM linear motor [10], but this technique cannot be applied to an IPM linear motor.

Many studies related to the design, modeling, and performance analysis for linear motors have mainly focused on the SPM-FLBMs: the improved MEC circuit models of the single-sided iron-core SPM-FLBM were introduced in [11], [12], and the modeling and analysis for the double-sided SPM-FLBM were investigated for an electromagnetic aircraft launcher [13]. The performance analysis for the single-sided IPM-FLBM with vertical magnetization and distributed windings was performed in [14], and the design criteria and optimization for slotted IPM-tubular linear motors with the axial magnetization were also presented in [15], [16]. Nevertheless, little research has been previously done in modeling and analysis for the double-sided IPM-FLBM.

Most slotted iron-core types listed in Table 1 use the laminated thin silicon steel sheets as the soft magnetic material for the minimization of the eddy-current loss. In order to overcome such drawbacks, new powder iron-composite material was developed in the early 2000s [17]. This SMC material has several advantages such as low eddy-current

loss, flexible machine design and assembly, three-dimensional isotropic ferromagnetic behavior, relatively good recyclability, and reduced production costs [18].

However, as shown in Fig. 2, the lower permeability than the conventional laminated steel core has hindered the extensive use of the SMC material in electric machines. Therefore, various studies considering such characteristics of the SMC material have been done on the various electric machine designs over the past decade. The optimal stator core teeth of a PM synchronous motor (PMSM) using the SMC material was studied [19]. The SMC hybrid BLDC motor and SMC claw-pole motors were analyzed [20], [21]. The axial-flux PMSM was introduced [22], [23]. The design optimizations for a tubular linear motor using the SMC were investigated with a finite-element analysis (FEA) [24].

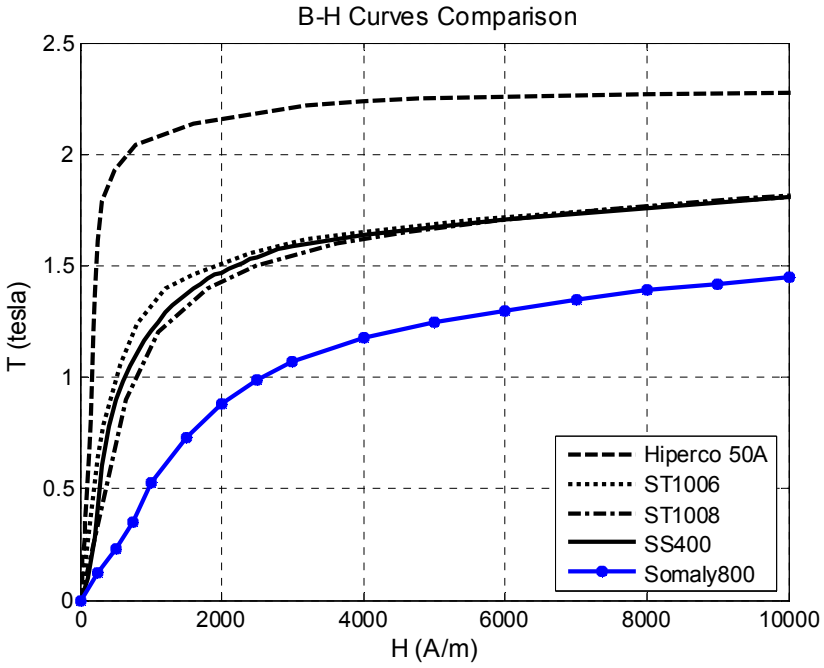

Fig. 2. Magnetization curves of various soft iron-core materials.

1.2.2 Linear Displacement Sensors

Linear displacement sensors in linear position-control systems play an indispensable role as a feedback device measuring the current position. Table 2 shows the pros and cons of these sensors. The conventional linear displacement sensors can be classified into the contact type like linear potentiometers and the non-contact types such as optical linear encoders, magnetic linear encoders, and linear variable differential transformers (LVDTs). The main advantage of the latter sensors is that high measurement accuracy, resolution, and reliability can be achieved without wearing-out. However, the high prices of these sensors and their electronics often act as an entry barrier in low-cost commercial applications. In contrast, low-cost linear resistive potentiometers (LRPs) have expanded the market share in commercial control applications. However, the drawbacks such as the debris accumulation or resistive surface wearing-out due to the inherent contact-sensing mechanism remain an unsettled problem during a long-term operation [25]. Therefore, the demands of new cost-effective noncontact linear displacement sensor that can replace the conventional linear displacement sensors are increasing in order to reduce the total cost of the linear motion systems.

Several new non-contact displacement sensors such as Hall-effect sensors and inductive sensors have been developed [26]–[29]. The first attempt to measure the linear displacement from the received optical power variation by the beam path interruption between a LED and a PD was introduced without an exact model of the interaction between an optoelectronics couple and a movable interrupter [30]. A LOP using the optical power change from a light passing through the cylindrical track with a triangular

aperture was conceptually designed [31]. However, the new sensors using the Hall-effect and inductance variation still need expensive interpolating converters to obtain a linear displacement from measured electrical signals. The introduced LOP that senses the variation of the direct optical power passing through the slit track do not consider the analytical derivation for its optical power propagation, and has the application limit due to the separated structure of the transmitter and receiver.

Table 2. Linear displacement sensors [25].

Transducers	Working principle	Advantages	Disadvantages
Linear optical encoder	quadratic pulse generation by interaction between optoelectronic pair and patterned scale	· accurate · high resolution · unlimited life time	· medium cost · required decoder
Magnetic linear encoder	quadratic pulse generation by interaction between magnetoresistive pickup and magnetic tape	· accurate · high resolution · unlimited life time	· medium cost · required decoder · weak to electromagnetic noise · long measurement range
LVDT	analog voltage induction due to magnetic field between windings and movable core	· rugged · accurate · infinite resolution · unlimited life time	· high cost · limited distance · signal conditioning electronics needed
Resistive Linear potentiometer	resistance change between the wiper and resistive strip	· low cost · infinite resolution · no electronics needed	· limited lifetime due to wear · nonlinearity · limited distance

1.2.3 Linear Motor Control Techniques

Especially, the linear brushless motor (LBM) is being used extensively thanks to the simple control scheme, higher efficiency and reliability, as well as its easy maintenance. The LBM commonly uses the concentrated windings with the fractional pitch, and its flux linkage and back electromotive force (back-EMF) can have either the trapezoidal or sinusoidal waveforms according to its permanent-magnet (PM) configuration [32]. Thus, the LBM can be classified into the brushless direct current (BLDC) and brushless alternate current (BLAC) types [33]. Generally, the BLDC motor has a greater force density than the BLAC type whereas the BLAC motor has the wider speed range and lower ripple force than the BLDC type. Thus, the BLAC motor is preferred for high-performance motion control applications [32]–[34]. Like conventional force control techniques for the rotary BLAC motor, various control schemes such as the 6-step commutation method based on the three Hall-effect sensors [35], [36], sinusoidal drive control [37], [38], direct torque control (DTC) [39]–[41] and FOC [35], [37], [42] can be employed in the precision linear BLAC motors. Although the conventional 6-step commutation method using Hall-effect sensors has an inevitable ripple force due to the coarse commutation based on the low resolution, this control scheme has strong advantages such as a cost effectiveness and simple control structure in comparison with the conventional FOC. Recently, to overcome this drawback in such cost-effective control scheme, Buja et al. [43] proposed the ripple-free operation using the petal-wave current form based on the Hall-effect sensor. Wang et al. and Kim et al. [44], [45] introduced twelve-step commutation methods to reduce the torque ripple in the sensorless BLDC

motor speed control without current control. Yang et al. [36] proposed an improved angular displacement estimation using Hall-effect sensor.

Table 3. Driving methods for the LBM [35]–[42].

Driving method	Advantages	Disadvantages	Remarks
Trapezoidal commutation	· simple control scheme · low cost · Hall device	· ripple force and low efficiency due to the misalignment from 0° to 30° · low precision at low speed	· only six different directional current space vectors · two-phase current control
Sinusoidal commutation	· precise motion control at low speed · less ripple force	· require precision feedback sensors such as encoder or LVDT · large error at high speed due to controller type and bandwidth	· rotating current space vector in the quadrature direction · third current is the sum of other two currents
Direct thrust control	· simple control scheme · no vector transformation	· ripple torque · require precision feedback sensors such as encoder or LVDT	· electromagnetic torque and flux linkage directly and independently · two hysteresis controllers
Field oriented control	· high efficiency · less ripple force · precision motion control at high and low speed	· high performance DSP or processors are needed	· isolating the PI controller from the time-varying current through d-q reference frame · $\alpha-\beta$ transform is usually needed

1.2.4 Dissertation Overview

This dissertation contains five chapters. Chapter I presents a literature review of existing conventional linear motors, position sensors, and their control schemes. The various types of linear motors are investigated, and their differences are reviewed. The pros and cons of the various displacement sensors are discussed. In addition, the current control techniques for the conventional motor are introduced.

In Chapter II, the conceptual design of the double-sided linear motor is performed on the basis of the conventional rotary motor with alternate teeth windings. The detent force minimization techniques are proposed using the experimental approach and finite-element analysis (FEA). The comprehensive analytic solutions for the performance parameters in the detent force-free model are presented. Especially, the variable winding function theory is newly presented. The new double-sided IPM-FLBM using the SMC material is developed using a nonlinear electromagnetic analysis, and its potential is discussed through the performance comparisons with the motor using the conventional electrical steel.

Chapter III covers the fundamental terminologies to understand the optical system. The typical optoelectronics devices are introduced. The working principle of the optical potentiometer is presented and its design is performed using the analytic solution and experimental optimization. The performance validations are provided using the rotary motion control system.

In Chapter IV, the various current control techniques for the BLAC motor are introduced. The detail design producers for the newly proposed 12-step current control scheme and its performances are presented. The analytic model for the linear motion system using the proposed linear motor is derived from the system identification based on the lumped-parameter method and FEA. The proportional controller with a lead compensator is designed from the open-loop frequency analysis and time responses under the given performance requirements. In the end, the performance comparisons of the two position-control loop with different current control scheme and LOP are presented.

Chapter V is devoted to the conclusions and suggestions for future work.

1.2.5 Contribution of Dissertation

The main contribution of this dissertation is the development of a novel double-sided IPM-FLBM and LOP. To reduce the detent force of the linear motor, new detent force minimization techniques were developed. The IPM-FLBM using the SMC material was optimized on basis of the nonlinear MEC analysis and developed. The novel cost-effective LOP as a displacement sensor is developed using optoelectronic devices. In addition, the new cost-effective 12-step current control scheme for the BLAC motor with slot-phase shift was developed. The applicability of the linear motion-control system constructed with newly developed actuator and sensor was demonstrated experimentally.

CHAPTER II

DESIGN AND ANALYSIS OF IPM-FLBM[1]

In Chapter II, firstly, the conceptual design of the double-sided linear motor is discussed on the basis of the conventional rotary motor with alternate teeth windings. The differences between the linear and rotary motor are discussed. In the following section, the detent force minimization techniques are investigated using the experimental approach and finite-element analysis (FEA). The analytic solutions for the detent force minimization in the double-sided IPM FLBM are presented. In the third section, the comprehensive analytic solution for the performance parameters are derived using the superposition theory. Especially, the new variable winding function theory is discussed and generalized for the same types of motors. In the last section, the electromagnetic analysis and steady-state performance for the double-sided IPM-FLBM using the SMC material is presented using a nonlinear MEC, and its potential is discussed through comparisons with the base model prototype using the conventional electrical steel.

[1] © 2016 IEEE. Reprinted in part with permission from "DetentForce Minimization of DoubleSided Interior PermanentMagnet Flat Linear Brushless Motor," by Y. S. Kwon and W. J. Kim, *IEEE Trans. Magnetics*, vol. 52, no. 4, pp. 8201609, Apr. 2016.

2.1 Conceptual Design of IPM-FLBM

2.1.1 Conventional Rotary Brushless Motors

The conventional rotary brushless motor can be defined as a rotary synchronous motor using the PMs and the concentrated windings based on the fractional slot pitch. This structural configuration can reduce the space harmonic flux distribution and the end-turn, increase the energy efficiency, as well as make the controller simple. This brushless motor can be classified into the BLDC motor with the trapezoidal back-EMF waveform and the BLAC motor with the sinusoidal back-EMF waveform, respectively. The back-EMF waveform in the brushless motor is mainly determined by the PM configuration because the brushless motor has the concentrated winding. The PM of the rotor can be configured with surface-mounted magnets, inset magnets, buried magnets with radial magnetization, and interior magnets with circumferential magnetization. Fig. 3 shows the axial views of two brushless motors with 3 stator poles and 4 rotor poles. The SPM configuration of Fig. 3(a) has a large air gap due to the relative permeability of the PM, has a low inductance in magnetized direction, and has a trapezoidal back-EMF. In contrast, the IPM configuration of Fig. 3(b) has greater air-gap flux density than that of the SPM configuration because of the flux-focusing effect, has much higher inductance in magnetized direction, as well as has the back-EMF close to the sinusoidal waveform. Thus, the IPM brushless motor can produce much more torque if the reluctance torque is used in the IPM brushless motor under the condition of the same weight and volume, as well as generate less ripple than those of the SPM brushless motor.

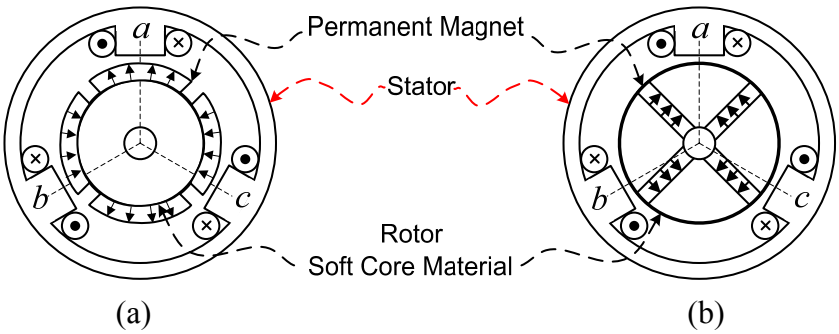

Fig. 3. PM rotor configurations: (a) surface-mounted magnets and (b) buried PMs with circumference magnetization.

2.1.2 6 /4 IPM Brushless Motor with Alternate Teeth Windings

The maximized linkage and torque of the rotary synchronous motor are obtained when the coil pitch is equal to the pole pitch. However, since it is impossible for the pitch of the concentrated windings of the three-phase brushless motor to be equal to the pole pitch, it is desirable for the coil pitch to be close to the pole pitch as it is possible. The minimum difference between the number of slots N_s and the number of pole pair N_p can be determined by $2N_p = N_s \pm 1$ as shown in Fig. 3. However, such configuration results in the excessive noise and vibration due to the unbalanced magnetic scheme. Hence, in practice, the general relation for N_s and N_p is given by

$$2N_p = N_s \pm 2 . \tag{2.1}$$

From (2.1), the possible $N_s/(2N_p)$ combination in the three-phase brushless motor can be 6/4, 6/8, 12/10, 12/14, 18/16, and 18/20. These combinations can produce a high-torque density due to the similar pitch between the magnet and stator poles, reduce the end-winding due to the non-overlapping winding, as well as generate a low cogging torque due to the fractional ratio of slot number to pole number. Fig. 4 shows two different 6/4 configurations using all teeth and alternate teeth windings, respectively [46].

(a) (b)

Fig. 4. 6/4-IPM brushless motors: (a) all teeth and (b) alternate teeth windings.

2.1.3 6-Slot/4-Pole IPM FLBM

Since a linear motor can be defined as the result of splitting a cylindrical rotary machine along a radial plane, and unrolling it, its fundamental working principle of LBMs is the same as that of the rotary brushless motor. Therefore, the IPM brushless motor with all teeth windings shown in Fig. 4(a) can be transformed into the IPM-FLBM depicted in Fig. 5 through cutting and unrolling of the rotary motor.

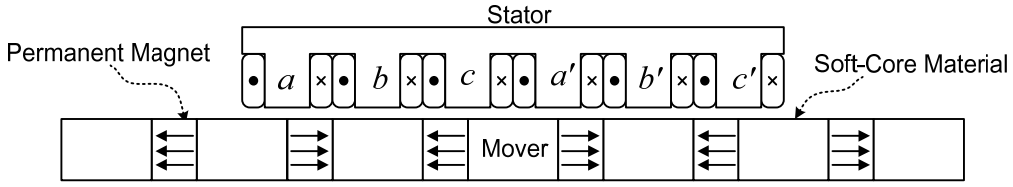

Fig. 5. 6/4 IPM-FLBM with all teeth windings

However, this structure cannot effectively use three-phase conduction mode because the flux path between the phases *a* and *c′* does not exist. This implies that the above structure can be driven by using three 120° quasi-square wave currents, but cannot be driven by the 180° quasi-sinusoidal wave current or space vector control using three-phase current conduction mode. Thus, the end frames shown in Fig. 6 should structurally be considered on both the end sides of stator in order to make the balanced magnetic flux

path in the three-phase conduction mode. As a result, the additional length (= one slot pitch) is needed for balanced magnetic circuit, as well as the weight and volume increase.

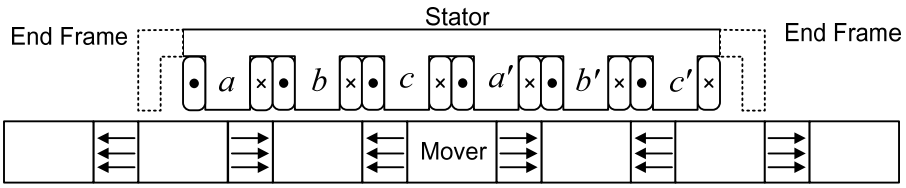

Fig. 6. 6/4 IPM-FLBM with all teeth windings and additional end frames

In contrast, the 6/4 configuration with alternate teeth windings shown in Fig. 4(b) can be transformed to Fig. 7 with no additional end frames because the empty teeth without a winding can play a role of the end frame. Thus, although the end-turns of each winding increase in order to generate the same magnetomotive force (MMF), this alternate teeth winding configuration can be more suitable in the small-sized linear brushless motor than all teeth winding configuration with respect to the overall volume and weight. This configuration also uses the three-phase current conduction mode..

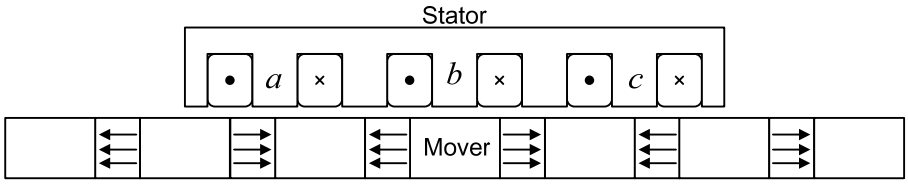

Fig. 7. 6/4 IPM-FLBM with alternate teeth windings.

2.1.4 Design Parameters of Double-Sided 6/4 IPM-FLBM

An advantage of linear motors compared to their rotary counterparts is that a double-sided configuration is possible. Since this configuration can produce a much larger thrust force than the single-sided type in a given volume, it is suitable for the applications that require high thrust forces. Fig. 8 shows the base model for the 6/4

double-sided IPM-FLBM with alternate teeth windings, configured on the basis of the stator of a rotary brushless DC (BLDC) motor [10], [11]. Therefore, the passive tooth between phases *a* and *c* in a rotary motor is substituted with two exterior teeth at both ends of the stator for the 180° six-step current control mode or the FOC. The mechanical specifications of this base model are listed in Table 4 .

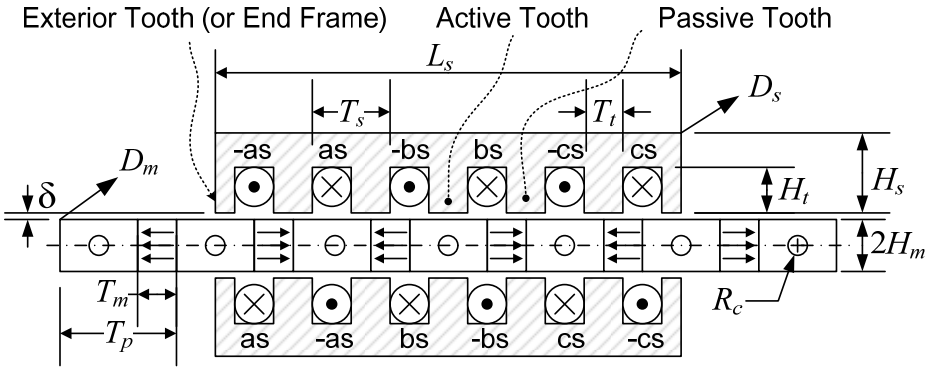

Fig. 8. Base model of the double-sided 6/4 IPM-FLBM with alternate teeth windings.

Table 4 Mechanical design specifications of the base model

Parameters	**Symbols**	**Values** (m)
Air gap	δ	0.001
Stack width of stator	D_s	0.020
Stack width of mover	D_m	0.020
Stator height	H_s	0.011
Stator tooth height	H_t	0.007
One half off PM height	H_m	0.004
PM width	T_m	0.006
Pole pitch	T_p	0.018
Slot pitch	T_s	0.012
Tooth width	T_t	0.006
Overall stator length	L_s	0.072
Mover core mount hole	R_c	0.003

2.2 Detent Force Minimization of Double-Sided 6/4 IPM-FLBM

Since the double-sided configuration can produce much larger force in a given volume, it is appropriate in high-force density applications [2]. However, its large detent force due to the end-effect and cogging forces is a significant drawback in high-precision motion control at a low speed. Especially, the end-effect force that is caused by the stator's finite length does not exist in a rotary motor. This end-effect force can also be a major or minor detent force depending on the configuration of the number of slots and poles with respect to its cogging force. Furthermore, it is not easy to formulate these detent forces with high nonlinearity with a generalized analytic solution.

In this section, new detent-force minimization techniques for the double-sided 6/4 IPM-FLBM having two short-length stators configured with alternate teeth windings are presented. The end-effect and cogging forces are separately investigated to minimize the total detent force by two independent techniques. The end-effect force is reduced by a two-dimensional optimization using an analytic solution and verified by experimental measurements for the slotless stator with an adjustable length and various stack widths. The net cogging force is minimized by a destructive interference technique using the slot-phase shift between the upper and lower stators. The optimal slot-phase shift is determined by an analytic solution using Fourier series and also verified with 3D-FEA and measurements. The optimal slot-phase-shift model is merged with the optimized slotless model. Finally, the steady-state thrust force and the minimized effective detent force according to mover positions are measured, and compared with the 3D-FEA result and analytic solution.

2.2.1 Steady-State Thrust and Detent Forces of Base Model

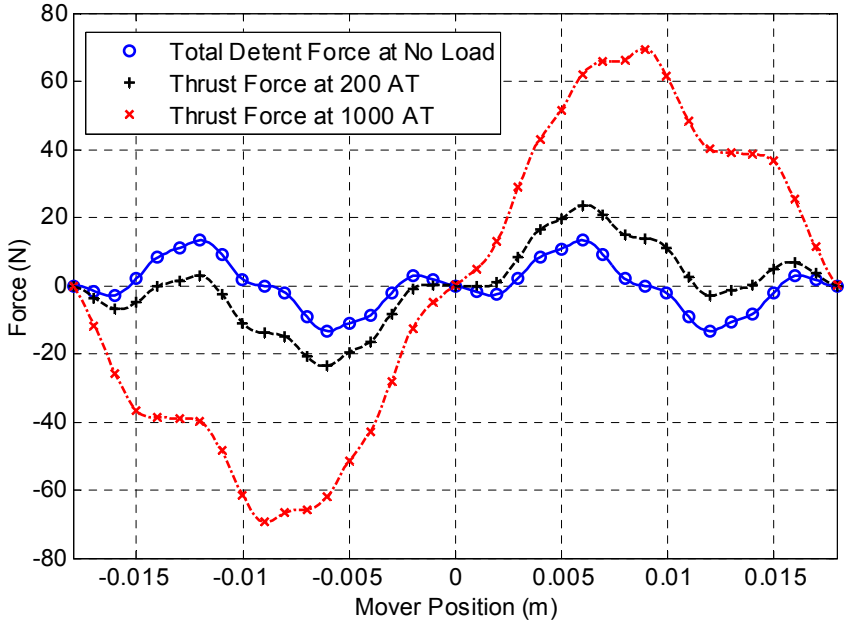

Fig. 9. FEA results for the thrust and detent forces of the base model according to the mover positions.

Since the end-effect force occurs at end frames or exterior teeth regardless of the stator length, the end-effect force of a linear motor with a short stator length takes a relatively larger portion of the total thrust force than that with a long stator [7]. It has a period of one pole pitch. Likewise, the cogging force acting on one slot has the same period, but the total cogging force of a linear motor with a fractional-slot configuration does not have the first-harmonic force because of the destructive interference between the cogging forces of each slot as follows:

$$N_h = \frac{\mathrm{LCM}(N_s, N_p)}{2} \tag{2.2}$$

where N_h is the harmonic order number with respect to one pole pitch, N_s is the total number of slot, and N_p is the total number of pole pair. Therefore, the detent force of the

base model shown in Fig. 9 implies that since it is mainly governed by the first-harmonic force term with respect to one pole pitch, the end-effect force is the major detent force in the base model. These FEA analysis also shows that the thrust force in the low-current (200 A-turns) and high-current modes (1000 A-turns) are distorted by the detent force over the entire travel range of the mover. These results indicate that the total effective thrust force cannot be expected as a sinusoidal thrust force, and the detent force should be minimized in order to produce the undistorted thrust force according to the mover positions.

2.2.2 End-Effect Force Minimization

2.2.2.A One-Dimensional End-Effect-Force Minimization

As mentioned in the previous section, since the end-effect force is dominant in the detent force in the base model, the minimization of the end-effect force is the most effective way to reduce the total detent force. Since the end-effect force is governed by the finite distance between only the two end frames in the stator, the end-effect force can be minimized by the stator's overall length adjustment [6], [47]. According to [47], the cogging force of a single rectangular prism iron-core structure can be expressed in Fourier series with the period of the pole pitch. The end-effect forces for the left and right ends, and the total resultant force of a single rectangular prism iron-core structure can be given respectively by

$$F_L = a_0 + \sum_{n=1}^{\infty} a_n \cos\left(\frac{2\pi n}{T_p}\left(x - \frac{L_s}{2}\right)\right) + \sum_{n=1}^{\infty} b_n \sin\left(\frac{2\pi n}{T_p}\left(x - \frac{L_s}{2}\right)\right) \tag{2.3}$$

$$F_R = -F_L\left(-\left(x + L_s\right)\right) = -a_0 - \sum_{n=1}^{\infty} a_n \cos\left(\frac{2\pi n}{T_p}\left(x + \frac{L_s}{2}\right)\right) + \sum_{n=1}^{\infty} b_n \sin\left(\frac{2\pi n}{T_p}\left(x + \frac{L_s}{2}\right)\right) \tag{2.4}$$

$$F_E = F_L + F_R = 2\sum_{n=1}^{\infty}\left[a_n \sin\left(\frac{\pi n L_s}{T_p}\right) + b_n \cos\left(\frac{\pi n L_s}{T_p}\right)\right]\sin\left(\frac{2\pi n}{T_p}x\right) \tag{2.5}$$

where F_L is the left end-effect force, F_R is the right end-effect force, F_E is the total end-effect force, and a_n and b_n are the Fourier coefficients. The total end-effect force (2.5) indicates that it can be minimized if the overall length of the stator has the following relationship.

$$a_n \sin\left(\frac{\pi n L_s}{T_p}\right) + b_n \cos\left(\frac{\pi n L_s}{T_p}\right) = 0 \;\Rightarrow\; L_s = 2N_p T_p - \frac{T_p}{n\pi}\tan^{-1}\left(\frac{b_n}{a_n}\right) \tag{2.6}$$

where N_p is the number of pole pairs of the mover. Hence, if the Fourier coefficients in (2.3) can be determined from the left end-effect force experimentally, the specific harmonic term of the end-effect force can be removed through the stator's length adjustment.

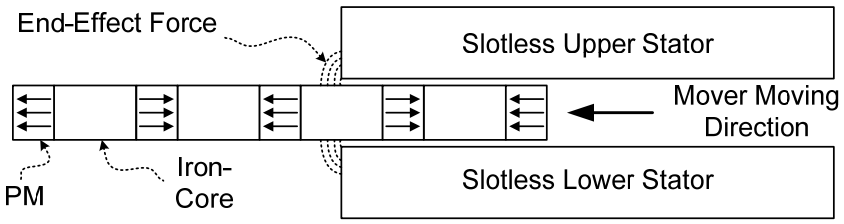

Fig. 10. Left end-effect force measurement using the slotless rectangular prim iron-core stator when the mover's position is at zero.

In order to verify this method, the left end-effect force of the slotless iron-core stator shown in Fig. 10 was measured experimentally instead of using the FEA because there is a difference between the mechanical and magnetic lengths [6].

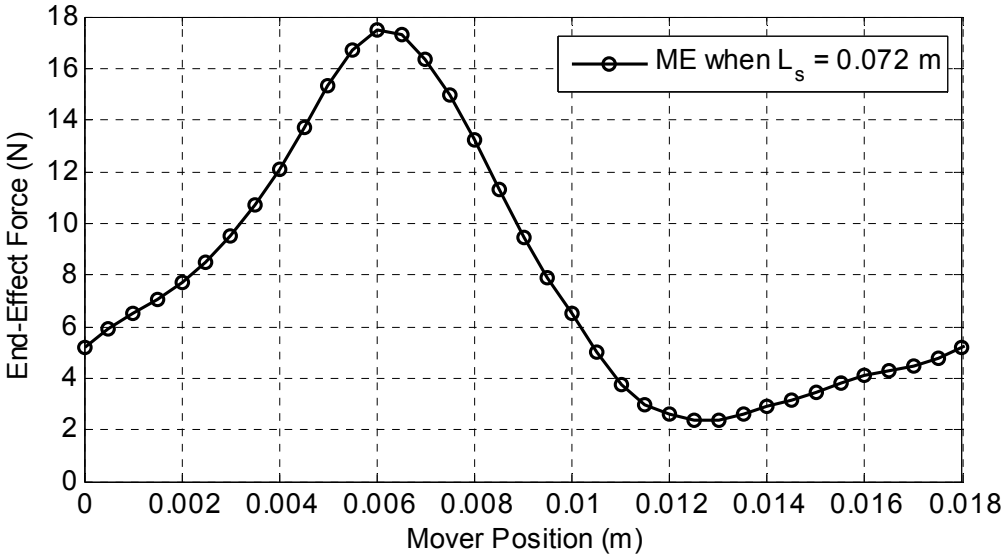

Fig. 11. Measured left end-effect force according to mover positions when the pole pitch is 0.018 m, and the magnet length is 0.006 m.

Table 5 Estimated Fourier coefficient of the left end-effect force

Harmonic order (*n*)	a_n	B_N
0	7.943	0.000
1	–2.441	5.924
2	0.387	–2.311
3	0.449	0.275
4	–0.167	0.267
5	–0.059	–0.095
6	–0.002	0.052
7	–0.065	0.027

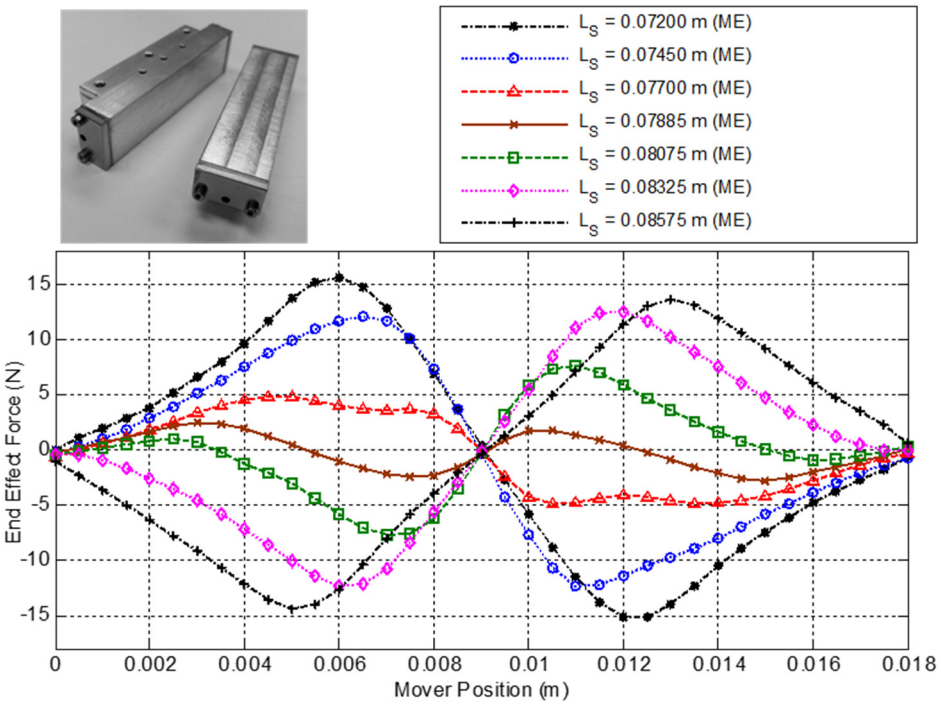

Fig. 12. Measured end-effect forces according to the slotless stator's overall lengths and mover positions: slotless stators (top) and end-effect forces (bottom).

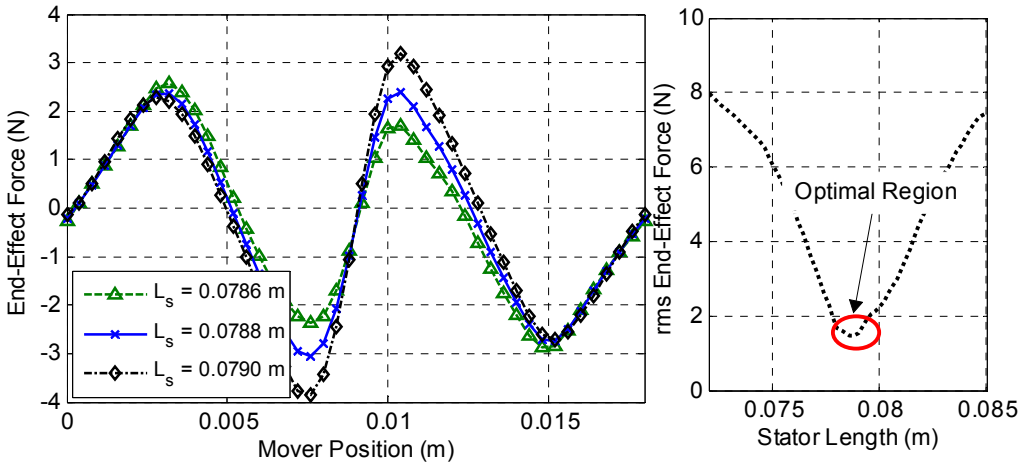

(a) (b)

Fig. 13. (a) Optimal stator length analysis according to mover positions with respect to the peak-to-peak end-effect forces, (b) rms end-effect force according to the stator lengths.

The measured end-effect force in Fig. 11 describes that the end-effect force has the maximum value at 0.006 m. The period of 0.018 m is the same as the pole pitch (T_p). Table 5 shows the Fourier coefficients of (2.3) calculated by curve-fitting from the measurement given in Fig. 11. These coefficients show that the first-harmonic force is dominant. Thus, if applying (2.6) in order to remove the first-harmonic force, the optimal overall stator length can be computed as 0.0788 m with $n = 1$ and $N_p = 2$. The experimental results in Fig. 12 show that the end-effect forces vary according to the slotless stator's overall lengths and the mover positions. The maximum end-effect force of over 15 N is generated in the base model. The end-effect force analysis in Fig. 13(a) and (b) describes that the optimal overall length is around 0.0788 m to minimize the end-effect force. This result is in good agreement with the optimal overall length estimated by (2.6) for the first-harmonic force. This also shows that the conventional approach using a half-pitch extension of the stator is not optimal although it can reduce the end-effect force to some extent.

2.2.2.B Two-Dimensional End-Effect-Force Minimization

The end-effect force was reduced by 83% through the one-dimensional overall length optimization as compared with the base model. However, the result in Fig. 13(b) shows that the second-harmonic force still remains because the proposed method can remove only one selected harmonic force according to (2.6). Thus, in order to further minimize the end-effect force, the second-harmonic force should be removed. In [6], the smooth-formed edge shape is added at both ends of the stator for the further reduction of

the remaining end-effect force. However, since this technique needs the optimal length plus an additional two pole-pitch length in the base model, it is not appropriate for the stator requiring a short length. In this sense, the experimental results in Fig. 12 illustrate that since the two end-effect forces for the lengths of 0.0745 m and 0.0833 m have an opposite phase, the end-effect force can be further reduced without the excessive length extension of the stator if a slotless stator with two different lengths shown in Fig. 14 is employed.

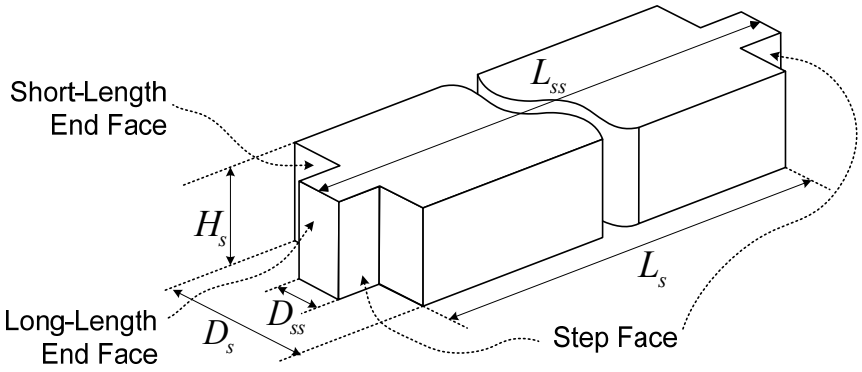

Fig. 14. Dimension definition of the slotless stator with two different lengths.

Therefore, assuming no lateral force perpendicular to the step faces formed by the two different lengths, and the mechanical stack width (D_{ss}) of the long-length portion is the same as the effective stack width (D_{sse}), the end forces acting on the end faces of the long length portion and the short length portion can be expressed as (2.7) and (2.8) from (2.5), respectively.

$$F_{LSS} = 2\frac{D_{sse}}{D_s}\sum_{n=1}^{\infty}\left[a_n \sin\left(\frac{\pi n L_{ss}}{T_p}\right) + b_n \cos\left(\frac{\pi n L_{ss}}{T_p}\right)\right]\sin\left(\frac{2\pi n}{T_p}x\right) \tag{2.7}$$

$$F_{LS} = 2\left(\frac{D_s - D_{sse}}{D_s}\right)\sum_{n=1}^{\infty}\left[a_n \sin\left(\frac{\pi n L_s}{T_p}\right) + b_n \cos\left(\frac{\pi n L_s}{T_p}\right)\right]\sin\left(\frac{2\pi n}{T_p}x\right) \tag{2.8}$$

where F_{LSS} and F_{LS} are the end-effect forces of the long- and short-length portions, respectively. L_{ss} is the longer stator length, L_s is the shorter stator length, and D_s is the total stack width of the stator. In (2.7) and (2.8), assuming that the D_{sse} is a half of D_s, the total end-effect force of the upper and lower stators with two different lengths is given as

$$F_E = F_{LSS} + F_{LS} = 2\sum_{n=1}^{\infty} A_n B_n \sin\left(\frac{2\pi n}{T_p}x\right) \tag{2.9}$$

where $A_n = a_n \sin\left(\frac{\pi n}{2T_p}\left(L_{SS} + L_S\right)\right) + b_n \cos\left(\frac{\pi n}{2T_p}\left(L_{SS} + L_S\right)\right)$ and $B_n = \cos\left(\frac{\pi n}{2T_p}\left(L_{SS} - L_S\right)\right)$.

The above equation indicates that the total end-effect force can be minimized when either A_n or B_n is zero. From these two conditions, equations between the two different lengths in a stator and the harmonic order can be given by

$$L_{ss} + L_s = 2\left(2N_p T_p\right) - \frac{2T_p}{n\pi}\tan^{-1}\left(\frac{b_n}{a_n}\right) \tag{2.10}$$

$$L_{ss} - L_s = \frac{T_p}{n} \tag{2.11}$$

The above two equations states that two selected harmonic forces can be removed by two different lengths (L_{ss} and L_s) of a stator depicted in Fig. 14. Thus, removing the dominant components in the end-effect force is very effective. In this case, (2.10) and (2.11) can be used to remove the first- and second-harmonic forces, respectively. The choice of these harmonic orders can also be switched, but the overall stator length would be longer than that from the former choice. Equation (2.12) shows the two different

lengths implemented in a stator when the harmonic orders (n) for (2.10) and (2.11) are 1 and 2, respectively, in order to remove the first and second-harmonic forces.

$$\begin{bmatrix} L_{SS} \\ L_S \end{bmatrix} = \begin{bmatrix} 1 & 1 \\ 1 & -1 \end{bmatrix}^{-1} \begin{bmatrix} 2\left(2N_pT_p\right) - \left(2T_p/\pi\right)\tan^{-1}\left(b_1/a_1\right) \\ T_p/2 \end{bmatrix}. \tag{2.12}$$

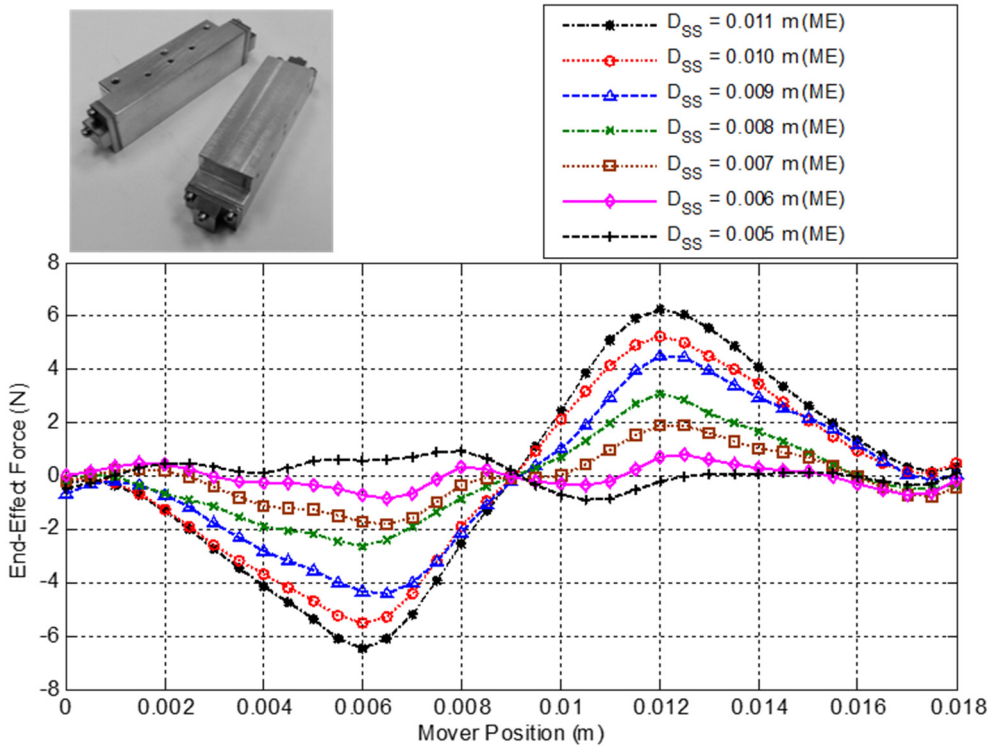

Fig. 15. Measured end-effect forces according to the mover positions with respect to the stack depths of the long-length portion.

Since such optimal lengths can be established when assuming no lateral force on the four step faces formed between the long and short lengths, the effect for the four step faces should be considered. In order to investigate this effect, the two lengths of 0.0745 m and 0.0835 m obtained from Table 5 and (2.12) were employed in both the upper and

lower stators. And then, the total end-effect forces were measured according to the stack widths of the long length portion of the stator. As expected, the results in Fig. 15 show that the end-effect force has been increased rather in a half stack width (D_{ss} = 0.01 m) for the precondition of (2.9) as compared with the one-dimensional optimization. This implies that the effective stack width to satisfy (2.9) is not the same as the mechanical stack width. This is the same as taking Carter's principle into account when calculating the air-gap permeance in the slotted stator [48].

Therefore, from (2.7) and (2.8), and the measured end-effect forces in Fig. 15, the effective stack-width ratio for the mechanical stack-width ratio is investigated as shown in Fig. 16. The dashed line shows the relationship when there is no lateral force on the step faces. The circles illustrate the values computed through comparisons of the measured results in Fig. 15 and the sum of (2.7) and (2.8) for the corresponding stack width. The dotted line describes a conversion function fitting the circled data and given as

$$\frac{D_{sse}}{D_s} = \frac{1}{2}\ln\left(1 + 2\pi\frac{D_{ss}}{D_s}\right) \tag{2.13}$$

Thus, applying the conversion function (2.13) to (2.7) and (2.8), they can be rewritten as

$$F_{LSS} = \ln\left(1 + 2\pi\frac{D_{ss}}{D_s}\right)\sum_{n=1}^{\infty} C_n \sin\left(\frac{2\pi n}{T_p}x\right) \tag{2.14}$$

$$F_{LS} = \left(2 - \ln\left(1 + 2\pi\frac{D_{ss}}{D_s}\right)\right)\sum_{n=1}^{\infty} D_n \sin\left(\frac{2\pi n}{T_p}x\right) \tag{2.15}$$

where $C_n = a_n \sin\left(\frac{\pi n L_{ss}}{T_p}\right) + b_n \cos\left(\frac{\pi n L_{ss}}{T_p}\right)$ and $D_n = a_n \sin\left(\frac{\pi n L_s}{T_p}\right) + b_n \cos\left(\frac{\pi n L_s}{T_p}\right)$.

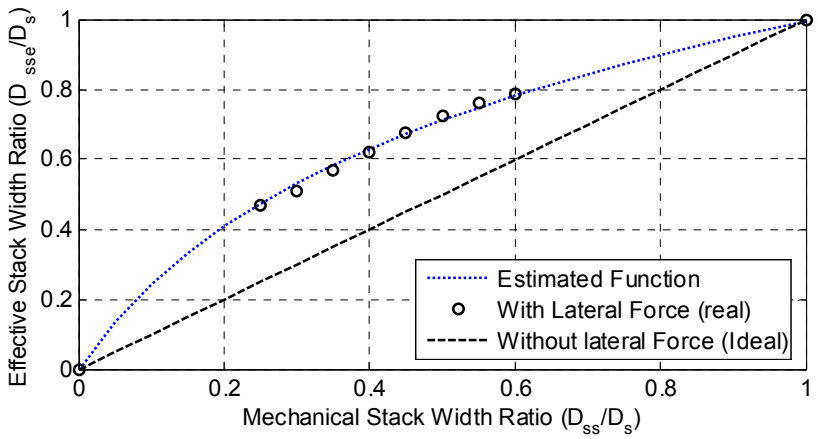

Fig. 16. Effective stack width ratio according to the mechanical stack width ratio of the long-length portion in the stator when $L_{ss} - L_s = 0.009$ m and $\delta = 0.001$ m.

According to the above equations, when the mechanical stack width of the long-length portion is 0.0055 m, the effective stack width ratio of the long-length and short-length portions is 0.5. Thus, (2.9) becomes valid, and the end-effect force can be minimized through the two lengths obtained from (2.12). The empirical conversion function (2.13) obtained in this paper needs more experiments for other cases in order to be a general formula. However, if (2.14) is chosen to remove the second-harmonic force as the same manner in (2.12), since the optimal-length difference between the two lengths always has a half of pole pitch in every case, (2.13) can be used in various pole-pitches of the same inset-type IPM configuration with the air gap of 0.001 m. Fig. 17 shows that the two-dimensional optimization can reduce the detent force further than that with one-dimensional optimization. The second-harmonic force that remains in the one-dimensional optimization was removed in the two-dimensional optimization. As a result, the end-effect force was reduced by 83% with the one-dimensional optimization and by 94% with the two-dimensional optimization, respectively, with respect to the base model.

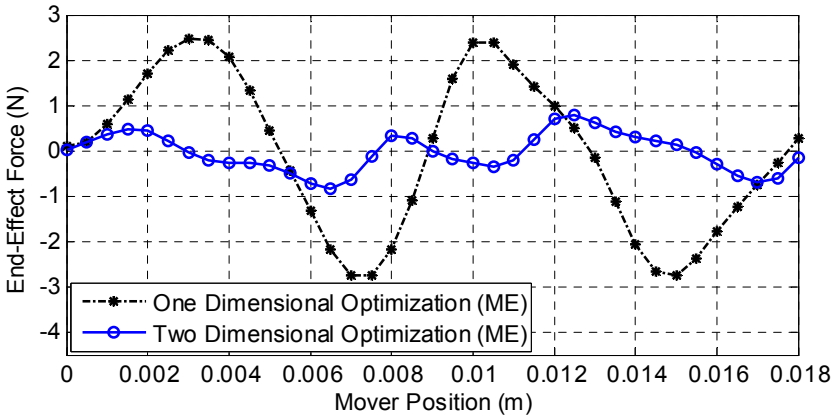

Fig. 17. End-effect force comparison of the one-dimensional optimization (L_s = 0.0788) and two-dimensional optimization (L_{ss} = 0.0835 m, L_s = 0.0745 m, D_s = 0.02 m and D_{ss} = 0.006 m).

2.2.3 Cogging Force Minimization

In this section, the cogging force minimization is discussed. Fig. 18 shows the 6-slot stator and 4-pole mover model with an infinite length. The left edge of each slot has an attractive force with the right edge of the mover core, and the right edge of each slot has an attractive force with the left edge of the mover core. Thus, if the previous end-effect force model in (2.5) is employed, the cogging force acting on one slot can be given as

$$F_{cog,m} = \sum_{k=1}^{\infty} F_k \sin\left(\frac{2\pi k}{T_p}\left(x + (m-1)T_s\right)\right) \tag{2.16}$$

where m is the slot number, and F_k is the magnitude of the kth-harmonic component. If there is no change in the ratio of the pole and slot pitches, the above relationship is valid although the magnitude of each harmonic component may change depending on the slot width and magnetic saturation condition. Thus, since the total number of slots in the 6/4 configuration is 6, the total cogging force can be expressed as

$$F_{cog} = \sum_{m=1}^{6}\sum_{k=1}^{\infty} F_k \sin\left(\frac{2\pi k}{T_p}\left(x+(m-1)T_s\right)\right). \tag{2.17}$$

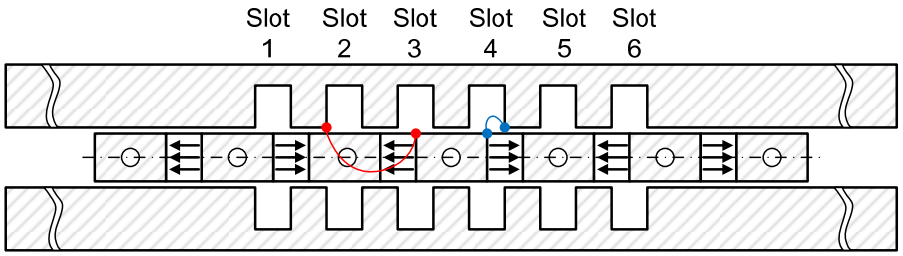

Fig. 18. Infinite-length stator model for the cogging force analysis.

Since the 6/4 configuration has the relation ($2T_p = 3T_s$), the cogging forces of the mth and (m+3)th slots are theoretically equal. Thus, (2.17) can be rewritten as

$$\begin{aligned} F_{cog} &= 2\sum_{m=1}^{3}\sum_{k=1}^{\infty} F_k \sin\left(\frac{2\pi k}{T_p}\left(x+(m-1)T_s\right)\right) \\ &= 2\sum_{k=1}^{\infty} F_k\left[1+2\cos\left(\frac{2\pi k}{T_p}T_s\right)\right]\sin\left(\frac{2\pi k}{T_p}x\right) \\ &= \begin{cases} = 0, & \text{for } k \neq 3n \\ = 2\sum_{k=1}^{\infty} F_k\left[1+2\cos\left(\frac{2\pi k}{T_p}T_s\right)\right]\sin\left(\frac{2\pi k}{T_p}x\right), & \text{for } k = 3n \end{cases} \end{aligned} \tag{2.18}$$

The above equation implies that the total cogging force has only triple-nth-harmonic components whereas the other components cancel each other regardless of the values of F_k even if the magnitude of the triple-nth-harmonic forces becomes twice as larger. The FEA results in Fig. 19 show that the first- and second-harmonic forces are eliminated by the destructive interference of the 6/4 configuration, and the third-harmonic force is dominant regardless of the force-magnitude change by the slot width. This also implies that (2.18) is valid. Although the first- and second-harmonic cogging forces are cancelled

by the destructive interference of each slot, the remaining third-harmonic force is still large for the precision control of a linear motor.

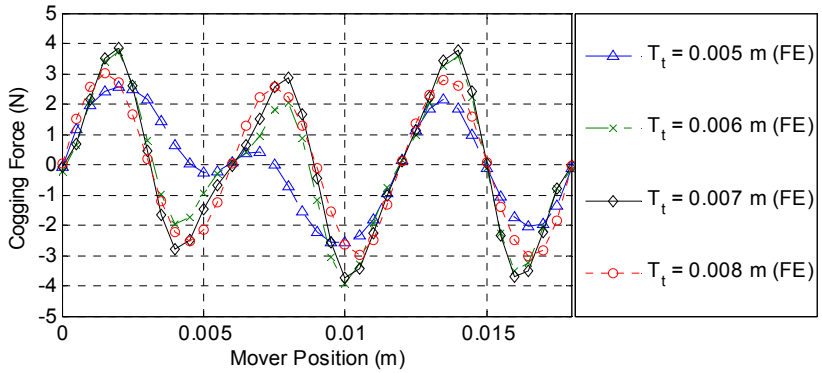

Fig. 19. FEA results for cogging forces of the infinite-length stator model according to the mover positions with respect to the stator's tooth widths.

Thus, adopting a semi-closed slot geometry or increasing the least common multiple (LCM) between the number of stator slots and the number of rotor poles can be an alternative way to reduce the remaining harmonic forces [4], [7]. However, these methods would complicate the winding fabrication, as well as are inappropriate in compact-sized motors. The asymmetrical PM placement presented in [8], [9] is ineffective in the IPM configuration because this technique needs variously sized magnets and iron-cores, as well as the previously minimized end-effect force is not applicable. The PM pole-shift technique introduced in [10] is also unavailable in the double-sided IPM configuration. However, if the basic principle for the stepped rotor skew in rotary motors or the PM phase-shift in SPM linear motors is adopted as a form of the slot-phase shift between the upper and lower stators as shown in Fig. 20, the remaining triple-*n*th-harmonic cogging forces can be removed without the modification for the fractional slot or winding configuration.

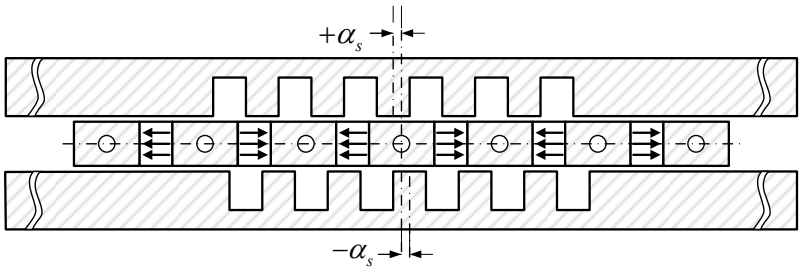

Fig. 20. Concept of the slot-phase shift configuration in the double-sided IPM-FLBM, where α_s is the slot-phase shift.

Furthermore, since the lower stator is just the rotation of the upper stator with respect to the lateral axis, only a single type of iron-core lamination plates is required. Therefore, this new method has an advantage in manufacturability as well and can be implemented on the double-sided SPM structure, and its performance can be predicted by the analytic solution developed in this section. From this conceptual design, the total cogging force of (2.18) can be decomposed into the cogging forces of the upper and lower stators as

$$F_{cog} = \underbrace{\sum_{k=1}^{\infty} F_k \left[1+2\cos\left(\frac{2\pi k}{T_p}T_s\right)\right]\sin\left(\frac{2\pi k}{T_p}(x-\alpha_s)\right)}_{\text{Cogging Force of Upper Stator}} + \underbrace{\sum_{k=1}^{\infty} F_k \left[1+2\cos\left(\frac{2\pi k}{T_p}T_s\right)\right]\sin\left(\frac{2\pi k}{T_p}(x+\alpha_s)\right)}_{\text{Cogging Force of Lower Stator}}$$
$$= 2\sum_{k=1}^{\infty} F_k \left[1+2\cos\left(\frac{2\pi k}{T_p}T_s\right)\right]\cos\left(\frac{2\pi k\alpha_s}{T_p}\right)\sin\left(\frac{2\pi k}{T_p}x\right) \tag{2.19}$$

Eventually, when the design parameter α_s is $T_p/12$, and $2T_p = 3T_s$, the total cogging force has only the sixth-harmonic force as (2.20) regardless of F_k

$$F_{cog} = \begin{cases} 0, & \text{for } k \neq 6n \\ 2\sum_{k=1}^{\infty} F_k \left[1+2\cos\left(\frac{4\pi k}{3}\right)\right]\cos\left(\frac{\pi k}{6}\right)\sin\left(\frac{2\pi k}{T_p}x\right), & \text{for } k = 6n \end{cases} \tag{2.20}$$

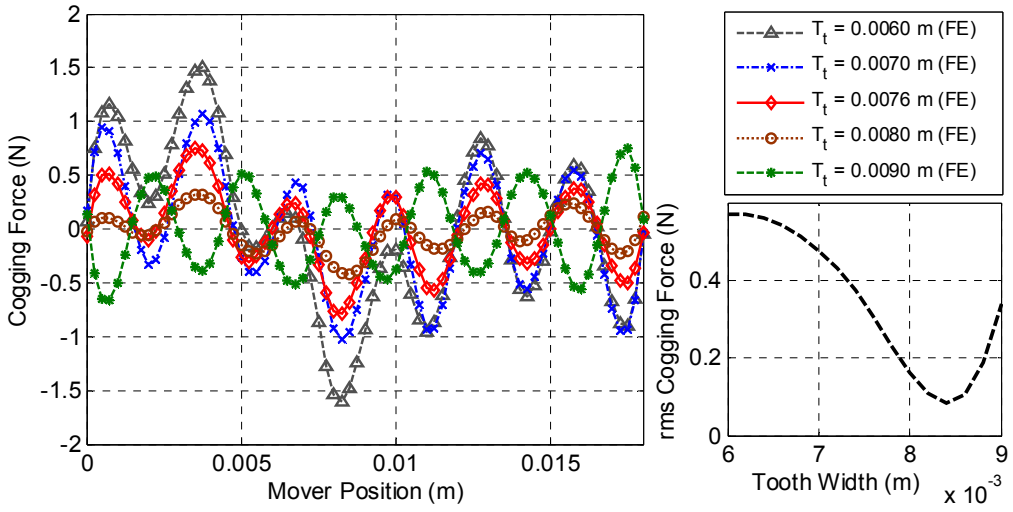

(a) (b)

Fig. 21. FEA results for the stator with the slot-phase shift of $T_p/6$ between the upper and lower stators. (a) Total cogging forces and (b) the rms cogging force according to the tooth widths.

The FEA results in Fig. 21(a) shows that the cogging forces have only the sixth-harmonic term when the slot-phase shift of $T_p/12$ is employed in the upper and lower stators, respectively. These results are in good agreement with (2.20). In addition, these results in Fig. 21 show that the magnitudes of the sixth-harmonic forces are determined by the magnitude of F_k according to slot widths. The rms cogging force in Fig. 21(b) shows that the slot width of 0.0084 m is optimal to minimize the cogging force.

2.2.4 Detent Force-Free Stator

Table 6 shows the final design parameters implemented on a new stator in the double-sided 6/4 IPM-FLBM. The lengths of the long- and short-length portions in the stator were determined as 0.0835 m and 0.0745 m, respectively. The stack width of the long-length portion was determined as 0.0060 m in order to use the available machined

pieces although 0.0055 m is the optimal stack width of the long-length portion according to (2.13). The slot-phase shifts of +0.0015 m and –0.0015 m were applied in the upper and lower stators with respect to the stator center line. As a result, the total slot phase shift of 0.0030 m between the upper and lower stators was introduced. In addition, according the result in Fig. 21(b), the minimized cogging force can be achieved when the stator tooth width is 0.0084 m, but the tooth width of 0.0076 m was used in order to secure a sufficient coil volume. Fig. 22(a) and (b) show the non-slot-phase and slot-phase-shift configurations with the same stators, respectively.

(a) (b)

Fig. 22. Comparison of two different arrangements for double-sided stators: (a) non-slot-phase-shift configuration, and (b) slot-phase-shift configuration.

Table 6. Final design parameter of the stator

Parameters	Symbols	Value (M)
Stator's stack width of short-length portion	D_s	0.0200
Stator's stack width of long-length portion	D_{ss}	0.0060
Tooth width	T_t	0.0076
Shorter length of stator	L_s	0.0745
Longer length of stator	L_{ss}	0.0835
Slot-phase shift	α_s	0.0015

2.2.5 Total Detent- and Steady-state Thrust Force Measurements

The experimental setup to measure the total detent- and steady-state thrust forces according to the mover positions is shown in Fig. 23. The copper wire of 26 AWG is used for the phase coils with the number of turns of 85 for each coil. The same phase coils in the upper and lower stators are connected in series in order to apply the phase currents.

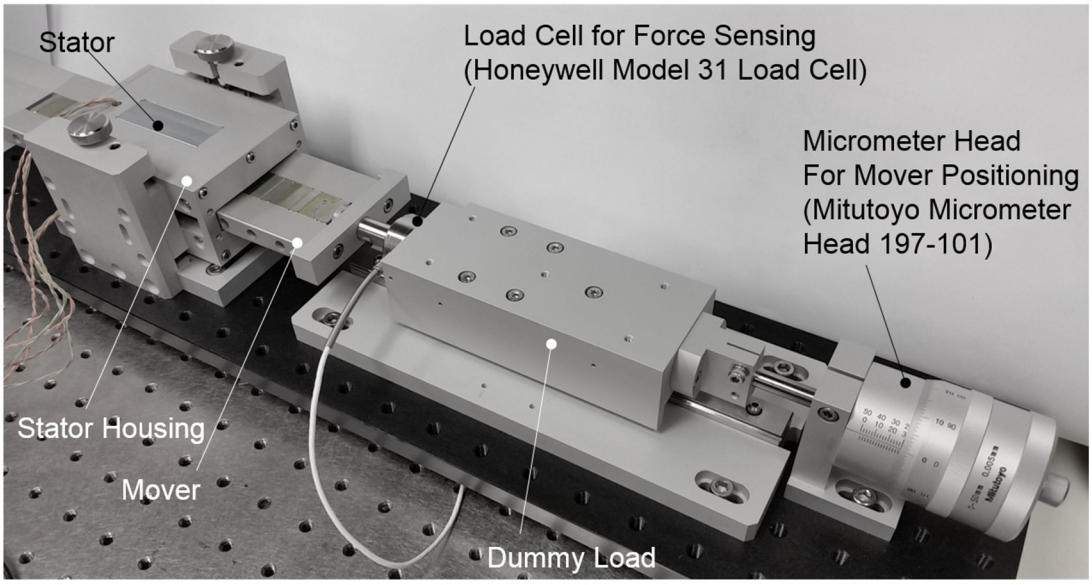

Fig. 23. Photograph of the experimental setup to measure the total detent- and steady-state thrust forces.

Fig. 24 illustrates the comparison of the predicted thrust forces of the infinite-length model and the measured thrust forces of the prototype configured with the step-shaped end frames and without slot-phase-shift as shown in Fig. 22(a). The steady-state thrust forces were evaluated according to the mover positions in the case that the currents of –5 A (–425 A-turns), 10 A (850 A-turns), and –5 A (–425 A-turns) are supplied to phases *a*, *b*, and *c*, respectively. The FEA results estimated a slightly smaller force than

the real measurements. This seems to be due to the fact that the practical permeability of the physical material was higher than the simulation value. The total detent force was also measured under the condition that all phase currents are set to be zero. It is apparent that the total cogging force becomes the dominant detent force due to the significant reduction of the end-effect force. This result also validates the proposed techniques using the separate optimal approaches for the cogging and end-effect forces. In addition, although the measured detent force was reduced to be 23% of that of the base model as compared with the results given in Fig. 9, the thrust force is still distorted by the 6th-harmonic cogging force.

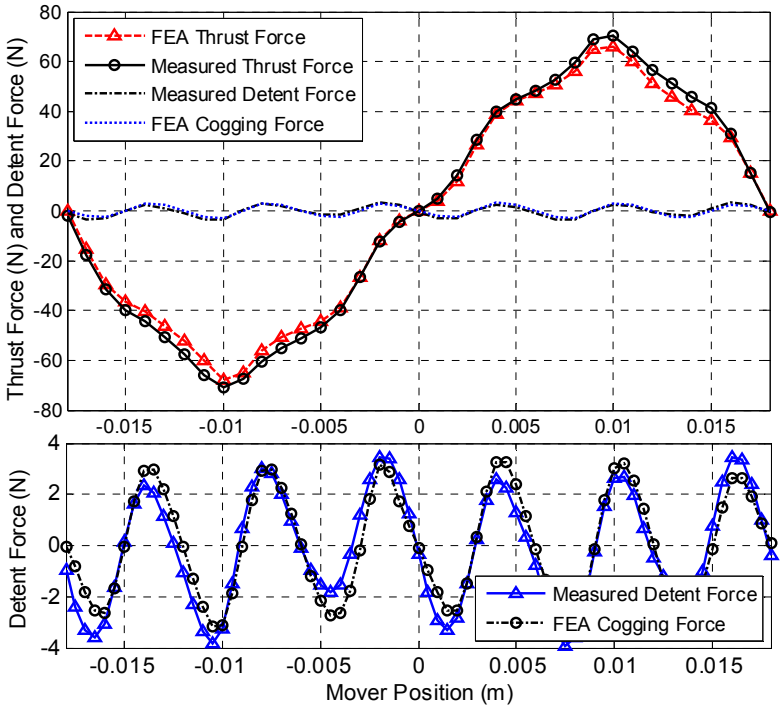

Fig. 24. Comparison of the predicted and measured thrust forces (top), and comparison of the predicted cogging and measured detent forces (bottom) when T_t = 0.0076 m.

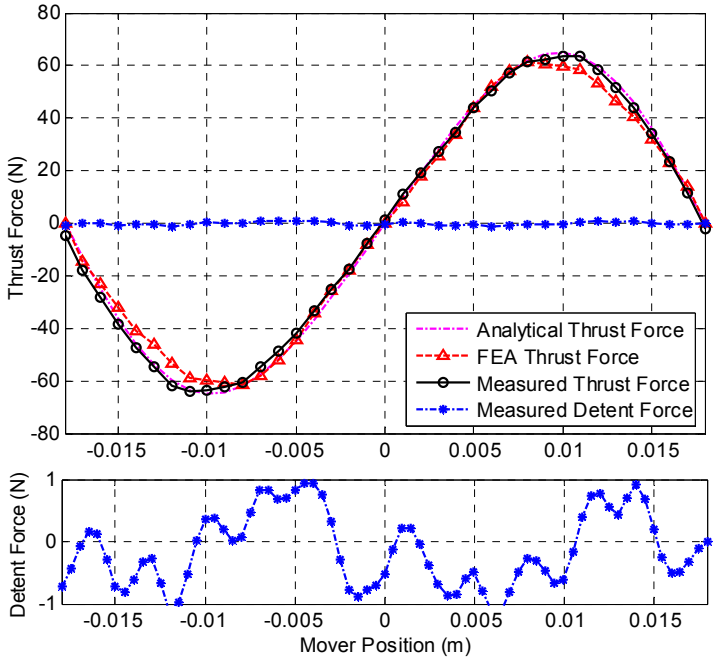

Fig. 25. Maximum thrust force and detent force comparison (top), and magnified view of the detent force from the top figure (bottom).

The results in Fig. 25 also illustrate the thrust-force comparisons of the slot-phase-shifted infinite length model and the prototype shown in Fig. 22(b). The same current conditions were applied. The thrust force was also calculated by analytic force equation. The analytic solution for the thrust force is in good agreement with the measurement, but the FEA result is estimated as a slightly smaller force than the real measurement like the above FEA result. The measured detent force was reduced to be 6% of that of the base model through the proposed detent-force-free techniques. Its value was about 1.5% of the maximum thrust force (≅ 63.5 N). In other words, the thrust force corresponding to the mover positions can be generated with no significant force distortion due to the minimization of the detent forces. In addition, high-precision motion control of the double-sided 6/4 IPM-FLBM can be achieved with a proper controller.

2.3 Steady-State Modeling and Analysis of Double-Sided IPM-FLBM

The IPM motors can produce the synchronous electromagnetic as well as reluctance forces because of their saliency. Generally, the LBM has a trapezoidal or sinusoidal back-EMF profile depending on the air-gap flux density shape or its winding configuration. In the case of the buried-type IPM-LBM, since its back-EMF is close to a sinusoidal rather than trapezoidal waveform [49], its optimal performance can be achieved when it is used in conjunction with vector control. In addition, since the FLBM can have the double-sided stators for a mover, a twice larger force can be generated. Therefore, the double-sided IPM-LBM exhibits superior performance in terms of the high-force density, low noise, as well as field weakening capability compared to other types of linear motors.

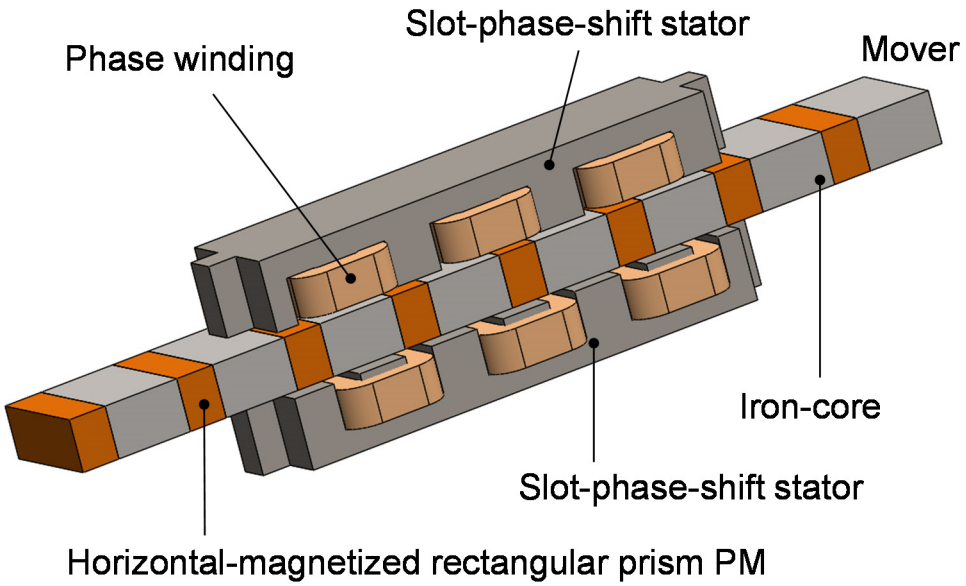

Fig. 26. 3-D rendering for the proposed double-sided 6/4 IPM-FLBM with slot-phase shift and alternate teeth windings.

In this section, the closed-form modeling methodologies for the new double-side 6/4 IPM-FLBM with slot-phase shift and alternate teeth windings shown in Fig. 26 are presented. The flowchart in Fig. 27 illustrates the modeling procedure in this paper. First, the mechanical dimension and the electrical configuration are described. The no-load maximum air-gap flux is estimated using a simplified MEC analysis. The no-load air-gap flux density function is modeled using the 2-D Fourier series based on the permeance of the stator. The superposed winding functions due to the slot-phase shift between the upper and lower stators are also evaluated. The no-load flux-linkages and back-EMF voltages are investigated. The inductances are calculated using a new variable winding function, incorporating the saliency of the mover. All analytic models are verified with 3-D FEAs in each modeling step. The steady-state thrust force is derived with a two-phase equivalent-circuit model, and the maximized static thrust force is studied. They are compared with the measured ones. Finally, the static end-effect and cogging forces for the ripple force evaluation are investigated using FEA.

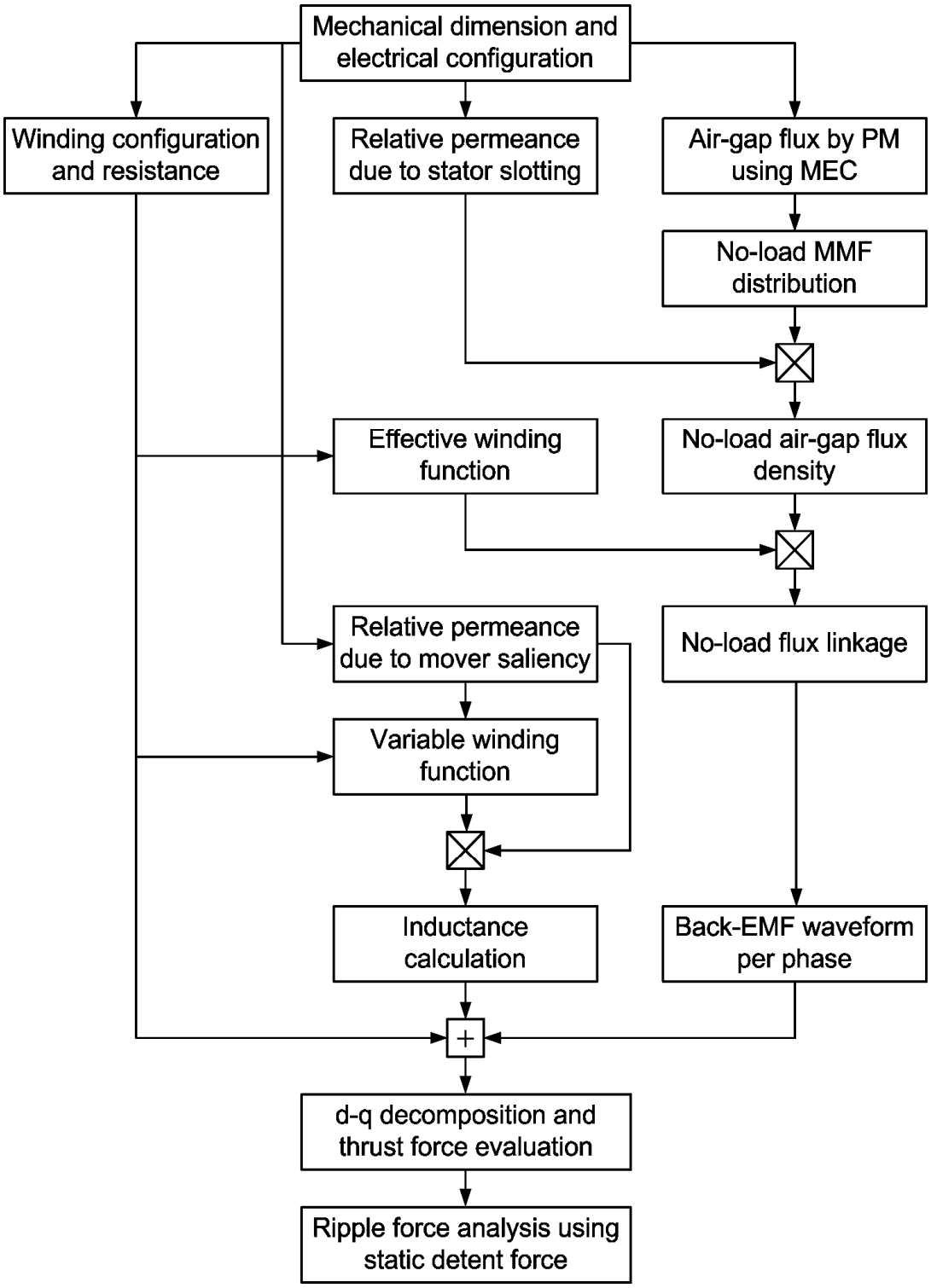

Fig. 27. Analysis flowchart for the double-sided 6/4 IPM-FLBM with the slot-phase shift and alternate teeth windings.

2.3.1 Detent Force-Free Base Model Description

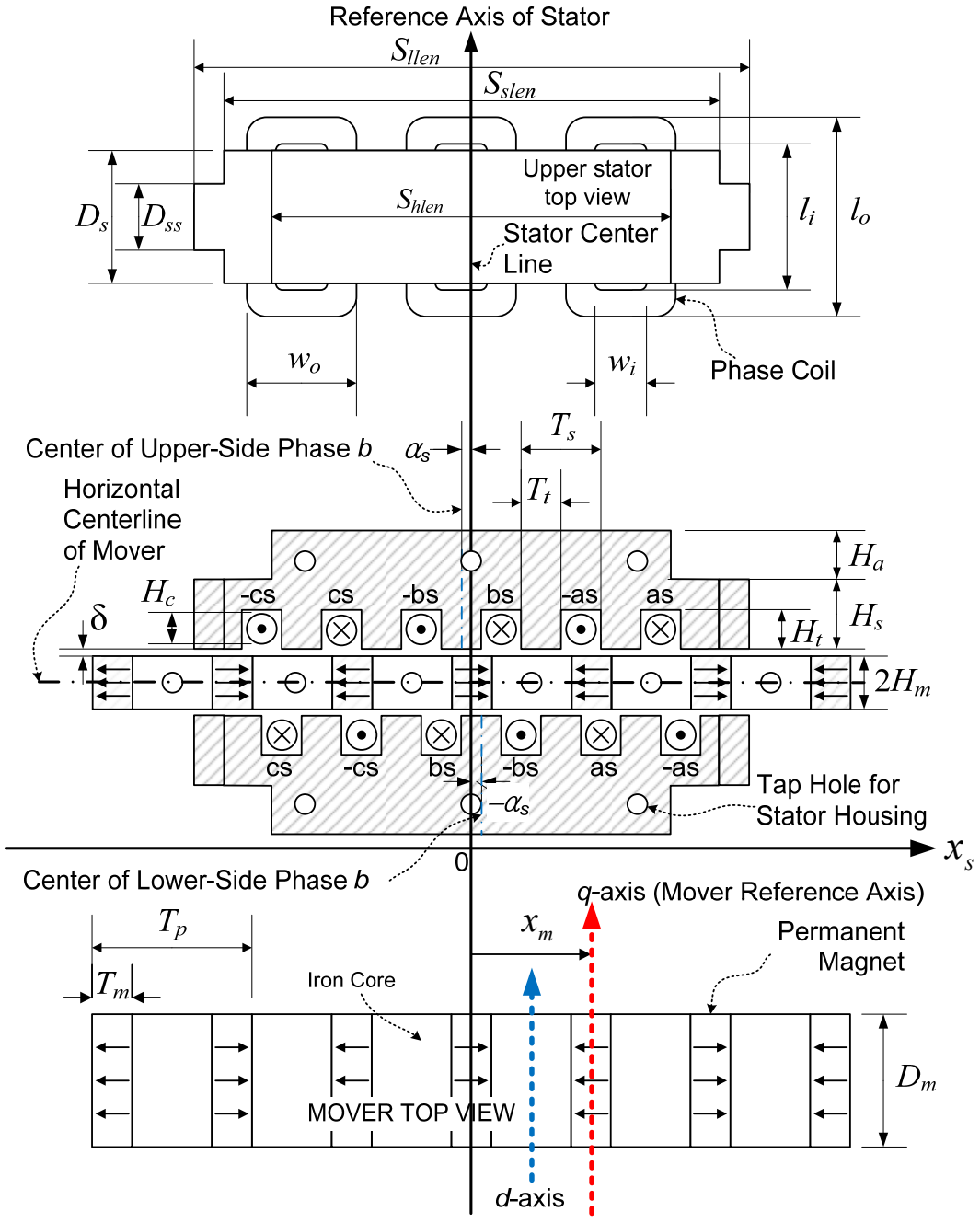

Fig. 28. Cross-sectional dimensions and coordinates of the double-sided 6/4 IPM-FLBM prototype using the electrical solid steel SS400.

Table 7 Mechanical specifications of the base model prototype

Parameters	Symbols	Values (m)
Longer length of stator	S_{llen}	0.0835
Shorter length of stator	S_{slen}	0.0745
Length of stator housing hole	S_{hlen}	0.0600
Air gap	δ	0.0010
Stator's stack width of long-length portion	D_{ss}	0.0050
Stator's stack width of short-length portion	D_s	0.0200
Stack width of mover	D_m	0.0200
Length of stator housing height	H_a	0.0080
Stator height	H_s	0.0110
Stator tooth height	H_t	0.0070
One half of PM height	H_m	0.0040
PM width	T_m	0.0060
Pole pitch	T_p	0.0180
Stator slot pitch	T_s	0.0120
Stator tooth width	T_t	0.0076
Slot-phase shift	α_s	0.0015
Outer length of winding	l_o	0.0278
Inner length of winding	li	0.0210
Outer width of winding	w_o	0.0164
Inner width of winding	w_i	0.0076
Winding height	H_c	0.0050

A cross-sectional schematic diagram in Fig. 28 illustrates the dimension definitions and reference frames of the base model prototype using the SS400 electrical solid steel. The step-shaped end frames and slot-phase-shift configuration between the upper and lower stators are employed to reduce the end-effect force and cogging force, respectively. Thus, all teeth's centerlines in the upper stator are shifted by α_s ahead of the stator centerline, and the lower teeth's centerlines are shifted by $-\alpha_s$. The horizontally

magnetized PMs are buried in the mover's iron core. The alternate teeth windings with a fractional pitch are used. Each phase consists of two series-connected coils of the upper and lower stators. The stator centerline is chosen as a stator reference axis. The mover reference axis follows the convention. Hence, the center of the iron core with the outgoing magnetic flux is defined as the *d*-axis. The *q*-axis leads the *d*-axis by $T_p/2$. The major mechanical design parameters of the base model using the electrical solid steel are tabulated in Table 7.

2.3.2 Simplified Magnetic Equivalent Circuit

Whenever the *d*-axis is aligned with the stator tooth centerline, a single-sided model of Fig. 29(a) can be made using the skew-symmetric characteristic with respect to the horizontal centerline of the mover shown in Fig. 28. In addition, the magnetic fluxes is symmetric with respect to the stator tooth centerline, the half-sided model in the dashed box of Fig. 29(a) can be used for a simplified nonlinear MEC shown in Fig. 29(b). The factor 2 multiplied in the reluctances is applied for the calculation convenience. Since this IPM structure has a relatively large effective air-gap due to the buried PMs, as well as the magnetomotive force (MMF) of the armature current is significantly smaller than that of the PM, an unsaturated model is considered in this section. The leakage reluctance between teeth is included in the model. The reluctances of the end frames are neglected assuming an infinitely long stator. From the MEC model, the maximum flux coming into and out of the stator teeth can be computed as

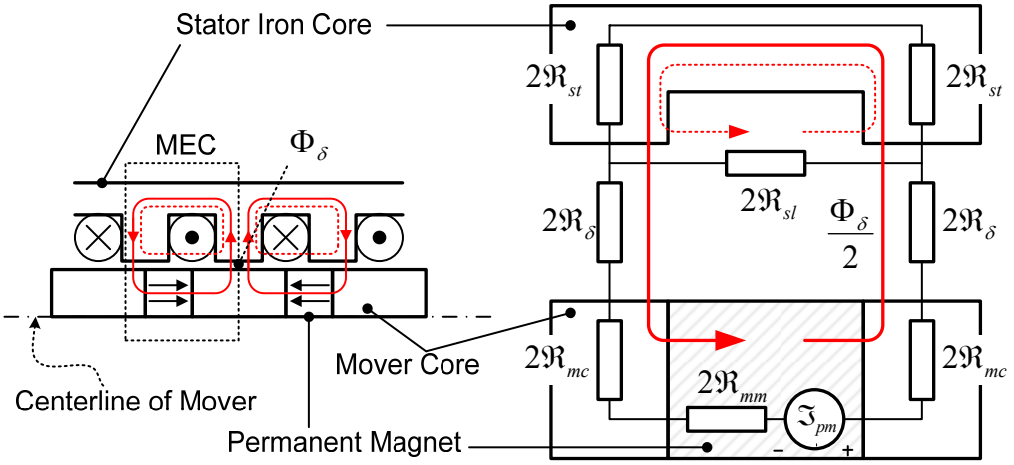

(a) (b)

Fig. 29. (a) Flux paths of the single-sided model when the *d*-axis is aligned with the stator reference axis under no-load condition. (b) Simplified MEC model with slot leakage reluctance under no-load condition.

Since this IPM structure has a relatively large effective air-gap due to the buried PMs, as well as the magnetomotive force (MMF) of the armature current is significantly smaller than that of the PM, an unsaturated model is considered in this paper. The leakage reluctance between teeth is included in the model. The reluctances of the end frames are neglected assuming an infinitely long stator. From the MEC model, the maximum flux Φ_δ coming into and out of the stator teeth can be computed as

$$\Phi_\delta = \frac{\Im_{pm}}{2\Re_\delta + 2\Re_{mc} + \Re_{mm} + \frac{2\Re_{st}\Re_{sl}}{2\Re_{st} + \Re_{sl}}} \tag{2.21}$$

where the MMF of the permanent magnet is given by

$$\Im_{pm} = \frac{B_r T_m}{\mu_0 \mu_m} \tag{2.22}$$

where B_r is the residual flux density (= 1.37 T), μ_o is the permeability of free space, and μ_m is the relative permeability of the PM (= 1.05) on the recoil line on its B-H curve. The air-gap reluctance with the symmetric fringing flux path is considered to calculate an accurate air-gap flux. According to [50], the air-gap reluctance with the symmetric fringing flux path with respect to the tooth centerline when the *d*-axis is aligned with the stator reference axis can be expressed as

$$\Re_\delta \cong \left\{ \mu_0 D_m \left[\frac{T_t}{\delta} + \frac{4}{\pi}\left(1 + \ln\left(\frac{\pi H_t}{4\delta} \right) \right) \right] \right\}^{-1}. \tag{2.23}$$

The reluctance of the PM is calculated as

$$\Re_{mm} = \frac{T_m}{1.55\mu_0\mu_m H_m D_m} \tag{2.24}$$

where the factor 1.55 is used to describe the effective contact face area reduced due to the PM with the H-shaped cross-section and all round edges with the radius of about 0.5 mm. The slot leakage, mover iron core [51], and stator tooth reluctances are obtained as

$$\Re_{sl} = \frac{T_s - T_t}{2\mu_0 H_t D_s} \tag{2.25}$$

$$\Re_{mc} = \frac{\pi}{8\mu_0\mu_c D_m} \tag{2.26}$$

$$\Re_{st} = \frac{H_s + H_t}{2\mu_0\mu_c T_t D_s} \tag{2.27}$$

where μ_c is the relative permeability of the iron core and the back-iron thickness $H_b = H_s - H_t$. When the maximum permeability value is given as 1550, the flux in the air-gap is estimated as 0.1417 mWb from (2.21).

2.3.3 No-Load Flux Density and Stator Relative Permeance

The air-gap MMF is produced by the armature currents and PMs. Especially, the air-gap MMF due to the PMs is the fundamental source of the thrust force in PM linear motors. The maximum air-gap MMF due to the PMs is given by

$$\Im_m = \Re_\delta \Phi_\delta \tag{2.28}$$

Assuming the stator to have smooth surfaces, the no-load air-gap MMF distribution function according to the mover positions with respect to the stator reference axis can be represented as a Fourier series

$$\Im_\delta\left(x_s, x_m\right) = \Im_m \sum_{n=1,3,5\cdots}^{\infty} F_n \sin\left(\frac{\pi n\left(x_m - x_s\right)}{T_p}\right) [\mathrm{A}] \tag{2.29}$$

where the *n*th-spatial harmonic component F_n is given by

$$F_n = (-1)^{\frac{n-1}{2}} \frac{8}{n\pi} \cdot \frac{\cos\left(n\pi\left(T_p - T_m\right)/2T_p\right)}{n\pi\left(T_p - T_m\right)/2T_p}. \tag{2.30}$$

The no-load air-gap flux density function of the slotted linear motor can also be given by the product of the no-load air-gap MMF and permeance of the stator as in [13], [52].

$$B_\delta\left(x_s, x_m, \alpha_s\right) = \frac{\mu_0}{\delta} P_s\left(x_s, \alpha_s\right) \Im_\delta\left(x_s, x_m\right) \quad [\mathrm{T}] \tag{2.31}$$

where the relative permeance function of the stator P_s (x_s,α_s) has a value between 0 and 1, and α_s is the slot-phase shift. The actual air-gap flux density is distributed nonlinearly in the slot opening. This slotting affects the distribution of the air-gap flux density as well as decreases the total flux per pole. Several models have been introduced previously to

consider such slotting effects [48], [52]. Likewise, the stator model with the infinitely deep rectilinear slots is used to derive the relative permeance function of the stator as

$$P_s\left(x_s,\alpha_s\right)=P_0+\left(1-P_0\right)\left|\sum_{n=1,3,5\ldots}^{\infty}P_n\cos\left(\frac{n\pi}{T_s}\left(x_s+\alpha_s\right)\right)\right| \tag{2.32}$$

where P_0 is calculated as

$$P_0=2K_{cs}u_s\Big/\left(1+u_s^2\right) \tag{2.33}$$

where the Carter coefficient K_{cs} and u_s are calculated as

$$K_{cs}=\frac{T_s}{T_s-T_{seo}}=\frac{T_s}{T_s-k_sT_{so}}\ \text{and}\ u_s=\frac{T_{so}}{2\delta}+\sqrt{1+\left(\frac{T_{so}}{2\delta}\right)^2} \tag{2.34}$$

where the slot opening T_{so} is $T_s - T_t$, and k_s is determined by

$$k_s\approx\frac{T_{so}}{5\delta+T_{so}} \tag{2.35}$$

and the nth-harmonic component P_n is computed as

$$P_n=\left(-1\right)^{\frac{n-1}{2}}\frac{4}{\pi}\cdot\frac{\sin\left(n\pi\left(1-k_s\right)T_{so}/4T_s\right)}{n\pi\left(1-k_s\right)T_{so}/4T_s}\cos\left(\frac{n\pi\left(1+k_s\right)T_{so}}{4T_s}\right). \tag{2.36}$$

The 3-D FEA result in Fig. 30 shows the flux density vector paths and magnitude in the middle cross-sectional plane when the *d*-axis is aligned with the stator reference axis. The top and bottom plots in Fig. 31 illustrate the air-gap flux density distributions including the slot-phase shift and slotting effect in the upper and lower air gaps. The analytic distribution with the maximum air-gap flux density of 0.642 T are in good agreement with the FEA result of 0.639 T. This implies that the air-gap flux and relative permeance functions are modeled accurately.

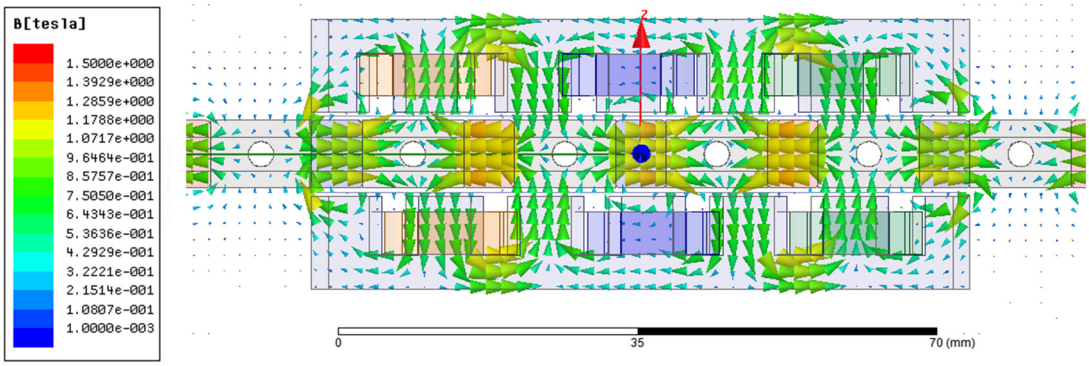

Fig. 30. FE flux density vector paths in the mid-cross-section plane when the d-axis is aligned with the stator reference axis under the no-load condition.

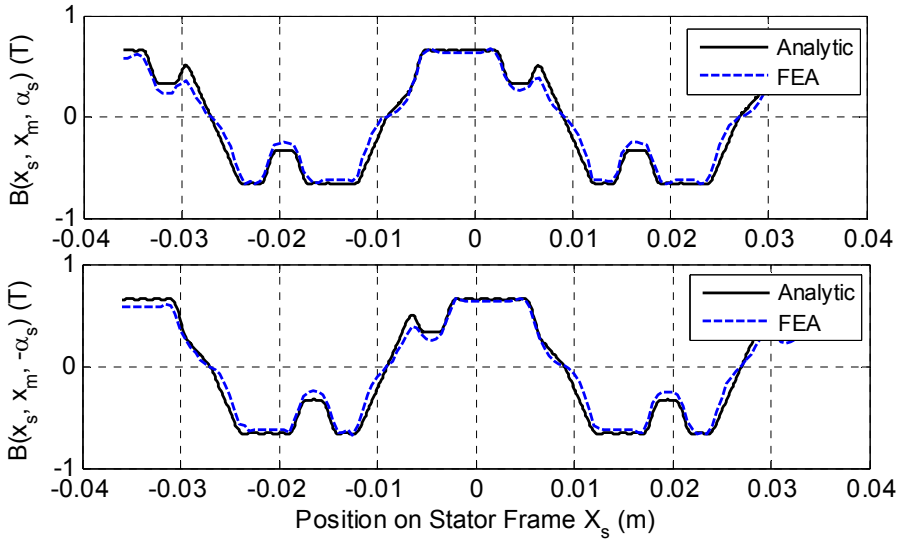

Fig. 31. Predicted air-gap flux density distributions (the top and bottom plots are for the upper- and lower-side air gaps) when the *d*-axis is aligned with the stator reference axis under the no-load condition

2.3.4 DC Resistance of Armature Winding

The armature DC resistance is one of the most important electrical parameters in electric machines from the efficiency point of view. Assuming that the skin effect by the alternating current and the flux in the winding are negligible, the DC resistance

calculation of the uniformly concentrated rectangular winding is straightforward. Fig. 32(a) and (b) show the dimensions and photograph of the uniformly concentrated rectangular armature winding used in this study.

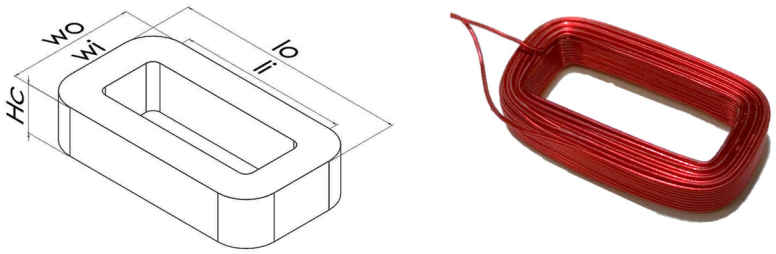

(a) (b)

Fig. 32. Uniformly concentrated rectangular winding: (a) the dimension definitions of the armature winding and (b) a photograph of the armature winding.

The DC resistance of a winding is dependent on the operation temperature of the electric machine. The variation of resistance in the temperature range from 0°C to 150°C is expressed by

$$R_a = R_{25}\left(1+\alpha_{25}\left(T-25^{\circ}\right)\right) \tag{2.37}$$

where R_{25} and α_{25} are the resistance and the temperature coefficient at 25°C, respectively, T is the given temperature, and α_{25} is 0.00393 1/°C for the copper wire. According to Ohm's law, the resistance R_{25} at 25°C is given by

$$R_{25} = \frac{\rho_{cu} l_{cu}}{S_{cu}} = \frac{4\rho_{cu} l_{cu} N}{\pi D_c^2} \tag{2.38}$$

where ρ_{cu} is the resistivity of copper (1.7×10^{-8} Ω-m), l_{cu} is the total length of a winding, S_{cu} and D_c are the cross-sectional area of conductor and the diameter of the copper wire, respectively. The average length l_{ac} per turn can be estimated as $2T_s + l_o + l_i$ where l_o and

l_i are the outer and inner lengths of a coil, respectively. The number of turns N per winding can be calculated as

$$N = \frac{k_f A_{cu}}{D_{ci}^2} = \frac{k_f H_c T_{so}}{D_{ci}^2} \tag{2.39}$$

where D_{ci} is the diameter of copper wire with the insulation layer, A_{cu} is the cross-sectional area of the slot, k_f is the fill factor of the slot. From (2.37)–(2.39), the DC resistance per winding can be written as

$$R_a = \frac{4\rho_{cu} l_{cu} N \left(1 + \alpha_{25}\left(\theta - 25^\circ\right)\right)}{\pi D_c^2} = R_{25}\left(1 + \alpha_{25}\left(T - 25^\circ\right)\right). \tag{2.40}$$

where H_c, l_o, l_i, the outer width w_o, and the inner width w_i of a coil were chosen as 0.005 m, 0.028 m, 0.021 m, 0.016 m, and 0.0078 m, respectively. The wire of the diameter D_{ci} of 0.00045 m (bondable cooper wire of 26 AWG) was used. As a result, the number of turns of 85 was achieved. The DC resistance per winding was calculated as 0.825 Ω and 1.25 Ω at 25°C and 150°C, respectively. The actual resistance per winding was measured as 0.836 Ω. Thus, the total DC resistance per phase of the double-sided model became 1.672 Ω.

2.3.5 No-Load Flux Linkage and Back-EMF Voltage

The total flux linkage in the IPM-FLBM is expressed as

$$\lambda_{phase} = \lambda_a + \lambda_{pm} \tag{2.41}$$

where λ_a is the armature flux linkage due to the phase currents and λ_{pm} is the no-load flux linkage due to the mover PMs. The no-load flux linkage of a winding is maximized when

the *d*-axis is aligned with the centerline of the winding tooth of each winding. The no-load flux linkage per winding with the slot-phase shift can be calculated as follow:

$$\lambda_{pm\_coil}\left(x_m,\alpha_s,\beta\right)=D_s\int_{-2T_p}^{2T_p}N\left(x_s,\alpha_s,\beta\right)B_\delta\left(x_s,x_m,\alpha_s\right)dx_s \tag{2.42}$$

where $N(x_s,\alpha_s,\beta)$ is the generalized winding function [53], β is $-2T_s$, 0, and $2T_s$ for phases *a*, *b*, and *c*, respectively. The slot-phase-shift term is α_s and $-\alpha_s$ for the upper and lower stators, respectively. Assuming the stator has a smooth surface, the generalized winding function is given as

$$N\left(x_s,\alpha_s,\beta\right)=n\left(x_s,\alpha_s,\beta\right)-\left\langle n\left(x_s,\alpha_s,\beta\right)\right\rangle \tag{2.43}$$

where the first term of the right-hand side is the turns function and the second term is the average turns function. Therefore, if each winding is uniformly concentrated as illustrated in Fig. 32, and has the period of $2T_s$ by the alternate teeth winding arrangement, the winding function with the slot-phase shift can be written in the form of a Fourier series as follows:

$$N\left(x_s,\alpha_s,\beta\right)=2N\sum_{n=1}^{\infty}N_n\frac{\sin\left(n\pi/4\right)}{n\pi}\cos\left(\frac{n\pi\left(x_s+\beta+\alpha_s\right)}{2T_p}\right) \tag{2.44}$$

where the *n*th-spatial harmonic winding factor N_n for the uniformly concentrated winding is given by

$$N_n=\frac{4T_p}{n\pi T_{so}\sin\left(n\pi/4\right)}\sin\left(\frac{n\pi T_s}{4T_p}\right)\sin\left(\frac{n\pi T_{so}}{4T_p}\right). \tag{2.45}$$

From (2.44), six winding functions are made, and a pair of winding functions for the same phase have the offset of $T_s/6$ between each other. However, since the windings of the

upper and lower stators for the same phase are connected in series, the two winding functions of the upper and lower sides are spatially superposed. Consequently, new three superposed winding functions can be derived as

$$\begin{aligned} N_{phase}(x_s,\beta) &= N(x_s,\alpha_s,\beta)+N(x_s,-\alpha_s,\beta) \\ &= 4N\sum_{n=1}^{\infty}N_n\frac{\sin(n\pi/4)}{n\pi}\cos\left(\frac{n\pi\alpha_s}{2T_p}\right)\cos\left(\frac{n\pi(x_s+\beta)}{2T_p}\right) \end{aligned} \tag{2.46}$$

Fig. 33 shows the six slot-phase-shift winding functions and new three superposed winding functions of phases *a*, *b* and *c*.

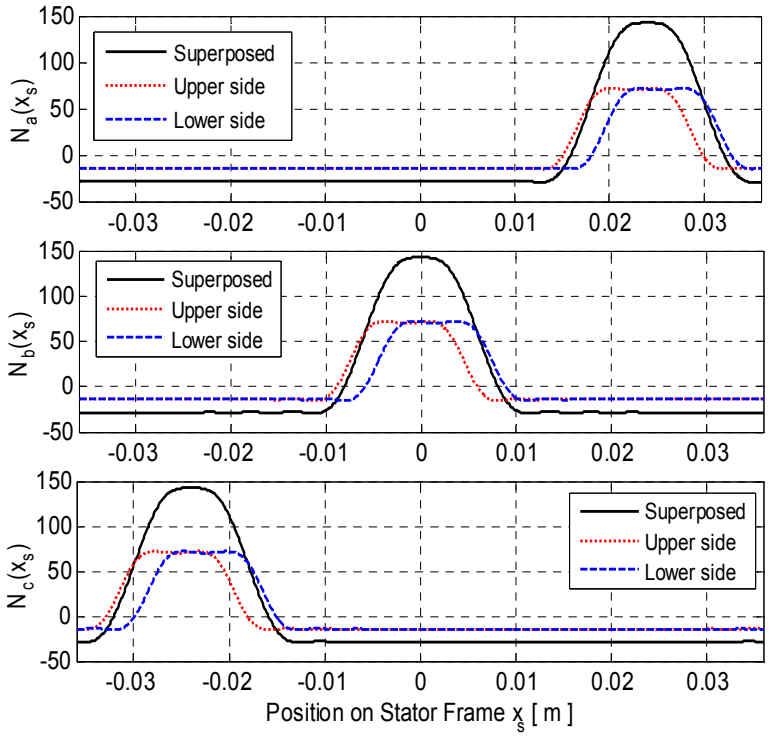

Fig. 33. Superposed winding functions of phases *a*, *b,* and *c* when a coil has the number of turns of 85.

Eventually, the no-load flux linkages for each phase can be obtained using the superposed winding functions (2.46) and the air-gap flux density function (2.31) as follows:

$$\lambda_{pm\_phase}(x_m,\beta) = D_s \int_{-2T_p}^{2T_p} N_{phase}(x_s,\beta) B_\delta(x_s,x_m,0)\,dx_s \ . \tag{2.47}$$

Fig. 34 illustrates that the no-load flux linkages of (2.47) has the very sinusoidal waveforms. As expected, the maximum no-load flux linkage for each phase occurs when the *d*-axis is aligned with the superposed winding centerline rather than the individual winding tooth centerline. This good agreement between the FEA and analytic solution indicates that the superposed winding function is valid in the slot-phase-shift structure. The maximum flux linkage is calculated as around 22.1 mW-turns.

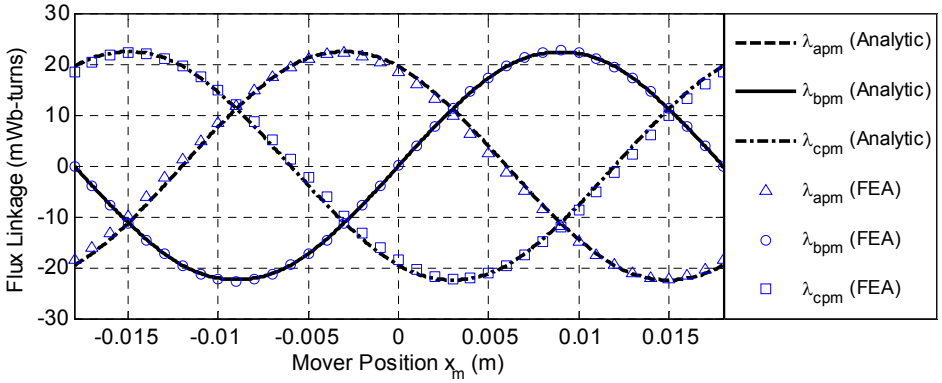

Fig. 34. Analytic and FEA results of the no-load flux linkages for each phase according to the mover positions.

The phase-to-neutral back-EMF can be derived through differentiating the flux linkage in (2.47) for the mover displacement x_m with respect to time as follows:

$$e_{phase}(x_m,\beta) = \frac{d\lambda_{pm}}{dt} = D_s \int_{-2T_p}^{2T_p} N_{phase}(x_s,\beta) \frac{dB_\delta(x_s,x_m,0)}{dt} dx_s. \tag{2.48}$$

Fig. 35 shows that the phase-to-neutral back-EMFs of the analytic model are in good agreement with the FEA results for each phase. The eddy current loss is not considered

in this simulation. The phase-to-neutral back-EMF constant is calculated as around 3.85 V-s/m.

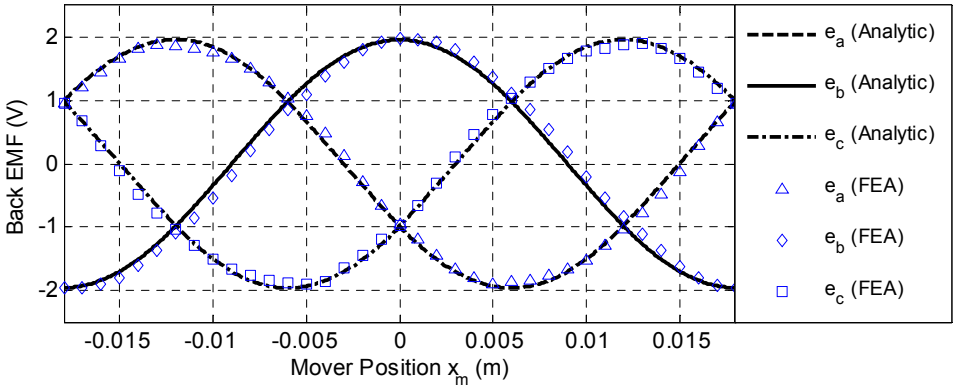

Fig. 35. Analytic and FEA results of the phase-to-neutral back-EMFs for each phase when the mover has the linear speed of 0.5 m/s.

2.3.6 Inductance Calculations

The inductance is an important parameter to calculate the armature flux linkage in (2.41). The self-inductance consists of the magnetizing, harmonic-leakage, slot-leakage, end-winding-leakage, and tooth-top-leakage (zig-zag-leakage) inductances [48], [53]. The end-winding- and tooth-top-leakage inductances in a common design practice are often ignored because their values are much smaller than other components. Thus, it is assumed that the tooth-top-leakage inductance of the open slot is negligible in this paper. However, since the end-winding-leakage inductance cannot be ignored in the non-overlapping winding machine with a short stack width close to the pole pitch, the self-inductance of a phase configured with two series-connected non-overlapping concentrated windings of the upper and lower stators can be expressed as [55]

$$L_s(x_m) = (Q/3)L_u + (Q/6)L_{ew} + L_m(x_m) \tag{2.49}$$

where L_u is the slot leakage inductance per slot, Q is the total slot number of the upper and lower stator, L_{ew} is the end-winding-leakage inductance per winding, and L_m is the total magnetizing inductance per phase. In the case of the iron-core SPM configured with the distributed winding, the magnetizing inductance can be calculated using the generalized winding function given in (2.43) and constant air gap. This is because the generalized winding function is defined under the assumption that the sum of incoming and outgoing fluxes in the entire air gap between the stator and mover are zero as follows:

$$\int_0^{2\pi} N(\theta)\, d\theta = 0 . \tag{2.50}$$

However, as shown in the top and bottom diagrams of Fig. 36, the fluxes induced by the armature MMF in the buried-type IPM configuration are not distributed to the entire air gap because of the alternate teeth windings and the large air gap between the mover iron cores. Thus, the generalized winding function is unavailable to calculate the inductance of this configuration. Furthermore, the generalized winding function cannot evaluate the variation of the maximum magnitude of MMF in the air gap according to the mover positions. For example, when the *d*-axis is aligned with the winding tooth center as shown in the top diagram of Fig. 36, the air-gap flux density is significantly decreased due to the large air gap between stator teeth and both sides of the iron core, and its magnitude is much less when the *q*-axis is aligned with the same tooth center as shown in the bottom diagram of Fig. 36. However, since the inductance calculation using (2.44) can evaluate only the cross-sectional area corresponding to the mover permeance profile, the inductance of the *d*-axis is calculated with much larger value than that of the *q*-axis.

Therefore, a new variable winding function based on the modified winding function [56] is developed in this study.

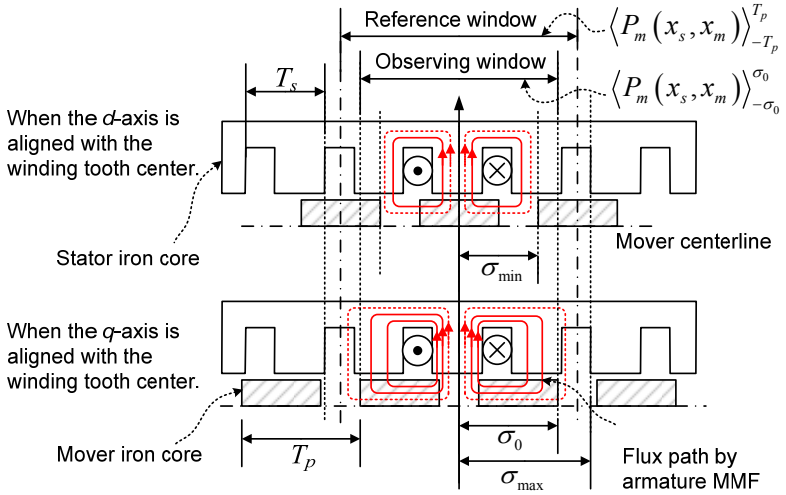

Fig. 36. Variable winding function model in the IPM-FLBM: flux paths when the *d*-axis is aligned with the winding tooth center (top) and when the *q*-axis is aligned with the winding tooth center (bottom).

The variable winding function has the flux distribution range of from $2\sigma_{min}$ to $2\sigma_{max}$. They are determined by the variation of the average permeance of the observing window according to the mover position versus the average permeance of the reference window. The distribution range variable σ with respect to the winding tooth center can be calculated as

$$\sigma = \sigma_0 + \frac{k}{2}\left[\langle P_m(x_s,x_m)\rangle_{-\sigma_0}^{\sigma_0} - \langle P_m(x_s,x_m)\rangle_{-T_p}^{T_p}\right] \tag{2.51}$$

where $\langle P_m(x_s,x_m)\rangle$ is the average relative permeance function of the mover in a given range. The relative permeance function of the mover is given as

$$P_m(x_s,x_m) = P_0 + (1-P_0)\left|\sum_{n=1,3,5\ldots}^{\infty} P_n \cos\left(\frac{n\pi}{T_p}(x_s - x_m) - \frac{n\pi}{2}\right)\right| \tag{2.52}$$

where all coefficients in (2.52) can be calculated using (2.33)–(2.36) after replacing T_s and T_{so} with T_p and T_m, respectively. The observing range $2\sigma_0$ is given as $2T_p - T_m$ from Fig. 36. The coefficient k is chosen as a number that makes the minimum value of the calculation result of (2.51) be equal to σ_{min} (= $2T_s$) as shown in Fig. 36. Thus, the new winding function of phase b in the upper side using the variable range is given by

$$VM_x\left(x_s, x_m, \alpha_s\right) = n_x(x_s, \alpha_s) - \frac{\int_{-\sigma}^{\sigma} n_x(x_s, \alpha_s) P_m\left(x_s, x_m\right) dx_s}{2\sigma \left\langle P_m\left(x_s, x_m\right)\right\rangle_{-\sigma}^{\sigma}} \tag{2.53}$$

The variable winding function in the lower side can be achieved replacing α_s with $-\alpha_s$. Fig. 37 illustrates that both the magnitude and the distribution range are minimized when the d-axis is aligned with the winding tooth center, and they are maximized when the q-axis is aligned with the winding tooth center.

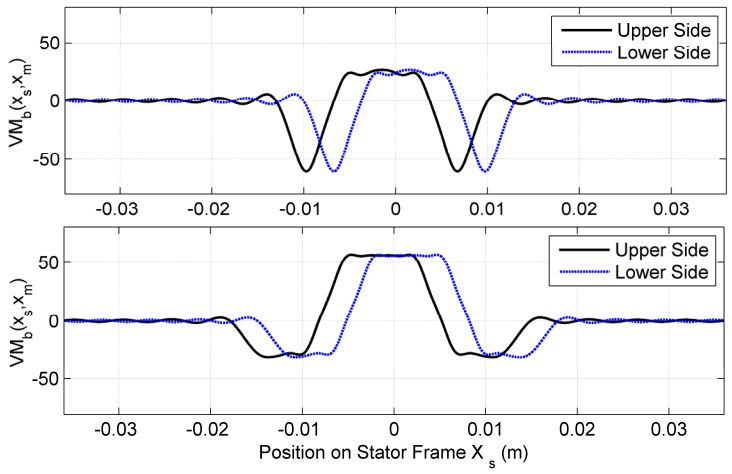

Fig. 37. Variable winding function of phase b in the upper and lower sides when the d-axis is aligned with the stator reference axis (top) and when the q-axis is aligned with the stator reference axis (bottom).

Therefore, the magnetizing inductance of the double-sided IPM-FLBM using (2.53) can be represented as

$$L_{xm}(x_m)=\frac{\mu_0 D_s}{\delta}\int_{-2T_p}^{2T_p}\left(VM_x^2(x_s,x_m,\alpha_s)+VM_x^2(x_s,x_m,-\alpha_s)\right)P_m(x_s,x_m)dx_s. \tag{2.54}$$

where the subscript x presents the each phase. Similarly, the mutual inductance is also given as

$$\begin{aligned}L_{xy}(x_m)=\frac{\mu_0 D_s}{\delta}\int_{-2T_p}^{2T_p}&\left(VM_x(x_s,x_m,\alpha_s)VM_y(x_s,x_m,\alpha_s)\right.\\&\left.+VM_x(x_s,x_m,-\alpha_s)VM_y(x_s,x_m,-\alpha_s)\right)P_m(x_s,x_m)dx_s\,.\end{aligned} \tag{2.55}$$

The slot-leakage inductance per slot is calculated as 0.151 mH by using a classical equation as [52], [53].

$$L_u=\frac{\mu_0 D_s N^2}{T_{so}}\left(H_t-\frac{2}{3}H_c\right). \tag{2.56}$$

The analytic model for the end-winding leakage inductance in the non-overlapping winding PM machine is developed in [54] .This equation takes the end-winding geometry and laminated stack effect into account. If adopting this equation into the double-sided IPM linear motor, since the average coil radius can be assumed to be $3T_s/\pi$, the end-winding-leakage inductance per winding can be expressed as

$$L_{ew}=1.257\left(\frac{6T_s l_e}{\pi(w_o-w_i)}\right)KN^2 \tag{2.57}$$

where the average end-length l_e is $w_o + (l_i - D_s)/2$ and the constant K is given as

$$K=k_1-k_2 \tag{2.58}$$

with k_1 and k_2 are written as a function of the dimensional variables a, b, and c in [54]. These variables can be given as $3T_s/\pi$, $w_o - w_i$, and H_c, respectively, in the double-sided IPM-FLBM. The end-winding-leakage inductance per winding is computed as 0.140 mH.

The self-inductance distributions in Fig. 38 illustrate illustrate that each inductance has its maximum value when the *q*-axis is aligned with the corresponding superposed axis. Although the FEA results and analytic solutions have slightly larger values than those of the measured self-inductances, they are in good agreement with each other in the perspective of a function of mover position. The average self-inductance comparison in Table II shows that the measured self-inductances have around 7% smaller values than FEA results and analytic solutions.

As shown in Fig. 36, since the passive teeth in the alternate-teeth-winding configuration play the role of alternate flux path, the mutual flux linkages between two adjacent phase windings have very small values [46]. Especially, the mutual inductance L_{ac} between phases *a* and *c* is much close to zero because the linear motor stator has the open circuit in its end frame. The mutual inductances in Fig. 14 obtained from the analytic solution, FEA, and measurement illustrate such an expected behavior. Although the varying amplitude of the analytic solution is much larger than those of the measured inductances because of the resolution limitation of the winding function model based on Fourier series, its trend according to the mover positions is in good agreement with the measurement one, and its average value is within the error of 20%. The FEA result shows the much more ideal case than others. This result also implies that the mutual inductances' roles in electromagnetic circuit are negligible as compared with the self-inductances. The average inductance comparisons in Table 8 imply that that our analytic inductance models are well established as well as the mutual inductance has around 3% of the self-inductance

value in the alternate-teeth-winding configuration. This value is even smaller than those of the conventional all teeth winding or sinusoidal winding structure.

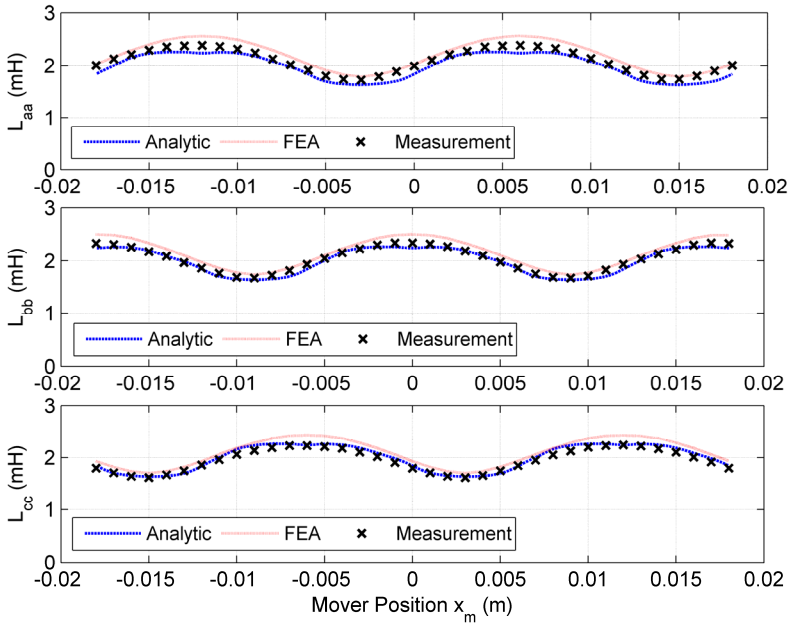

Fig. 38. Self-inductance distributions of each phase according to the mover positions.

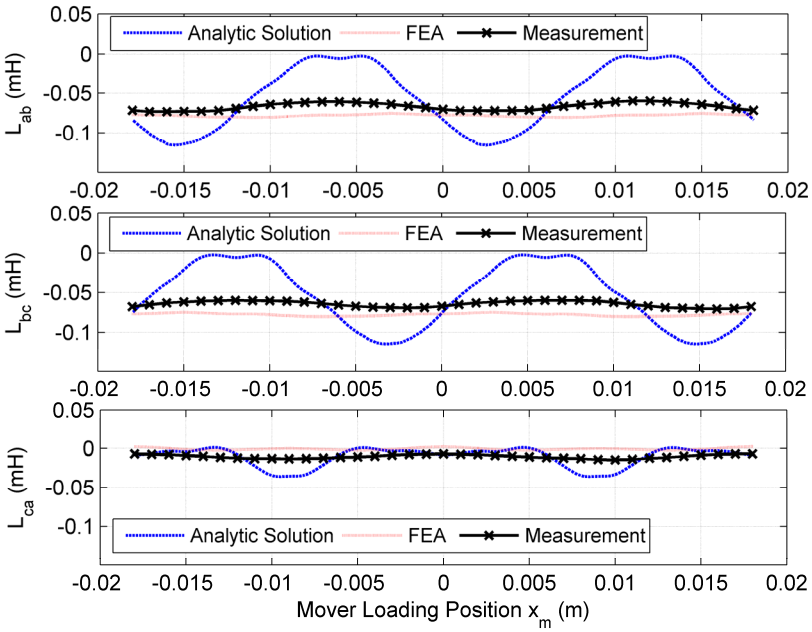

Fig. 39. Mutual inductance distributions of each phase according to the mover positions.

Table 8. Average values of the inductances.

	L_{aa}	L_{bb}	L_{cc}	L_{ab}, L_{ab}	L_{bc}, L_{cb}	L_{ac}, L_{ca}
Measured (mH)	2.092	2.042	1.952	-0.065	-0.067	-0.010
FE analysis (mH)	2.200	2.200	2.200	-0.078	-0.078	-0.007
Calculated (mH)	2.151	2.151	2.151	-0.054	-0.054	-0.011

2.3.7 Thrust Force Calculation

In this section, the steady-state thrust-force calculation is presented using the *d-q* model of the three-phase IPM-FLBM. On the basis of the analyses presented in Section III, the following assumptions are made: (1) the no-load flux linkage is sinusoidal, and the space harmonics in the air gap are neglected, (2) the armature linkage flux is also sinusoidal, and the space harmonics in the air gap are neglected, (3) the balanced three-phase currents and voltages are considered, and (4) the eddy-current and hysteretic effects are neglected.

2.3.7.A Voltage Equations

The matrix form of the voltage equations in terms of the phase currents and flux linkages is given by

$$\begin{bmatrix} v_a \\ v_b \\ v_c \end{bmatrix} = \begin{bmatrix} R_s & 0 & 0 \\ 0 & R_s & 0 \\ 0 & 0 & R_s \end{bmatrix} \begin{bmatrix} i_{as} \\ i_{bs} \\ i_{cs} \end{bmatrix} + \frac{d}{dt} \left(\begin{bmatrix} L_{aa} & L_{ab} & L_{ac} \\ L_{ba} & L_{bb} & L_{bc} \\ L_{ca} & L_{cb} & L_{cc} \end{bmatrix} \begin{bmatrix} i_{as} \\ i_{bs} \\ i_{cs} \end{bmatrix} + \begin{bmatrix} \lambda_{ma} \\ \lambda_{mb} \\ \lambda_{ma} \end{bmatrix} \right) \tag{2.59}$$

where R_s is the armature resistance. The balanced three-phase armature currents i_{as}, i_{bs}, and i_{cs} are given by

$$\boldsymbol{i}_{abc} = I_m \begin{bmatrix} \cos(\omega_e t + 2\pi/3) \\ \cos(\omega_e t) \\ \cos(\omega_e t - 2\pi/3) \end{bmatrix} \tag{2.60}$$

where I_m is the magnitude of applied current, and ω_e is the electric frequency. The no-load linkage terms can be given from the results in Fig. 34 and assumption in this Section as

$$\boldsymbol{\lambda}_m = \lambda_m \begin{bmatrix} \sin(\theta + 2\pi/3) \\ \sin(\theta) \\ \sin(\theta - 2\pi/3) \end{bmatrix} \tag{2.61}$$

where $\theta = \pi x_m / T_p$. According to [35], the generalized inductance of the salient PM synchronous motor can be modeled with the function of the mover positions as below

$$\begin{aligned} L_{aa}(x_m) &= 4L_u + 2L_{ew} + L_{ma}(x_m) = L_{ls} + L_{os} + L_{2s}\cos\left(2(\theta + 2\pi/3)\right) \\ L_{bb}(x_m) &= 4L_u + 2L_{ew} + L_{mb}(x_m) = L_{ls} + L_{os} + L_{2s}\cos(2\theta) \\ L_{cc}(x_m) &= 4L_u + 2L_{ew} + L_{mc}(x_m) = L_{ls} + L_{os} + L_{2s}\cos\left(2(\theta - 2\pi/3)\right) \end{aligned} \tag{2.62}$$

where L_{ma}, L_{mb}, and L_{mc} are the magnetizing inductances of each phase, L_{ls} is the sum of the leakage inductance, L_{os} is the constant value of the magnetizing inductance, and L_{2s} is the amplitude of the second-harmonic term of the magnetizing inductance. From the inductance-distribution plots in Fig. 38, the parameters L_{ls}, L_{os}, and L_{2s} in (2.62) can be evaluated as 0.886 mH, 1.12 mH, and 0.34 mH, respectively. From Fig. 39 and Table 8, the mutual inductances are assumed as zeros in the inductance matrix of (2.59) as follows:

$$L_{ab}(x_m) = L_{ba}(x_m) = L_{bc}(x_m) = L_{cb}(x_m) = L_{ca}(x_m) = L_{ca}(x_m) \approx 0 \tag{2.63}$$

2.3.7.B Steady-State Thrust Force Calculation

In the rotary machine, the general scalar voltage equations of the two-phase circuit through the *d-q* decomposition of (2.59) are given by

$$V_{qs} = (R_s + L_q p) I_{qs} + \omega L_d I_{ds} + \omega \lambda_{dm}$$
$$V_{ds} = (R_s + L_d p) I_{ds} - \omega L_q I_{qs} \tag{2.64}$$

where p is d/dt, I_q and I_d are the q-axis and d-axis currents, ω is the mechanical angular rotating speed, and λ_{dm} is the d-axis flux linkage. L_q and L_d are the q-axis and d-axis inductances that are given as

$$L_q = L_{ls} + L_{os} + L_{2s} \text{ and } L_d = L_{ls} + L_{os} - L_{2s}. \tag{2.65}$$

Thus, the q- and d-axis inductances are calculated as 2.34 mH and 1.66 mH, respectively. Since the linear speed V_m of the linear motor is equal to the synchronous speed of the traveling magnetic field, the linear and rotating speeds have the following relationship

$$V_m = \omega T_p / \pi. \tag{2.66}$$

From (2.64)–(2.66), the voltage equations according to the mover speed are given as

$$V_{qs} = (R_s + L_q p) I_{qs} + \left(\pi / T_p\right)\left(L_d I_{ds} + \lambda_{dm}\right) V_m$$
$$V_{ds} = (R_s + L_d p) I_{ds} - \left(\pi / T_p\right) L_q I_{qs} V_m. \tag{2.67}$$

The mechanical power can be obtained by subtracting the ohmic loss and the rate of the change of the stored energy in the magnetic circuit from the instantaneous power computed with (2.66) [56]. The developed thrust force can be expressed in terms of the d- and q-axis current variables as below:

$$F_x = \frac{3\pi}{2T_p}\left(\lambda_{dm} I_{qs} + (L_d - L_q) I_{ds} I_{qs}\right). \tag{2.68}$$

2.3.8 Steady-State Force Validation

The photograph in Fig. 40 shows the experimental setup that measures the inductances and steady-state thrust force of the double-sided 6/4 IPM-FLBM modeled in

this paper. A 300 W DC power supply was used. A precision bidirectional load cell with the 0.1% nonlinearity and a micrometer head with the accuracy of ±0.0005 mm were employed to measure the steady-state thrust forces according to the mover positions. The inductances were measured using a 60-Hz sinusoidal current source of 1.0 A.

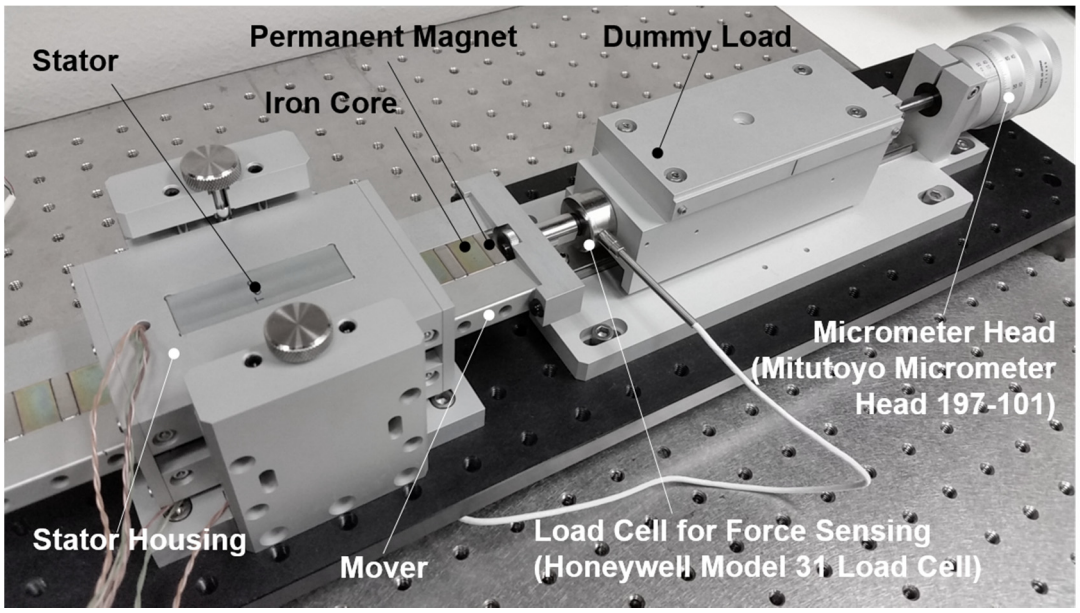

Fig. 40. Photograph of the experimental setup to measure the inductances and steady-state thrust force.

The thrust force of (2.68) is composed of two distinct mechanisms. The first term corresponds to the magnetizing force occurring between I_{qs} and the PM, whereas the second term is the reluctance force generated due to the differences between the d-axis and q-axis inductances. Assuming that the supply voltage and current are limited and the supplied current vector leads the q-axis current by the phase angle γ in steady state, (2.68) can be rewritten using the magnitude of the current vector I_s as

$$F_x = \frac{3\pi}{2T_p}\left(\lambda_m I_s \cos\gamma + \frac{1}{2}\left(L_q - L_d\right) I_s^2 \sin 2\gamma\right) \tag{2.69}$$

where I_s is given as

$$I_s = \sqrt{I_q^2 + I_d^2}\,. \tag{2.70}$$

Thus, the maximized thrust force can be obtained through field weakening due to the *d*-axis armature reaction. Fig. 41 shows that the maximum thrust force is produced when the phase angle (= $\tan^{-1}(I_d/I_q)$) is around 15° although the reluctance force at the current vector of 10 A is not significantly large due to the small difference between the *q*- and *d*-axis inductances. The measured total thrust forces are achieved within maximum 2% error when compared with the total thrust forces in the calculation and FEA. The predicted total thrust force using a closed-form analysis matches quite well with the measurement and FEA.

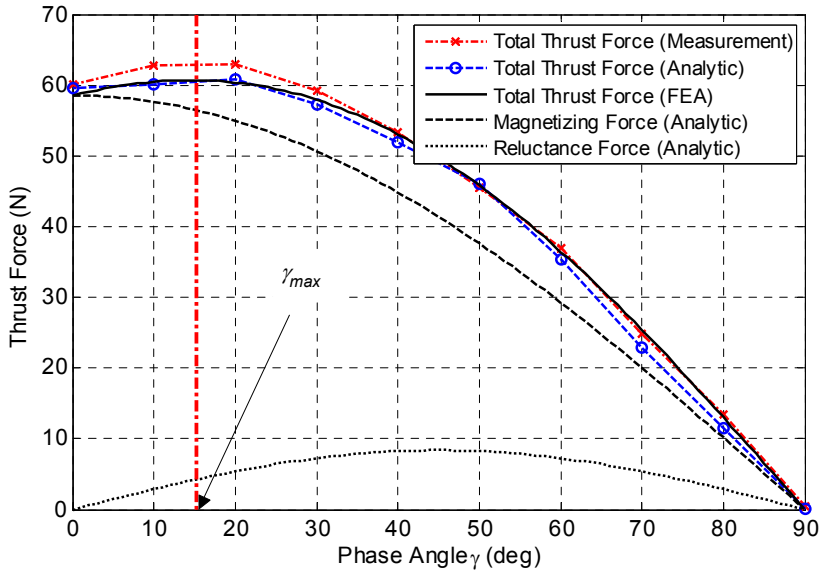

Fig. 41. Thrust force components accordin to the current phase angle γ when the magnitude of the current vector I_s of 10 A is applied.

The plots in Fig. 42 show that the maximum force control (MFC) scheme using the reluctance force can produce more force than that of the FOC scheme for the same input power. This implies that if the residual flux density of the PM is not deteriorated by *d*-axis armature reaction in the high temperature, the more the current increases, the larger force difference is produced. The calculated force constants of the FOC and MFC were evaluated as 5.8 N/A and 6.1 N/A, and the measured ones were estimated as 5.9 N/A and 6.2 N/A, respectively, in the given current range. The measured force constants for both cases are slightly higher than the calculated ones. It seems that the residual flux density of the actual PM is slightly higher than that used in the calculation and FEA.

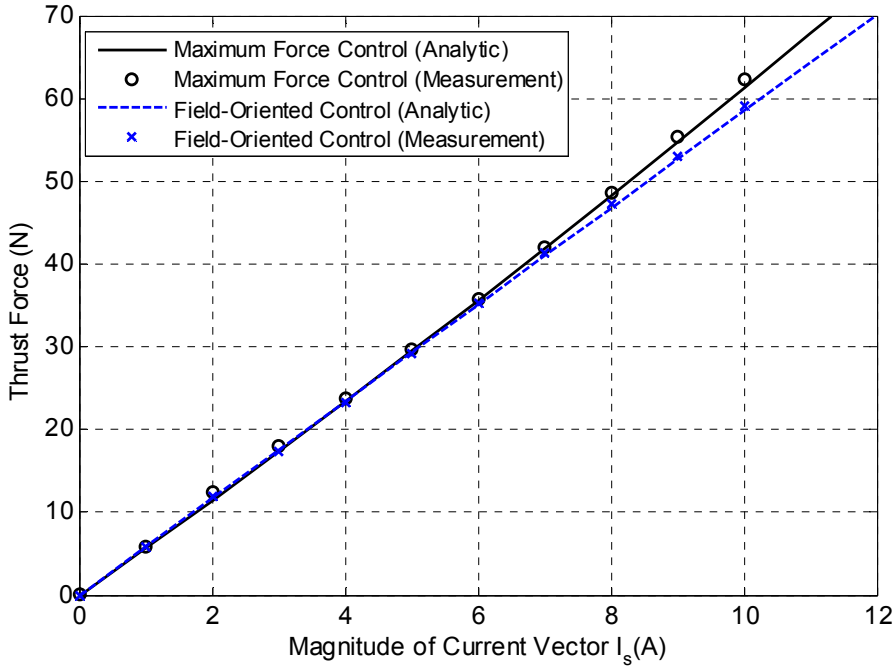

Fig. 42. Force-to-current ratios in the MFC and FOC scheme.

The force pulsation, also called force ripple, is caused by the detent force and the switching power circuit. Unlike the conventional rotary motor, the detent force in an iron-

cored PM linear motor has not only the cogging force but also the end-effect force [7], [57]. Furthermore, since the end-effect force acting on the complex end frame in the linear motor exhibits the highly nonlinear behavior, there is no analytic solution for the end-effect force until now. Therefore, in this paper, the cogging force for the infinite-long stator model was simulated using 3-D FEA for the ripple force comparison. The top and bottom plots in Fig. 43 show the steady-state thrust forces when I_q = 10 A and I_d = 0 A, and the detent forces when I_q = I_d = 0 A, respectively. The measured detent force in the bottom plot of Fig. 43 shows that the cogging force predicted in an ideal FEA model is distorted by the residual harmonic term of the end-effect force. As a result, the actual detent force becomes much larger than the cogging force of the ideal FEA model. Thus, the peak-to-peak cogging force in the FEA model was evaluated as around 1.2 N, but the actual detent force was measured as 2.4 N, corresponding to approximately 2% and 4% of the rated thrust force. In addition, the resultant detent force directly affects the steady-state ripple force as shown in the upper plot of Fig. 43. Hence, the standard deviations of the steady-state forces in the FEA and measurement were evaluated as 0.81 N and 1.13 N, respectively. The averages of the steady-state forces in the FEA and measurement were calculated as 58.4 N and 58.9 N, respectively. Similar to the previous result, the measured average force has a 1% higher value than the simulated one.

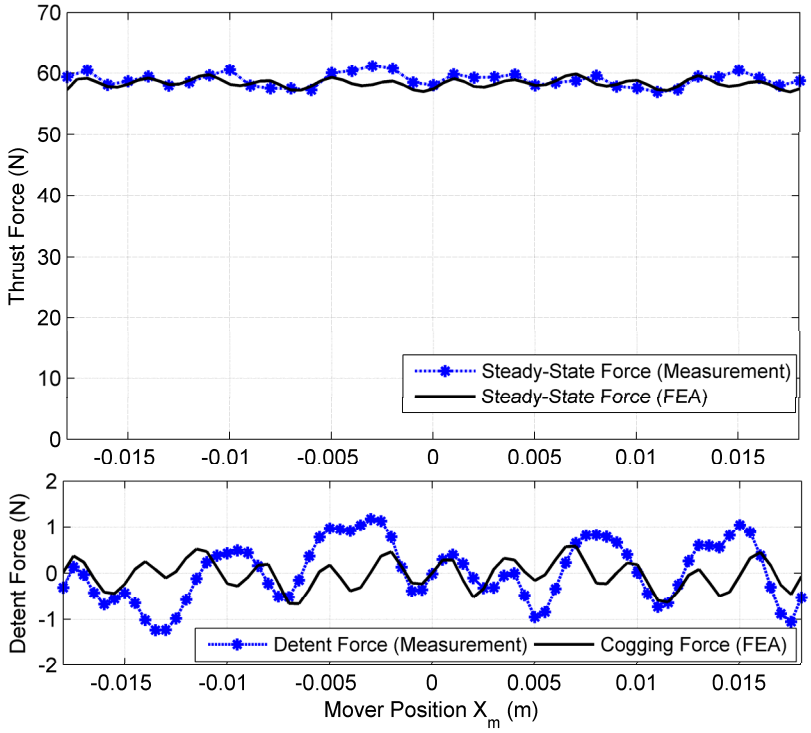

Fig. 43. Steady-state force and detent force according to the mover positions when I_{qs} and I_{ds} are controlled as 10 A and 0 A, respectively.

2.4 IPM-FLBM Using SMC

Most iron-core types use the laminated thin silicon steel sheets as the soft magnetic material for the minimization of the eddy-current loss. In order to overcome such drawbacks, new powder iron-composite material was developed in the early 2000s. This SMC material has several advantages such as low eddy-current loss, flexible machine design and assembly, three-dimensional isotropic ferromagnetic behavior, relatively good recyclability, and reduced production costs.

However, its lower permeability than that of the laminated steel core hindered the extensive use of the SMC material in electric machines. Therefore, many studies

considering such characteristics of the SMC material have been performed on the various electric machine designs over the past decade.

In this section, the applicability of the SMC material to a small-sized IPM linear motor is presented. A 6/4 double-sided IPM-FLBM machined with SS400 electrical solid steel shown in Section 2.3.1 is used as the base model prototype. The electromagnetic analysis for the new prototype using a Somaloy prototyping material (SPM) is studied with a simplified nonlinear MEC analysis under the no-load and electrical-load conditions. The back-EMFs and inductances are measured experimentally, and compared with the analytic solutions. The iron and copper losses were investigated in the aspect of the heat dissipation capability. The steady-state thrust and ripple forces of the base model and SPM prototypes are measured and compared experimentally. Fig. 44 shows the stator and mover cores of the IPM-FLBM prototype were machined using the SPM.

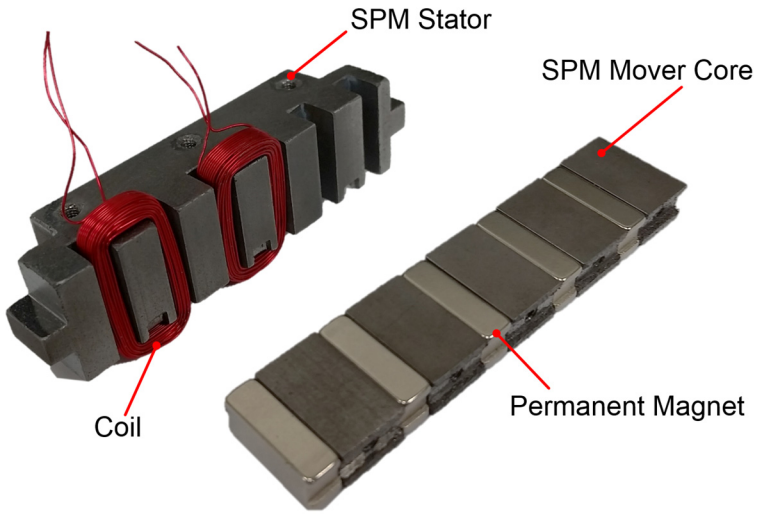

Fig. 44. Photograph of the stator core with the phase coils (right) and mover with PMs (left).

2.4.1 Inductance Calculations

From the inductance model using the variable winding function in Section 2.3.6, it is shown that the inductance of phase *b* in a single-sided IPM-FLBM with the saliency can be generalized using the function of the mover position as follows:

$$L_{bb\_s}(x_m) = 2L_u + L_{ew} + L_{mb}(x_m) = L_{ls} + L_{os} + L_{2s}\cos\left(p\pi x_m / T_p\right) \tag{2.71}$$

where L_{mb} is the total magnetizing inductance of phase *b*, L_u is the slot leakage inductance per slot, L_{ew} is the end-winding leakage, L_{ls} is the sum of the leakage inductances, L_{os} is the constant value of the magnetizing inductance, L_{2s} is the amplitude of the second harmonic term of the magnetizing inductance, and *p* is the number of pole pairs.

Assuming that the permeance of the iron core is infinite under the unsaturation condition, the magnetizing inductances of the self- and mutual inductances can be obtained from the *q*- and *d*-axis air-gap permeances in the single-sided IPM-FLBM model shown in Fig. 45.

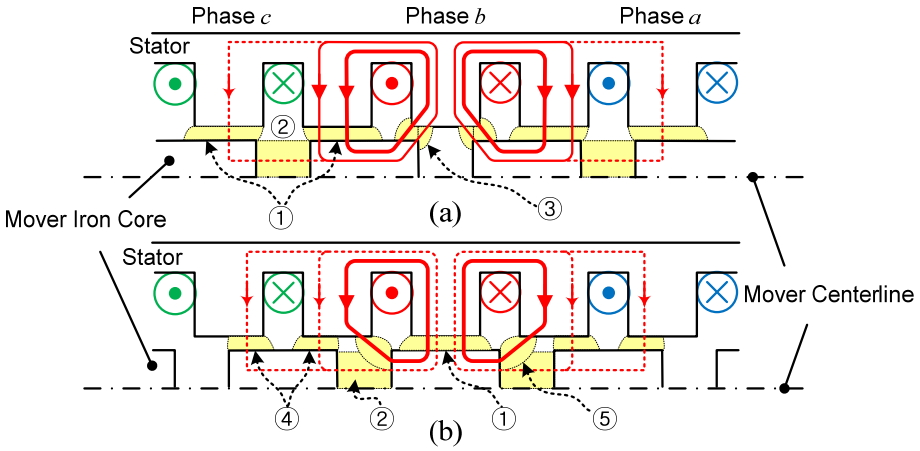

Fig. 45. The air-gap permeance models when the phase *b* is an armature MMF source: (a) the *q*-axis is aligned with the tooth center of phase *b*, (b) the *d*-axis is aligned with the tooth center of phase *b*.

The *q*- and *d*-axis magnetizing inductances of phase *b* can be given as, respectively.

$$L_{qm} = L_{os} + L_{2s} \cong \frac{2N^2\left(P_1 + P_2\right)}{P_1 P_2\left(\left(P_1 \parallel P_1 \parallel P_2\right)^{-1}\left(P_1 \parallel P_3\right)^{-1} - P_1^{-2}\right)} \tag{2.72}$$

$$L_{dm} = L_{os} - L_{2s} \cong \frac{2N^2}{\left(P_1 \parallel P_2 \parallel P_5\right)\left(\left(P_1 \parallel P_2 \parallel P_5\right)^{-1}\left(P_1 \parallel P_1 \parallel P_5\right)^{-1} - P_5^{-2}\right)} \tag{2.73}$$

where the permeance P_1, P_2, P_3, P_4, and P_5, are given as

$$P_1 = 2P_4 \cong \frac{\mu_0 D_s\left(T_t + T_p - T_m\right)}{2\delta} \tag{2.74}$$

$$P_2 \cong \frac{\mu_0 \mu_m D_s H_m}{0.95 T_m} \tag{2.75}$$

$$P_4 \cong 2\mu_0 D_s\left[\frac{T_t - T_m}{4\delta} + \frac{2}{\pi}\left(1 + \ln\left(\frac{\pi H_t}{18\delta}\right)\right)\right] \tag{2.76}$$

$$P_5 \cong \frac{\mu_0 D_s\left(0.125T_t + 0.25H_m\right)}{\pi\left(T_m + 0.5H_m + \delta\right)} \tag{2.77}$$

From (2.56), (2.57), and (2.72)–(2.77), the parameters L_{ls}, L_{os}, and L_{2s} can be evaluated. As a results, the self-inductance function of phase *b* in the double-sided model with the slot-phase shift can be written as

$$L_{bb}\left(x_m\right) = 2L_{ls} + 2L_{os} + 2L_{2s}\cos\left(2\pi\alpha_s / T_p\right)\cos\left(2\pi x_m / T_p\right). \tag{2.78}$$

where the first cosine term is the coefficient due to the slot-phase shift. The magnetizing inductance functions for other phases are shifted by ±120° electrically from phase *b*. The mutual inductances L_{ba} and L_{bc} in Fig. 45 can be expressed as

$$L_{ba\_q} = L_{bc\_q} \cong \frac{N^2}{P_1\left(\left(P_1 \parallel P_1 \parallel P_2\right)^{-1}\left(P_1 \parallel P_3\right)^{-1} - P_1^{-2}\right)} \tag{2.79}$$

$$L_{ba\_d} = L_{bc\_d} \cong \frac{N^2}{2P_5\left(\left(P_1 \parallel P_2 \parallel P_5\right)^{-1}\left(P_1 \parallel P_1 \parallel P_5\right)^{-1} - P_5^{-2}\right)} \ . \tag{2.80}$$

Since the mutual inductances in two different positions have the interval of π, a half of the sum of two inductances is the average mutual inductance, and the reduced magnitude ratio of the mutual inductance that is $2T_s$ away from the armature MMF source can be calculated by

$$L_{bc}\left(x_m\right) = -2mL_{os} + 2mL_{2s}\cos\left(2\pi\alpha_s / T_p\right)\cos\left(\tfrac{2\pi}{T_p}x_m - 120^\circ\right) \tag{2.81}$$

The two other mutual inductances are shifted by electrically ±120° from L_{bc}. However, since the L_{ac} has the distance of $4T_s$ due to the open-circuit structure of linear motor's stator, its magnitude can be approximated as

$$L_{ca}\left(x_m\right) = -2m^2L_{os} + 2m^2L_{2s}\cos\left(2\pi\alpha_s / T_p\right)\cos\left(\tfrac{2\pi}{T_p}x_m\right) \tag{2.82}$$

2.4.2 No-Load Flux Linkage and Back-EMF Voltage

From the integral form of (2.47), the no-load flux linkage of the phase *b* can be represented using a Fourier series.

$$\lambda_{pm\_b}\left(x_m\right) = \frac{4B_\delta D_s N_b P_{avg} T_p}{\pi}\sum_n \frac{N_n B_n}{n}\sin\left(\frac{n\pi}{T_p}x_m\right) \tag{2.83}$$

where N_b is the number of turns per winding, B_n is the Fourier coefficient of the air-gap flux density distribution function is described as

$$B_n = \frac{8\sin\left(n\pi/2\right)}{n\pi}\cos\left(\frac{n\pi\left(T_p - T_m\right)}{2T_p}\right)\Bigg/\left(\frac{n\pi\left(T_p - T_m\right)}{2T_p}\right), \tag{2.84}$$

the winding factor N_n for the superimposed rectangular winding function is given as

$$N_n = \sin\left(\frac{n\pi T_s}{2T_p}\right)\cos\left(\frac{n\pi\alpha_s}{2T_p}\right)\sin\left(\frac{n\pi T_{so}}{2T_p}\right)\Big/\left(\frac{n\pi T_{so}}{2T_p}\right), \tag{2.85}$$

and P_{avg} is the unitless average value of the relative permeance function of the slotted stator, which is given as

$$P_{avg} = \frac{1}{T_p}\int_{-T_s/2}^{T_s/2} P(x_s)\,dx_s = 0.8037 \tag{2.86}$$

where the relative permeance function $P(x_s)$ is described in (2.82)–(2.86). The phase-to-neutral back-EMF of the phase *b* can be derived through differentiating the no-load flux linkage in (2.83) for the mover displacement x_m with respect to time as follows.

$$e_{phase}(x_m) = 4B_\delta D_s N_b P_{avg} V_m \sum_{n=1} N_n B_n \cos\left(n\pi x_m / T_p\right) \tag{2.87}$$

where V_m [m/s] is the mover speed. The voltages induced in other phases are shifted by ±120° electrically from phase *b*.

2.4.3 Simplified Nonlinear Magnetic Equivalent Circuit

Unlike the MEC model in Section 2.3.2, the half flux-path models in the dashed boxes of Figs. 46(a) and (b) can be used according to the no-load and electrical load conditions, respectively. Since the flux path due to the armature current is partially different from that of the PM, it is not easy to apply a single circuit model. Therefore, the flux values under the no-load condition in Fig. 46(c) are calculated according to the design parameters, and then the stator tooth flux Φ_1 is used as the initial value to compute the ingoing flux Φ_3 into the stator tooth under the electrical load condition of Fig. 46(d). The factor 2 is presented since the reluctance is doubled from the half-sided model. All

reluctances in the stator and mover cores are defined as the variable reluctances according to the B-H curves shown in Fig. 47.

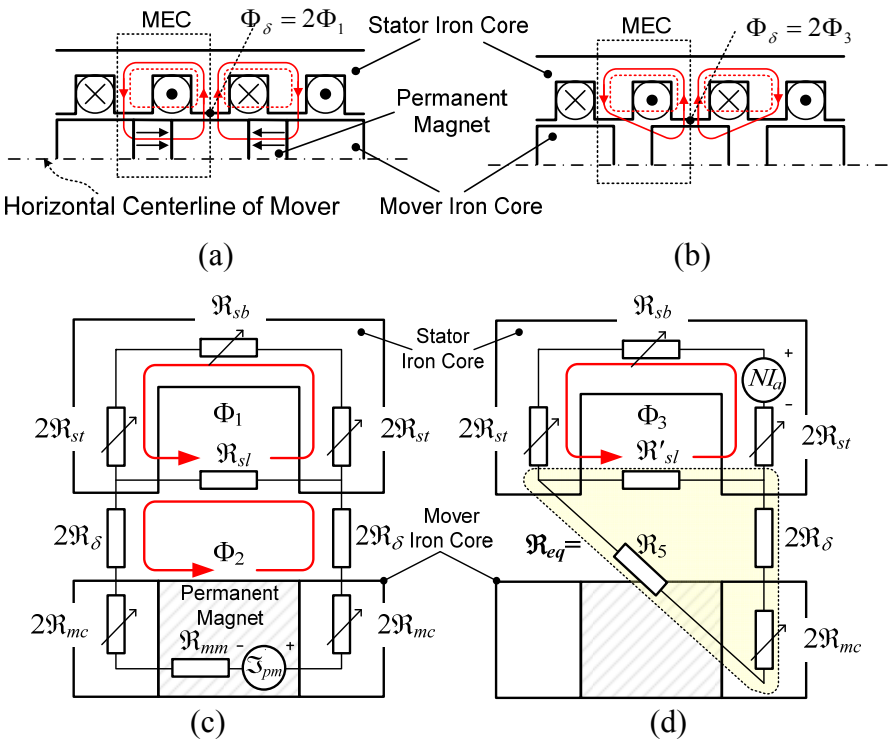

Fig. 46. Flux paths of the single-sided models due to (a) PM and (b) armature current when the *d*-axis is aligned with the stator tooth centerline of phase *b*. Corresponding simplified nonlinear MEC models under (c) the no-load condition and (d) the electrical load condition.

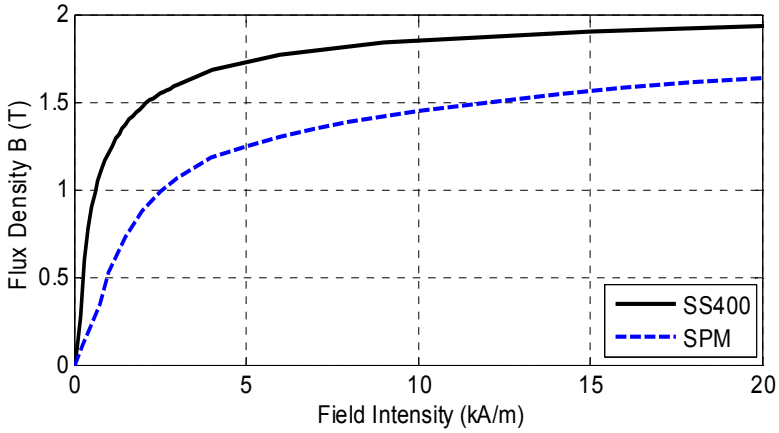

Fig. 47. B-H curves of the SS400 and SPM.

From the simplified MEC model of Fig. 46(c), the fluxes in the stator and mover cores under the no-load condition can be written as a reluctance matrix and the magnetomotive forces (MMFs) generated due to the PM as follows.

$$\mathbf{\Phi} = \begin{bmatrix} \Phi_1 \\ \Phi_2 \end{bmatrix} = \mathbf{A}_\mathbf{R}^{-1} \begin{bmatrix} 0 \\ \Im_{pm} \end{bmatrix} \tag{2.88}$$

where the reluctance matrix $\mathbf{A_R}$ is given as

$$\mathbf{A}_\mathbf{R} = \begin{bmatrix} \Re_{sb} + 4\Re_{st} + \Re_{sl} & -\Re_{sl} \\ -\Re_{sl} & 4\Re_{\delta} + 4\Re_{mc} + \Re_{mm} + \Re_{sl} \end{bmatrix} \tag{2.89}$$

and $\Im_{pm}$ is the MMF of the PM which is given as

$$\Im_{pm} = \frac{B_r T_m}{\mu_0 \mu_m} \tag{2.90}$$

where B_r is the residual flux density, μ_o is the permeability of free space, and μ_m (= 1.05) is the relative permeability of the PM on the recoil line on its B-H curve. From the simplified MEC model of Fig. 46(d), the incoming flux into the stator tooth is given as

$$\Phi_3 = \frac{NI_a}{\Re_{eq} + 4\Re_{st} + R_{sb}} + \Phi_1 \tag{2.91}$$

where N is the number turns of a winding, I_a is the magnitude of the armature current, and $\Re_{eq}$ is written by

$$\Re_{eq} = \Re'_{sl} \left(2\Re_{\delta} + 2\Re_{mc} + \Re_5 \right) / \left(\Re'_{sl} + 2\Re_{\delta} + 2\Re_{mc} + \Re_5 \right) \tag{2.92}$$

where $\Re_5$ is the inverse of P_5. Unlike (2.24), the reluctance of the PM is redefined in order for the calculation convenience as

$$\Re_{mm} = \frac{T_m}{0.775 \mu_0 \mu_m H_m D_m} \tag{2.93}$$

The factor 0.775 was introduced to describe the effective contact face area reduced due to the PM with the H-shaped cross-section and all round edges with the radius of about 0.5 mm. Likewise, the slot leakage reluctances are also redefined by

$$\Re_{sl} = \frac{T_{so}}{2\mu_0 H_t D_s} \quad \text{and} \quad \Re'_{sl} = \frac{N^2}{L_u} \tag{2.94}$$

where the open-slot width T_{so} is $T_s - T_t$. The mover iron core, stator tooth, stator back-iron reluctances are written as

$$\Re_{mc} = \frac{\pi}{16\mu_0 \mu_{cm} D_m} \tag{2.95}$$

$$\Re_{st} = \frac{H_s + H_t}{2\mu_0 \mu_{cs} T_t D_s} \tag{2.96}$$

$$\Re_{sb} = \frac{T_s}{\mu_0 \mu_{cs} \left(H_s - H_t\right) D_s} \tag{2.97}$$

where μ_{cm} and μ_{cs} are the variable relative permeabilities of the mover and stator cores, respectively. The flux densities in the stator tooth under no-load and electrical conditions can be calculated by, respectively,

$$B_{s1} = \frac{2\Phi_1}{T_t D_s} \quad \text{and} \quad B_{s3} = \frac{2\Phi_3}{T_t D_s} \tag{2.98}$$

The relative permeance values of the stator and mover cores are updated using (2.98) by the B-H curves of the corresponding materials. Finally, the air-gap flux density of the incoming stator tooth flux can be calculated as

$$B_\delta = 2\mu_0 \Re_\delta \Phi_3 / \delta \quad . \tag{2.99}$$

2.4.4 Magnetic Field Analysis

Since the magnetizing thrust force of (2.68) is determined by the no-load flux linkage and armature current, the magnetic-field analysis for the ingoing flux into the stator tooth is very important. Fig. 48 shows that the SPM prototype has lower flux values than those of the base model prototype when the SPM prototype has the same dimensions as the base model prototype. Moreover, this flux difference increases as the armature current increases. This prediction indicates that the design parameter modification is needed to produce the same or more thrust force than the base model prototype. Thus, the following constraints are made for the magnetic-field analysis of the SPM prototype: (1) the step-shaped end frame does not change, (2) the same slot pitch (= 0.012 m) and pole pitch (= 0.018 m) as those of the base model are employed to obtain the similar detent force, and (3) the open-slot width of larger than the minimum of 0.003 m is used.

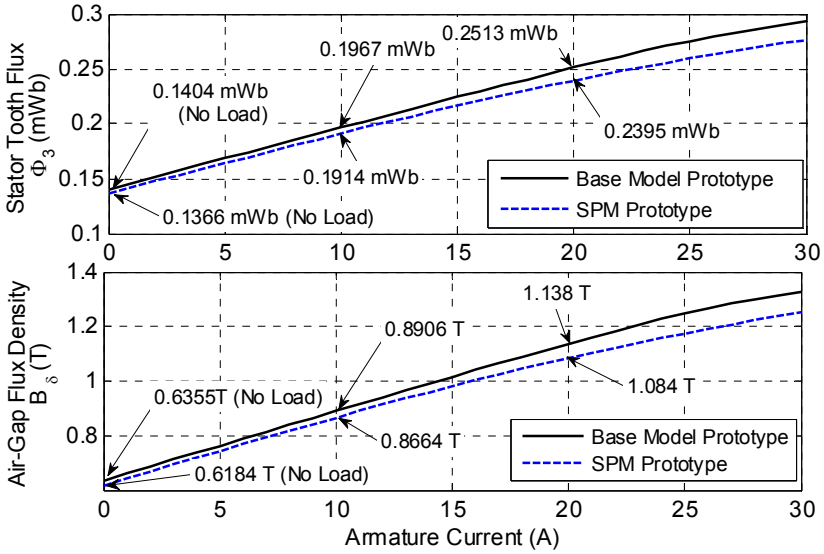

Fig. 48. Stator-tooth flux curves (top) and air-gap flux density curves (bottom) according to the armature current.

2.4.4.A Analysis for PM and Stator Tooth Widths

According to the given design constraints and machinability of the PM and SPM materials, the possible mechanical dimensions for the stator tooth and PM widths can be given by

$$0.005 \le T_t \le 0.009 \text{ and } 0.003 \le T_m \le 0.015 \text{ [m]}. \quad (2.100)$$

The flux contour plot in Fig. 49 illustrates that the extended PM width increases the stator tooth flux. If the tooth width is larger than 0.007 m in terms of the same PM width, the tooth flux is rather decreased by the reduction of the applied total current amount. Thus, if the stator tooth and PM widths are chosen depending on the required power consumption in the optimal region, the SPM prototype becomes to obtain much larger stator tooth flux than the base model prototype under the same electrical load condition of 10 A. This indicates that the base model is not fully optimized neither with respect to the magnetic field. The same or higher flux than that of the base model can also be achieved through other design parameter optimization methods

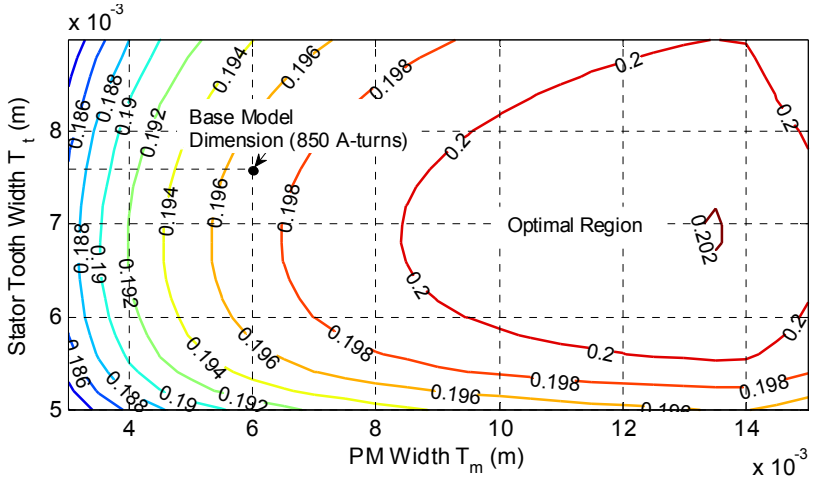

Fig. 49. Stator-tooth flux Φ_3 (mWb) contour plot according to the PM and stator tooth widths when I_a = 10 A.

2.4.4.B Analysis for Height of PM and Mover Core

The MEC analysis according to the PM height in Fig. 50 shows that when the stator tooth and PM widths have the same dimensions as the base model prototype, the stator tooth fluxes in two different loads except the 20-A electrical load achieve larger values than those of the base model prototype if the PM height increment of more than 0.0004 m is employed. However, unlike the previous method presented in Section *2.4.4.A* this approach resulted in the 5.0% mover weight increment due to the increased mover volume in order to produce the same thrust force.

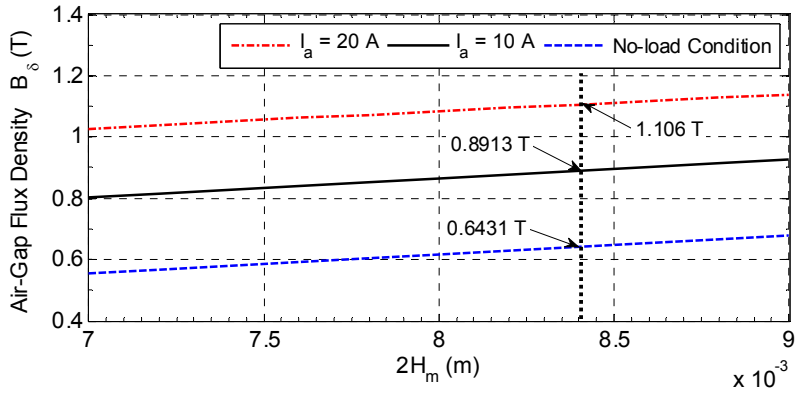

Fig. 50. Air-gap flux density curves according to the PM height for the three different load conditions when T_m = 0.006 m and T_t = 0.0076 m.

2.4.4.C Analysis for Air Gap

The air-gap size analysis in Fig. 51 illustrates that when the air gap of 0.0009 m is used, the air-gap flux density can be increased for two load conditions except the 20-A electrical load condition as compared with the flux density of the base model prototype shown in the bottom plot of Fig. 5. This implies that the SPM prototype will produce the same or more thrust force than that of the base model prototype under the electrical-load

condition of less than 10 A. The air-gap size adjustment can be achieved without the mover's weight increase or the use of the newly sized PM and mover cores.

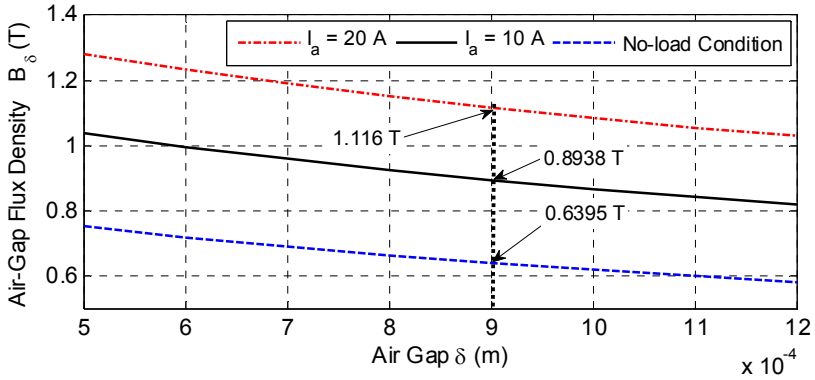

Fig. 51. Air-gap flux density curves according to the air-gap size for the three different load conditions when T_m = 0.006 m and T_t = 0.0076 m.

2.4.4.D Analysis for Back Iron Height

The back-iron height H_b (i.e. $H_s - H_t$) analysis in Fig. 52 shows that the air-gap flux density of the SPM prototype is hardly increased in the height of larger than 0.004 m, and cannot be larger than that of the base model prototype. Therefore, this approach is not an effective way to increase the magnetic field capability.

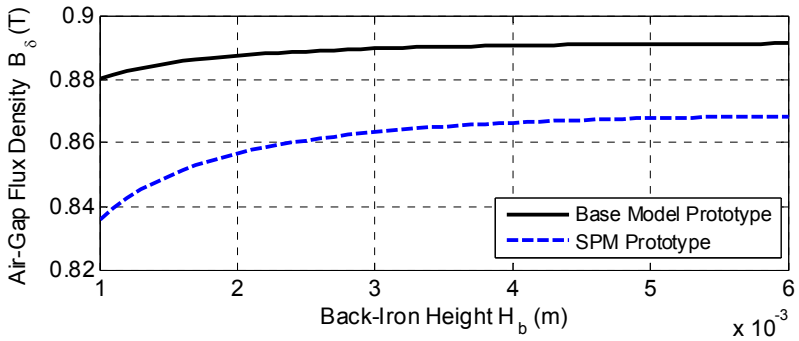

Fig. 52. Air-gap flux density variation curve in the mover core according to the back-iron height under the 10-A electrical load condition when T_m = 0.006 m and T_t = 0.0076 m.

From the magnetic-field analysis using the MEC, it is found that the relatively low magnetic field performance of the SPM can be improved through modifying various design parameters in the buried-type PM linear motor using a limited armature current. In this paper, although the analysis results indicate that the method in Section *2.4.4.A* can have the further improved magnetic field than the method in Section *2.4.4.C* with no increase of the weight or volume, the reduced air-gap size of 0.0009 m that can reuse the PMs of the base model is employed in terms of cost saving and detent force suppression.

2.4.5 Loss Analysis and Thermal Consideration

The iron loss is generally expressed as a form of the sum of the hysteresis loss P_h and eddy-current loss P_e. The hysterectic loss originated from the residual energy during the energy exchange by the applied current. The eddy current loss is generated by the magnetic flux density changing in the core due to the PM. Since the SMC material does not use the lamination unlike the conventional electrical steel, the total iron loss of the SMC material is

$$P_{iron} = P_h + P_e = K_h B_s^a f + K_e B_s^2 f^2 \quad \text{[W/kg]} \tag{2.101}$$

where a varies in the range from 1.5 to 2.5, f is the operating frequency, and K_h and K_e can be empirically determined. From Table II, K_h, K_e, and a can be evaluated as 0.092, 0.000058, and 1.6, respectively.

Table 9. Iron loss per kilogram of the SPM [58].

Flux Density (T)	FREQUENCY (HZ)									
	50	**60**	**100**	**200**	**300**	**400**	**500**	**600**	**700**	**800**
0.5	1.5	1.8	3.1	6.6	10	14	18	23	27	32
1.0	4.9	5.9	10	21	34	47	61	75	91	105
1.5	9.3	11	19	44	71	102	132	166	202	241

On the other hand, the copper loss is governed by the winding resistance and the magnitude of the phase current regardless of its operating frequency. From (2.40), the copper loss in the balanced three-phase operation can be written as

$$P_{cu} = (3/2) I_a^2 R_c \left(1 + \alpha_{25}(T - 25)\right) \quad [\mathrm{W}] \tag{2.102}$$

where I_a is the magnitude of the phase current.

Assuming that the thermal contact resistance between the stator tooth and the coil is negligible, they have the same temperatures in steady state. The dissipation capability of the winding-stator assembly can be expressed with the sum of the iron and copper losses as

$$hA_{es}\Delta T = m_s P_{iron} + P_{cu} \tag{2.103}$$

where h is the average natural convection coefficient, m_s is the SPM stator mass, A_{es} is the effective dissipation surface area exposed to the air, and ΔT is the temperature rise of the winding-stator assembly. Thus, the steady-state temperature according to the phase current can approximately be formulated using (2.98) and (2.101)–(2.103) as

$$T_{ss} = \frac{m_s \left(K_h \left(B_s(I_a)\right)^{1.6} f + K_e \left(B_s(I_a)\right)^2 f^2\right) + (3/2) I_a^2 R_a}{hA_{es} - \alpha_{25}(3/2) I_a^2 R_a} + 25 \tag{2.104}$$

where $B_s(I_a)$ is the flux density function of (2.98), h is empirically obtained from the temperature measurement in the stator winding assembly as

$$h \cong 16.1 \text{ [W/m}^2\text{-°K]}, \tag{2.105}$$

A_{es} is calculated as

$$\begin{aligned} A_{es} \cong\ & 2L_sD_s + 2(L_s + D_s)H_s + 2(L_a + D_s)H_a \\ & + 2(L_{ss} - L_s)(H_s + D_{ss}) - 6(2H_t + D_s)(T_s - T_t) \\ & + 3\left(2(H_c + W_o)(L_o - D_s) + 2D_s(T_s - T_t) + 2W_oH_c\right), \end{aligned} \tag{2.106}$$

and m_s is given as

$$m_s \cong \rho_s\left(L_sD_sH_s + (L_{ss} - L_s)D_{ss}H_s - 6(T_s - T_t)D_sH_t\right) \tag{2.107}$$

where ρ_s is the mass density of the SPM (= 7300 kg/m^3). The steady-state temperature prediction in Fig. 53 indicates that when the maximum permissible temperature is 100°C, the maximum continuous-rated current can be 2.4 A at 30 Hz. Although these predicted results do not include the convection coefficient variation Δh according to the mover motion, the ratio of the iron loss to the total loss in (2.103) does not change because this varying coefficient is evenly applied in the total loss. The iron-loss ratio in the bottom plot of Fig. 53 shows that the iron loss is not critical in the perspective of the permissible temperature limit. Although the hysteretic loss of the SMC material is relatively larger than that of the laminated thin steel, as compared with the copper loss, the iron loss is not the major concern in a small-size lightweight IPM-FLBM operating at a low frequency of less than 30 Hz.

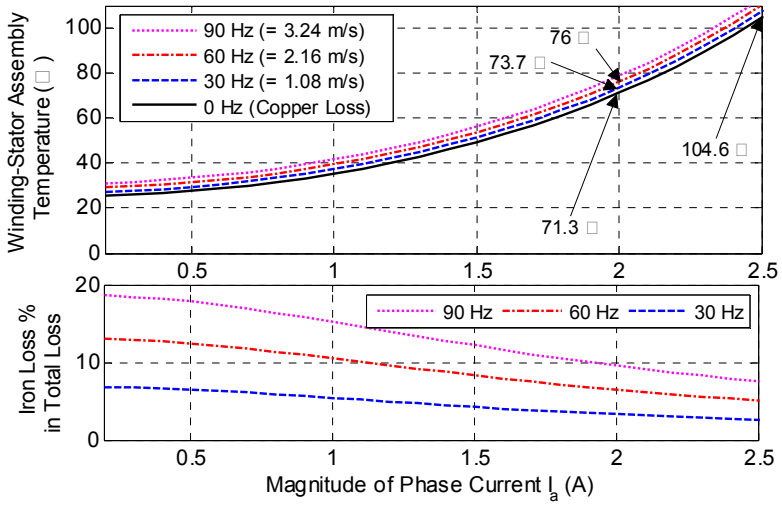

Fig. 53. Steady-state temperature responses (top) and iron loss ratios (bottom) of the stator-winding assembly according to the phase current and operating frequency under the natural convection condition when A_{es} = 0.0079 m^2 and m_s = 0.0936 kg.

2.4.6 Steady-State Performance Validation

Fig. 54 shows that although the measured phase-to-neutral back-EMF voltages are slightly more distorted than those of the analytic solutions by the third harmonic term, they are in good agreement with the predicted ones. The back-EMF constant is estimated as 3.81 V-s/m per phase.

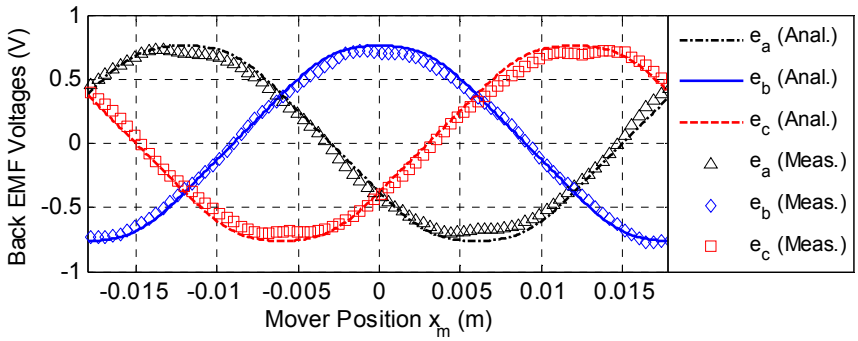

Fig. 54. Analytic and measurement results of the back-EMFs for each phase when the mover has the linear speed of 0.2 m/s.

The inductances were measured using the 1.0-A current source at 60 Hz. The self-inductance distributions in Fig. 55 illustrate that each inductance has its maximum value whenever the *q*-axis is aligned with the resultant phase axis. Since the analytic solution assumes the permeance of the core as infinite, they seem to have 3% larger values than the measured inductances in their maximum amplitudes. Especially, these measured inductances are almost the same as those of the base model using the electrical solid steel and the air gap of 0.001 mm. This points out that the self-inductances do not much increase although the air gap is reduced to be 0.0009 m.

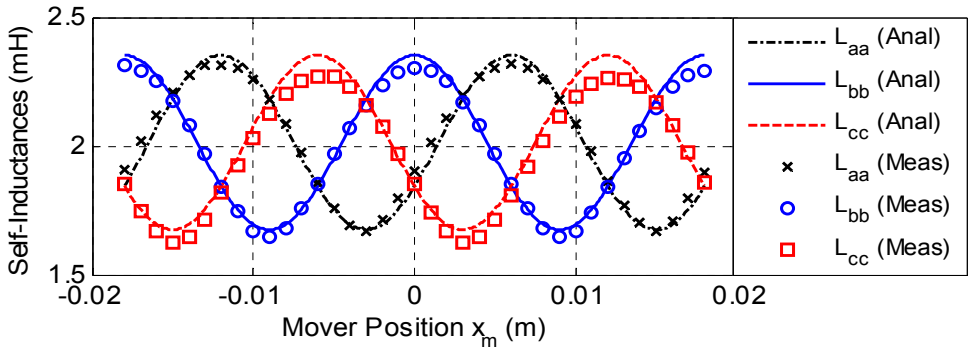

Fig. 55. Self-inductance distributions of the SPM prototype according to positions

The mutual inductances in Fig. 56 show that although the amplitudes of the analytic solutions for L_{ba} and L_{cb} are twice than measured ones, their average values in Table III are very small as expected, and their trends are in good agreement with the analytic ones. This implies that the mutual inductances can be ignored in the buried-type IPM motor with the alternate teeth windings and large longitudinal air gap. Table 10 shows that the analytic inductance models are well established.

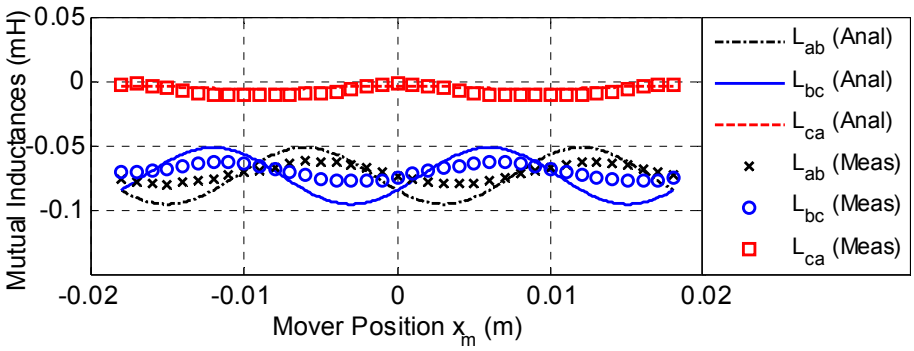

Fig. 56. Mutual inductance distributions of the SPM prototype according to positions.

Table 10. Average inductances of the SPM and base model prototypes.

	L_{aa}	L_{bb}	L_{cc}	L_{ab}, L_{ba}	L_{bc}, L_{cb}	L_{ac}, L_{ca}
SPM calculated (mH)	2.015	2.015	2.015	–0.074	–0.074	–0.005
SPM measured (mH)	2.022	2.006	1.973	–0.070	–0.070	–0.007
SS400 measured (mH)	2.034	2.042	1.975	–0.065	–0.067	–0.019

The results in Fig. 57 illustrate that the thrust force profile of the SPM prototype is slightly larger than that of the base model prototype. This implies that the magnetic flux has been increased by the reduced air gap. Although the developed reluctance force is not significantly large because of the small difference between the *d*- and *q*-axis inductances, the maximum thrust force can be achieved when the phase current leads the *q*-axis current by around 15°. The analytic magnetizing force term of (2.68) was computed using the maximum no-load flux linkage (≅ 22 mWb-turns) obtained from (2.83), and the analytic reluctance force was calculated using the *d*- and *q*- axis inductances (L_d = 1.676 mH and L_q = 2.352 mH) obtained from the maximum and minimum values of (2.78). Herein, the reluctance force was predicted as around 19% of the magnetizing force. The analytic total thrust force for the SPM prototype was estimated

as 3 % less than both measurement results. The residual flux density of the actual PM seems to be slightly higher than the analytic model.

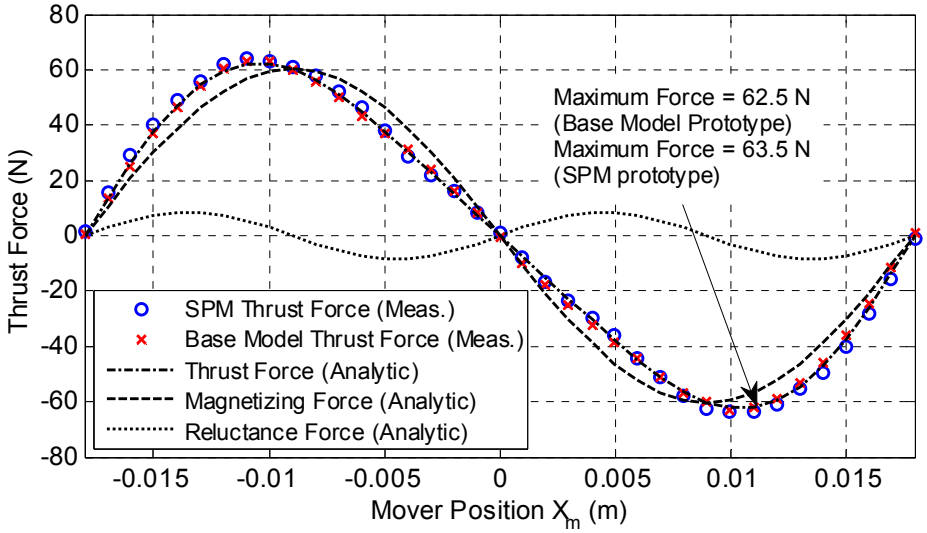

Fig. 57. Steady-state thrust forces of the SPM and base model (SS400) prototypes according to the mover positions when I_a = 8.66 A, I_b = 0 A and I_c = –8.66 A.

Unlike the conventional rotary motor, the detent force in an iron-core PM linear motor has not only the cogging force but also the end-effect force. This detent force is one of the causes of the force pulsation. The top and bottom plots in Fig. 58 show the steady-state thrust forces in the base model and SPM prototypes according to the mover positions when I_q = 10 A and I_d = 0 A, and the detent forces when I_q = I_d = 0 A, respectively. The average steady-state thrust forces of the SPM prototype are slightly improved as compared with those of the base model prototype, and the detent force is also slightly increased due to the reduced air-gap in the SPM prototype. Table 11 shows the steady-state performance comparisons between the two prototypes for the measurements and analytic solutions.

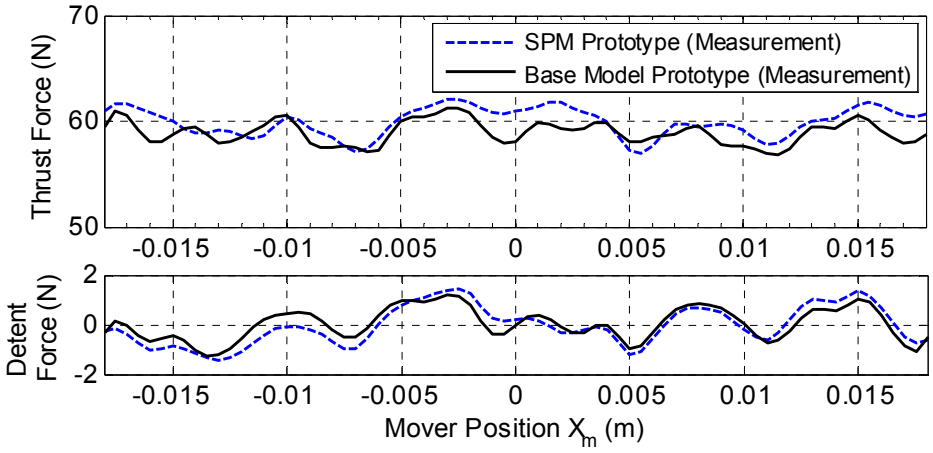

Fig. 58. Steady-state forces (top) and detent forces (bottom) of the SPM and base model (SS400) prototypes according to the mover positions when I_{qs} and I_{ds} are controlled as 10 A and 0 A, respectively.

Table 11. Performance comparison of the SS400 and SPM prototypes.

	Base Model	**SPM**
Thrust force in the field-oriented control (N)	58.9 (57.1)	59.8 (57.6)
Thrust force in the maximum force control (N)	62.5 (59.2)	63.5 (60.7)
Peak-to-peak detent force (N)	2.4	2.8
Ripple force due to the detent force (%)	4	4.7
***q*-axis inductance (mH)**	2.322 (2.277)	2.338 (2.352)
***d*-axis inductance (mH)**	1.685 (1.611)	1.671 (1.676)
Air gap (m)	0.001	0.0009

*( ) is the analytic solution

The transient response of the temperature rise due to the instantaneous current is important to determine the stall current defined when the speed of the mover is zero under a full-load condition. In addition, since there is no motion, the copper loss can be considered the only heat source in the natural convection condition. The measured temperature responses in Fig. 59 illustrate that when the phase current of 10 A is applied, the temperature reaches 100°C within 29 s. This implies that if the stall current is defined

as 10 A when the speed of the mover is zero under the full-load condition, the corresponding operating time should be less than 29 s in order to protect the winding insulator. The steady-state temperature for the phase currents of 2.5 A at around 2600 s is agreement with the prediction of Fig. 53. Since the temperature according to the operating frequencies of the phase current of 2.0A did not reach the steady state responses, the temperature difference per 30-Hz increment was measured as around 1.5°C. Although the difference is less than the prediction of Fig. 53, this result indicates that the iron loss is not critical in lightweight SMC motor. Table 12 summarizes the thermal conductivities of the materials between the winding and stator in this paper.

Table 12. Thermal conductivity and material thickness.

Materials	Path thickness L_n (mm)	THERMAL CONDUCTIVITIES K_N (W/(M-K))	MAXIMUM ALLOWABLE TEMPERATURE (°C)
Polyurethane	0.0178	0.03	155
Thermal compound	0.2500	8.50	180
Kapton	0.0500	0.42	285

.

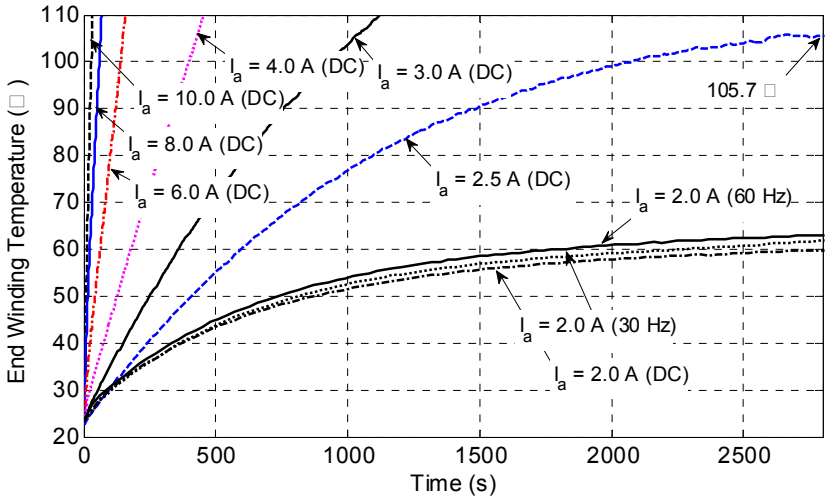

Fig. 59. Temperature responses in the end winding of the stator-winding assembly according to the magnitude of the phase current.

CHAPTER III

OPTICAL POTENTIOMETER[2]

In Chapter III, firstly, the nature of light and the terminologies for its optical properties are briefly introduced. In the following sections, the fundamental theories and properties for the LED and PD are introduced in order to understand the new optical potentiometer in this study. The basic sensing mechanism of this optical potentiometer is presented. The dynamic and steady-state models of the sensor are also discussed. The specific patterns and various color tracks are investigated to generate the reflected power that is directly proportional to physical displacement through the optimal designs. Finally, its performance verification as a feedback sensor in the rotary position-control system are discussed.

3.1 Light and Its Terminologies

3.1.1 Light

Before discussing optoelectronic device, it is essential to understand the fundamental nature of light. Light is a type of electromagnetic wave like radio wave. This wave consists of the time varying electric and magnetic fields propagating through space.

---

[2] ⓒ 2014 IEEE. Reprinted in part with permission from "Development of a new high resolution angle sensing mechanism using an RGB sensor," by Y. S. Kwon and W. J. Kim, *IEEE/ASME Trans. Mechatronics*, vol. 19, no. 5, pp. 1707–1715, Oct. 2014.

According to its wavelength, this can be divided into high frequency (HF), medium frequency (MF), low frequency (LF), and very low frequency (VLF). These electromagnetic waves have the characteristics of both waves and particles (photons). The photoelectric effect when light illuminates onto a substance is one example of particle property of light. The energy of one photon at a certain frequency is given by

$$E = h\upsilon = hc/\lambda \tag{3.1}$$

where h is the Planck's constant (= 6.626×10^{-34} Js), ν is the frequency of light (Hz), c is the speed of light in vacuum (= 2.998×10^{8} m/s), and λ is the wavelength (m). The light level can be expressed by the number of photons per one second using

$$W = N_{pt}E = N_{pt}h\upsilon = Nhc/\lambda \tag{3.2}$$

where W is the light level, and N_{pt} is the number of photons per second.

3.1.2 Radiometry and Photometry

Table 13. Photometric and corresponding radiometric unit.

Light Level Condition	**Photometric Unit**	**Dimension**	**Radiometric Unit**	**Dimension**
Total radiant energy emitted from a light source	Luminous flux (Φ_v)	lm	Radiant flux (optical power) (Φ_e)	W
energy emitted from a point light source per unit solid angle	Luminous intensity (I_v)	lm/sr = cd	Radiant intensity (I_e)	W/sr
Luminous and radiant flux incident on a surface.	Iluminance (E_v)	lm/m^2 = lux	Irradiance (power density) (E_e)	W/m^2
Luminous or radiant flux per unit solid angle per unit projected source area	Luminance (L_v)	$\frac{lm}{sr\cdot m^2}=\frac{cd}{m^2}$	Radiance (L_e)	$\frac{W}{sr\cdot m^2}$

The properties of light are generally characterized by two types of units−radiometric and photometric. In contrast, the radiometric units characterize light in terms of physical quantities such as optical power. The photometric units are characterized on the basis of perception by a human being. According to the SI Unit, the definition of luminous intensity is the optical power of 1/683 W at the wavelength of 555 nm into the solid angle of 1 steradian (sr) is 1 cd. Table 13 shows the definitions of the radiometric and photometric units.

Understanding the technical terminologies for the optical measurement is a prerequisite of studying the optical potentiometer. Thus, the physical meaning of the fundamental terminologies are presented as follows:

- *Luminous flux* (Φ_v) *and radiant flux* (Φ_e): as the definitions for the optical power (P_t) in the photometric and radiometric units, the luminous flux's unit is lumen and the radiant flux's unit is watt. Hence, radiant flux can be called as optical power. The relation between two quantities is given by

$$\Phi_v = 683\frac{\text{lm}}{\text{W}}\int_\lambda V(\lambda)P(\lambda)d\lambda \quad [\text{lm}], \qquad \Phi_e = \int_\lambda P(\lambda)d\lambda \quad [\text{W}] \tag{3.3}$$

  where $V(\lambda)$ is the eye sensitivity function, $P(\lambda)$ is the power spectral density, and the prefactor 683 lm/W is a normalized factor.

- *Luminous efficacy* (η_v): is defined as the conversion efficiency from optical power to luminous flux.

$$\eta_v = \Phi_v/\Phi_e = \left[683\frac{\text{lm}}{\text{W}}\int_\lambda V(\lambda)P(\lambda)d\lambda\right] \Big/ \left[\int_\lambda P(\lambda)d\lambda\right] \quad [\text{lm/W}] \tag{3.4}$$

- *Solid angle* (Ω): is the ratio of a portion of the area on the surface of a sphere to the square of the radius r of the sphere. For instance, the solid angle of circular cone is $2\pi(1-\cos\theta) = 4\pi\sin^2(\theta/2)$.

$$d\Omega = \frac{dA}{r^2} \quad [\text{sr}] \tag{3.5}$$

- *Luminous intensity* (I_v) *and radiant intensity* (I_e): are defined as luminous flux per unit solid angle and optical power per unit solid angle, respectively, and both quantities don't depend on the distance.

$$I_v = \frac{d\Phi_v}{d\Omega} \ [\text{lm/sr or cd}], \quad I_e = \frac{d\Phi_e}{d\Omega} \ [\text{W/sr}] \tag{3.6}$$

- *Illuminance* (E_v) *and Irradiance* (E_e): are defined as luminous flux and radiant flux per square meter, respectively. These are also inversely proportional to the square of the distance from the light source.

$$E_v = \frac{d\Phi_v}{dA_s} [\text{lm/m}^2], \quad E_e = \frac{d\Phi_e}{dA_s} [\text{W/m}^2] \tag{3.7}$$

- *Luminance* (L_v) *and Radiance* (L_e): are defined as luminous flux and radiant flux per unit steradian and square meter, respectively. This quantity plays a special role in optics because it is the propagation of the radiance that is conserved in a lossless optical system

$$L_v = \frac{\mathrm{d}}{\mathrm{d}\Omega}\left(\frac{\mathrm{d}\Phi_v}{\mathrm{d}A_s}\right) [\text{lm/sr-m}^2], \quad L_e = \frac{\mathrm{d}}{\mathrm{d}\Omega}\left(\frac{\mathrm{d}\Phi_e}{\mathrm{d}A_s}\right) [\text{W/sr-m}^2] \tag{3.8}$$

- *Reflectance* (ρ)*:* are defined as the ratio of incident radiant flux to the reflected radiant flux. This term is related to the material properties.

$$\rho = \Phi_{ei} / \Phi_{er} \tag{3.9}$$

- *Projection Area*: Area of surface element dA as viewed from an angle θ.

3.2 Optoelectronic Devices

Optoelectronics is a terminology involving both electronics and optics. It can be defined as the study for electronic devices interacting with light. Thus, LED and the PD can be defined as primary components in optoelectronics. Fig. 60 shows the typical optoelectronic devices that are easily available in market.

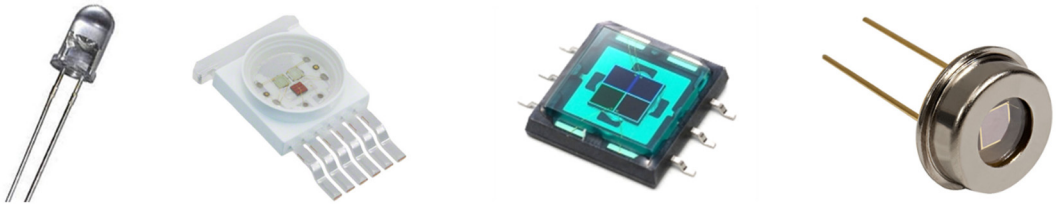

Fig. 60. Light emitting diodes and photo diodes: (a) Precision optical Performance Red color LED (HLMP-EG08_YZ000, Avago Technology), (b) High power Tri-Color LED (Moonstone, Avago Technology), (c) Red-green-blue (RGB) Photodiode (S7505-5, Hamamatsu, and (d) Gap Photodiode (FGAP71, ThorLabs.

3.2.1 Light-Emitting Diodes (LEDs)

An LED is a diode that convert electrical energy into light energy. Most high-intensity LEDs use the heterojunction rather than homojunction in order to have much higher carrier in active region. LEDs are mainly used in the forward bias region of the *p-n* diode. Generally, when the forward-bias current flows in the silicon or germanium *p-n* junction diode, the recombination between the holes and electrons gives off most of

energy as a form of heat. On the other hand, the materials such as gallium arsenide phosphide (GaAsP) or gallium phosphide (GaP) emits a significant number of photons to create a visible light. Fig. 61 (a) and (b) show the LED electroluminescene mechanism of the standard structure and point source emitter structure, respectively.

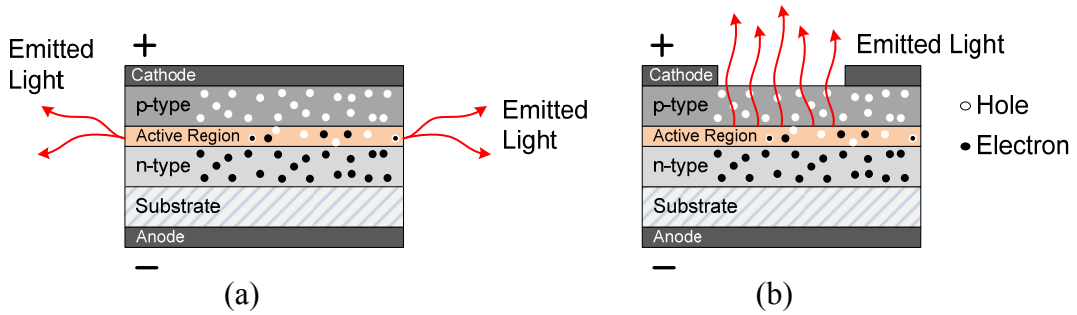

Fig. 61. LED electroluminescene mechanism: (a) standard structure and (b) point source. emitter structure.

In an ideal diode, assuming that every electron that injects into the active region can create a photon, the required energy to electron-hole recombination is equal to the phone energy of (3.1) according to energy conservation. Thus, the threshold voltage to drive the LED can be written as

$$h\upsilon = E \approx E_g = qV \quad \Rightarrow \quad V_{th} \approx \frac{E_g}{q} \tag{3.10}$$

For example, the drive voltage of the red LED with the wavelength of 650 nm can be evaluated as around 1.9 V ($= h\nu / q = hc/(\lambda q) = (6.626\times10^{-34})(2.998\times10^{8})/(650\times10^{6} \cdot 1.602\times10^{-19})$). Fig. 62 shows the forward voltage at a diode current of 20 mA versus bandgap energy of various LEDs made from different materials [59]. This plot illustrates

that the required forward voltages of most LEDs except LEDs based on nitrides are in good agreement with the expected solid line made by

$$I = I_S\left(e^{V/\eta V_T} - 1\right) \quad \text{for } V > -V_T \tag{3.11}$$

where V is the applied voltage, η is the emission coefficient of diode (Si: $\eta = 2$, Ge: $\eta = 1$), I_s is the reverse saturation current ($\approx 10^{-6}$ A at silicon), and V_T is the thermal voltage. This also indicates that the threshold voltages of the LEDs are higher than the pure *p*-*n* type diode as well as vary depending on its adding material.

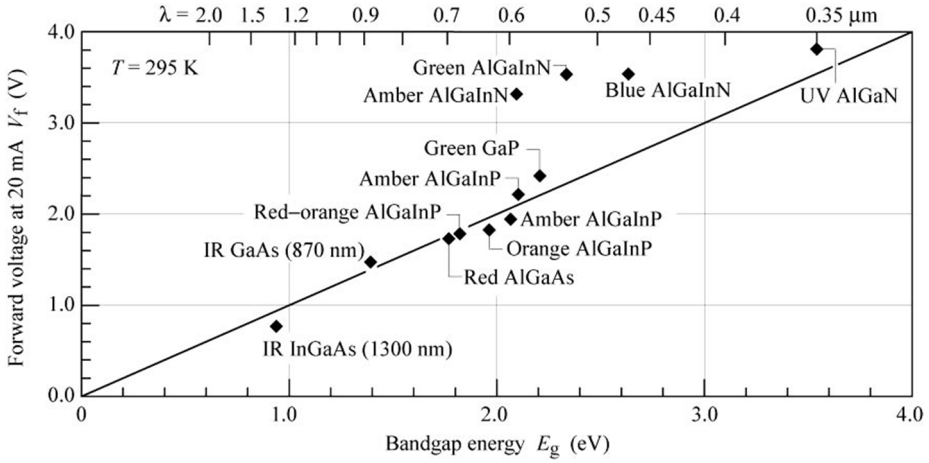

Fig. 62. Forward diode voltage versus bandgap energy of various LEDs using materials.

Photons generated in the active region should pass through two different mediums in order to emit the visible light. However, the internal reflection reduces the external efficiency significantly due to oblique and grazing-angle incidence. According to Snell's law, when a light ray travels from a higher refractive index medium into a lower refractive index medium, the emitted light can pass through the semiconductor-air interface only if

the angle of incidence of a light ray is less than the critical angle. Fig. 63 shows the critical angle and the definition of the escape cone for the point light source. Since the critical angle for the internal reflection is defined when the incidence of air is 90° as shown in Fig. 63(a), the critical angle can be given as the below from the Snell's law.

$$\bar{n}_s \sin\varphi_c = \bar{n}_a \sin\varphi_a \;\Rightarrow\; \bar{n}_s \sin\varphi_c = \bar{n}_a \sin 90^\circ \;\Rightarrow\; \varphi_c = \sin^{-1}\left(\frac{\bar{n}_a}{\bar{n}_s}\right) \tag{3.12}$$

where $\bar{n}_s$ and $\bar{n}_a$ are the refractive indices of the semiconductor and the air, respectively, φ_c is the critical angle.

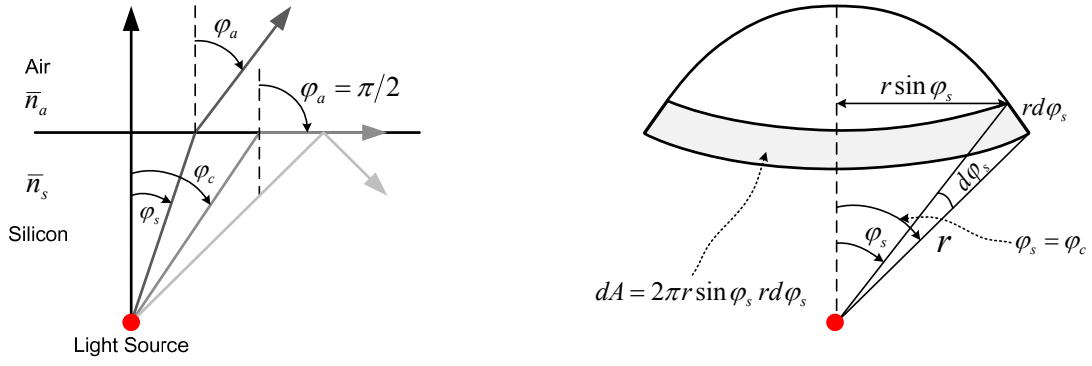

(a) (b)

Fig. 63. (a) Definition of the critical angle. (b) Area element of calotte-shaped surface of the sphere defined by radius r and the critical angle.

Assuming that the light source is a point-like source, the fractional power for the source power can be written as (3.13) using the thermal voltage (i.e. $V_T = kT/q$) and the area element described in Fig. 63(b). This equation implies that the only 4% optical power can escape from the semiconductor if the semiconductor refractive index is 2.5.

$$P_{esc} = P_{src}\frac{1}{4\pi r^2}\int dA = P_{src}\frac{2\pi r^2\left(1-\cos\varphi_c\right)}{4\pi r^2} = P_{src}\frac{\left(1-\cos\varphi_c\right)}{2} \;\Rightarrow\; \frac{P_{esc}}{P_{src}} \approx \frac{\bar{n}_a^2}{4\bar{n}_s^2} \tag{3.13}$$

The light extraction efficiency can be improved through the dome-shaped epoxy encapsulation. The refractive indices of typical epoxies have the range between 1.4 and 1.8 [59]. Therefore, assuming that all photons leave the semiconductor die, the optical power (radiant flux) emitted in air for the applied electric power can be computed as

$$P_t \approx \frac{\eta_{epx}}{4}\frac{\overline{n}_a^2}{\overline{n}_s^2} V_f I_f \ \text{[W]} \tag{3.14}$$

where η_{epx} is the efficiency of encapsulated dome, V_f and I_f are the applied diode voltage and current, respectively. For example, assuming that the red LED (AlGaAs) of Fig. 62 has the semiconductor refractive index of 2.5 and the extraction efficiency ratio for air of 2.25, the ideal optical power emitted in air can be expected as 3.24 mW when the forward current of 20 mA and the forward bias voltage of 1.8 V are applied. Since the forward DC resistance in the forward bias region of the *p*-*n* diode after the threshold voltage has the following relation

$$R_{dc} = V_f / I_f \,, \tag{3.15}$$

where the diode forward voltage and current in the steady-state conditions should be constant in order to keep the constant optical power. In case that a constant-voltage supply is used, however, the small variation of input voltage or temperature even causes a significant change because the diode current is the exponential function of the forward voltage due to the V-I characteristics curve of the *p*-*n* diode. When a constant-current source is used, it can be the best driving method if there are no temperature variations, but cannot avoid the decrease of the emission intensity due to non-radiative recombination if there are any temperature variations. Thus, theoretically, since the

constant-voltage source with an external series resistor can compensate for the change of forward voltage due to temperature variations through the load line on the I-V curve of the *p-n* diode, it can be the best way to keep the constant optical power for temperature variations.

Correct understanding for the optical specifications of LED is a prerequisite to select and employ the proper LED to meet its purpose. Thus, the definitions and meanings of the main optical specifications are introduced.

- *Luminous efficiency* (η_e), is defined in units of lm/W, and is given as luminous flux divided by the electrical input. The equation is given as

$$\eta_e = \Phi_v / P_e = \Phi_v / V_f I_f \ \text{[lm/W]} \tag{3.16}$$

  where V_f *and* I_f are the forward LED voltage and current. From (3.11) and (3.13). Since the optical power efficiency for the electrical input power can be computed as η_e / η_v, the optical power for electrical input power can be given as

$$P_t = \frac{\eta_e}{\eta_v} V_f I_f \approx \frac{\eta_{epx}}{4} \frac{\overline{n}_a^2}{\overline{n}_s^2} V_f I_f \ \text{[W]}. \tag{3.17}$$

- *Response time* (T_r) *and bandwidth* (BW): response time is defined as the rise time of light emission for a squared-wave pulse current. The bandwidth can usually be computed as $0.35/T_r$.
- *Viewing angle* ($\theta_{½}$): is the angle at which the light output is a half of the maximum output or a half of the maximum intensity. Fig. 64(a) shows its definition [59].
- *Spectral half width*: is defined as full width at half magnitude (FWHM) in emission spectrums of LEDs. Fig. 64(b) shows the definition of the spectral half width. The peak wavelength vary by the epitaxial material, and it determines its color emitted

from LED. The horizon axis on upper side of Fig. 62 also shows the corresponding wavelengths for various colors.

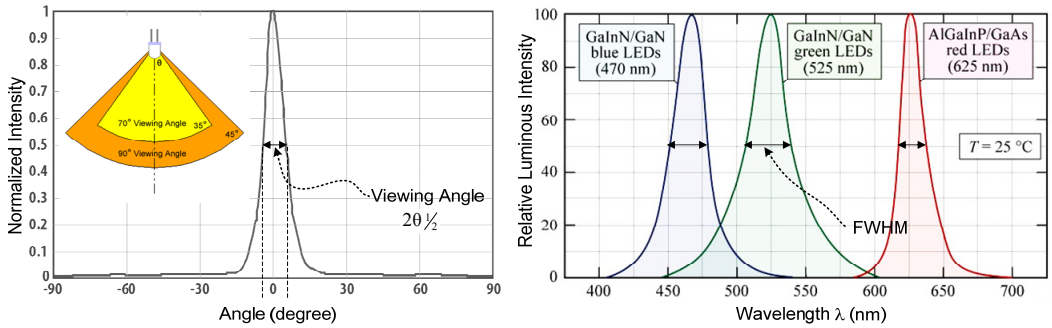

(a) (b)

Fig. 64. (a) Viewing angle, (b) Emission spectrum and FWHM.

3.2.2 Photo Diodes (PDs)

PD is a diode that generate a current from illumination. Unlike the LED that emit light through the hole-electron recombination in the active region under the condition of the forward bias, the PDs operate on the basis of the photoelectric effect that the free electron-hole pairs generated through absorbing photons produces a current through electric field in the reverse bias region. Fig. 65 shows the mechanism for the photoelectric effect.

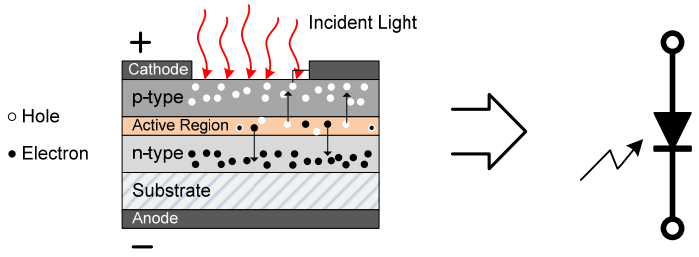

Fig. 65. Photoelectric current mechanism (left) and symbol of PD (right)

Fig. 66(a) shows the PD model using discrete circuit components. The circuit model includes the current source, the ideal diode, the dark resistance, the series resistance, and the junction capacitance. The current source I_P presents the current generated by the incident radiation. Since the dark (shunt) resistance has high value, its effect is little, and can be ignored. The series resistance determines the linearity in photovoltaic mode, but it can generally be ignored because of its small value. The capacitance C_D presents the stored charge effect of the PD junction. It is proportional to the diffusion area and inversely proportional to the width of the depletion width. Assuming that C_{D0} is the junction capacitance at zero bias (V = 0), the junction capacitance with respect to the reverse bias voltage is given by

$$C_D = C_{D0} \Big/ \sqrt{1 + V_R / \varphi_B} \tag{3.18}$$

where V_R is the reverse bias voltage and φ_B is the built-in voltage of diode junction [60]. The bandwidth of PD can be determined by the rise time t_r for the square waved light. The equation is given as

$$f_{BW} \cong 0.35 / t_r \ , \quad t_r = \sqrt{t_{dr}^2 + t_{dif}^2 + t_{RC}^2} \tag{3.19}$$

where t_{dr} is the charge collection time in depletion layer, t_{dif} is the carrier generation time outside of the depletion layer, and t_{RC} is determined by the terminal capacitance and load resistance. Since most of PDs have extremely high bandwidth (more than 1 GHz), although this capacitance is very important element that affects the dynamic performance of PD, it can also be ignored in the analysis for the steady-state I–V characteristics or low frequency applications. Thus, the simplified steady-state model of PD can be described as Fig. 66(b).

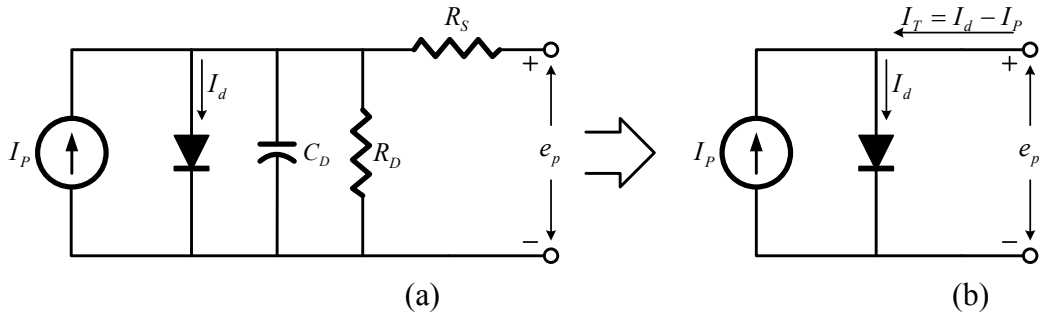

Fig. 66. (a) Equivalent circuit model of PD. (b) Steady-state model of PD.

For a given PD and wavelength, the responsivity r_ϕ of the PD is defined as a sensitivity of generated electrical current to input radiant flux as the below [61].

$$r_\phi = \frac{I_P}{\Phi_e} = (\text{Q.E.})\frac{q\lambda}{hc} \text{ [A/W]} \tag{3.20}$$

where Q.E. is the quantum efficiency. The spectral responsivity of the typical silicon PD shown in Fig. 67 reveals that its responsivity is a function of the incident wavelength as well as has relatively higher value as the wavelength increases.

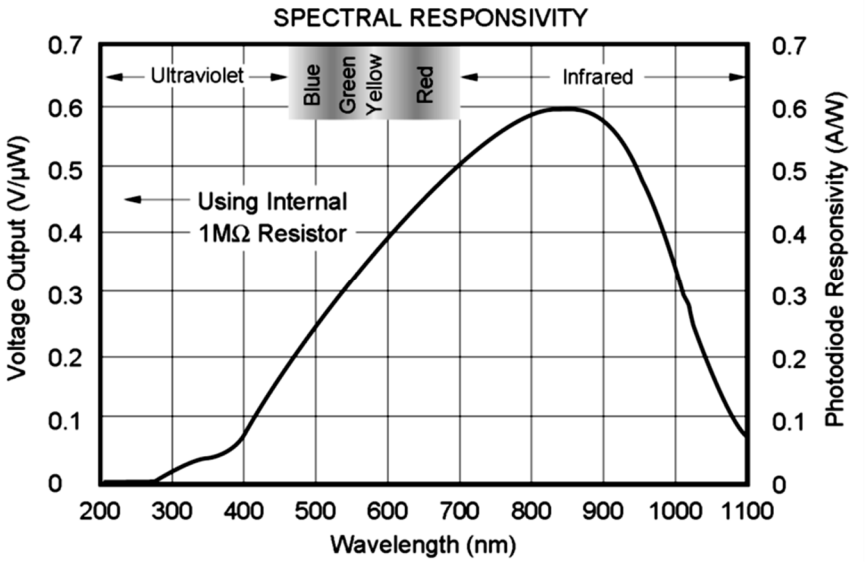

Fig. 67. Responsivity of silicon diode (OPA 101).

From the simplified model of Fig. 66(a), the current-voltage characteristic of a PD can be achieved as below by adding the photocurrent term to (3.11).

$$I = I_S\left(e^{V/\eta V_T} - 1\right) - I_P \tag{3.21}$$

The above equation can be defined as three states. The first state is that when the diode voltage is zero (= short circuit), the output current of PD becomes equal to the photo current ($I = I_P$). The second state is that when the reverse bias voltage is applied, the dark current becomes the reverse saturation current, and diode current becomes the sum of the dark current and photo current. The last is the case that the forward bias voltage is applied. The first case is called as the *photovoltaic mode* (PV). An operational amplifier with transimpedance configuration should be used to measure the photo current. This operation mode is usually used in low frequency applications (< 350 Hz), and is suitable for the ultra-low light condition. The right side in Fig. 68 describes the concept of the PV mode. The second case is named as the *Photoconductive mode* (PC). This configuration using the reverse bias can enhance the response speed and linearity. The equal spacing between the curves for the same increment in luminous flux reveals that the reverse current and luminous flux are almost linearly related. The only drawback is the dark and noise current increase due to the reverse bias. This operational mode is often employed in high speed applications such as short pulse measurement [60]. The right side in Fig. 68 presents the concept of the PC mode. Assuming that the junction capacitance is much smaller than the feedback capacitance of the preamplifier, the dynamic bandwidth of both configurations can be evaluated as

$$f_{BW} = 1/2\pi R_F C_F \ . \tag{3.22}$$

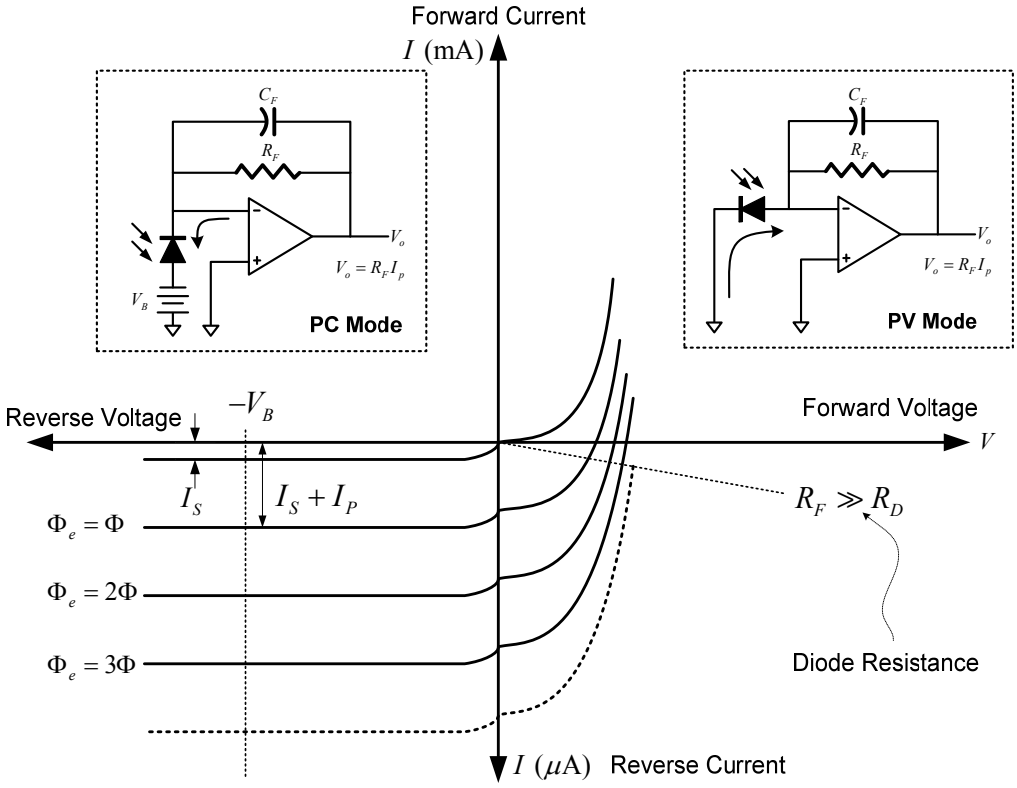

Fig. 68. Photoconductive mode (PC) and Photovoltaic Mode (PV).

There are two types of noises in a PD. The one is shot noise, and the other is thermal noise. The shot noise is defined as statistical fluctuation of the photo current and dark current. The individual pulses illustrated are exponentially decaying step functions but they can assume an arbitrary shape. Its magnitude is given by

$$I_{sn} = \sqrt{2q\left(I_P + I_D\right)\Delta f} \tag{3.23}$$

where Δf is the measurement bandwidth. The thermal noise (also kwon as Johnson noise) is associated with the parallel resistance. It is due to the thermal generation of carrier. The magnitude is given by

$$I_{jn} = \sqrt{4kT\Delta f / R_D} \tag{3.24}$$

Therefore, the total noise can be written as

$$I_{tn} = \sqrt{I_{sn}^2 + I_{jn}^2} \tag{3.25}$$

The noise equivalent power (NEP) is evaluated as below from (3.26) and the responsivity.

$$NEP = I_{tn} / r_\phi \tag{3.26}$$

3.3 Optical Potentiometer Concept and Dynamic Model

3.3.1 Position-Sensing Mechanism Using Indirect Light

Unlike the conventional approaches that directly senses the optical power penetrated through the mechanical structures with slit or cavity, new optical potentiometer sensing the indirect optical power reflected from the track pattern (or colors) illuminated by an LED light source is presented in this research. The two conceptual drawings shown in the below illustrate the optical potentiometer's working principle. Although two schemes have different types of tracks (one uses color variation, the other uses area variation), their working principle are fundamentally identical. The light emitted from a red LED illuminates the track with the specific pattern or color codes designated corresponding to absolute position. The RGB sensor (or PD) senses the irradiance variation reflected from the track and generates a reverse-bias current in proportion to the irradiance of the reflected light. A built-in transimpedance amplifier in the RGB sensor (or PD) transforms the reverse-bias current to a measurable voltage level. The measured voltage signal is translated into a physical displacement through a conversion constant.

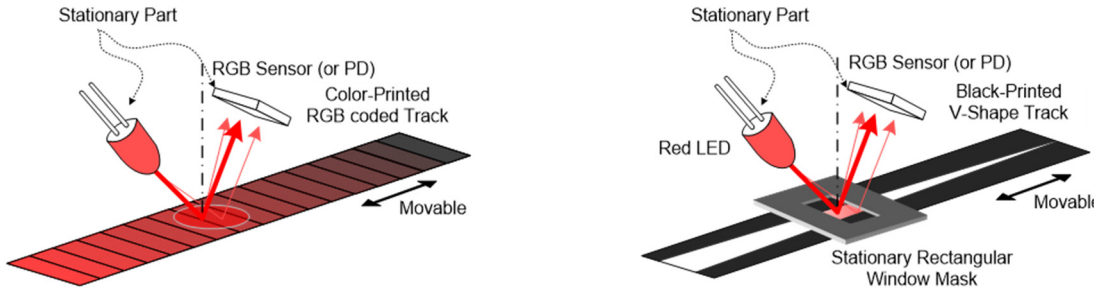

(a) (b)

Fig. 69. Optical potentiometer sensing mechanism: (a) RGB coded track. (b) V-shaped track.

3.3.2 Dynamic Model of Optical Potentiometer

As mentioned in previous section, the LED and PD have very fast responses by themselves. Thus, in case that the LED is used as a constant light source, the dynamic model between the LED source and the RGB sensor (or PD) can be derived from the time delay due to propagation distance and the time constant of the transimpedance amplifier built in the RGB sensor (or PD) as shown in Fig. 70.

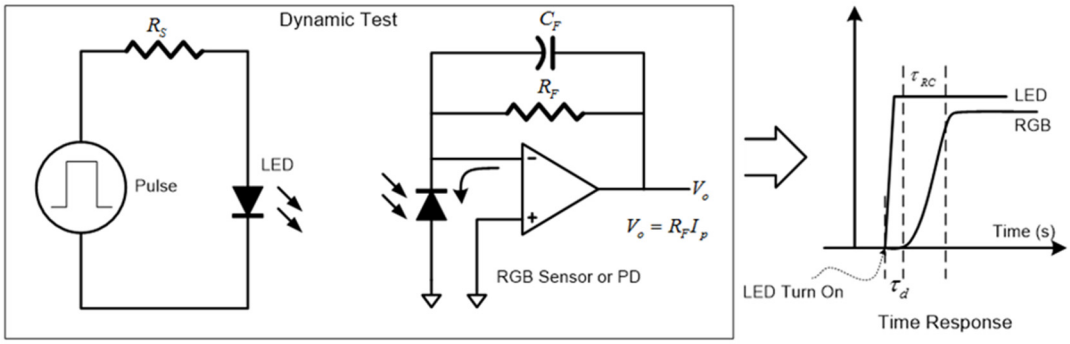

(a) (b)

Fig. 70. Dynamic analysis between LED and RGB: (a) Test scheme. (b) Time responses.

From the dynamic test scheme in Fig. 70, the propagation delay (τ_d) can be calculated by

$$\tau_d = (d_{LS} + d_{SR}) / c \tag{3.27}$$

where c is the speed of light, d_{LS} is the distance between the LED center and the light incident point of the track, and d_{SR} is the distance between the light incident point and the sensing face of the RGB sensor (or PD). The transfer function of the output voltage of the RGB (or PD) sensor for the photocurrent due to the irradiance can also be derived as

$$V_o(s) = \frac{R_F}{R_F C_F s + 1} I_P(s) = \frac{R_F}{\tau_{RC} s + 1} I_P(s) \tag{3.28}$$

where R_r and C_r are the feedback resistance and the capacitance in the transimpedance amplifier circuit, τ_{RC} is the time constant of the amplifier circuit, and I_P is the photocurrent current of the photodiode. From (3.27) and (3.28), the BW of the propagation mechanism can be approximated as

$$f_{BW} \approx \frac{1}{2\pi(\tau_d + \tau_{RC})}. \tag{3.29}$$

Since the propagation-delay time constant is much smaller than the time constant of the current-to-voltage converter, the bandwidth (BW) is mainly governed by the RGB sensor (or PD). Eventually, the effective BWs of this sensing mechanism in the RGB sensor and PD are computed as about 4.42 kHz and 14 kHz at the maximum-gain condition, respectively. This BWs implies that this sensing mechanism can be modeled from the steady-state scale factor in the low-frequency control system. The steady-state output voltage of the RGB sensor (or PD) can be written as the below from (3.28).

$$V_o = R_F I_P \tag{3.30}$$

The photocurrent of the RGB sensor (or PD) is expressed linearly in terms of the diode's responsivity (r_ϕ) and the received radiant flux (Φ_e) as [60], [61].

$$I_p = r_\phi \Phi_e \tag{3.31}$$

Thus, from (3.30) and (3.31), the output voltages of the RGB sensor for the received irradiance and the PD for the incident optical power can respectively be derived as.

$$V_o = \begin{cases} R_F r_\phi \Phi_e = R_F r_\phi \left(A_R E_{rr} \right) = r_e E_{rr} & \text{for RGB sensor} \\ R_F r_\phi \Phi_e & \text{for PD} \end{cases}, \tag{3.32}$$

where A_R is the effective sensing area of the RGB sensor and E_{rr} is the received irradiance. The irradiance responsivity coefficient r_e is given in Table 14.

Table 14. Performance parameters of LED, RGB Sensor, and PD.

Devices	Specs	Typical Values	Unit
LED (HLMP-EG08-Y2000)	Wavelength	635 (Red)	nm
	Emitted radiant power (Φ_e)	0.0033 at I_F =20 mA	W
	Viewing angle at half power ($\theta_{1/2}$)	±4	deg
	Radiant intensity (I_e)	0.062 ~ 0.180	W/sr
RGB sensor (HDJD-S822-QR999)	Irradiant responsivity coefficient (r_e)	2.73 at 645nm 2.04 at 542nm 1.54 at 460nm	V/mW/cm^2
	Detector effective area (A_R)	0.1 × 0.1	cm^2
	Dark voltage (V_D)	15	mV
PD (OPT101)	Radiant flux responsivity (r_ϕ)	0.45 at 650 nm	A/W
	Dark current(Is)	7.5	mA
	Bandwidth	14	kHz
	Supply voltage	2.7 ~ 36	V
	Feedback resistance (R_F)	1.0	MΩ
	Photodiode area (A_R)	2.29 × 2.29	mm^2

3.4 Rotary Optical Potentiometer

3.4.1 Mechanical Geometry Configuration

The schematic diagram shown in Fig. 71 illustrates the geometrical configuration of the ROP using the indirect optical power and non-contact sensing scheme.

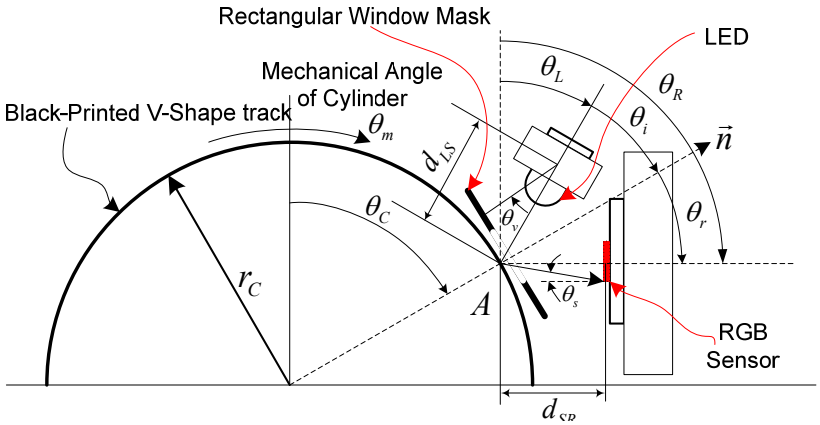

Fig. 71. 2-D cross-sectional view of the rotary optical potentiometer.

As shown in Fig. 71, the rotary optical potentiometer (ROP) consists of a red LED light source, an RGB sensor, and a cylindrical color coded (or V-shaped) track, and stationary rectangular mask window for linearization of the received optical power (is only applied in V-shaped track). In this research, assuming that the roughness of the printed plain paper is slightly less than the wavelength of the LED light, a conventional directional-diffusion model is used as the surface reflectance model [62], [63]. In such a case, since the main transmitting power still lies on the specular line as shown in Fig. 71, when the viewing angle (θ_v) of the LED is zero, the optimal angle to obtain the maximum optical power is given as

$$\theta_R = \theta_L + 2\theta_i = \theta_L + 2(\theta_C - \theta_L) = 2\theta_C - \theta_L \tag{3.33}$$

where θ_R is the mechanical angle of the RGB sensor, θ_L is the mechanical angle of the LED, and θ_C is the arc angle of the point A, and their values are determined as 90°, 30°, and 60°, respectively so that the specular line lies in perpendicular to the sensing face. As a result, the incident angle (θ_i) becomes equal to the reflection angle (θ_r). This is also the purpose to avoid the refraction effect due to the plastic cover of the RGB sensor and the direct interference due to the direct emitted light from the full viewing angle of the LED. The incident angle according to the arbitrary viewing angle of the LED can be written as

$$\theta_i = \theta_C - \theta_L - \theta_v + \Delta\theta_C \tag{3.34}$$

where $\Delta\theta_c = -d_{LS}\sin\theta_v \big/ \left(r_C \cos\left(\theta_C - \theta_L - \theta_v\right)\right)$, d_{LS} is the distance from the light origin of the LED to the point *A*, and r_c is the radius of the cylindrical track.

3.4.2 Steady-State Propagation Model in Color Coded Track

The received power of the RGB sensor transmitted from the LED source can be computed effectively by considering the line-of-sight (LOS) propagation path and directed-non-LOS path. Assuming that the emission of the LED light source has a Lambertian radiation pattern, the radiant intensity according to the viewing angle of the LED is given by [59], [64].

$$I_e\left(\theta_v\right) = P_t\left[\frac{m+1}{2\pi}\cos^m\left(\theta_v\right)\right] \tag{3.35}$$

where P_t is the radiant flux (optical power) emitted from the LED, *m* is the order of the Lambertian emission, and given by the semi-angle at half power as $m = -\ln 2 / \ln(\cos(\theta_{1/2}))$ [59], [65], and the half power angle $\Phi_{1/2}$ is given from the LED datasheet. Fig. 72 shows

the normalized 3-D Lambertian radiant intensity pattern and the definitions for the full power-viewing angle, and a half power-viewing angle of the LED used in this study.

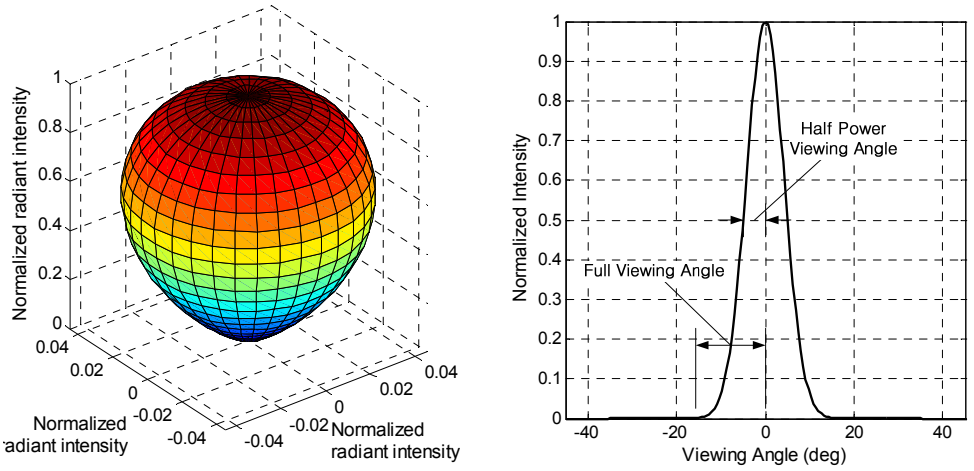

(a) (b)

Fig. 72. (a) Normalized 3-D Lambertian radiant intensity pattern of the LED. (b) Normalized radiant intensity according to the angle displacement of the LED (HLMP-EG08-Y2000).

The irradiance (E_{ts}) and the received optical power (P_{ts}) on the tangential surface on the crossing point A can be written as, respectively.

$$E_{ts}(\theta_v) = P_t\left[\frac{m+1}{2\pi}\cos^m(\theta_v)\right]\frac{\cos(\theta_i)}{d_{LS}^2} \tag{3.36}$$

$$P_{ts}(\theta_v) = E_{ts}(\theta_v)\,A_I \tag{3.37}$$

where dA_I is the infinitesimal incident-beam area in the vicinity of the point A. The received optical power on the incident surface becomes the new light source of the RGB sensor. The emitted power (P_{rs}) from the surface at point A can be expressed by the linear combination of the Lambertian irradiance and the specular irradiance as [66].

$$dP_{rs}(\theta_v,\theta_r,\varphi_r) = \rho\left(E_{ts}(\theta_v) + E_{ss}(\theta_i,\theta_r,\varphi_r)\right) dA_I$$
$$= \rho\left[E_{ts}(\theta_v) + \alpha\exp\left\{-\frac{1}{2}\left(\left(\frac{\theta_i-\theta_r}{\sigma_s}\right)^2 + \left(\frac{\varphi_r}{2\sigma_s}\right)^2\right)\right\}\right] dA_I \quad (3.38)$$

where ρ is the reflectance factor which varies according to the reflector type and has the value between 0 and 1, E_{ss} is the irradiance of the specular diffusion function, σ_s is the standard deviation of roughness of the surface, $\alpha = I_e k_s / \left(d_{LS}^2 \sqrt{2\pi\sigma_s}\right)$, where k_s that takes the value between 0 and 1 is determined by ρ, and φ_r is the azimuth angle on the surface. The directional diffusion pattern of irradiance in Fig. 73 illustrates that the expected reflected optical power density decreased due to the surface color, the surface roughness, and the viewing angle of the LED for the single color surface.

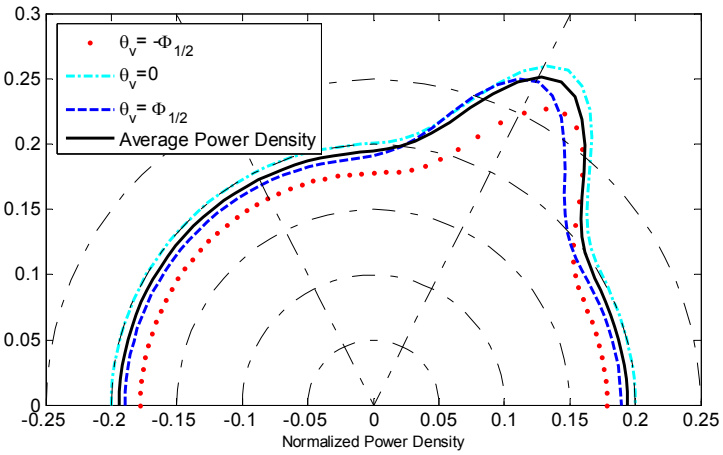

Fig. 73. Expected normalized reflected power density on the tangential surface ($\rho(E_{ts}(\theta_v)+E_{ss}(\theta_i,\theta_r,0))/E_{ts}(0)$ with $\rho = 0.2$, $k_s = 0.4$, and $\sigma_S = 10°$).

The received irradiance (E_{rr}) on the sensing face of the RGB sensor is given as

$$dE_{rr}(\theta_v,\theta_r,\varphi_r) = \frac{dP_{rs}(\theta_v,\theta_r,\varphi_r)}{\pi d_{SR}^2}\cos(\theta_s), \quad (3.39)$$

where θ_s is the incident angle of the reflected light with respect to the normal vector of the RGB sensing face. The received power is a constant if the stationary system with a constant optical power source has a constant reflectance factor such as a wall or a fixed color surface. However, if the reflectance factor is defined as a function of the rotation angle of the cylindrical color track, the RGB sensor's output voltage can be derived as the below by plugging (3.38) and (3.39).

$$V_o(\theta_m,\theta_v,\theta_r,\varphi_r) = r_e E_{rr}(\theta_m,\theta_v,\theta_r,\varphi_r) = r_e P_t \frac{(m+1)}{2\pi^2} \int_{A_I} \Gamma(\theta_m) \frac{\cos^m(\theta_v)\cos(\theta_s)}{d_{LS}^2 d_{SR}^2} (\cos(\theta_i)+B)\, dA_I \tag{3.40}$$

where $B = k_s \exp(-0.5\sigma^2)/\sqrt{2\pi\sigma_s}$, $\sigma = \left((\theta_i-\theta_r)/\sigma_s\right)^2 + \left(\varphi_r/2\sigma_s\right)^2$ and $\Gamma(\theta_m)$ is the reflectance-factor function according to the rotation angle of the cylindrical color track. The RGB coded pattern using the red color depicted in Fig. 74 shows that the angular resolution of the RGB sensor is determined by the diameter of the beam and the rectangular cell printed with a designated RGB code per the interval of 1.0°. For example, if the diameter of the incident-beam area is less than the rectangular cell width, the resolution will be 1.0° because the irradiance change can occur only whenever the incident cell changes. In contrast, if the diameter of the incident-beam area is larger than the cell width, the analog output voltage of the RGB sensor becomes the sum of irradiance reflected from several red RGB coded colors. This reveals that since the value of the sum can vary even with a tiny motion, the angle-sensing resolution becomes theoretically infinite. Thus, the actual resolution is limited by the resolution of the analog-to-digital converter (ADC) if there is no noise or nonlinearities. The normal distributions described in Fig. 74 show the varying

power densities of the reflected light in accordance with the movement of the incident-beam area due to the rotation of the cylindrical color track. As a result, the output of the RGB sensor indicates the mechanical angular displacement.

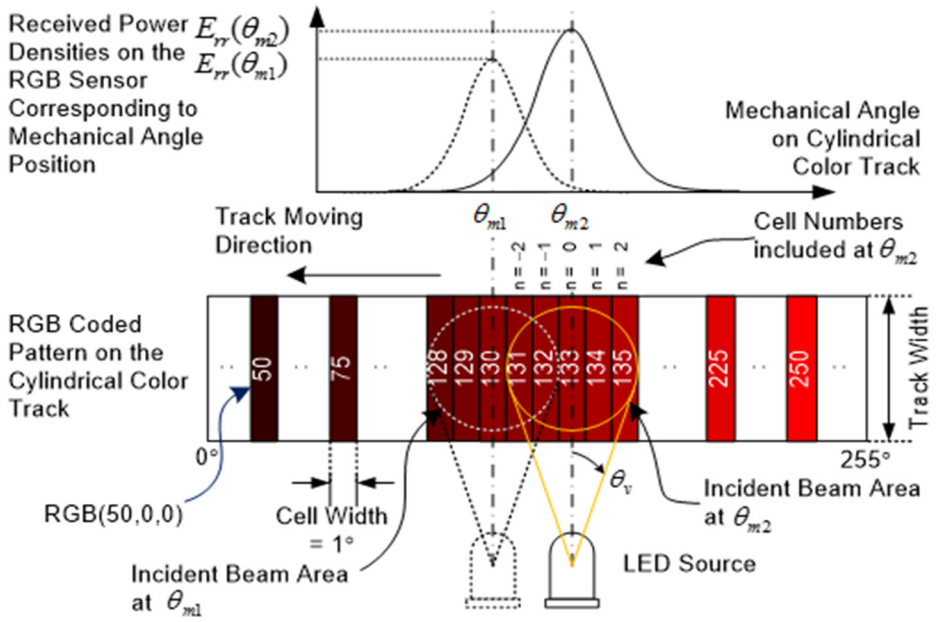

Fig. 74. Power densities due to the red RGB colored track and the incident area illuminated by the LED.

Therefore, the integration in (3.4.8) can be rewritten as a sum (3.4.9) with the small cell size and the reflectance factor corresponding to each designated color code in Fig. 3.20.

$$V_o(\theta_m,\theta_v,\theta_r,\varphi_r) = r_e P_t \frac{(m+1)}{2\pi^2} \sum_{k=-n}^{n} \Gamma_k(\theta_m + k\Delta\theta_m) H(k) \Delta A_I \tag{3.41}$$

where $H(k)$ is $\left[\cos^m(\theta_{vk})\cos(\theta_{sk})\left(\cos(\theta_{ik})+B_k\right)\right] / \left[d_{LSk}^2 d_{SRk}^2\right]$ and $2n+1$ is the total number of the RGB cells in the incident area. Assuming that the light source with a small viewing angle also has the small incident-beam area due to the short distance, the irradiance on

the incident surface area is the same on the entire incident-beam area. Thus, the output voltage of the RGB sensor can be presented as the product of the constant $H(0)$ and the sum of the each reflectance factor of the RGB cells in the incident-beam area corresponding to the rotation angle. This relation can be rewritten by means of the average reflectance factor because the reflectance function is assumed as a function of the rotating angle $\left(\Gamma_k(\theta_m)=\rho_k\theta_m\right)$.

$$V_o(\theta_m) \approx r_e P_t \frac{m+1}{2\pi^2} H(0)\left[\Gamma_{-n}(\theta_m - n\Delta\theta_m) + \cdots + \Gamma_0(\theta_m) + \cdots + \Gamma_n(\theta_m n\Delta\theta_m)\right]\Delta A_I$$
$$\approx r_e P_t \frac{(m+1)(2n+1)}{2\pi^2} H(0)\Delta A_I\, \bar{\rho}\theta_m = h_1\, \bar{\rho}\theta_m \tag{3.42}$$

where $\bar{\rho}$ is the average reflectance factor of the incident area and, $h1$ is $r_e P_t\left((m+1)(2n+1)/2\pi^2\right)H(0)\Delta A_I$. Since the output voltage in the above physically implies the sensing-angle of the RGB sensor for the mechanical angle, the initial angle -sensing constant of the output voltage for the input angle can be derived as follows:

$$h_1\bar{\rho} = \frac{V_o(\theta_{m2}) - V_o(\theta_{m1})}{\theta_{m2} - \theta_{m1}} \triangleq K_{RGB} \tag{3.43}$$

where θ_{m1} and θ_{m2} are the minimum and maximum angles of the color track with a full scale range, respectively, $V_o(\theta_{m1})$ and $V_o(\theta_{m2})$ are the output voltages corresponding to the each rotating angle, respectively, and K_r is the angle-sensing constant between the RGB sensor and the color track. From (3.43), the directional angle can be obtained in (3.44) by defining the RGB code 127 as 0.0°.

$$V_o = K_{RGB}\theta_m - V_{RGB127} \tag{3.44}$$

3.4.3 Steady-State Propagation Model in V-Shaped Track

In this section, the steady-state propagation model for the V-shaped track is presented. Although the color-coded track in the previous section is replaced with the V-shaped track, the received optical power density is the same as (3.37). Thus, the derivations for the equations after the received optical power density are presented. The received optical power on the incident surface becomes the new light source of the RGB sensor. The emitted power (P_{rs}) from the surface at point A can be expressed by

$$dP_{rs}\left(\theta_v,\theta_r,\varphi_r\right)=\rho_w E_{ts}\left(\theta_v\right)dA_{Iw}+\rho_b E_{ts}\left(\theta_v\right)dA_{Ib} \tag{3.45}$$

where ρ_w and ρ_b are the reflectance factor on the whited-colored and black-colored surfaces (0–1), respectively. A_{Iw} and A_{Ib} are the white-colored and black-colored areas of A_I on the point A, respectively. In addition, assuming that reflectance factor of black color is zero, the effective emitted optical power of (3.45) can be rewritten as the below by using the average irradiance (E_{tsa}) in the viewing angle range.

$$dP_{rs}\left(\theta_v,\theta_r,\varphi_r\right)\approx\rho_w E_{tsa}dA_{Iw} \tag{3.46}$$

The received irradiance (E_{rr}) on the sensing face of the RGB sensor is given as

$$dE_{rr}(\theta_v,\theta_r,\varphi_r)=\frac{dP_{rs}\left(\theta_v,\theta_r,\varphi_r\right)}{\pi d_{SR}^2}\cos\left(\theta_s\right)=\frac{\rho_w E_{tsa}\cos\left(\theta_s\right)}{\pi d_{SR}^2}dA_{Iw}\ . \tag{3.47}$$

Since the viewing angle of the LED and the incident angle of the RGB sensor's surface are very small, the cosine terms of (3.47) can be assumed to be unity. Thus, the RGB sensor's output voltage can be derived from (3.32) and (3.47) as follows.

$$V_o(\theta_m,\theta_v,\theta_r,\varphi_r) = r_e E_{rr}(\theta_m,\theta_v,\theta_r,\varphi_r) = r_e \rho_w P_t \frac{(m+1)}{2\pi^2} \int_{A_{Iw}} \frac{\cos^m(\theta_v)\cos(\theta_s)}{d_{LS}^2 d_{SR}^2} dA_{Iw}$$

$$= \frac{r_e \rho_w P_t (m+1)}{2\pi^2 d_{LS}^2 d_{SR}^2} A_{Iw}(\theta_m) \tag{3.48}$$

This equation implies that the RGB sensor's output voltage can be determined by the white-colored area portion in the incident-beam area of the point *A* if the design parameters such as d_{LS} and d_{SR} are properly determined in the linear response region of the RGB sensor. Since the incident-beam area by the LED has circular shape with the origin at the point *A*, the white-colored area on the black-colored V-shape track pattern is formulated with nonlinear terms. Thus, the RGB sensor output is also presented by a nonlinear function for the corresponding angle. However, if the additional stationary mask with a rectangular window shown in Fig. 75 is employed, the received optical power can theoretically be linearized because the rectangular window makes the white-colored area vary linearly with the corresponding rotating angle as

$$A_{Iw} = \frac{L_r}{2}\left[2w - 2m\left(x_C - \frac{L_r}{2}\right) - 2m\left(x_C + \frac{L_r}{2}\right)\right] = -2mx_C + wL_r = -2mr_C\theta_m + wL_r \tag{3.49}$$

where L_r is the length of rectangular window of mask, L_t is the entire length of the V-shaped track, *w* is the maximum gap width between upper and lower line, m is the slope of the V-shaped line, and x_C is linear distance of the measured angle from the reference axis on the black-colored V-shape track. This is expressed by $r_C\theta_m$, and *m* is computed as $w/2L_t$.

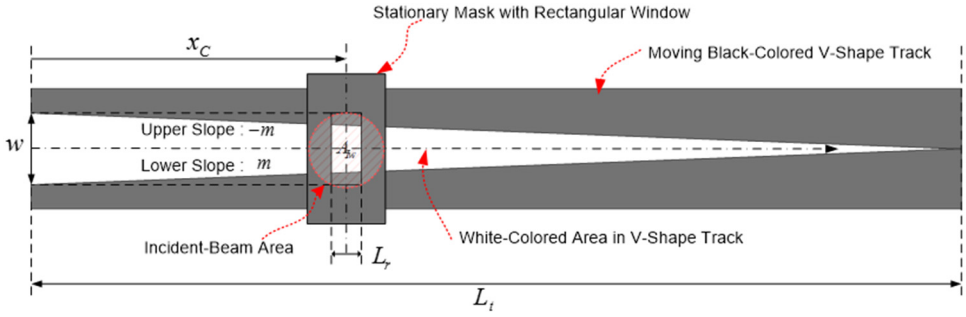

Fig. 75. V-shaped track and the rectangular mask for linearization of the received optical power.

Eventually, the RGB sensor's output voltage can be rewritten by (3.50) as a linear function for the moving angle.

$$V_o(\theta_m) = r_e \rho_w \frac{P_t(m+1)}{2\pi^2 d_{LS}^2 d_{SR}^2}\left(-2mr_C\theta_m + wL\right) = K_{VS}\theta_m + V_{os} \tag{3.50}$$

where $K_{VS} = -2mr_C r_e \rho_w P_t(m+1)/2\pi^2 d_{LS}^2 d_{SR}^2$ and $V_{os} = wLr_e\rho_w P_t(m+1)/2\pi^2 d_{LS}^2 d_{SR}^2$.

3.5 Design Parameter Optimization and Calibration

3.5.1 Design Parameter Optimization

The red LED (HLMP-EG08-Y2000) that has a wavelength of 635 nm and a half power at the viewing angle of ±4° was used in this paper as shown in Fig. 72(b). The incident-beam area is given by the visible viewing angle that is larger than the half-powered viewing angle. The solid and dash lines in Fig. 76 show the visible viewing angle and the diameter of the incident–beam area according to the displacement of d_{LS}, respectively. These measurement results reveal that d_{LS} should be less than 0.042 m due to the critical viewing angle defined in (3.51) as well as less than 0.017 m due to the

maximum allowable incident-beam area. For instances, if the distance is longer than 0.042 m, the larger beam than the critical viewing angle is reflected in the opposite direction. Also, if the distance is longer than 0.017 m, the diameter of the incident area is bigger than the width of the track of 0.01 m depicted in Fig. 74 and 75. Finally, the distance of less than 0.015 m causes the direct interference from the visible viewing angle and blocks the reflected beam path with respect to the configuration of Fig. 71. Hence, the distance was selected as 0.015 m in this study. The critical angle for the full viewing angle and LED's XY-coordinates from the center of the cylinder can be written by

$$\theta_{CA} = \tan^{-1}\left(\frac{r_C \sin\theta_C + d_{LS}\sin\theta_L}{r_C \cos\theta_C + d_{LS}\cos\theta_L}\right) - \theta_L . \tag{3.51}$$

$$\left(r_c \sin\theta_C + d_{LS}\sin\theta_L,\, r_c \cos\theta_C + d_{LS}\cos\theta_L\right) \tag{3.52}$$

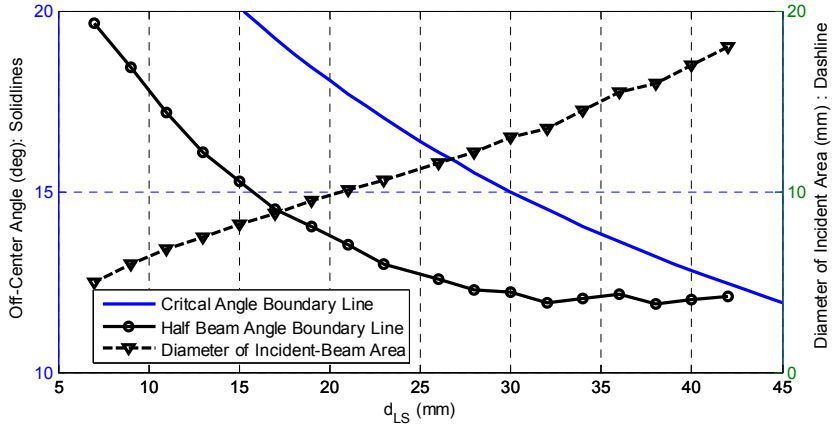

Fig. 76. Diameter of the incident-beam area and the visible viewing angle of the LED according to the displacement of d_{LS} when I_F is 20 mA.

The experimental data given in Fig. 77 reveal that when d_{LS} is 15 mm and the LED forward current I_F is 20 mA, the optimal d_{SR} for the geometrical configuration given in Fig. 71 is 6.5 mm in order to obtain the maximum received power in the red channel voltage of the

RGB sensor (HDJD-S822-QR999) and avoid the blocking of the incident beam due to the sensor module.

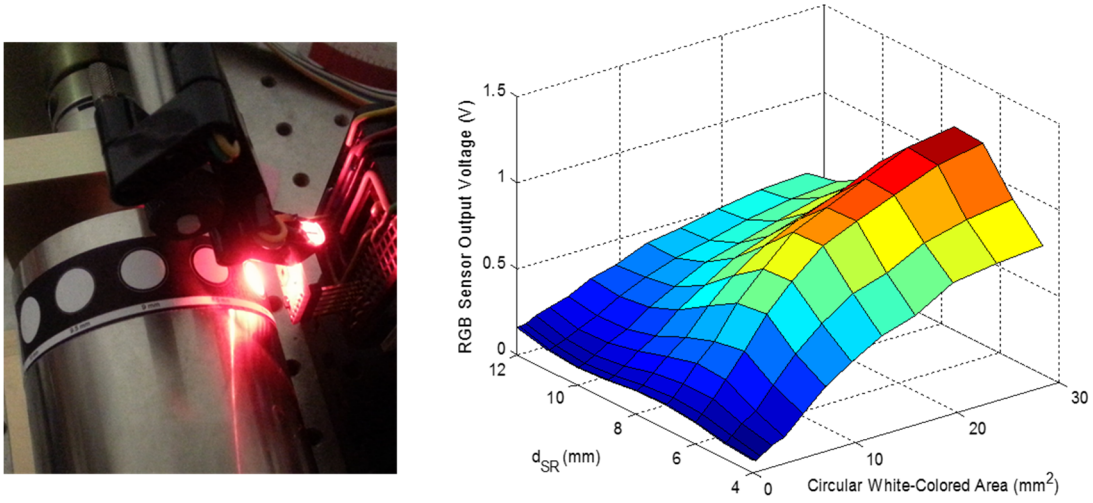

(a) (b)

Fig. 77. (a) Experiment photo for optimal distance (d_{SR}). (b)The output voltages of the red color channel of the RGB sensor according to circular white-colored area and distance (d_{SR}).

3.5.2 Calibration of Colored-Coded Track and Sensing Constant

The color laser printer was used to print the color track with only red RGB codes on plain paper. Each cell with its own red RGB code from 0 to 255 (where $G = 0$ and $B = 0$) was sequentially printed with the interval of 1.0° (0.0005236 m) and the track width of 0.01 m as shown in Fig. 74. Since the undesired ambient light source affects the bias voltage of the RGB sensor, a black plastic cover is used to minimize the magnitude and fluctuation of the bias voltage. Although the measured bias voltage of 36.8 mV (when the LED light source is turned off in our indoor lab) was larger than the dark voltage of RGB sensor of 15 mV, this voltage is still much smaller than the peak voltage for the full RGB

code as shown in Fig. 77. Thus, the configuration of Fig. 71 is applicable to angle sensing within the desired angular range.

The color track expressed as the reflectance-factor function in (3.48) is mainly affected by the printer's color variety. The uncompensated result of Fig. 78 shows that the color track using the initially designated sequential red RGB codes from 0 to 255 exhibits the nonlinear characteristics. This implies that the sequential RGB codes should be compensated for to be employed for a new angle-sensing mechanism. For this purpose, the errors of the uncompensated sensing angle were iteratively calibrated with a quarter-error compensation formula (3.53) and the reference angles measured by a precision potentiometer (Samuris HP-200) with the nonlinearity of less than 0.1 %.

$$\theta_{ce} = (\theta_p - \theta_{rgb})/4\,, \tag{3.53}$$

where θ_p is the potentiometer angle, θ_{rgb} is the angle of the RGB sensor, and θ_{ce} is the compensated angle. The factor of 4 was empirically selected to make the error converge to zero without error-bounce. This is due to the fact that an error is correlated with the other errors in the range of the same incident beam area. And then, the new RGB code of each angle cell was generated by using (3.53) and

$$CODE_{RGB} = round\,[255(\theta_{rgb} - \theta_{ce})]\,, \tag{3.54}$$

where $CODE_{RGB}$ is the digital RGB value from 0 to 255. The results in Fig. 78 indicate that the nonlinearity for the scaling factor is remarkably improved after four iterations. Eventually, if the bias voltage of (3.44) is defined as 0°, the transfer function of the RGB angle sensor with a high BW can be expressed as (3.55) with the angle-sensing constant

(K^*_{RGB}) compensated for by the quarter-error compensation formula and the least-square estimation.

$$V_o \approx K^*_{RGB}\theta_m \tag{3.55}$$

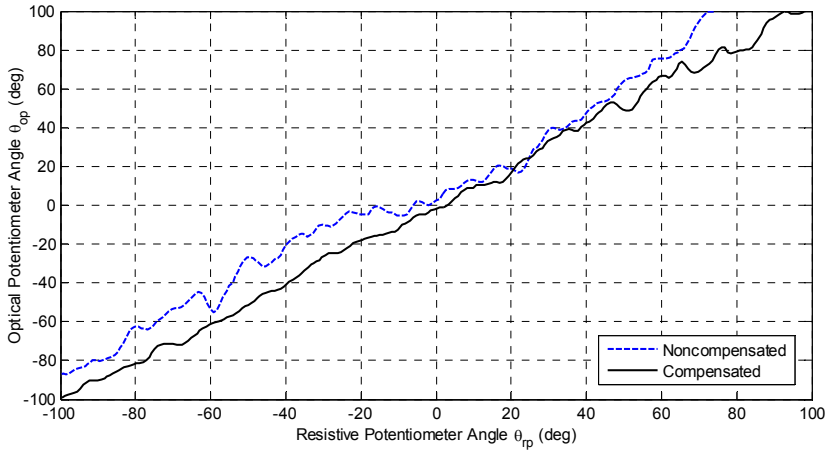

Fig. 78. Non-compensated and compensated angle of the optical potentiometer in color-coded Track. (when $I_F = 20$ mA, $d_{LS} = 0.015$ m, $d_{SR} = 0.0065$ m, and the physical cell size of each color code on the cylinder is 0.0005236×0.1 m^2).

The statistic performance index for the uncompensated and compensated sensing angles in Table 15 demonstrates that the uncertainties of this RGB angle-sensing mechanism are reduced by the compensation formula given in (3.53).

Table 15. Statistic performance of uncompensated and compensated tracks in the range of −60° to 60°.

	Uncompensated	**Compensated**
Least-square slope (θ_{op}/θ_{rp})	1.05	1.02
Nonlinearity (%FSO)	19.97	6.631
RMS error (deg)	13.08	2.617
Standard deviation (deg)	6.994	2.582

3.5.3 Calibration of V-Shaped Track and Angle-Sensing Constant

When d_{SR} is 0.0065 m, the result in Fig. 77 shows that the output signal is saturated for the circular area of larger than 10 mm^2, and it is too small to measure the circular area of smaller than 1 mm^2 correctly. Thus, the differential op-amp with the gain of 4.5 is employed to amplify the signal in the linear region of the RGB sensor. Fig. 79 shows the voltage of the analog-to-digital converter (ADC) input stage through this differential op-amp. The usable linear region is well located in the range between 2 mm^2 and 7.5 mm^2 when d_{LS} = 15 mm and d_{SR} = 6.5 mm.

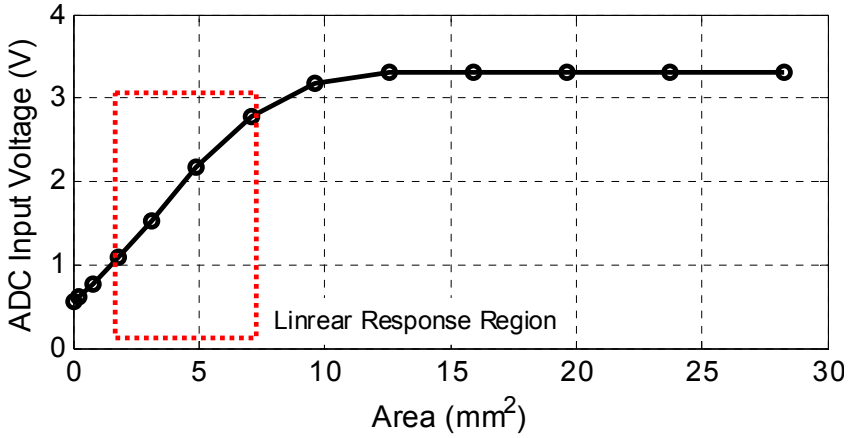

Fig. 79. Output voltage of the differential OP-amp with gain of 4.5.

A commercial laser printer (Brother HL-4150) was used to print the black-colored V-shape track on plain paper. The resolution options with 600 DPI and 2400 DPI were setup in order to compare their performances. The maximum width of the white-colored region in Fig. 75 was determined as 4.0 mm on the basis of the result of Fig. 79 and the overall length of the V-shape track was designed as longer than 125 mm so as to cover the angle range from −120° to 120°. The width and the length of the rectangular window

of the mask are determined as 8.0 mm and 3.0 mm, respectively. The bidirectional angle representation can be formulated as (3.57) through subtracting the voltage of the mechanically defined center of (3.56) from (3.50).

$$V_{rc} = K_{VS}\theta_{mc} + V_{os} \tag{3.56}$$

$$V_o(\theta_m) - V_{rc} = K_{VS}(\theta_m - \theta_{mc}) \triangleq V_{op}(\theta_{bm}), \tag{3.57}$$

where K_{VS} is computed as 0.01183 V/deg. Thus, the relation between the mechanical angle and the output voltage of the optical potentiometer can be simply written as

$$V_{op} = K_{VS}\theta_{bm}. \tag{3.58}$$

The results in Fig. 80 show the measured angles by the optical potentiometers using the 600 DPI and 2400 DPI tracks. The measured angles by the resistive potentiometer (Samuris HP-200) are assumed to be real mechanical angles. The angles larger than of 80° exhibit some distortion due to the saturation effect. The statistical analysis results in Table 16 reveal that the resolution of the printer cannot be the major factor affecting the position-sensing performance.

Table 16. Statistical performance analysis between −60° and 60° for printer DPI.

	600 DPI	**2400 DPI**
Least-square slope (θ_{op} / θ_{rp})	0.9987	1.000
Nonlinearity (% FSO)	3.0728	2.8036
RMS error (deg)	0.7308	0.6500
Standard deviation (deg)	0.8791	0.7966

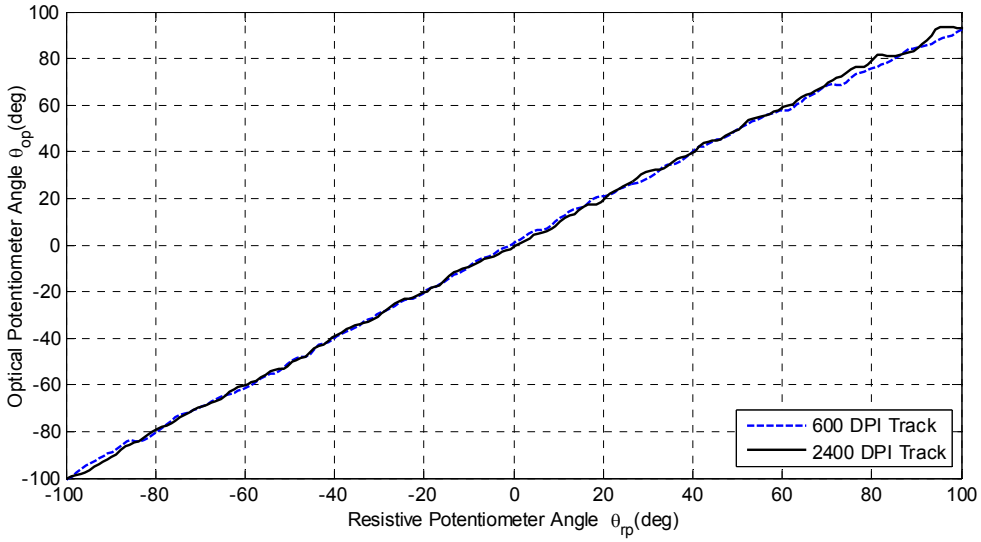

Fig. 80. Optical potentiometer angle vs. resistive potentiometer angle in V-shaped Track (when $I_F = 20$ mA, $d_{LS} = 0.015$ m, $d_{SR} = 0.0065$ m).

3.6 Performance Validation

3.6.1 Hardware Implementation and Controller

The hardware block diagram in Fig. 81 shows the test bed of the rotary position-control system implemented with six components: the mechanical part consisting of a cylindrical inertia, a brush-type DC motor, a mechanical coupler, and a rotary potentiometer; the OP module; the sensor interface board between a color sensor and a DSP (digital signal processor) module; the TMS320F28069 module (control stick by Texas Instruments) running the digital controller and the real time serial communication with a LabVIEW console on a PC; a DAQ (data acquisition, ACPI-3120 by ADDI data) board generating the analog voltage output corresponding to the control command received from the DSP; the analog output circuit board interfacing between the DAQ board and transconductance amplifier. The DSP with a 1-kHz update rate generates the

control command using the error between the reference command and the filtered output voltage of the ROP through an internal 12-bit ADC built in the DSP. The lead compensator implemented on the DSP outputs the control command into the DAQ board through the RS422 real-time serial communication at 250 Hz. This command is conveyed through the DAC of the DAQ board by LabVIEW. The output voltage of the DAC is delivered as a current output through the transconductance amplifier. The motor starts to rotate to meet the desired reference angle. The OP module measures the irradiance change of the reflected light corresponding to the rotating angle, and then converts it into the voltage output proportional to the reflected luminous intensity. Fig. 82 shows the photo of experimental setup for the rotary-position control system.

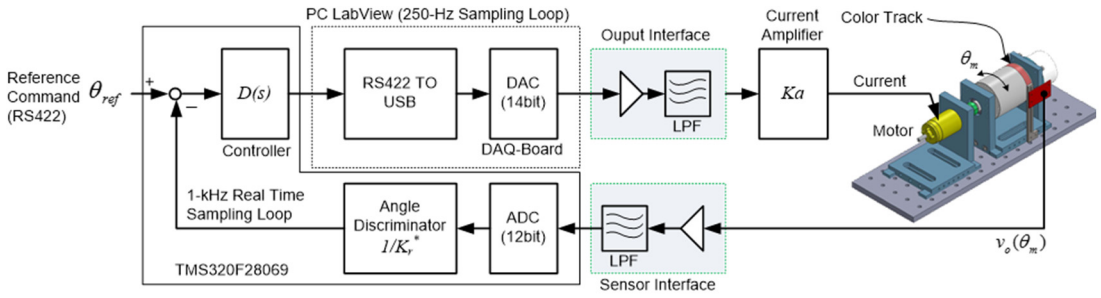

Fig. 81. Hardware block diagram of the rotary-position control system.

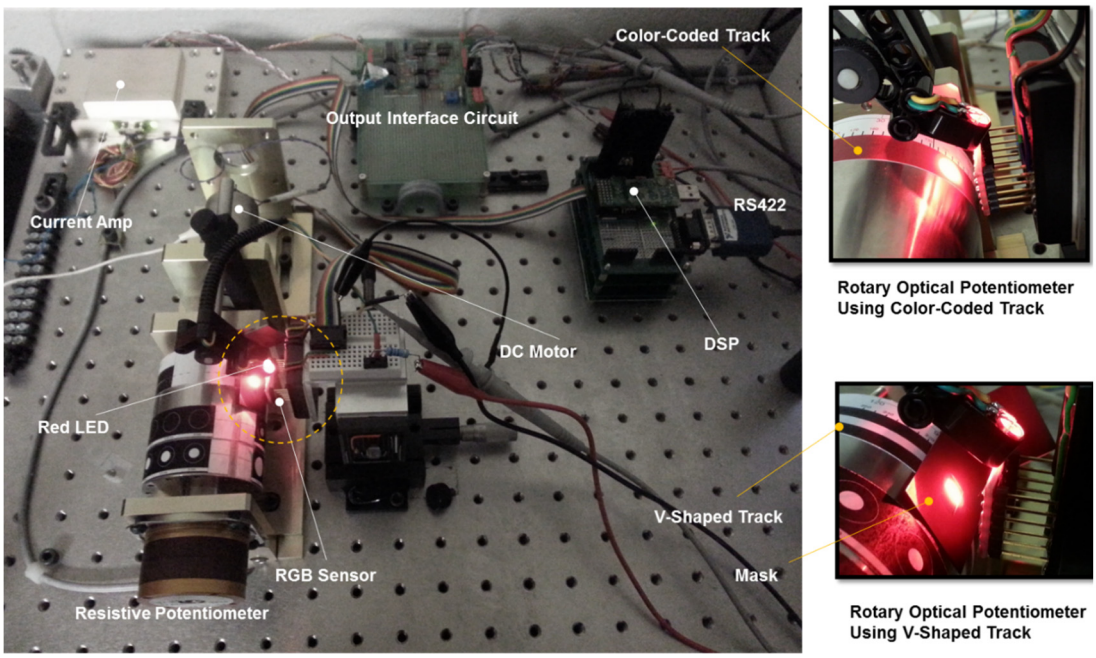

Fig. 82. Rotary position-control system with ROP.

3.6.2 Experimental Results

Fig. 83 shows the step responses of the position-control loop using the ROP with the color-coded track (CCT) for various step angle commands. Although there happen jerks or ridges due to the nonlinearity for the sensing angle during the transient interval, most of step responses well keep track of the angle commands at steady state. Also, the steady-state errors for the command inputs are within the range of less than 0.4° due to the controller's performance. However, assuming that the rotary resistive potentiometer (RRP) angles are very close to the true values, the angle differences between the solid line and dash line in certain angles reveals that there are still large accuracy errors in the ROP using the CCT.

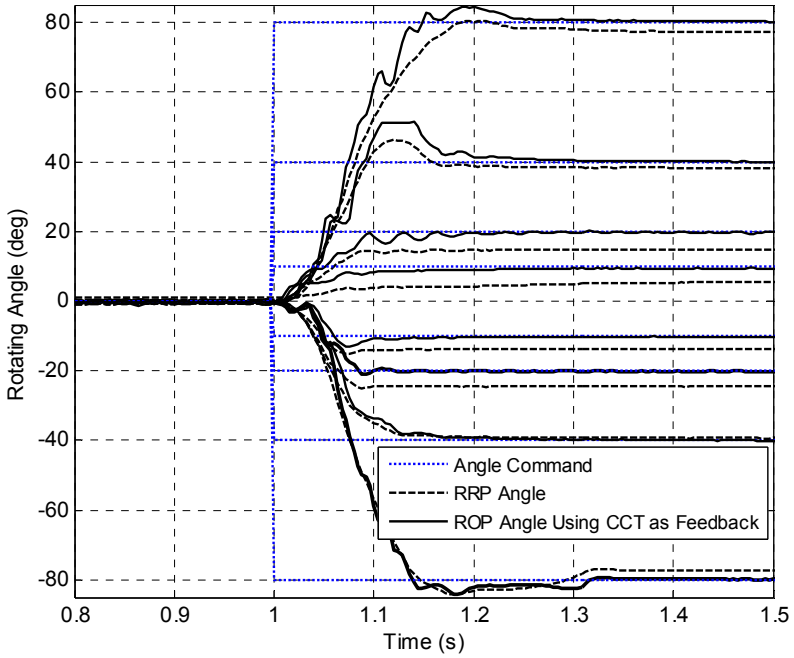

Fig. 83. Step responses of the position-control loop using the ROP with the CCT for various reference commands (±10°, ±20°, ±40°, and ±80°).

In order to verify the performance of the ROP using V-shaped track (VST), the black-colored VST printed at 2400 DPI is used. Fig. 84 shows the step responses for various reference angle commands. Although the ROP angles have some distortions due to the nonlinearity in the transient interval, the step responses follow the reference angle commands very well. The number of the jerks in transient interval are remarkably decreased comparing with the ROP using the CCT. In addition, the angle differences between the RRP and ROP are significantly reduced by the accuracy improvement through adopting the VST. These results reveals that the ROP using VST can be a good candidate for the cost-effective angle sensor.

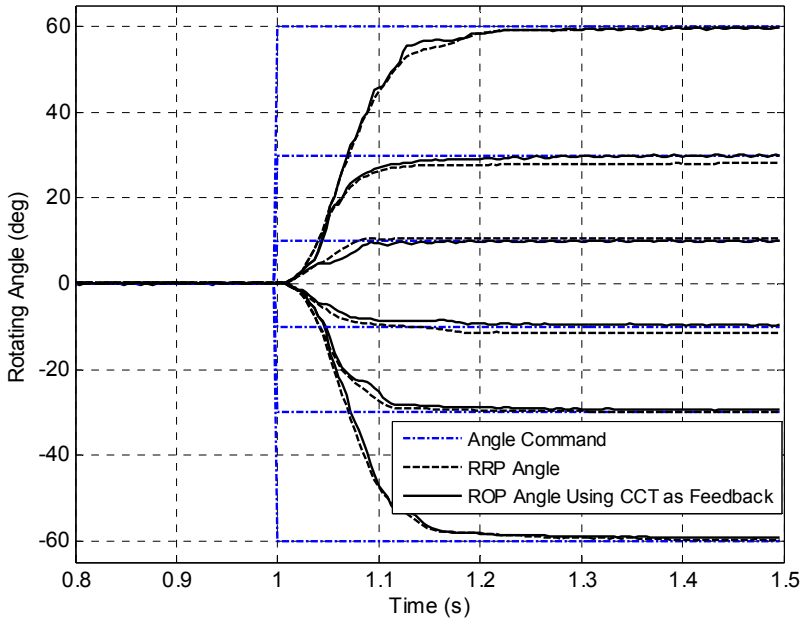

Fig. 84. Step responses of the position-control loop using the ROP with the VST for various reference commands (±10°, ±20°, ±30°, and ±60°).

The responses to a sinusoidal reference command with the magnitude of 60° and the period of 1 s are investigated for two types of ROPs. The response in the top of Fig. 85 shows RRP angle and command angle when the RRP is used as a feedback sensor. The response follows the reference angle command very smoothly well without any jerks. The response in the middle of Fig. 85 shows the response of the ROP with CCT when the ROP is employed as the feedback sensor in the rotary position-control system. The response to a sinusoidal reference command with the magnitude of 60° tracks the input command well. However, there are still large angle difference between the RRP and ROP. This implies that the ROP using the CCT can be used in the sinusoidal motion system, but cannot guarantee the accuracy, assuming the RRP angle is the true values. The response in the bottom on Fig. 85 shows the response of the ROP with VS when the ROP

is employed as the feedback sensor in the rotary position-control system. Although these nonlinearity of 2.80% degrades the angle accuracy as compared with the high precision RRP, its response is better than the response of the ROP with CCT. The response tracks the input command very well. These results reveals that this cost-effective sensing mechanism is still sufficient to be used in a fast position-control system with permissible error bounds. Thus, both step and sinusoidal responses validate the feasibility that this new angle-sensing mechanism can be employed in a rotary or linear position-control system.

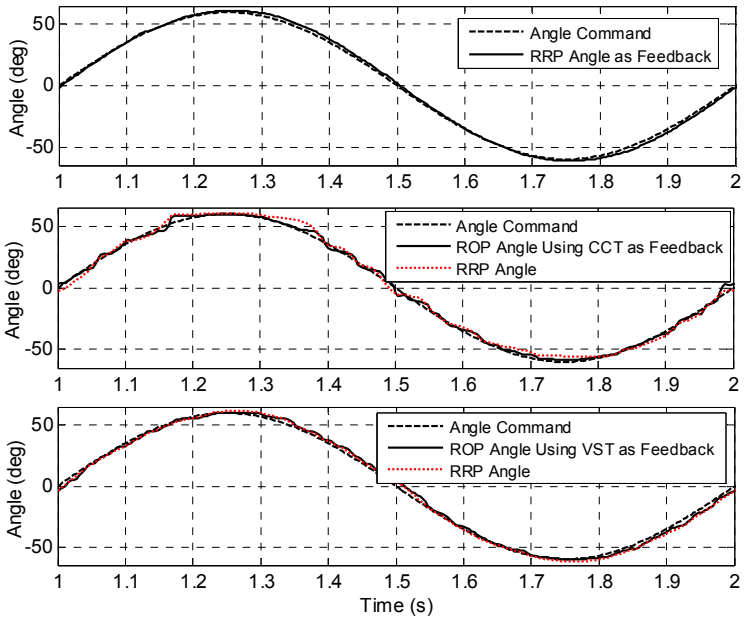

Fig. 85. Sinusoidal response to a 1-Hz sinusoidal reference input with the magnitude of 60° and the period of 1 s (Position control using RRP (Top figure), position control using ROP with CCT (middle figure), and position control using ROP with VST (bottom).

CHAPTER IV

SYSTEM MODELING AND ITS CONTROL

In Chapter IV, firstly, the detail design and implementation procedure for the new cost-effective 12-step current control scheme with a low ripple force is presented for the new double-sided IPM-FLBM with slot-phase shift. The conventional FOC scheme is also implemented for the performance comparison with the proposed 12-step current controller.

In following section, the mechanical modeling and identification for the linear motion platform using the double-sided IPM-FLBM are investigated using the lumped-parameter method and FEA tool (i.e. SolidWorks static analysis). The dynamic friction model is established from measurement. A simplified single-mass model is presented with the dynamic frictions.

In the last section, the transfer function including the position controller and the dynamic frictions is derived. The control parameters in the position loop are determined by the error analysis at steady state. The performances for the designed position-control loop are verified using the time- and frequency-domain response experimentally. In the end, the applicability in the position-control loop using the LOP is demonstrated using the time response for various input commands.

4.1 Current Control of Double-Sided IPM-FLBM

4.1.1 Electromechanical Specification

Fig. 86 shows the double-sided 6/4 IPM-FLBM prototype using the SMC. A cross-sectional schematic diagram in Fig. 87(a) illustrates the internal structure and reference frames of the upper and lower stators in the double-sided IPM-FLBM prototype. Fig. 87(b) illustrates the electrical angle model with slot-phase shift for a pole pair. Herein, L is the inductance, R is the armature resistance, e is the phase-to-neutral back-EMF voltage, θ_e is the electrical angle, the subscript a, b, and c present each phase, and the subscript u and l are the upper and lower components, respectively. Fig. 87(c) describes a further simplified equivalent model using the resultant phase winding superimposed by each phase winding of the upper and lower stators. Herein, V_a, V_b, and V_c are the phase voltages, V_n is the neutral voltage, and I_a, I_b, and I_c are the phase currents. These notations are used throughout this paper. Since the mutual inductances in the alternate teeth winding configuration have almost zero values, they are not considered in this model. The major electrical and mechanical parameters are given in Table 17.

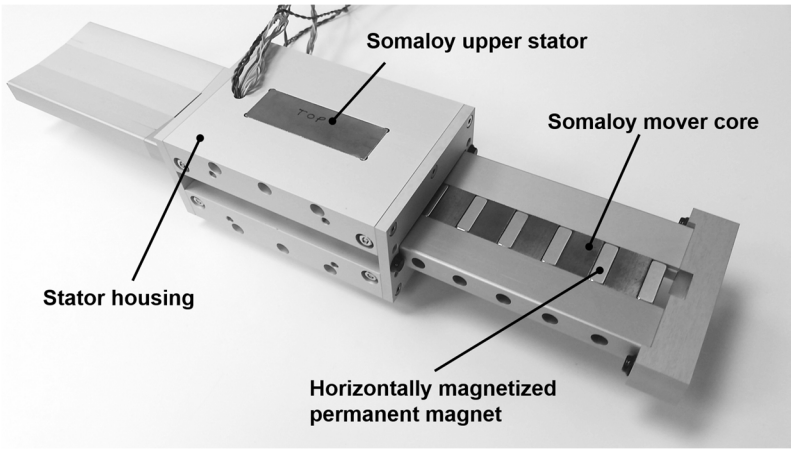

Fig. 86. Photograph of the new double-sided 6/4 IPM-FLBM prototype

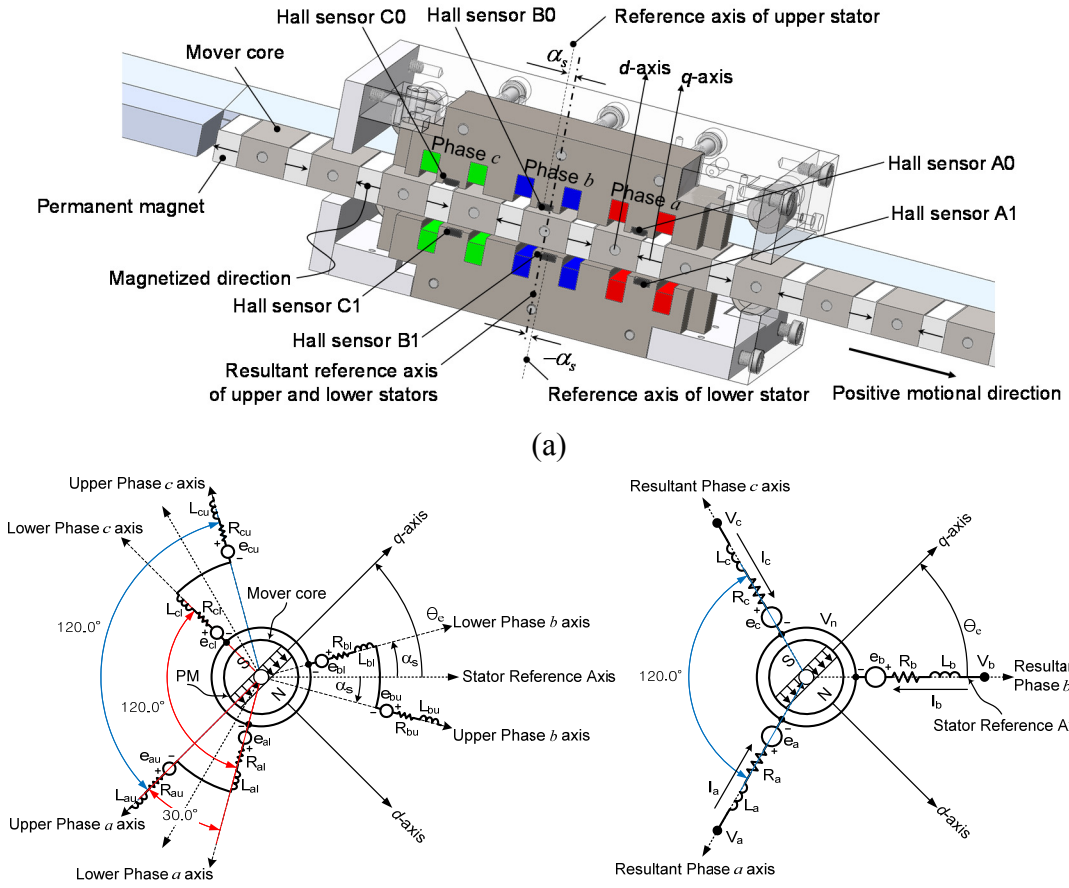

Fig. 87. Coordinate definitions of the double-sided 6/4 IPM-FLBM: (a) 3-D cross-sectional view of the mechanical model, (b) electrical angle model using the current vector coordinates with slot-phase shift, and (c) simplified equivalent electrical angle model using the resultant current vector coordinates.

Table 17. Specification of the double-sided IPM-FLBM

Parameters	Symbols	Values	Tolerances
Phase resistance (Ω)	R_a, R_b, R_c	1.672	±5%
***q*-axis inductance (mH)**	L_q	2.322	±5%
***d*-axis inductance (mH)**	L_d	1.646	±5%
Force constant (N/A)	K_f	5.980	±5%
Phase-to-neutral back EMF constant (V-s/m)	K_{emf}	3.81	±5%
Peak-to-peak detent force (N)	F_d	< 2.4	-
Stall current (A)	I_{stall}	10.0	< 30 s
Continuous rated current (A)	I_{cont}	2.5	
Maximum travel range of mover (m)		0.01	
Mover mass (kg)	M_m	0.718	

4.1.2 12-Step Current Control.

As shown in Fig. 87(a), the three Hall-effect sensors are embedded in the upper and lower stators, respectively, in order to detect the mover-pole position with respect to each reference axis of the upper and lower stators. Therefore, two independent 6-step commutation controllers and PWM drivers can be used. However, if the phase windings of the upper and lower stators are connected in series as shown in Fig. 87(b), the 12-step commutation (150° conduction mode) sequence that generates a quasi-sinusoidal current waveform can be designed using a single controller and the six Hall-effect sensors with respect to the resultant vector of each phase in Fig. 87(c).

4.1.2.A 12-Step Current Control Principle

Assuming that the reluctance force is negligible or the *d*-axis current is controlled as zero, the instantaneous electromagnetic thrust force *F* of the double-sided IPM-FLBM can be given by

$$F = \frac{e_a i_a + e_b i_b + e_c i_c}{v_m} . \tag{4.1}$$

where v_m is the mover speed (m/s). The measured back-EMF voltages in the bottom of Fig. 3 show that they can be modeled as a sinusoidal form on the resultant phase axes defined in Fig. 2(c) as follows:

$$\begin{aligned} e_a(\theta_e) &= v_m K_{emf} \cos(\theta_e + 2\pi/3) \\ e_b(\theta_e) &= v_m K_{emf} \cos(\theta_e) \\ e_c(\theta_e) &= v_m K_{emf} \cos(\theta_e - 2\pi/3) \end{aligned} \tag{4.2}$$

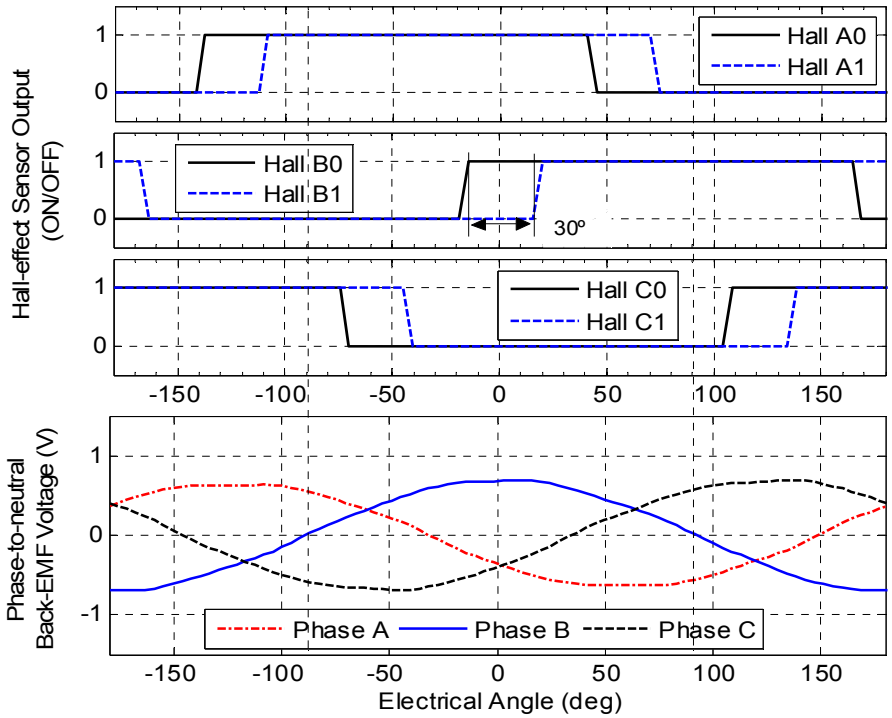

Fig. 88. Measured Hall-effect sensor outputs (top) and back-EMF voltages (bottom) according to the mover positions when the mover moves at 0.2 m/s.

In addition, if the quasi-sinusoidal phase current waveform shown in Fig. 89 can be made using the six Hall-effect sensors, the current waveform of the phase *b* with the 12 steps can be represented as a Fourier series

$$i_b(\theta_e) = \frac{2I_m}{\pi}\sum_{n=1}^{\infty}\frac{I_n}{n}\sin\left(\frac{n\pi}{2}\right)\cos(n\theta_e) \tag{4.3}$$

where I_m is the magnitude of the phase current, I_n is given as

$$I_n = \cos\left(\frac{n\pi}{12}\right) + \left(\sqrt{3}-1\right)\cos\left(\frac{n\pi}{4}\right) + \left(2-\sqrt{3}\right)\cos\left(\frac{5n\pi}{12}\right), \tag{4.4}$$

and the currents for phases *a* and *c* are shifted by ±120° electrically from phase *b*

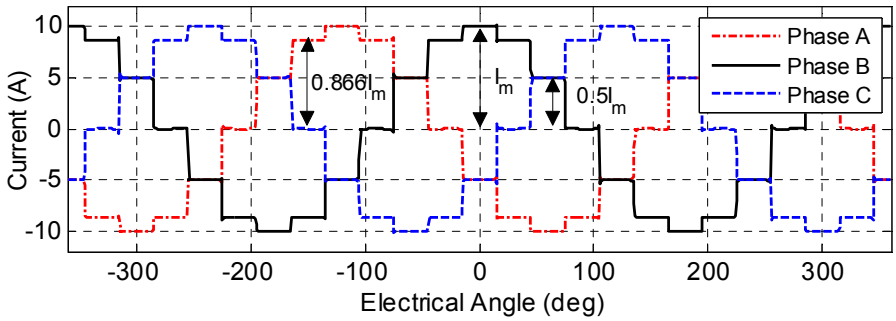

Fig. 89. Predicted 12-step quasi-sinusoidal phase current waveforms according to the electrical angles when I_m = 10.0 A.

The results in Fig. 90 show that the steady-state force of the proposed 12-step current control calculated from (4.1) to (4.3) can produce a much smaller ripple force than those of two other conventional 6-step commutation methods (i.e. two-phase conduction and three-phase conduction) in the double-sided IPM-FLBM. This implies that the 12-step current control scheme is suitable in the low-speed precision motion-control applications. Furthermore, the thrust force of (4.1) can be approximated as

$$F = \frac{3}{2} K_{emf} I_m \cong K_f I_m \,. \tag{4.5}$$

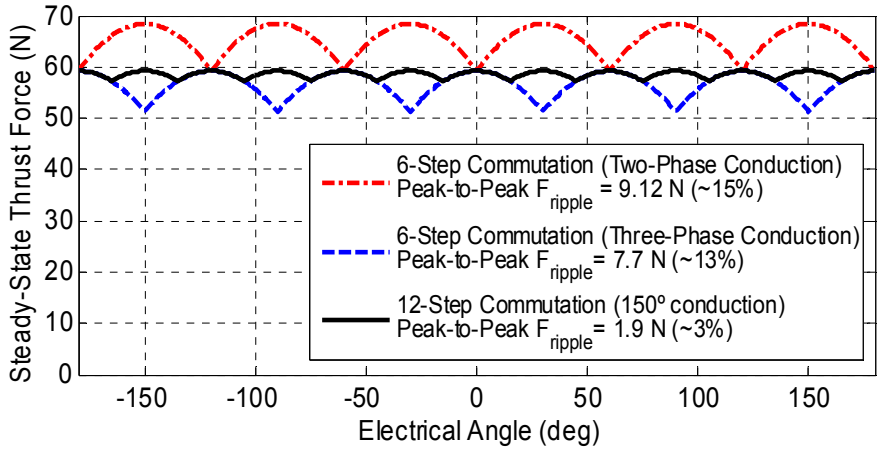

Fig. 90. Predicted ripple forces according to the commutation schemes and electrical angle when the phase current of 10 A is applied.

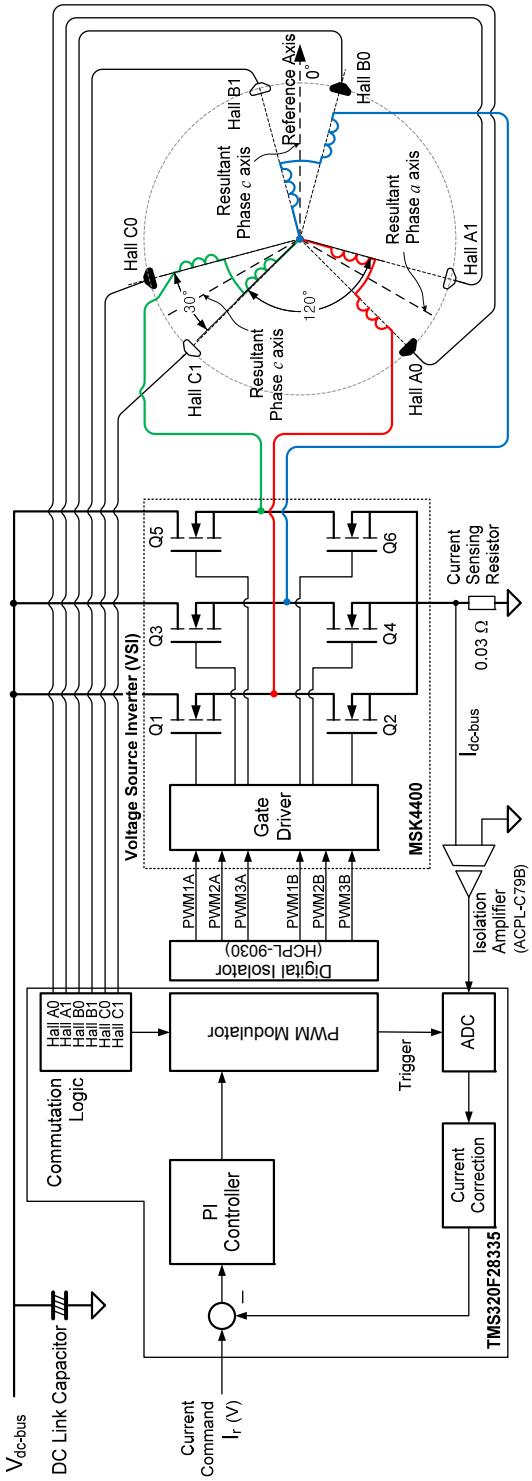

Fig. 91. Hardware block diagram of the 12-step current control for the double-sided IPM-FLBM with slot-phase shift.

4.1.2.B 12-Step Commutation Sequence

Fig. 91 shows the hardware block diagram that consists of the three high-side N-channel MOSFET switches (Q_1, Q_3, and Q_5), three low-side N-channel MOSFET switches (Q_2, Q_4, and Q_6), three Hall-effect sensors (HA0, HB0, and HC0) in the upper stator, and three Hall-effect sensors (HA1, HB1, and HC1) in the lower stator. As shown in Fig. 91, since the upper and lower Hall sensors are placed at the electrical angle of 15° for each resultant phase axis, the twelve position states from the six Hall-effect sensors as shown in Fig. 92 can be achieved for the electrical angle of 360°. Thus, the three quasi-sinusoidal phase voltages are generated using the voltage source inverter (VSI). Furthermore, assuming that the current controller with a high bandwidth is employed, the current space vector at the motor terminal is always located within the nearest 15° of the *q*-axis. This 12-commutation process alternately consists of six two-phase conduction modes (③ in Fig. 92) and six three-phase conduction modes (① and ②). The three-phase conduction mode has two different switching modes. The unipolar pulse-width modulation (PWM) drive is employed for a single DC power supply. The PWM carrier frequency of 20 kHz is used. In addition, in order to reduce the power consumption and increase the lifetime of the VSI, the high-side switches are driven by the PWM, and the low-side MOSFETs are used as an on-off switch for the commutation. Thus, the dead band between the switching times is not considered. The dc-link current is used to estimate the phase current as depicted in

Fig. 91. The voltage drop across a single shunt resistor at the dc-link is amplified through the high-bandwidth isolation amplifier with the bandwidth of 200 kHz (AVAGO

ACPL-C79B). Since the dc-link current in the single-side PWM drive scheme can only be detected during the PWM duty cycle [67], [68], it is sampled using an analog-to-digital converter (ADC) at the center of the PWM duty cycle. Hence, no anti-aliasing analog prefilter is needed in the input stage of the ADC.

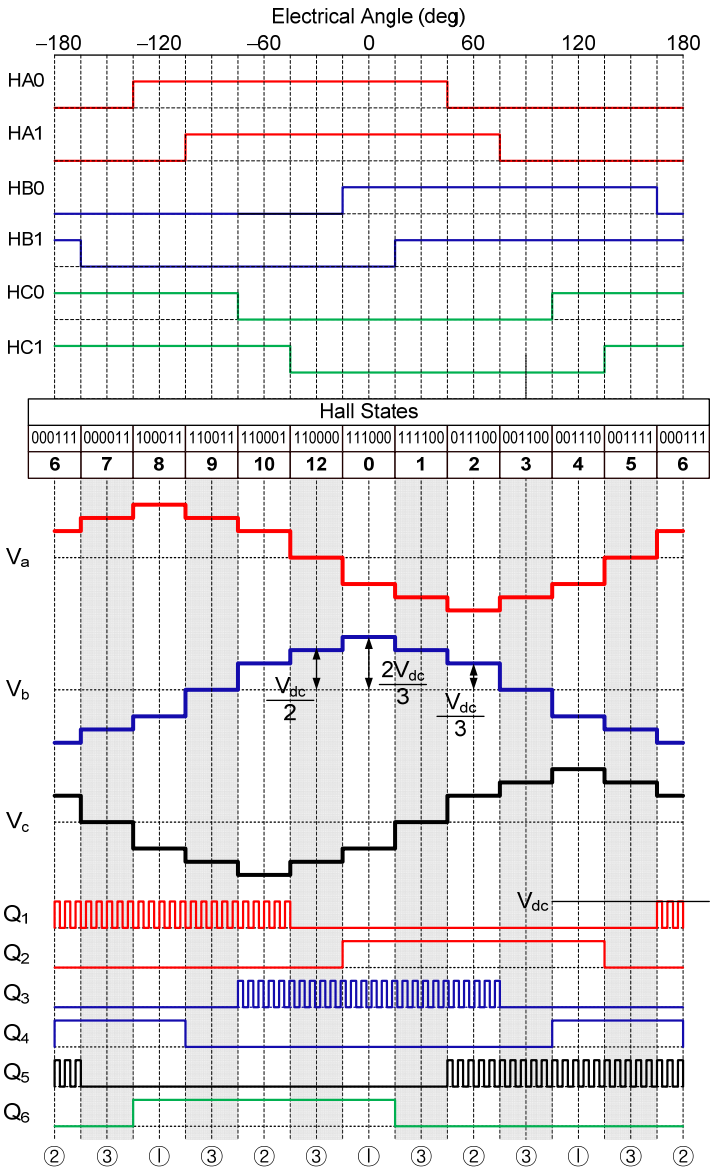

Fig. 92. 12-Step commutation sequence during one electrical angle cycle.

4.1.2.C DC-Link Current Correction

In the single side PWM drive, the dc-link current is one of three phase currents depending on the inverter switching state as listed in Table 18.

Table 18. Phase current measured according to switching states.

Hall States	Electrical Angle	Q						DC-Link Current I_{dc}
		1	3	5	2	4	6	
6	**–180° ~ –165°**	1	0	1	0	1	0	$-i_b$
7	**–165° ~ –135°**	1	0	0	0	1	0	$i_a = -i_b$
8	**–135° ~ –105°**	1	0	0	0	1	1	i_a
9	**–135° ~ –75°**	1	0	0	0	0	1	$i_a = -i_c$
10	**–75° ~ –45°**	1	1	0	0	0	1	$-i_c$
11	**–45° ~ –15°**	0	1	0	0	0	1	$i_b = -i_c$
0	**–15° ~ 15°**	0	1	0	1	0	1	i_b
1	**15° ~ 45°**	0	1	0	1	0	0	$i_b = -i_a$
2	**45° ~ 75°**	0	1	1	1	0	0	$-i_a$
3	**75° ~ 105°**	0	0	1	1	0	0	$i_c = -i_a$
4	**105° ~ 135°**	0	0	1	1	1	0	i_c
5	**135° ~ 165°**	0	0	1	0	1	0	$i_c = -i_b$
6	**165° ~ 180°**	1	0	1	0	1	0	$-i_b$

Hence, it can be used to estimate the phase current in each commutation step. The drawback of this simple method is that when the PWM duty cycle is small, the dc-link current is distorted from the ripple current due to the dc-link capacitor and inductance [67]. However, it can be expressed as a function of the duty cycle. Thus, this distortion is assumed to be a deterministic error due to the applied duty cycle and can be corrected using an error-correction equation as follows:

$$I_{dc}^{*} = \left(1 - I_{ex}\left(T_{dc}\right)\right)\tilde{I}_{dc} \tag{4.6}$$

where I_{dc}^{*} and $\tilde{I}_{dc}$ are the corrected and measured dc-link currents, respectively, T_{dc} is the duty cycle, and $I_{ex}\left(T_{dc}\right)$ is the error function. The results in Fig. 93 show that the maximum current errors of 0.3 A at the switching mode ① is reduced to 0.02 A by using (4.6) in the range of the duty cycle of 50%. In the same way, the maximum errors of 0.4 and 0.45 A at switching modes ② and ③ are also reduced to 0.02 A by using (4.6). The error function is obtained from subtracting the actual phase current from the uncompensated dc-link current. This function with the two piecewise square curves is given as

$$I_e = \begin{cases} a_2\left(T_{dc}/10 + a_1\right)^2 + a_0, & T_{dc} < 7\% \\ b_2\left(T_{dc}/10 + b_1\right)^2, & 7\% \le T_{dc} < 23\% \\ \tilde{I}_{dc}, & T_{dc} \ge 23\% \end{cases} \tag{4.7}$$

where the coefficients of the error function are listed in Table VI.

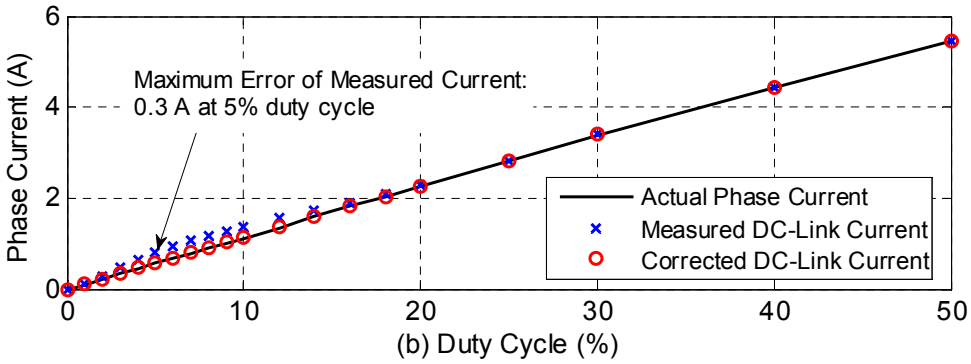

Fig. 93. Actual phase, measured, and corrected dc-link currents according to the duty cycle variation in the switching modes when the dc-link voltage of 30 V is applied.

Table 19. Coefficients of the error function according to switching modes

Switching Modes	a_2	a_1	a_0	b_2	b_1
1	–1.2	–0.50	0.30	0.098	–2.3
2	–1.8	–0.48	0.40	0.139	–2.2
3	–2.0	–0.48	0.45	0.156	–2.2

4.1.2.D Current Control Loop Design

Although the inductances of the IPM motor vary as a sinusoidal function of the mover positions [35], from the *q*- and *d*-inductance values given in Table 17, the only two possible combinations for the equivalent inductance and resistance of the armature winding can be made with respect to the 12-step commutation positions as follows:

$$\begin{cases} L_e = 3.23 \text{ mH}, \quad R_e = 2.52\ \Omega, & \text{for three-phase conduction} \\ L_e = 4.31 \text{ mH}, \quad R_e = 3.36\ \Omega, & \text{for two-phase conduction.} \end{cases} \tag{4.8}$$

This result implies that the bandwidths of the two different conduction modes are the same, but the dc-gain difference of 2.5 dB exists. However, if the high-gain current control loop is achieved by a proportional-integral (PI) controller, this difference becomes negligible. Therefore, the admittance of the armature winding, $P_1(s)$ of Fig. 94 can be written using the average inductance L_{ea} and resistance R_{ea}.

$$P_1(s) \cong \frac{1}{L_{ea}s + R_{ea}}. \tag{4.9}$$

The duty cycle in the 30-V dc-link voltage can be modeled as an equivalent voltage conversion coefficient K_{dv} of Fig. 94. This coefficient can be calculated by (4.10) using the slope of the phase current curve for the duty cycle obtained in Fig. 93. In this

research, since the corresponding value from 0 to 100% duty cycle is implemented as 0 to 10.0, K_{dv} is calculated as

$$K_{dv} \cong \left(I_{dc}^{*} / T_{dc} \right) R_e = 2.85 \text{ [V/Duty Cycle]}. \tag{4.11}$$

The magnitude of the phase current in the three-phase conduction mode is the same as that of the *q*-axis current whenever the *q*-axis is aligned with the center position of each Hall state described in Table 18. However, if the same current command is applied in the two-phase conduction mode, the magnitude of the *q*-axis current becomes much larger than that of the three-phase conduction mode. Thus, the predetermined coefficient for the corresponding current vector is employed to avoid the force pulsation as follows:

$$K_c = \begin{cases} 1.0, & \text{in three-phase conduction} \\ \sqrt{3}/2, & \text{in two-phase conduction} \end{cases}. \tag{4.12}$$

The transfer function of Fig. 94 for the sample and hold delay is given by

$$T_{SH}(s) \cong e^{-sT_S} \tag{4.13}$$

where T_S is the delay time of the current control loop with the update rate of 3.3 kHz. Since the measured dc-link current has only the positive value in the unipolar PWM drive, the absolute value of the current command is used to generate the corresponding current error, and the output sign of the PI controller is determined by the sign of the current command. Thus, the response to either the positive or negative commands with a non-zero value follows the linear model, but its behavior for a bipolar command does not follow the linear model at high frequency. This is due to the dc-bias component of the absolute values generated by the phase lag at high frequency.

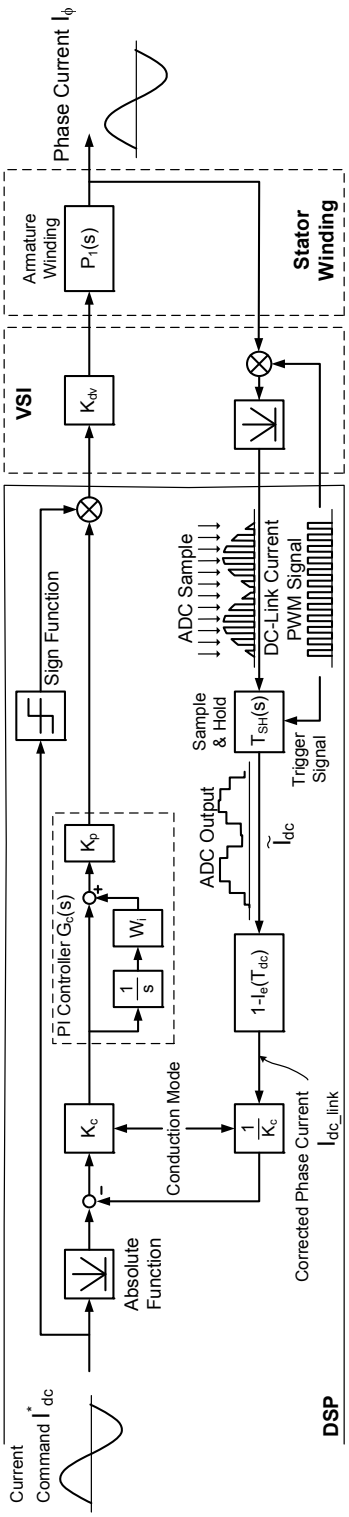

Fig. 94. Block diagram of the 12-step current control using the dc-link current.

Therefore, in this paper, the linear open-loop transfer function obtained from (4.9) to (4.12) is used to determine the initial open-loop gains and relative stability, and the optimal gains of the PI controller are tuned using the empirical approach based on the open-loop frequency response. The open-loop frequency responses in Fig. 95 illustrate that the measured frequency responses for the non-negative sinusoidal current command in the two- and three-phase conduction modes are in good agreement with the calculated ones, but the measured frequency responses for the bipolar sinusoidal command have much higher zero-crossover frequencies than that in the linear models. This is caused by the dc-component error term of the absolute function. As a result, the current control loop has a variable control bandwidth according to the input types. Although its magnitude in the closed-loop has an overshoot of around 1.2 dB at around 450 Hz by the reduced phase margin, this design is still useful in the current control loop with respect to the stability margin. The three-phase conduction mode also has the similar responses. Table 20 shows the performance parameters of the designed current control loop.

Table 20. Open-loop performance of 12-step current control scheme

K_p = 0.7 Duty Cycle/A and W_i = 754 rad/s	**Equivalent Linear Model**	**Measured Values**	
		Minimum	**Maximum**
Open-loop gain at 1.0 Hz (dB)	38.2	34.5	37.5
Crossover frequency (Hz)	82	67.0	316
Phase margin (deg)	83.6	52	83
Gain margin (dB)	21.5	9.4	20.3

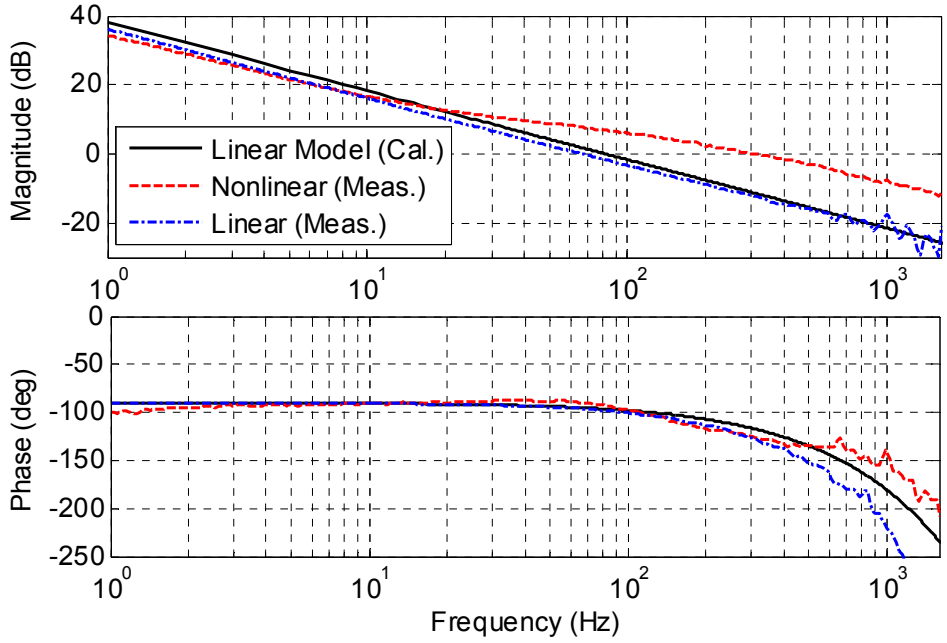

(a)

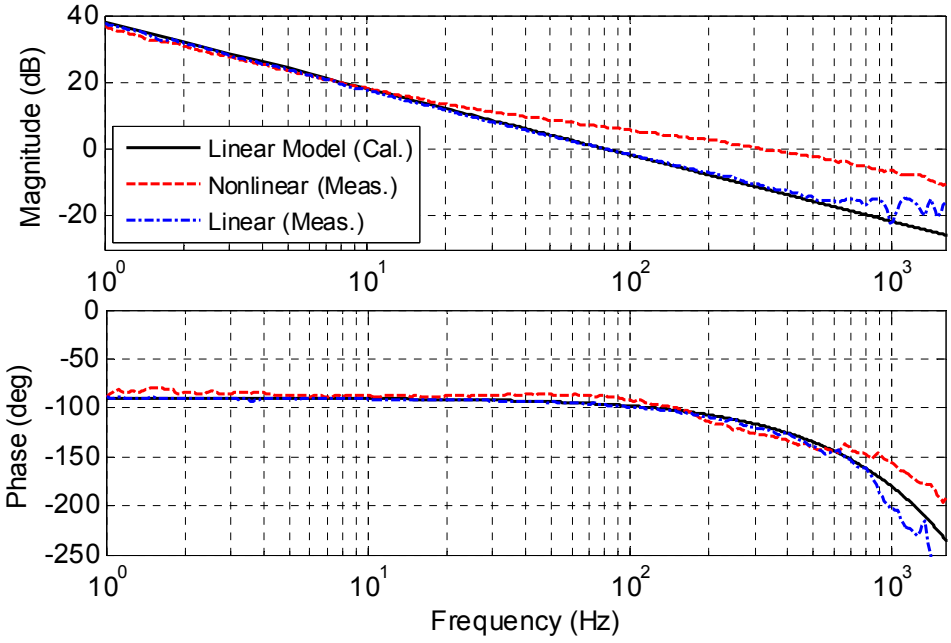

(b)

Fig. 95. Open-loop frequency responses of the phase current I_ϕ for the current command I^*_{dc} in the two-phase conduction mode (a) and three-phase conduction mode (b) when the dc-link voltage is 30.0 V, and the proportional gain K_p and integral gain W_i are 0.7 Duty Cycle/A and 754 rad/s, respectively.

4.1.3 Field-Oriented Control

Recently, the FOC, a branch of vector control emerged in the mid-1980s, is becoming an industrial standard for the force control due to its remarkable advantages such as wide speed range and little ripple force [42]. Therefore, the conventional indirect FOC scheme in Fig. 96 is also implemented on the resultant vector coordinates defined in Fig. 87(c) for the performance comparison with the proposed 12-step current control scheme.

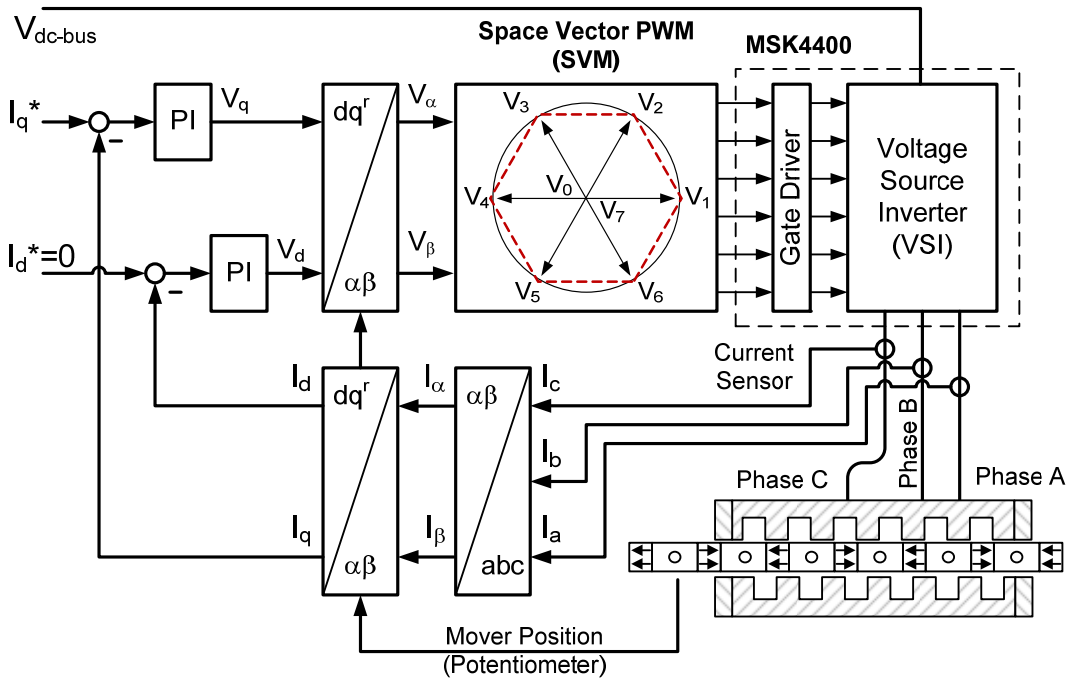

Fig. 96. Control block diagram of the indirect FOC scheme for the double-sided IPM-FLBM with the slot-phase shift.

4.1.3.A Clarke and Park Transformation

As shown in the control block diagram in Fig. 96, Clarke and Park transformations [35] are used to transform the stator currents into the current space vector in the *d-q* reference frame. The stationary two-axis currents for the three-phase currents in the stator frame defined in Fig.2(c) are given through the Clarke transformation as follows:

$$\begin{cases} i_\alpha = i_b \\ i_\beta = \left(i_c - i_a\right)/\sqrt{3} \end{cases} \tag{4.13}$$

By using Park transformation, the currents in the *d-q* reference frame are given as

$$\begin{cases} I_q = i_\alpha \cos\left(\theta_e\right) + i_\beta \sin\left(\theta_e\right) \\ I_d = i_\alpha \sin\left(\theta_e\right) - i_\beta \cos\left(\theta_e\right) \end{cases} \tag{4.14}$$

4.1.3.B Space Vector Pulse Width Modulation

The space vector PWM (SVM) method that can generate a higher modulation index and lower current harmonics as compared with other PWM drive methods [69], [70] is used in this study. Thus, the complimentary PWM drive scheme is also employed to implement this SVM. Fig. 97(a) shows the eight states according to the eight switching positions of the VSI [70]. Since the resultant axis of the phase *b* is defined as the reference axis as shown in Fig. 87(c), the space vector sequences are rotated counterclockwise by 120° as compared with [69], [70]. The magnitude V_{ref} and angle $\theta_{\alpha\beta}$ of the reference voltage space vector are calculated by

$$V_{ref} = \sqrt{V_\alpha^2 + V_\beta^2}, \quad \theta_{\alpha\beta} = \tan^{-1}\left(V_\beta / V_\alpha\right) \tag{4.15}$$

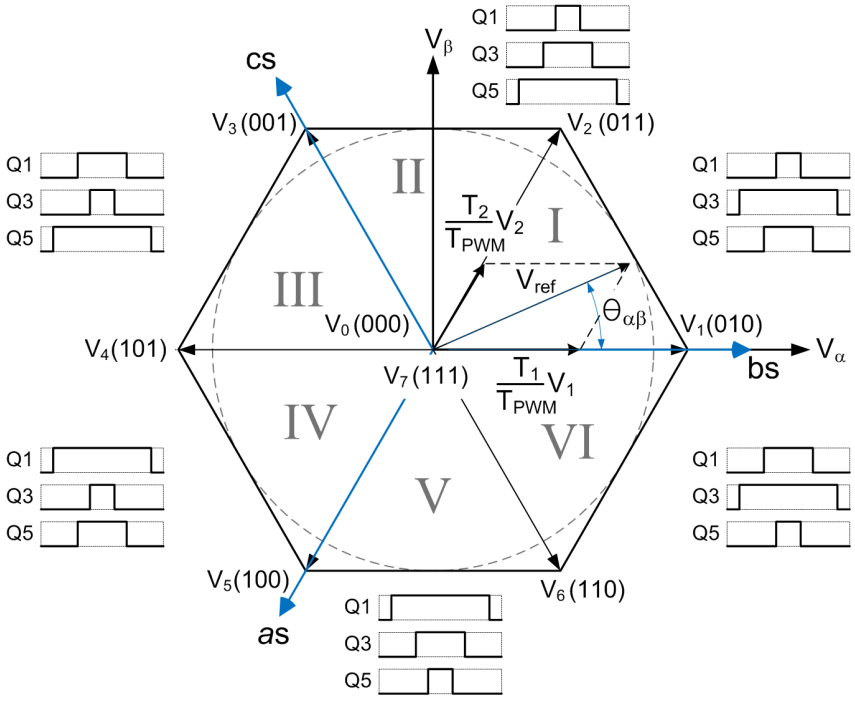

(a)

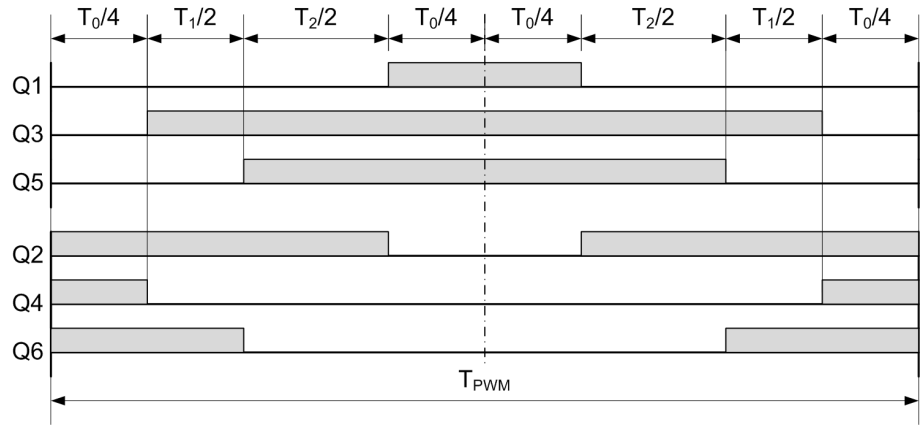

(b)

Fig. 97. (a) A representation of the space vectors V_1 to V_6, and a voltage vector V_{ref}. (b) The space vector modulation of the three-phase voltages in sector I.

The reference voltage space vector is represented using two adjacent vectors in the sector determined by (4.15) as follows:

$$\begin{cases} V_{ref} T_{pwm} = V_n T_n + V_{n+1} T_{n+1} \\ T_{pwm} = T_0 + T_n + T_{n+1} \end{cases} \tag{4.16}$$

where T_{pwm} is the period of the PWM carrier frequency. The sector number n is calculated using the sector detect algorithm in [71]. The switching times of Q_1, Q_2, and Q_3 during the next period PWM shown in Fig. 97(b) are defined as

$$\begin{cases} T_n = \left(\sqrt{3} T_{pwm} V_{ref} / V_{dc}\right) \sin\left(n\pi/3 - \theta_{\alpha\beta}\right) \\ T_{n+1} = \left(\sqrt{3} T_{pwm} V_{ref} / V_{dc}\right) \sin\left(\theta_{\alpha\beta} - (n-1)\pi/3\right) \\ T_0 = T_{pwm} - \left(T_n + T_{n+1}\right) \end{cases} \tag{4.17}$$

4.1.3.C Current Measurement and PI Controller

The current sensor (Melexis, MLX91205LB) with a 0.5% nonlinearity and 100-kHz bandwidth is implemented to measure the phase current. The two high-gain PI controllers are independently designed for the *q*- and *d*-axes. Like the 12-step current control loop, the current control loop with the update rate of 3.3 kHz is used. The voltage commands in the *d-q* reference frame calculated from the two PI controllers are transformed to the stationary two-axis voltage commands using the inverse Park transformation as follows:

$$\begin{cases} V_\alpha = V_q \cos\left(\theta_e\right) + V_d \sin\left(\theta_e\right) \\ V_\beta = V_q \sin\left(\theta_e\right) - V_d \cos\left(\theta_e\right) \end{cases}, \tag{4.18}$$

and then are fed to the SVM. The open-loop performance parameters in Table 21 illustrate that the measured frequency responses are in good agreement with the calculated ones.

Table 21. Open-loop performance of FOC scheme

	***q*-axis** K_p **= 2.6 V/V,** W_i **= 522 rad/s**		***d*-axis** K_p **= 1.7 V/V,** W_i **= 691 rad/s**	
	Calculations	**Measurements**	**Calculations**	**Measurements**
Open-loop gain (dB) at 1.0 Hz	38.6	38.5	38.6	38.3
Zero-crossover frequency (Hz)	103	96	100	88
Phase margin (deg)	64.2	71.7	62.1	69.3
Gain margin (dB)	6.6	7.0	7.3	7.7

4.1.4 Performance Comparisons

A 150-W DC power supply was used for the VSI. A precision bidirectional load cell with the 0.1% nonlinearity was employed to measure the steady-state thrust and pulsating forces. The linear potentiometer with the 0.1% nonlinearity was also used to estimate the electrical angle of the mover. The measured signals were recorded with the update rate of 1.2 ms through the control area network (CAN) between the DSP and the LabVIEW GUI command console.

Fig. 98 shows the dc-link current and the phase current waveforms for the step current command of 1.0 A in the 12-step current control scheme. Although the phase current spike by the overshoot of the current loop exists whenever the conduction mode

is switched, the three 12-step phase currents are well generated as the electrical angle interval of 30° (i.e. 3.0 mm in linear displacement) with respect to the mover positions.

The results of Fig. 99 for the step current command of 1.0A in the FOC scheme illustrate that although the noise in the *d*-axis current increases whenever each sinusoidal phase current passes through the zero-cross point, the *q*-axis current does follow the current command.

The unit current vector trajectories of Fig. 100 obtained from the results of Fig. 98 and 97 show that the 12-step current control is in good agreement with the dodecagon calculated from (4.3), and the FOC scheme follows the unit-circle trajectory as expected. The magnitude of the current vector in stationary αβ-reference frame is given as $I_s = \sqrt{i_\alpha^2 + i_\beta^2}$.

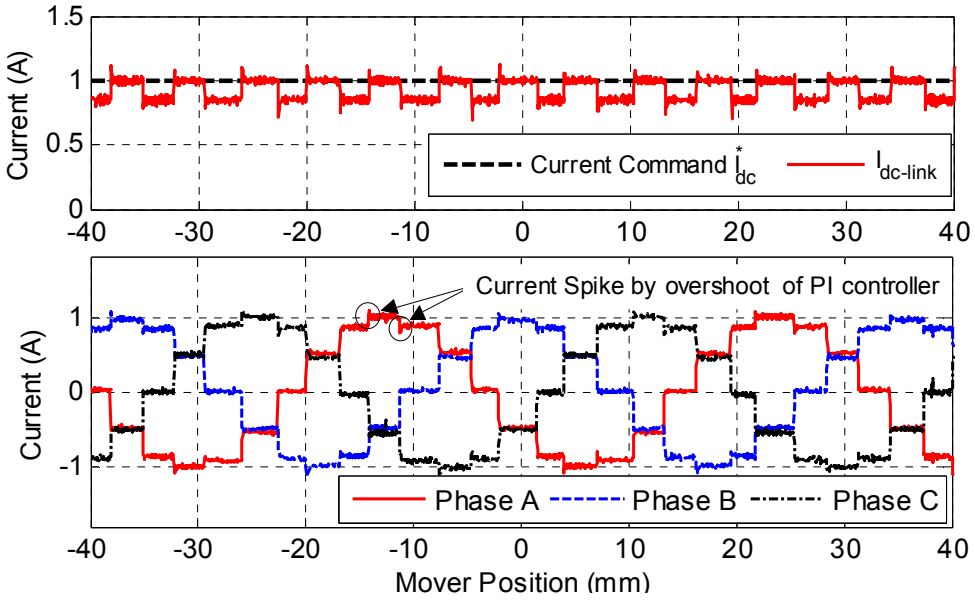

Fig. 98. The dc-link current (top) and phase current waveforms (bottom) with respect to the mover positions when the step current command of 1.0 A is applied in the 12-step current control scheme.

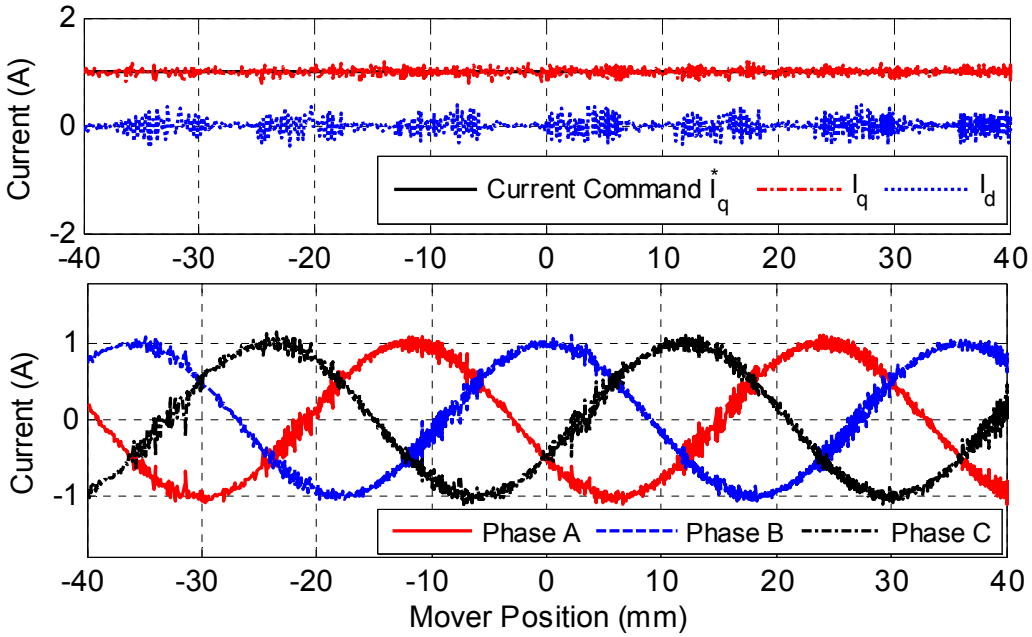

Fig. 99. The measured *q*- and *d*-axis current (top) and phase current waveforms (bottom) according to the mover positions when the step current command of 1.0 A is applied in the FOC scheme.

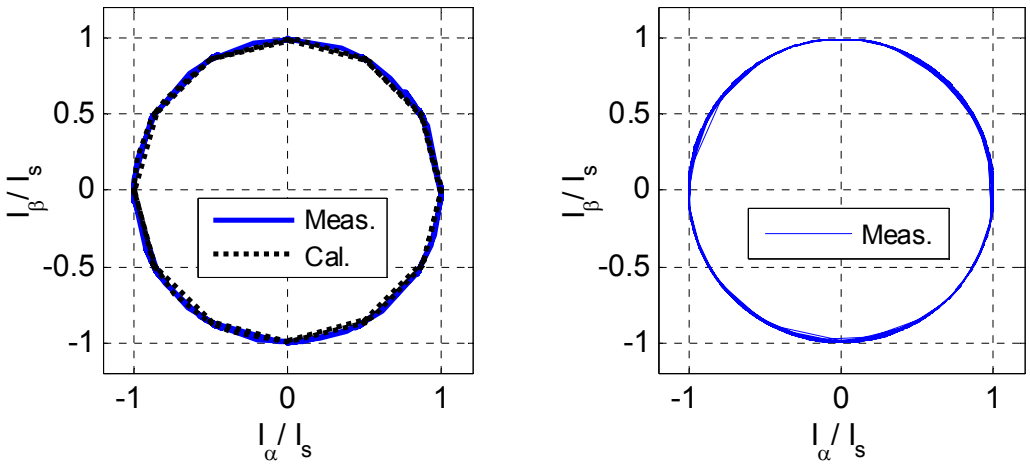

(a) (b)

Fig. 100. The current vector trajectories in the stationary αβ-reference frame: (a) 12-step current control scheme and (b) FOC scheme.

The results in the top plot of Fig. 101 show the thrust forces for the sinusoidal current command of 1.0 A with 3.0 Hz in two different current control schemes. Since the measured thrust force is not the blocked force, it can directly be expressed by the simple equation using the force constant, but the results illustrate that the FOC scheme produces around 3% more force than the 12-step current-control scheme. The middle and bottom plots in Fig. 101 show the corresponding dc-link current and *q*-axis current in two different current control schemes.

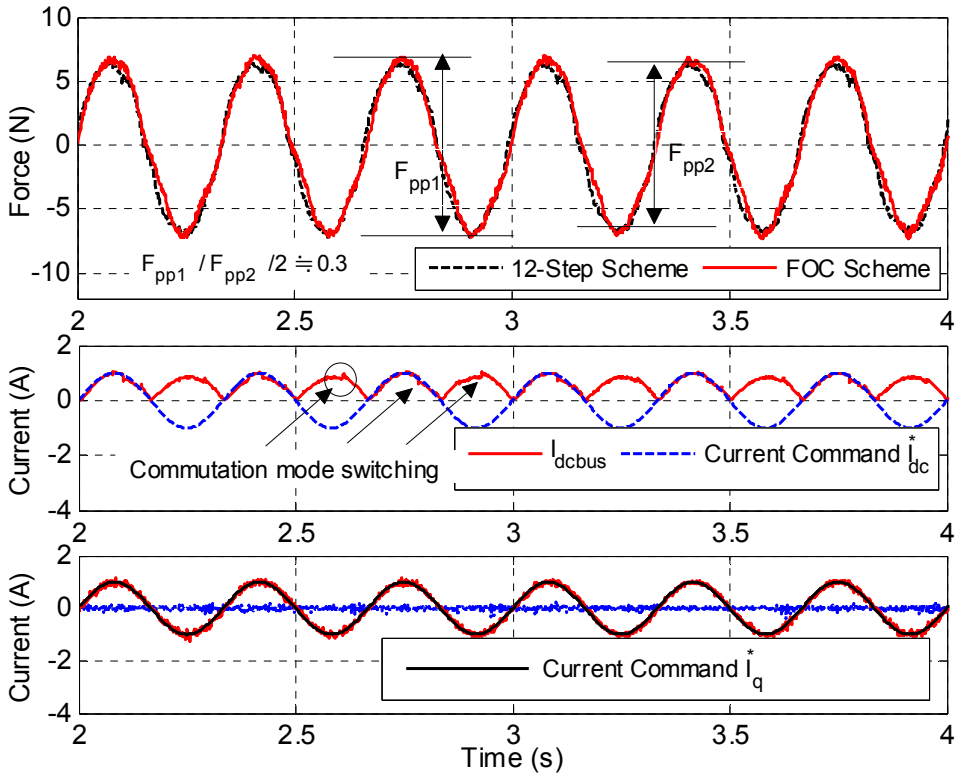

Fig. 101. Thrust forces of the 12-step current control and FOC schemes according to the sinusoidal current command of 1.0 A and 3.0 Hz: thrust forces (top), current command I^*_{dc} and dc-link current $I_{dc\text{-}link}$ (middle), and current command I^*_q, q-axis current I_q, and d-axis current $I_d = 0$ (bottom).

The top plot of Fig. 102 gives the measured pulsating forces when the mover connected with the dummy load of 1.1 kg is moved at a constant speed of 0.1 m/s. The results are governed by the periodic detent force (i.e. the cogging and end-effect forces) and friction force (i.e. Coulomb and viscous friction) because the ripple force was relatively small. However, since the average force of the measured pulsating force is the friction force at a constant speed, and the detent force can be measured under no electrical load condition, the ripple force due to the control scheme can be calculated by

$$F_{ripple} = F_{pls} - F_{frn} - F_{dnt} \tag{4.19}$$

where F_{pls}, F_{frn}, and F_{dnt} are the pulsating, friction, and detent forces, respectively. In theory, the FOC has much lower ripple force than the 12-step current control. Nonetheless, the measurements in the bottom of Fig. 102 show that both current control schemes exhibit almost the same performance. This is because the ripple force was generated by the mechanical imperfection rather than the electrical commutation in the case that the controller performance was improved. The ripple force of approximately 316 Hz shown in the FOC scheme was caused by the mechanical vibration between the roller and mover guide. The peak-to-peak, standard deviation, and rms ripple forces of the 12-step current control and FOC schemes are measured as 1.697 N, 1.597 N, 0.177 N, 0.194 N, 0.255 N, and 0.277 N, respectively. The peak-to-peak ripple forces in both current control schemes are a 2.8% of the maximum thrust force given in Table 17. The results in Fig. 103 show the force-constant and power-consumption comparisons between the two current control schemes in this paper. The FOC consumes much more electric power due to the SVM nature than the 12-step current control scheme.

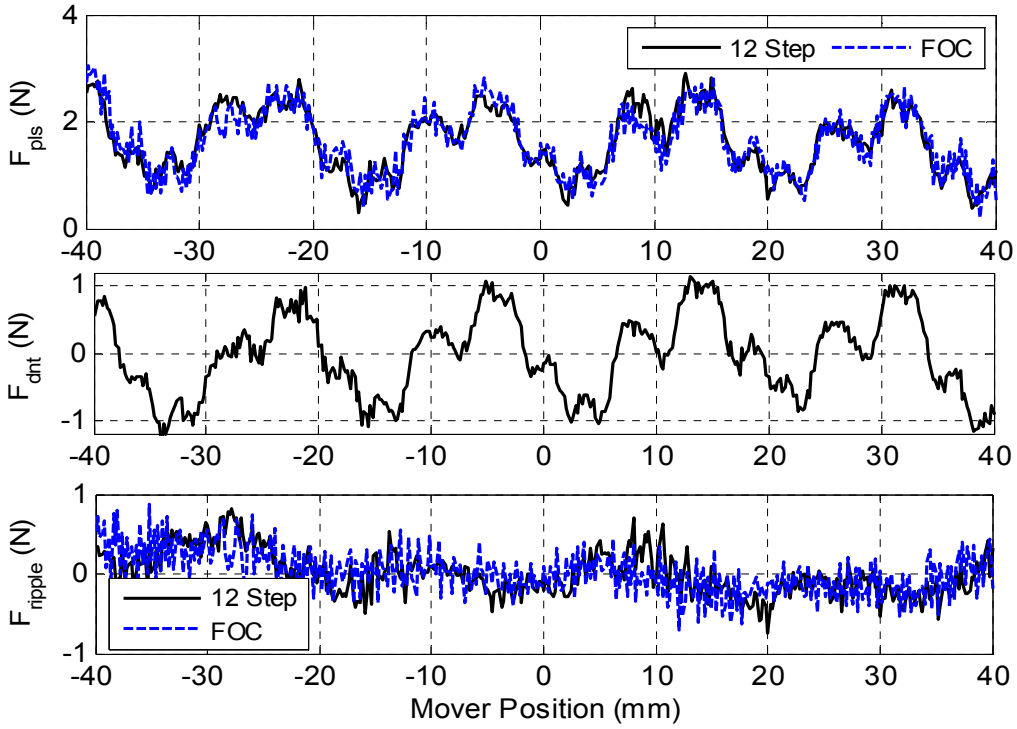

Fig. 102. Pulsating forces (top), detent force (middle), and ripple forces (bottom) of the 12-step current control and FOC schemes when the mover moves at the constant speed of 0.1 m/s.

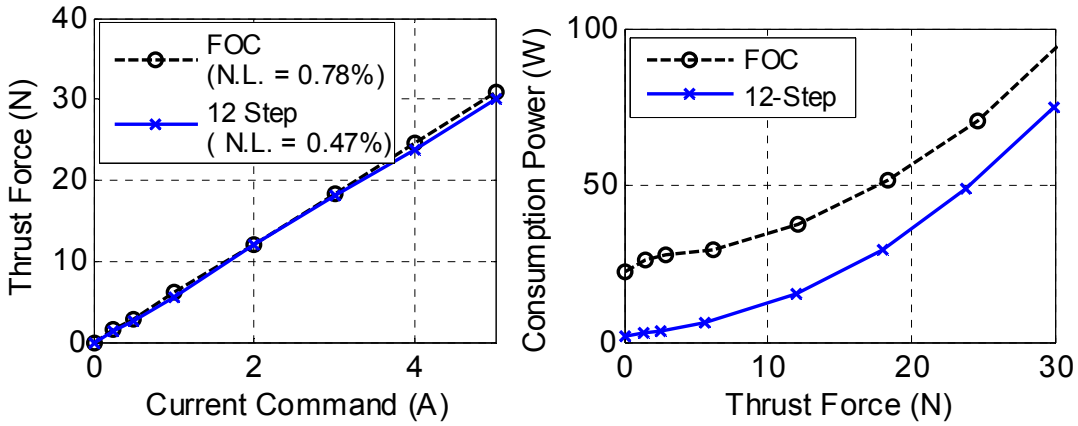

Fig. 103. (a) Thrust force versus current command (K_f = 6.05 and 6.18 N/A for the 12-step current control and FOC schemes, respectively). (b) Electric power consumption comparison according to the thrust force.

4.2 Linear Motion System Model

4.2.1 Lumped-Parameter Model

Since the dynamic modeling presents its inherent behavior, obtaining a proper model is very important to design a controller. In this sense, a lumped-parameter approach for a dynamic system with a low control bandwidth can be an effective tool to model the control objectives in the initial design phase.

Therefore, the system identification of the linear motion platform is investigated using the lumped-parameter model as shown in Fig. 104. The mover of the IPM-FLBM is assumed to be a composite rod with a concentrated mass. Since the dummy mass and mover are constrained by a linear guide rail and the eight roller bearings of the stator housing, respectively, the x-direction motion is only considered. The equivalent spring constants of the mover, two side frames, and front frame are employed between the mover and dummy masses. The loading force due to the gravity and the structural damping of the mover are not considered.

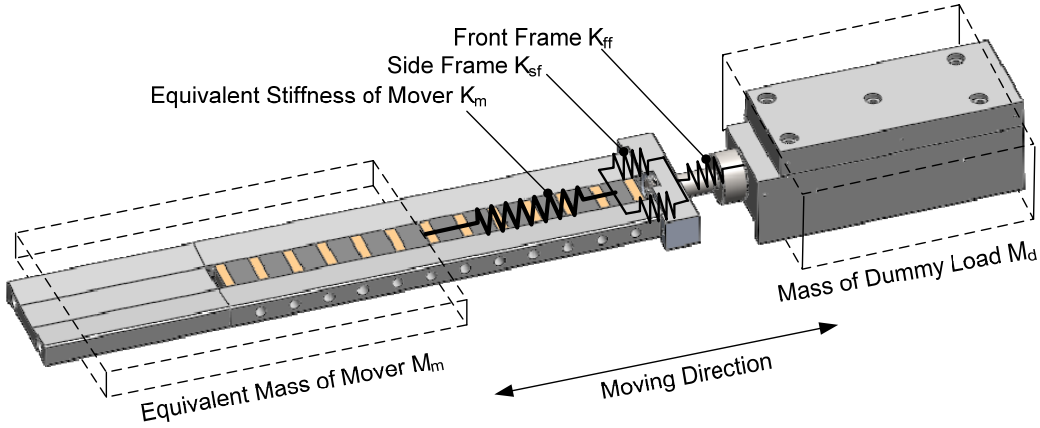

Fig. 104. Lumped-parameter model concept for linear motion platform.

4.2.2 Identification of Equivalent Stiffness

The mover of the IPM-FLBM consists of three different materials such as PM, iron core, and aluminum alloy. Thus, the stiffness of the mover can be represented by the spring constant of a composite material with three different stiffness values. The effective stiffness of the mover can be expressed as

$$K_m \approx \frac{K_{ic}\left(2K_{sf}+K_{pm}\right)}{n\left(2K_{sf}+K_{pm}+K_{ic}\right)} \tag{4.20}$$

where K_m is the equivalent stiffness of the mover, K_{sf} is the stiffness of the side frame for one pole pitch, K_{ic} is the stiffness of the iron-core block, K_{pm} is the stiffness of the PM block, and n is the number of the pole pitches pushed out from the stator housing. This equation indicates that its value varies depending on the mover position because the stiffness of the mover is inversely proportional to the displacement of mover pushed out from the stator due to its operating structure. The equivalent stiffness of the side and front frame can be given by

$$K_{ef} \approx \frac{2K_{sf}K_{ff}}{2K_{sf}+K_{ff}}. \tag{4.21}$$

where K_{ff} is the stiffness of the front frame. As a result, the total equivalent stiffness between two masses can be approximated as

$$K_e(n) \approx \frac{K_m K_{ef}}{K_m+K_{ef}} = \frac{2K_{sf}K_{ff}K_{ic}\left(2K_{sf}+K_{pm}\right)}{\left(2K_{sf}+K_{pm}\right)\left(2K_{sf}+K_{ff}\right)K_{ic}+2nK_{sf}K_{ff}\left(2K_{sf}+K_{pm}+K_{ic}\right)} \tag{4.22}$$

Equation (4.22) indicates that the exact stiffness evaluation per a node in the composite structure is required in order to calculate the equivalent stiffness of the mover assembly.

However, it is not easy to compute its exact values and boundaries. In this study, thus, the FEA using Solidworks is used to evaluate the equivalent stiffness of the mover assembly. The FEA model in Fig. 105 shows the constraints and materials employed in the mover model when the mover is fully deployed from the stator housing. The four iron cores of the mover are assumed to be fixed by the electromagnetic force. The component contacts between the iron cores, PMs, and side frames are assumed to be bonded.

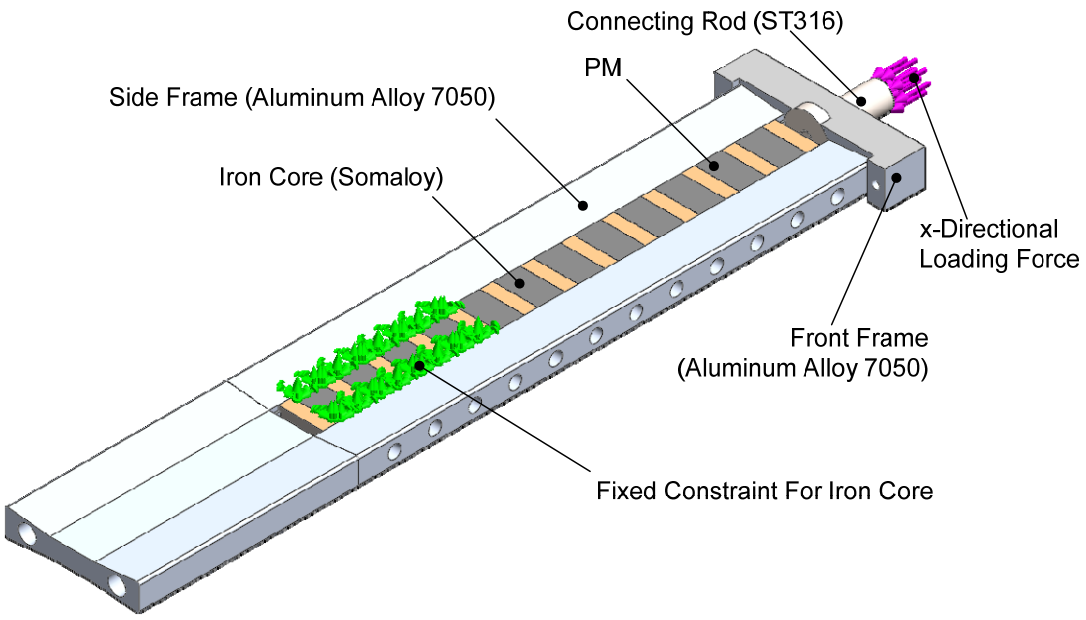

Fig. 105. Isometric view of the FEA model to evaluate the equivalent stiffness.

The simulation result in Fig. 106 shows the static deformation for the x-directional loading force of 100 N. The maximum cumulative deformation in the x-direction occurs at the center of the front frame, and its value is evaluated as 0.00065 mm. The maximum cumulative deformations in the y- and z-directions are evaluated as 0.000018 mm and

0.000056 mm, respectively at the center and side of the front frame. As expected, the deformations in the y- and z-directions are much smaller than the x-directional deformation. Table 22 describes the material properties used in this study.

Table 22. Material properties used in FEA

Characteristic	Unit	AL 7050	ST 316	PM	Somaloy
Density	kg/m^3	2830	8000	7474	7300
Young's modulus	$10^{11} N/m^2$	7.2	1.93	1.6	1.9
Tensile mtress	$10^6 N/m^2$	550	550	75	448
Poisson's ratio		0.33	0.3	0.24	0.26

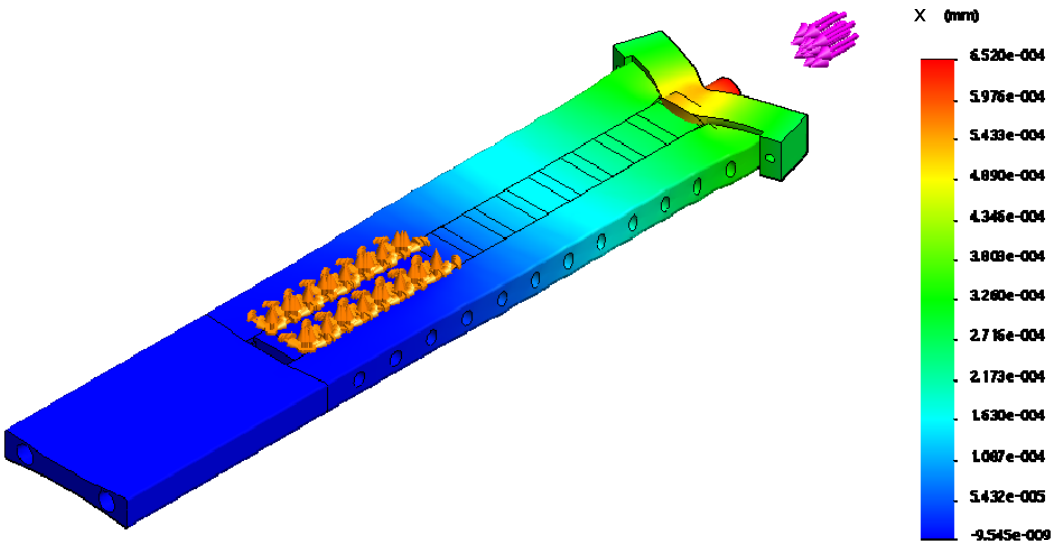

Fig. 106. Static deformation of the mover assembly when the x-directional loading force of 100 N is applied.

The result in Fig. 107 illustrates the x-directional deformation of the mover assembly according to the applied forces and mover positions. The more the mover moves to the

positive displacement limit, the larger deformation the mover assembly has under the same applied force. The larger the applied force is, the larger deformation the mover assembly has at the same mover position.

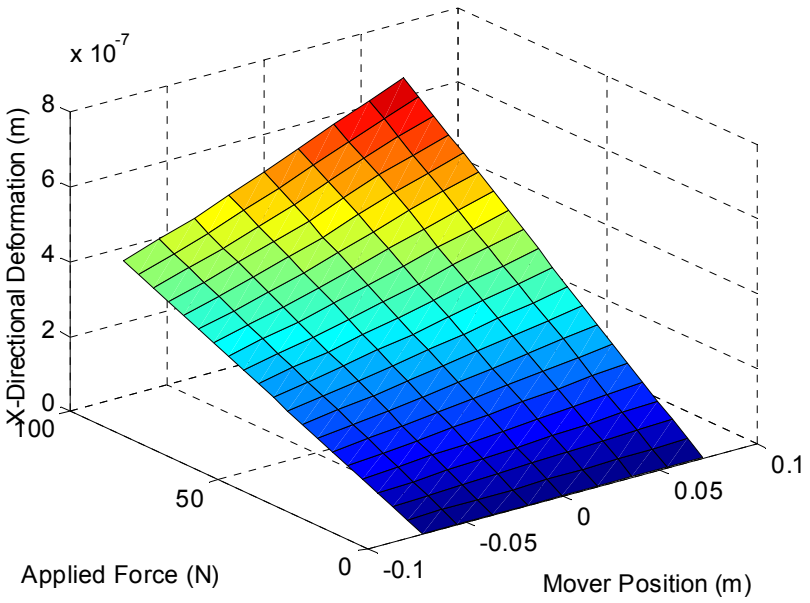

Fig. 107. X-directional deformation according to the applied forces and the mover positions.

The result in Fig. 108 shows the equivalent spring constant calculated using Hookes' law and the result of Fig. 107. As expected, the equivalent stiffness K_e is given as a nonlinear function for the mover position. The equivalent spring constant has the range from 153710 N/m to 275260 N/m. However, since it is not easy to employ this nonlinear spring constant in the control loop design, the equivalent spring constant when the mover is located at the zero position is used as a typical value in this study.

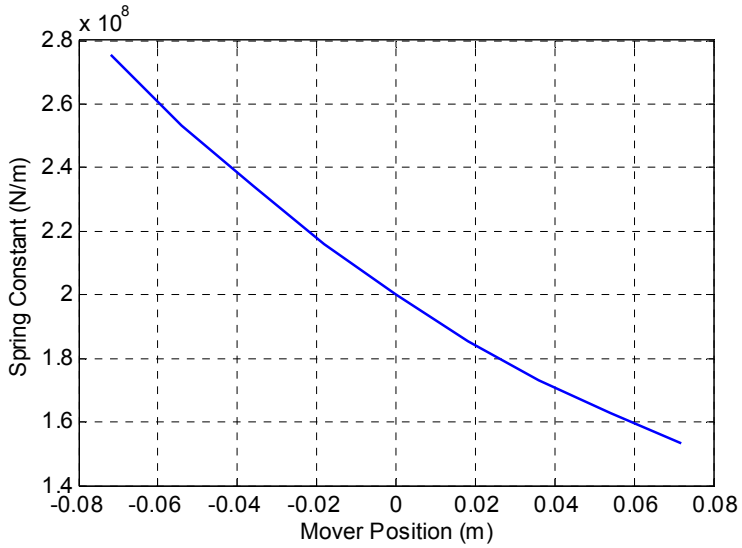

Fig. 108. Equivalent spring constant of the mover assembly according to the mover positions.

4.2.3 Simplified Model of Linear Motion Platform

The schematic diagram in Fig. 109 shows the 2-DOF lumped-parameter model of the linear motion system modeled on the basis of Section 4.2.1–4.2.2.

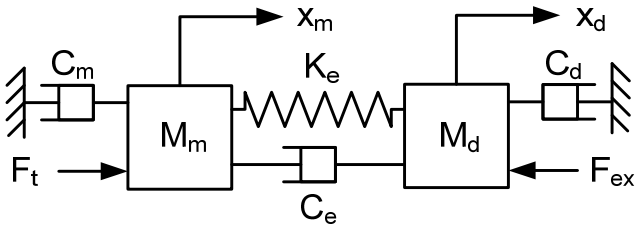

Fig. 109. Parameters and variables in the lumped-parameter model.

Here K_e and C_e are the equivalent stiffness and structural damping between the mover and dummy mass, respectively, M_m is the mover mass including the connecting rod, M_d is the dummy mass, x_m and x_d are the x-directional motion variables of the mover

and dummy masses, respectively, C_m is the viscous friction of the mover mass, C_d is the viscous friction of the linear guide rail of the dummy mass, F_t is the thrust forces of the IPM-FLBM, and F_e is the external disturbance acting on the dummy mass. The state-space matrix form for the lumped-parameter model in Fig. 109 can be written as

$$\begin{aligned} \dot{\mathbf{x}} &= \mathbf{A}\mathbf{x} + \mathbf{B}\mathbf{u} \\ \mathbf{y} &= \mathbf{C}\mathbf{x} \end{aligned} \tag{4.23}$$

where **A**, **B**, and **C** are the system, input, and output matrices, respectively, and **x** and **u** are the state and input vectors, respectively. Assuming that the measurable output is only X_d from the position sensor attached in the dummy mass, the elements in each matrix can be given as

$$\mathbf{A} = \begin{bmatrix} 0 & 1 & 0 & 0 \\ -\dfrac{K_e}{M_m} & -\dfrac{C_m + C_e}{M_m} & \dfrac{K_e}{M_m} & \dfrac{C_e}{M_m} \\ 0 & 0 & 1 & 0 \\ \dfrac{K_e}{M_d} & \dfrac{C_e}{M_d} & -\dfrac{K_e}{M_d} & -\dfrac{C_d + C_e}{M_d} \end{bmatrix} \tag{4.24}$$

$$\mathbf{B} = \begin{bmatrix} 0 & 0 \\ \dfrac{1}{M_m} & 0 \\ 0 & 0 \\ 0 & \dfrac{1}{M_d} \end{bmatrix} \tag{4.25}$$

$$\mathbf{C} = \begin{bmatrix} 0 & 0 & 0 & 0 \\ 0 & 0 & 1 & 0 \end{bmatrix} \tag{4.26}$$

Therefore, the transfer function for the input force is given by

$$\frac{X_d(s)}{F_t(s)} = \mathbf{C}\left(s\mathbf{I}-\mathbf{A}\right)^{-1}\mathbf{B}$$
$$= \frac{C_e s + K_e}{M_m M_d s^4 + \left(M_m\left(C_d + C_e\right) + M_d\left(C_m + C_e\right)\right)s^3}$$
$$\frac{}{+\left(K_e\left(M_m + M_d\right) + C_d C_m + C_m C_e + C_d C_e\right)s^2 + K_e\left(C_m + C_d\right)s} \quad (4.27)$$

From the above transfer function, assuming that the damping coefficients are negligible because the values are much smaller than the spring constants, the resonant frequency is governed by the spring constant and its value can be expressed as

$$f_{res} = \frac{1}{2\pi}\sqrt{\frac{K_e\left(M_m + M_d\right)}{M_m M_d}} \quad \text{[Hz]} \quad (4.28)$$

where the mover mass M_m and dummy mass M_d are given as 0718 kg and 1.0936 kg, respectively. If the equivalent stiffness K_e is chosen as around 2×10^8 N/m from Fig. 108, the lowest resonant frequency due to the mechanical system is calculated as 1.081 kHz. This implies that the linear motion platform can be modeled as a pure mass system (i.e. a rigid-body motion) at the position loop with a low bandwidth. As a result, the linear motion platform in this study can be simplified as Fig. 110.

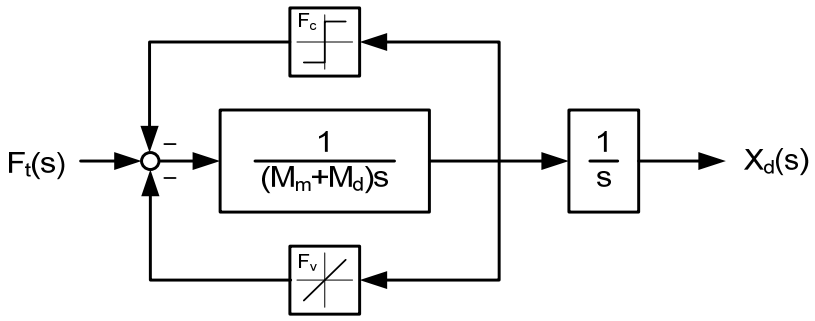

Fig. 110. Simplified pure mass model with a friction model.

4.2.4 Dynamic Friction Model

The friction in the mechanical motion system can be defined as an external disturbance in a control loop. This friction is generally expressed as the function of a velocity as

$$F_f(x_m) = F_v \dot{x}_m + \left(F_c + \left(F_s - F_c \right) e^{-\left(\dot{x}_m / \dot{x}_s \right)^2} \right) sgn(\dot{x}_m) \tag{4.29}$$

where F_c is the Coulomb friction, F_v is the viscous friction coefficient, F_s is the stiction, $\dot{x}_s$ is the Stribeck velocity, and $\dot{x}_m$ is the velocity of the mover. Since the friction is one of major disturbances which degrade the position tracking performance of the position control loop, its proper modeling plays a key role in minimizing the error between the simulation and real system. However, since it is difficult to use this model in the frequency response analysis, the friction model of (4.29) is used for the time response analysis. The first order function of (4.30) is separately employed in the frequency response analysis.

$$F_f(s) = \frac{\sigma_1 s + F_v}{s} \tag{4.30}$$

where σ_1 is the empirical coefficient corresponding to the Coulomb friction. This value can be obtained from the frequency response of the real system. Since the F_v and F_c can be determined by measuring the steady-state friction force when the velocity is held constant, the velocity control loop shown with a unity feedback gain in Fig. 111 is made to measure the error command according to the velocity command.

$$K_v K_a K_f e_s = F_v \dot{x}_m + F_c sgn(\dot{x}_m) \tag{4.31}$$

where K_v is the proportional gain of the velocity control loop, K_a is the current controller gain, K_f is the force constant of the IPM-FLBM, and e_s is the velocity error. Fig. 112 illustrates the measured friction and the friction model obtained from the least-square curve fit. The detent force is not considered in the measurement and simulation model.

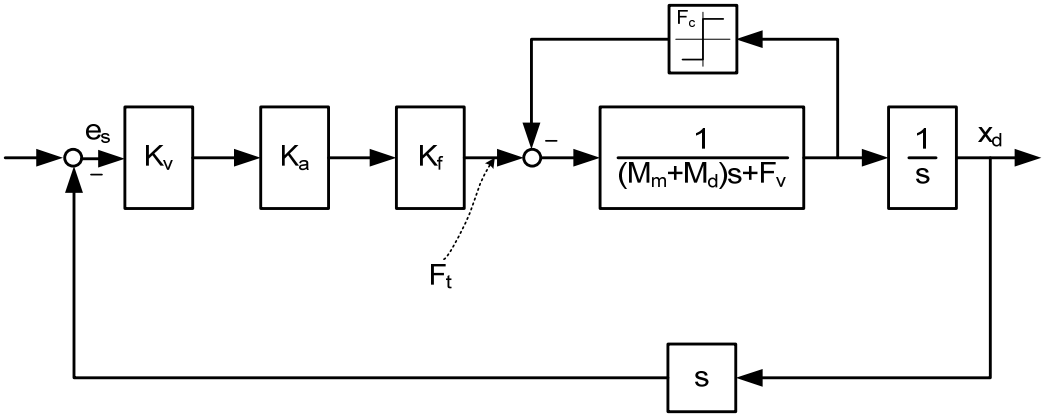

Fig. 111. Velocity control loop to measure the friction coefficients.

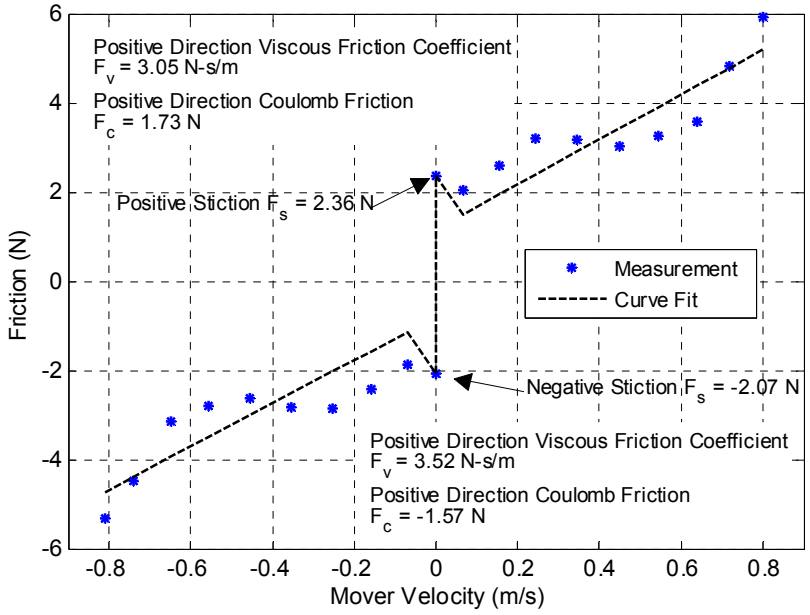

Fig. 112. Measured and modeled frictions.

4.3 Position Loop Design and Performance

The current controllers with a high gain are designed in Section 4.1. These current control loops with the BLAC can be considered as a DC motor with a current controller as shown in Fig. 113. When the Coulomb friction is zero, the transfer function can be written as

$$X_d(s) = \frac{K_A K_f}{M_e L s^2 + \left(M_e R + F_v L + \frac{K_A}{K_a} m\right) s + \left(F_v R + K_e K_f + \frac{K_A}{K_a} F_v\right)} V_r(s) = G_a(s) V_r(s) \quad (4.32)$$

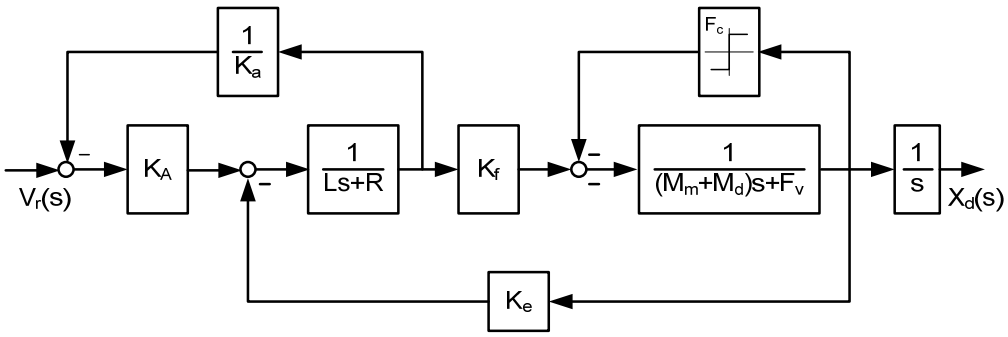

Fig. 113. Current loop model of the linear motion system.

Equation (4.3.1) implies that the gain K_A of the current amplifier is larger than other parameters, the transfer function can be simplified as

$$X_d(s) \cong \lim_{K_A \to \infty} G_a(s) V_{cmd}^* = \frac{K_f K_a}{M_e s + F_v} V_r(s) \quad (4.33)$$

where M_e is the sum of the mover M_m and dummy masses M_d, K_A is the current amplifier gain, K_a is the feedback gain of current loop, K_e is the back-emf of the IPM-FLBM, K_f is thrust force constant, L is the inductance, R is the armature resistance, and V_r is the

reference voltage command. Thus, the simplified linear motion system with the current controller can be described as Fig. 114. Table 23 shows the simulation parameters used in the time- and frequency-domain analyses. The average values of the viscous and Coulomb frictions in the positive and negative directions are used in the model.

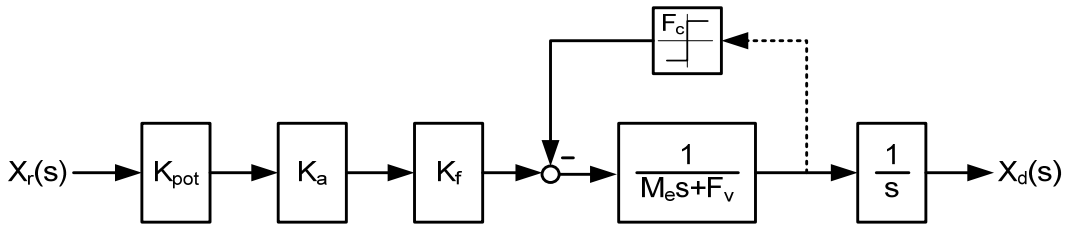

Fig. 114. Simplified open-loop model for the linear motion system.

Table 23. Simulation parameters

Parameters	Symbols	Units	Values
Equivalent mass	M_e	Kg	1.82
Force constant	K_f	N/A	5.9
Transconductance gain	K_a	A/V	1.0
Potentiometer scale factor	K_{pot}	V/m	200
Viscous friction	F_v	N-s/m	3.28
Coulomb friction	F_c	N	1.65

4.3.1 Frequency Response of Uncompensated System

In order to design the position controller, the open-loop frequency response for the analytical model of the uncompensated system shown in Fig. 114 is compared the measured frequency responses in the 12-step current controller and FOC. The attenuated

magnitude and lagged phase due to the Coulomb friction is modeled using (4.31). The value of σ_l is assigned as 15 in order to match with the measurements. Although there are slight distortions due to the small signal level in the high frequency region of the measured phase response, the open-loop frequency responses in Fig. 115 show the analytic response are in good agreement with measured ones. Table 24 shows the characteristic comparisons between the analytic model and measured ones.

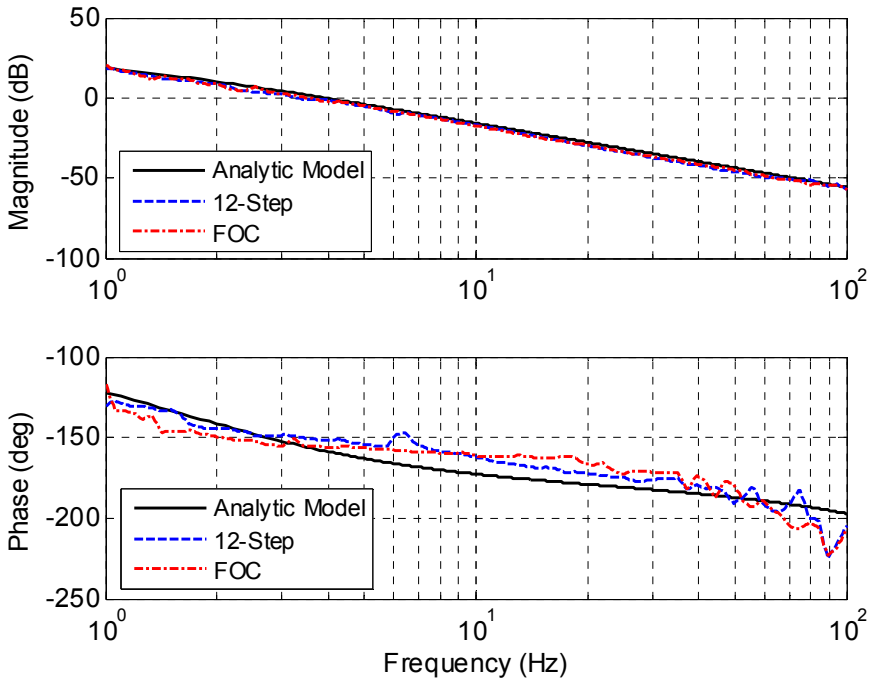

Fig. 115. Open-loop frequency responses of the uncompensated system.

Table 24. Open-loop frequency response characteristics of the uncompensated systems

Characteristics	Analytic Model	12-Step Current Control	FOC
Open-loop gain	18.8	18.6	19.1
Zero-cross over frequency (Hz)	3.9	3.3	3.5
Phase margin (deg)	22.3	23.9	24.6
Gain margin (dB)	31.6	41.1	40.7

4.3.2 Design of Proportional Controller and Lead Compensator

The majority of motion-control applications require precise velocity and position control. As shown in Fig. 114, the phase margin in the position loop with a double integrator is usually insufficient to provide a good response for the abrupt step input command without overshoot in a fast position-control system. To mitigate this drawback, a lead compensator can be a good candidate, leading to a desirable open-loop gain at low frequency. Fig. 116 illustrates the closed-loop block diagram of the position-control loop. Since the sampling rate (833 Hz) of the position controller is much faster than the position loop BW (≅ 10 Hz), the transfer function is described as a continuous form instead of a discrete form as shown in (4.34).

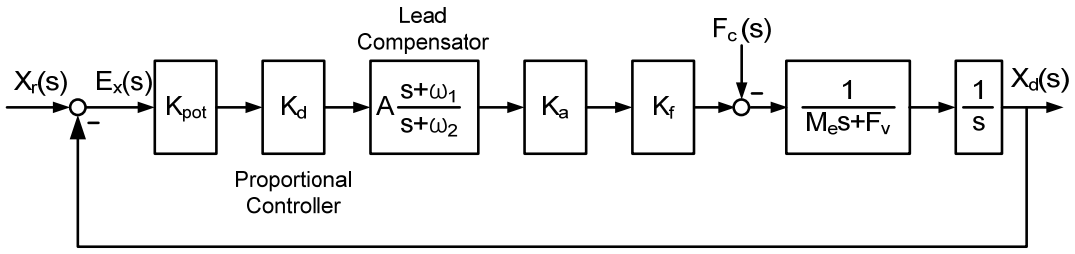

Fig. 116. Closed-loop control block diagram of the linear motion system.

$$X_d(s) = \frac{K_{pot}K_dK_aK_f\alpha(s+\omega_1)}{D(s)}X_r(s) - \frac{(s+\omega_2)}{D(s)}F_c(s) \tag{4.34}$$

where $D(s) = M_e s^3 + (F_v + M_e\omega_2)s^2 + (F_v\omega_2 + K_{pot}K_dK_aK_f\alpha)s + K_{pot}K_dK_aK_f\alpha\omega_1$.

For the position controller using the proportional controller and lead compensator, the following requirements are established: (1) the steady-state error for the step of 0.03 m

should be less than 0.0005 m, (2) the steady-state error for the ramp input of 0.01 m/s should be less than 0.0005 m, (3) the required steady-state error for the maximum input command should be reached within 0.2 s, (4) the phase margin should be larger than 50°, and (5) the gain margin should be larger than 10 dB. The first and second design conditions can be determined by the error analysis using the error transfer function.

$$E_x(s) = \frac{s(s+\omega_2)(M_e s + F_v)}{D(s)} X_r(s) + \frac{(s+\omega_2)}{D(s)} F_c(s) \tag{4.35}$$

From (4.35), the proportional gains that satisfies the required steady-state errors for the step and ramp input commands are given by

$$K_d \geq \frac{F_c}{K_{pot} K_a K_f e_{ss}} \quad \text{for the step input command} \tag{4.36}$$

$$K_d \geq \frac{F_v V_r + F_c}{K_{pot} K_a K_f e_{ss}} \quad \text{for the ramp input command} \tag{4.37}$$

where e_{ss} is the steady-state error, V_r is the slope of the ramp input. The third design condition can be determined by the settling time specification. In this study, the settling time is defined as a 10% error condition. Thus, assuming that there is no lead compensator, the cutoff frequency that satisfies the 10% error condition in the settling time is given by

$$K_d \geq \frac{\sqrt{M_e^2 \omega^4 + F_v^2 \omega^2}}{K_{pot} K_a K_f} \quad \text{where } \omega = -\frac{2.3}{t_s} \ln\left(\frac{e_{ss}}{X_{\max}}\right) \tag{4.38}$$

where t_s is the required settling time, and X_{max} is the maximum travel distance of the mover. In a practical system, the thrust force is mainly limited by the current capability of the power supply. Thus, this constraint should be considered in the design procedure as follows:

$$K_d \le \frac{\sqrt{M_e^2\omega^4 + F_v^2\omega^2}}{K_{pot}K_aK_f} \quad \text{where } \omega = 2\pi\sqrt{\frac{F_{\max}}{4M_eX_{\max}}} = 2\pi\sqrt{\frac{K_fI_{\max}}{4M_eX_{\max}}} \tag{4.39}$$

where F_{max} is the maximum developed thrust force, and I_{max} is the maximum allowable supply current of the power supply. From (4.36)–(4.39), the desirable proportional gain is given as

$$3.41 \le K_d \le 4.84 \tag{4.40}$$

From the result of (4.40), the proportional gain of 3.5 is chosen to minimize the phase margin loss due to the new zero-crossover frequency. The transfer function of the lead compensator is given by

$$L(s) = A\frac{s+\omega_1}{s+\omega_2} \tag{4.41}$$

The coefficient A of (4.41) can be determined by the desired phase as follows.

$$A = \frac{1+\sin(\varphi_{ds})}{1+\sin(\varphi_{ds})} \tag{4.42}$$

where φ_{ds} is the desired phase. The center, zero, and pole frequencies is calculated using

$$\left|K_dG_p(\omega_{\max})\right| = 1/\sqrt{A} \tag{4.43}$$

$$\omega_1 = \omega_{\max}/\sqrt{A} \text{ and } \omega_2 = A\omega_1 \tag{4.44}$$

where $G_P(s)$ is the open-loop transfer function of the uncompensated system shown in Fig. 114. The results in Fig. 117 show the frequency responses of the compensated systems with the proportional controller and lead compensator in the position-control loop using the two different current control schemes. Both the responses are in good agreement with the analytic response although the open-loop gains are slightly less than

the analytic one. This is because the detent force is not included in the friction model of (4.30). Table 25 shows the performance comparisons between the analytic model, 12-step current control, and FOC scheme.

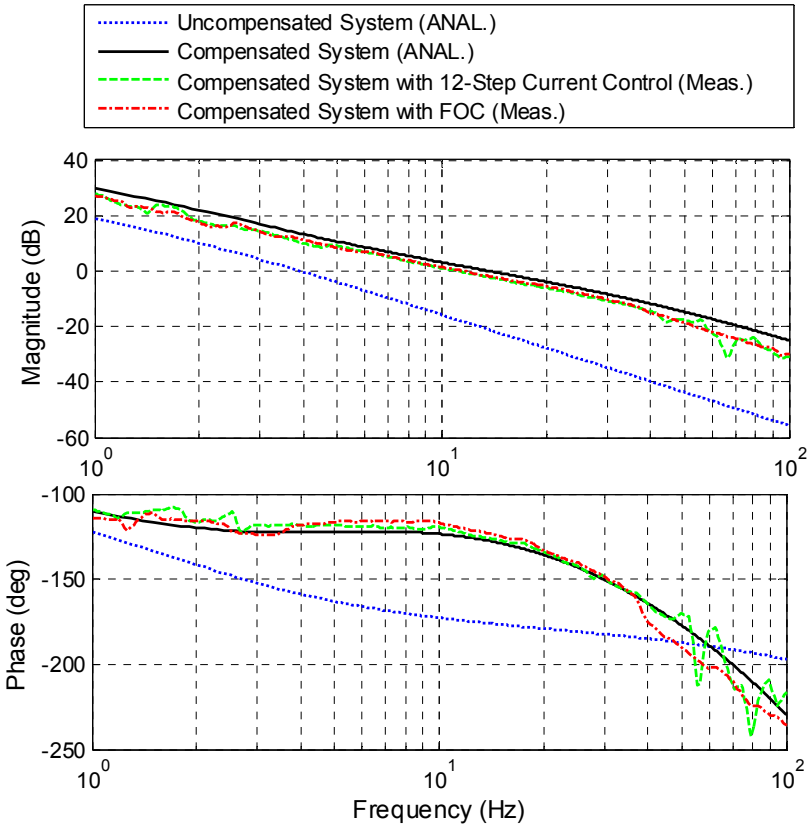

Fig. 117. Open-loop frequency responses of the uncompensated and compensated systems when K_d = 3.5, A = 10.7, ω_l = 26.4 rad/s, and ω_l = 282.6 rad/s.

Table 25. Open-loop frequency-response characteristics in two different current control schemes

Characteristics	Analytic Model	12-Step current control	FOC
Open-loop gain	29.1	28.3	28.1
Zero-cross over frequency (Hz)	13.2	11.75	11.6
Phase margin (deg)	52.3	57.1	60.2
Gain margin (dB)	15.4	18.3	15.9

4.3.3 Performance Validation and Comparisons

The photograph in Fig. 118 shows the experimental setup to measure the performances according to the current control schemes. A 150-W (30 V, 5 A) DC power supply was used for the VSI. The LRP with the 0.1% nonlinearity was also used to estimate the electrical angle of the mover. The LOP with the 2.8% nonlinearity developed in Section 3.5.3 was employed in order to demonstrate the feasibility of the new LOP sensor. The TMS320F28335 module for implementing the digital controller was employed, and the control area network (CAN) with a 1 Mbps was used for the real-time serial communication between the DSP and the LabVIEW GUI command console on a PC. The measured signals were recorded at the update rate of 1.2 ms. The frequency responses were measured using a K35670A dynamic signal analyzer.

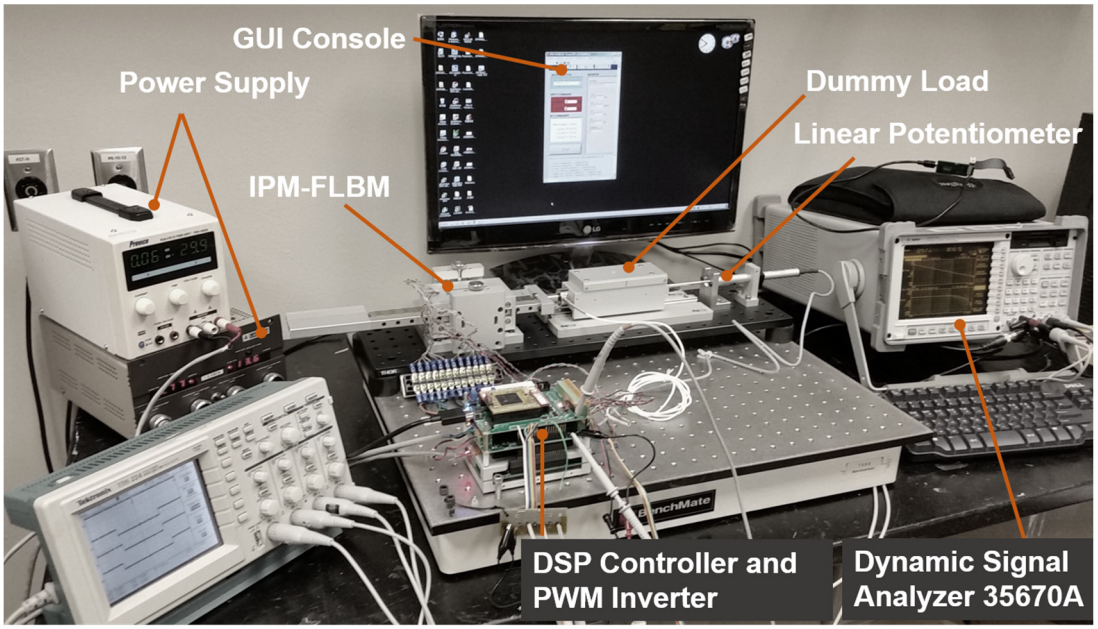

Fig. 118. Photograph of the experimental setup to measure the performances of the linear motion platform.

4.3.3.A Position-Control Loop Test Using LRP

Fig. 119 shows that the step responses in two position-control loops according to the current control schemes. Although the same position controller is used, the position-control loop using the 12-step current control scheme is less affected from the saturation interval than the position-control loop using the FOC scheme. As a result, there is no overshoot, and its steady-state error is larger than the design error criterion because of the detent force. On the contrary, the steady-state error of the position loop using the FOC is smaller than the design error criterion because of the initial overshoot.

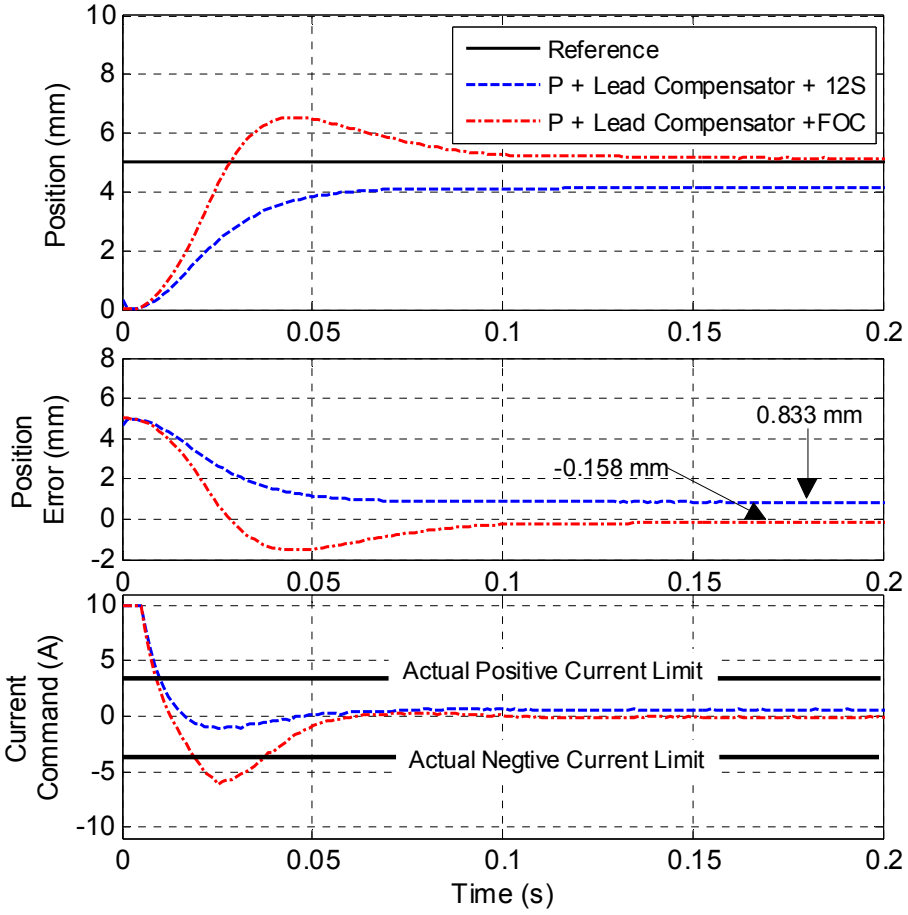

Fig. 119. Step responses of the same position-control loops according to the two different current control schemes.

The responses of Fig. 120 for the ramp input command of 10 mm/s show that the two position-control control loops using the different current control schemes have the same performance as predicted in the frequency responses. The average steady-state errors are calculated as 0.72 mm and 0.71 mm in the 12-step current control and FOC scheme, respectively. These steady-state errors slightly larger than the design criteria are caused by the detent force of the IPM-FLBM. In addition, the current command of the position-control loop using the FOC illustrates that the current command is much more sensitive to the detent force.

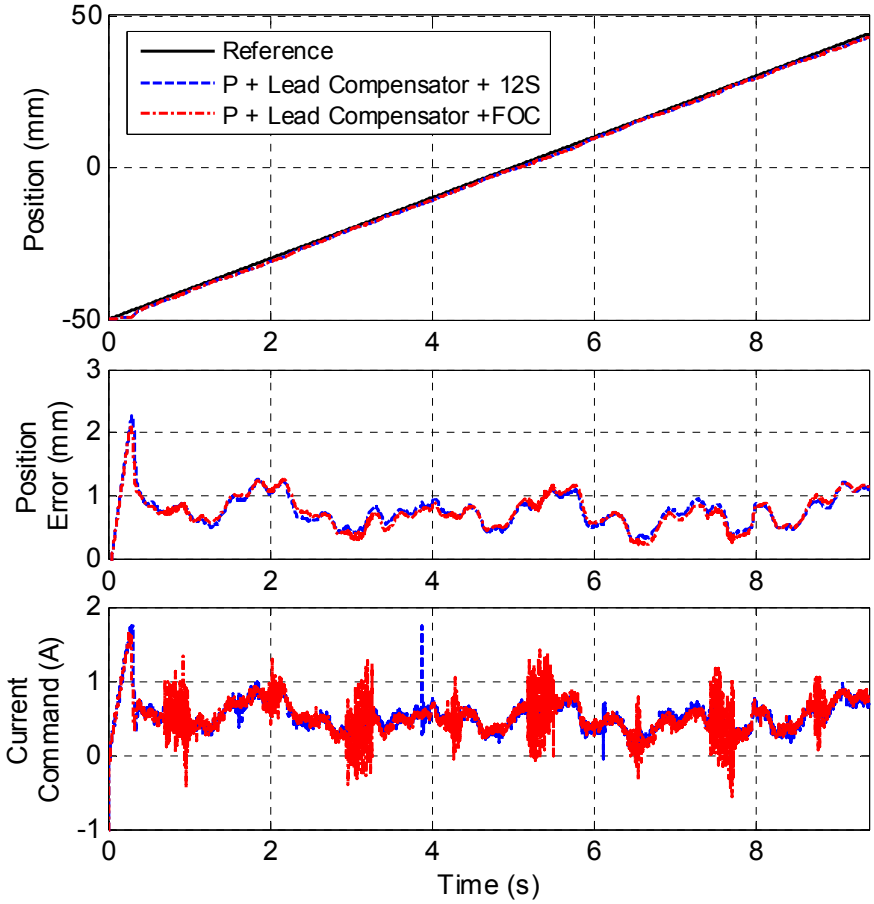

Fig. 120. The responses of the same position-control loops according to the two different current control schemes for the ramp input command of 10 mm/s.

Like the results in Fig. 120, the responses to the sinusoidal input command of 15 mm at 1.0 Hz in Fig. 121 show that the two position-control loops for the two different current control schemes have the same performance if there is no current saturation in the physical system. The position error in steady state illustrates that it has a form of the sinusoidal waveform distorted by the detent force waveform. The peak-to-peak error of around 2.4 mm occurs in both the position-control loops.

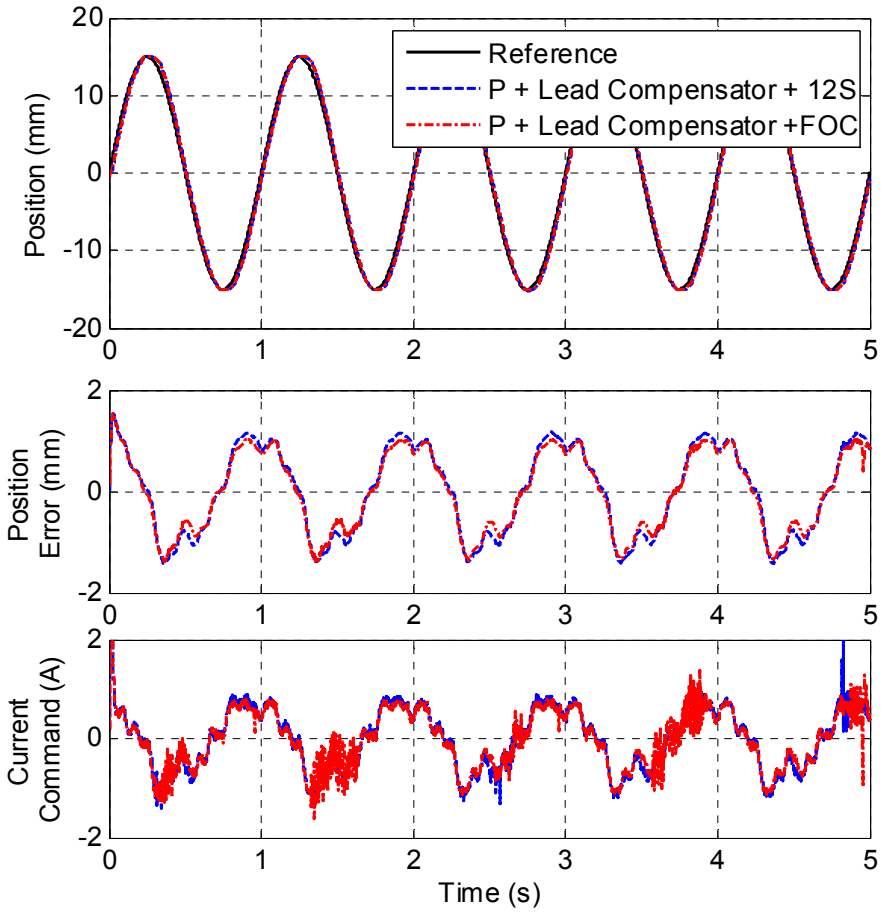

Fig. 121. The responses of two position-control loops using the different current control schemes for the sinusoidal input command of 15 mm at 1 Hz.

4.3.3.B. Position-Control Loop Test Using LOP

The plots in Fig. 122 show the responses for various step inputs in the position-control loop using the 12-step current control scheme. The LOP is used as the position-feedback sensor, and the LRP is employed for the observation and comparison. The middle plot of Fig. 122 illustrates that although there is an error between the LLP and the LOP due to the nonlinearity of the LOP, the steady-state errors for the reference command in the region where the detent force is relatively small under the design criteria.

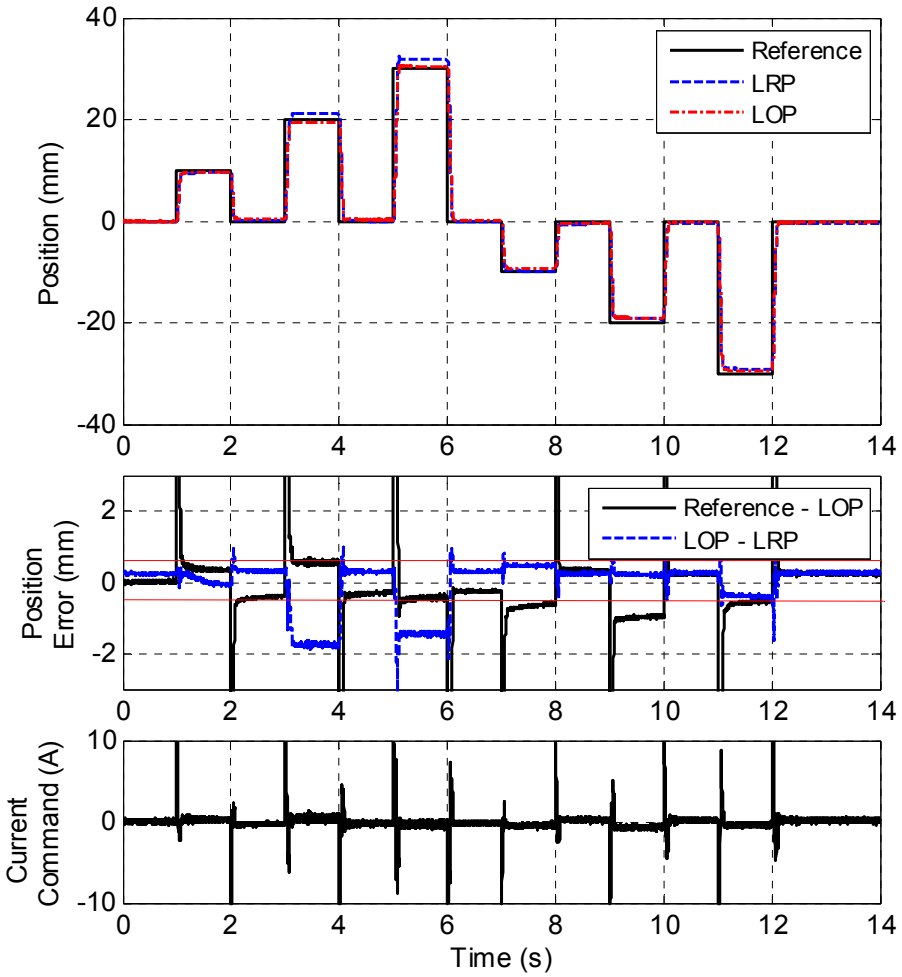

Fig. 122. Responses for various step inputs in the position-control loop using the 12-step current control and LOP.

The results in Fig. 123 show the responses of the position-control loop using the FOC for the ramp input command of 10 mm/s. The LOP is used as a position-feedback sensor, and the LRP is employed for the observation and comparison. The steady-state errors for the reference command is almost the same as the result of Fig. 120. This implies that the LOP sensor can be a cost-effective alternative in a low-cost system if the nonlinearity is improved. The maximum error between the LRP and LOP is estimated as 2.8 mm through subtracting the LLP from LOP in the middle plot of Fig. 123.

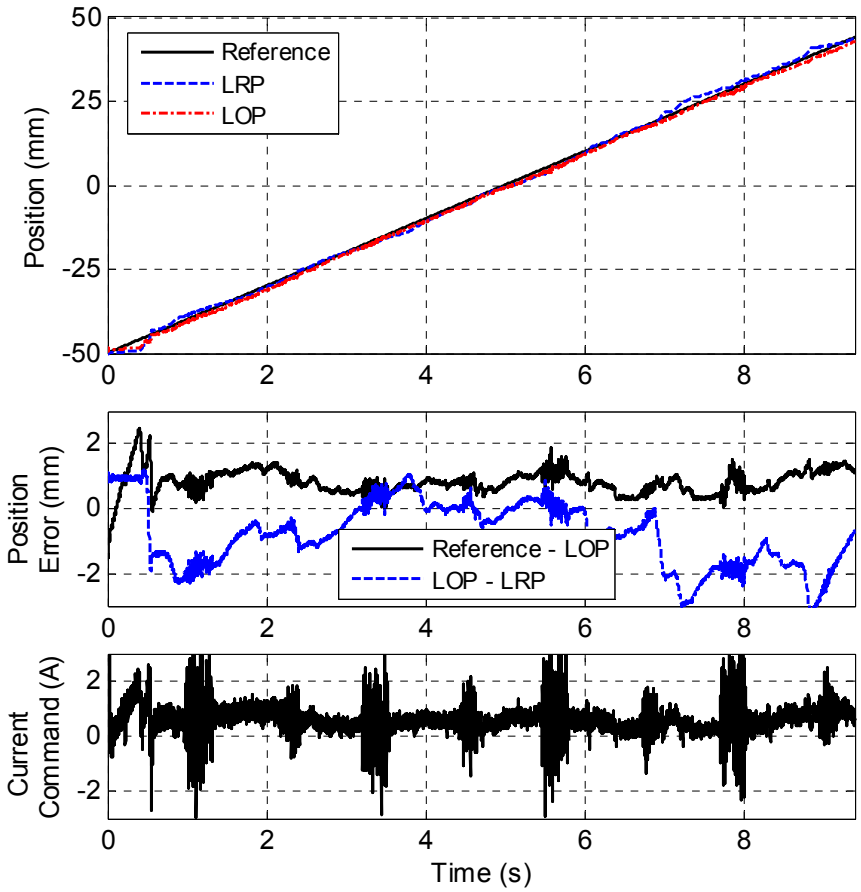

Fig. 123. The responses of the position-control loops using the FOC and LOP for the ramp input command of 10 mm/s.

The sinusoidal response in Fig. 124 shows that although the position errors for the reference command are slightly increased due to the nonlinearity of the LOP as compared with the result of the position-control loop using the LRP, the response follows the reference command as shown in the top plot of Fig. 124. This also implies that the dynamic response of the LOP is appropriate to the cost-effective motion-control applications.

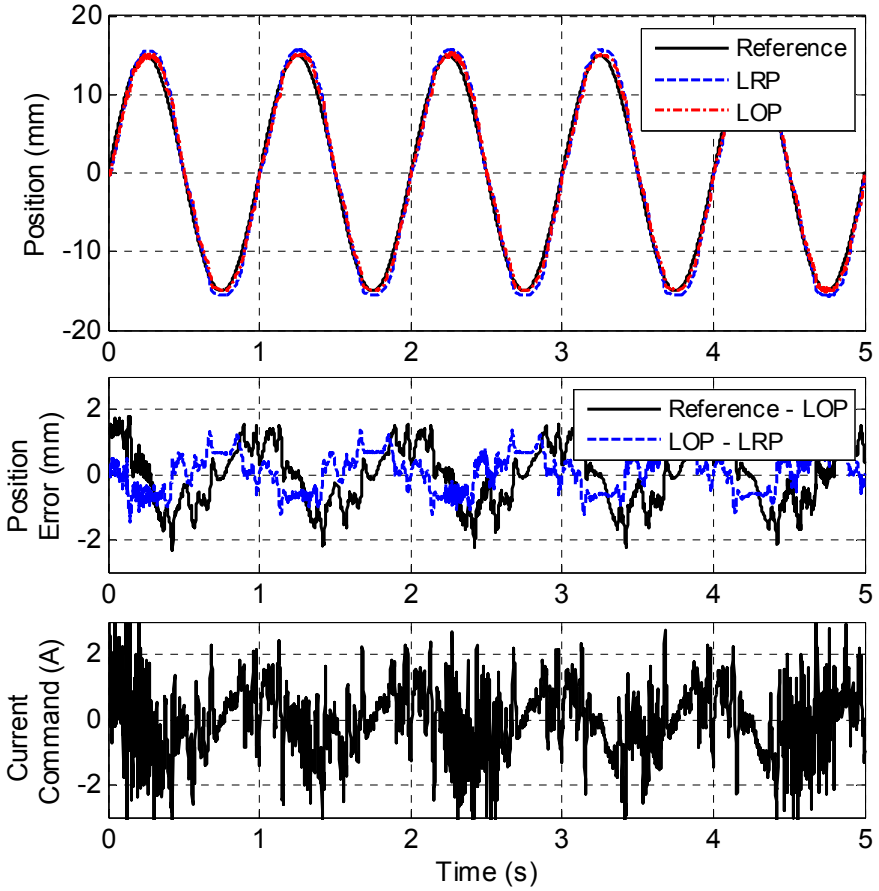

Fig. 124. The responses of the position-control loops using the FOC and LOP for the sinusoidal input command of 15mm with 1 Hz.

CHAPTER V

CONCLUSIONS AND SUGGESTIONS

In this chapter the accomplishment in this research is summarized, and the suggestions for future work are provided to improve the performance of the linear motion system.

5.1 Conclusions

A new double-sided IPM-FLBM was designed on the basis of the conventional brushless rotary motor with the alternate teeth windings. New practical detent-force minimization methodologies for this new linear motor were developed in terms of the two-dimensional minimization and slot-phase-shift techniques for the end-effect and cogging forces, respectively. Consequently, the IPM-FLBM with a detent force of 1.5% of the maximum thrust force was constructed using the electrical solid steel.

Analytic modeling techniques were developed to analyze the double-sided IPM-FLBM with slot-phase shift and alternate teeth windings. A superposed winding function was established in the slot-phase shift configuration. A variable winding function method was newly developed in order to evaluate the inductances of the linear motor configured with the salient iron core and alternate teeth winding. This was also sufficiently generalized to handle the same types of motor as an effective and reliable method.

The magnetic-field analysis for the double-sided IPM-FLBM machined with the SMC material was performed using a simplified nonlinear MEC without using an FEA tool. In addition, through the analysis for the iron and copper losses, it was found that the

iron loss is not critical in the lightweight and small-sized motor using the SMC. Finally, it was demonstrated that the low-magnetic-field performance of the SMC in the PM-based motor can be improved by the design analysis through comparing the measured steady-state thrust forces between the electrical steel and SPM prototypes.

The new angle-sensing mechanism to be employed in a low-cost rotary or linear position-control systems was studied using the photo diode and LED. The red color-coded and black-colored V-shape tracks were developed using plain paper by a commercial laser printer. A comprehensive dynamic model and a steady-state propagation model for this sensing mechanism were derived on the basis of the LOS path, the directed non-LOS path, and the Lambertian emission pattern of the LED light source. In addition, the feasibility of this cost-effective high-precision non-contact sensing system was demonstrated by the promising experimental results such as the high bandwidth of 4.42 kHz and the nonlinearity of 2.80%.

The new cost-effective 12-step current control scheme with a low ripple force was developed for the new double-sided IPM-FLBM with slot-phase shift. The 12-step commutation sequence and the current feedback loop design using the dc-link current and six Hall-effect sensors were presented in detail. Its performances were experimentally verified through the comparison with the conventional FOC scheme.

In the end, the linear motion-control system using the new double-sided IPM-FLBM and LOP was modeled analytically. Its performances were demonstrated through various experiments in the time and frequency domains.

5.2 Suggestions for Future Work

Although all objectives of this research were satisfied, there are still some aspects of this linear motion system that have been unexplored. Based on that, I list the suggested future works as follows:

Although the detent force of the linear motor with the iron core was significantly reduced using the proposed new techniques as compared with the base model, the remaining detent force is not sufficiently small for the purpose of precision motion control applications. Therefore, in the future, more advanced control techniques can also be implemented to minimize the position error due to the remaining detent force.

The LOP that was effective in meeting the initial requirements, but its nonlinearity might not be suitable for precision-motion control applications. In order to improve the positioning accuracy and nonlinearity, the double-track scaler or phase-differential tracking method using multiple LEDs and photodiodes can be investigated.

The thermal analysis the steady state was presented in the double-sided IPM-FLBM using the SMC material. However, the analytic solution for the transient response to determine the maximum stall current was not investigated because of the lack of the experimental material and setup. Furthermore, since most research papers have focused on the rated operation condition, there are not many relevant studies. Hence, the analytic transient response model can be explored on the basis of a lumped-parameter method and empirical experiments.

REFERENCES

[1] E. R. Laithwaite and S. A. Nasar, “Linear-motion electrical machines,” *Proc. IEEE*. vol. 58. no. 4, Apr. 1970.

[2] J. F. Gieras, Z. J. Piech, and B. Z. Tomczuk, “Topologies and Selection,” in *Linear Synchronous Motors*, 2nd Ed., CRC Press, 2012, pp. 1–22.

[3] I. S. Jung, J. Hur, and D. S. Hyun, “Performance analysis of skewed PM linear synchronous motor according to various design parameters,” *IEEE Trans. Magnetics*, vol. 37, no. 5, pp. 3653–3657, Sep. 2001.

[4] Y. W. Zhu, D. H. Koo, and Y. H. Cho, “Detent force minimization of permanent magnet linear synchronous motor by means of two different methods,” *IEEE Trans. Magnetics*, vol. 44, no. 11, pp. 4345–4348, Nov. 2008.

[5] C. C. Hwang, P. L. Li, and C. T. Liu, “Optimal design of permanent magnet synchronous motor with low cogging force,” *IEEE Trans. Magnetics*, vol. 48, no. 2, pp. 1039–1042, Feb. 2012.

[6] M. Inoue and K. Sato, “An approach to a suitable stator length for minimizing the detent force of permanent magnet linear synchronous motors,” *IEEE Trans. Magnetics*, vol. 36, no. 4, pp. 1890–1893, Jul. 2000.

[7] S. W. Youn, J. J. Lee, H. S. Yoon, and C. S. Koh, “A new cogging-free permanent magnet linear motor,” *IEEE Trans. Magnetics*, vol. 44, no. 7, pp. 1785–1790, Jul. 2008.

[8] N. Bianchi, S. Bolognani, and A. D. F. Cappello, "Reduction of cogging force in PM linear motors by pole-shifting," *IEE Proc-Electro. Power Appl.,* vol. 152, no. 3, pp. 703−709, May 2005.

[9] K. C. Lim, J. K. Woo, G. H. Kang, J. P. Hong, and G. T. Kim, "Detent force minimization techniques in permanent magnet linear synchronous motors," *IEEE Trans. Magnetics*, vol. 38, no. 2, pp. 1157−1160, Mar. 2002.

[10] S. G. Lee, S. A. Kim, S. Saha, Y. W. Zhu, and Y. H. Cho, "Optimal structure design for minimizing detent force of PMLSM for a ropeless elevator," *IEEE Trans. Magnetics*, vol. 50, no. 1, article no. 4001104, Jan. 2014.

[11] H. Polinder, J. G. Slootweg, and M. J. Hoeijmakers, "Modeling of a linear PM machine including magnetic saturation and end effects: maximum force-to-current ratio," *IEEE Trans. Industrial Applications*, vol. 39, no. 6, pp. 1681−1688, Nov. 2003.

[12] B. S. Ghalavand, S. V. Zadeh, and A. H. Isfahani, "An improved magnetic equivalent circuit model for iron-core linear permanent magnet synchronous motors," *IEEE Trans, Magnetics*, vol. 46, no. 1, pp. 112−120, Jan. 2010.

[13] G. Srumberger, D. Zarko, M. Timur, and T. A. Lipo, "Design and comparison of linear synchronous motor and linear induction motor for electromagnetic aircraft launch system," in *Proc. IEEE Int. Conf. Electric Machines and Drives*, vol. 1, pp. 494−500, Jun. 2003.

[14] M. Sanada, S. Morimoto, and Y. Takeda, "Interior permanent magnet linear synchronous motor for high-performance drives," *IEEE Trans. Industrial Applications*, vol. 33, no. 4, pp. 966–972, Jul. 1997.

[15] N. Bianchi, S. Bolognani, and F. Tonel, "Design criteria of a tubular linear IPM motor," in *Proc. IEEE Int. Conf. Electric Machines and Drives*, vol. 1, pp. 1–7, Jun. 2001.

[16] J. Wang, D. Howe, and G. W. Jewell, "Analysis and design optimization of an improved axially magnetized tubular permanent-magnet machine," *IEEE Trans. Energy Conversion*, vol. 19, no. 2, pp. 289–295, Jun. 2004.

[17] L. O. Hultman and A. G. Jack, "Soft magnet composites-material and application," in *Proc. IEEE Int. Elect. Mach. Drives Conf*., Jun. 2003, pp. 516–522.

[18] H. Shokrollahi and K. Janghorban, "Soft magnetic composite materials (SMCs)," *J. Mater. Process. Technol.,* vol. 189, pp. 1–12, Jul. 2007.

[19] G. Cvetkovski and L. Petkovska, "Performance improvement of PM synchronous motor by using soft magnetic composite material," *IEEE Trans. Magnetics*, vol. 44, no. 11, pp. 3812–3815, Nov. 2008.

[20] T. Ishikawa, K. Takahashi, Q. V. Ho, M. Matsunami, and N. Kurita, "Analysis of novel brushless DC motors made of soft magnetic composite core," *IEEE Trans. Magnetics*, vol. 48, no. 2, pp. 971–974, Feb. 2012.

[21] Y. G. Guo, J. G. Zhu, and D. G. Dorell, "Design and analysis of a claw pole permanent magnet motor with molded soft magnetic composite core," *IEEE Trans. Magnetics*, vol. 45, no. 10, pp. 4582–4585, Oct. 2009.

[22] R. D. Stefano and F. Marignetti, "Electromagnetic analysis of axial-flux permanent magnet synchronous machines with fractional windings with experimental validation," *IEEE Trans. Ind. Elect.*, vol. 59, no. 6, pp. 2573–2581, Jun. 2012.

[23] H. Vansompel, P. Sergeant, L. Dupré, and A. den Bossche "Axial-flux PM machines with variable air gap," *IEEE Trans. Ind. Elect.*, vol. 61, no. 2, pp. 730–737, Feb. 2014.

[24] J. Wang, D. Howe, and Z. Lin, "Design optimization of short-stroke single-phase tubular permanent-magnet motor for refrigeration applications," *IEEE Trans. Ind. Elect.,* vol. 57, no. 10, pp. 327–334, Jan. 2010

[25] D. S. Nyce*, Linear position sensors: theory and application*. 1th Ed., John Wiley & Sons, 2004.

[26] M. Gasulia, X. Li, G. C. M. Miijer, L. Ham, and J. W. Spronck, "A contactless capacitive angular-position sensor," *IEEE Sensors J.*, vol. 3, no. 5, pp. 607–613, Sep., 2005.

[27] F. Seco, J. M. Martin, A. R. Jimenez, "A high accuracy magnetostrictive linear position sensor," *Sensors and Actuators A: Physical*, vol. 124–124, pp. 216–223, Nov., 2013.

[28] Z. Zhang, F. Ni, Y. Dong, M. Jin, and H. Liu, "A novel absolute angular position sensor based on electromagnetism," *Sensors and Actuators A: Physical*, vol. 194, pp. 196–203, Nov., 2013.

[29] J. B. Finlay, "High speed linear analog position transducer," *IEEE Trans. Instrumt. Meas.*, vol. 26, no. 2, pp. 184–185, Jun., 1977.

[30] H. Guretzky, “Angle-position transducer,” U.S. Patent 4,320,293, 1982.

[31] G. Palli and S. Pirozzi, “Optical sensor for angular position measurements embedded in robotic figure joints,” *Advanced Robotics*, vol. 27, no. 15, pp. 1209–1220, Jun., 2013.

[32] T. M. Jahns and W. L. Soong, “Pulsating minimization techniques for permanent magnet AC motor drives–A review,” *IEEE Trans. Ind. Electron.,* vol. 43, no. 2, pp. 321–330, Apr. 1996.

[33] M. Bertoluzzo, G. Buja, R. K. Keshri, and R. Menis, “Sinusoidal versus square-wave current supply of PM brushless DC drives: A convenience analysis,” *IEEE Trans. Ind. Electron.,* vol. 62, no. 12, pp. 7339–7349, Dec. 2015.

[34] P. Pillay and R. Krishnan, “Application characteristics of permanent magnet synchronous and brushless dc motors for servo drive,” *IEEE Trans. Ind. Appl.,* vol. 27, no. 5, pp. 986–996, Sep. 1991.

[35] D. W. Novotny and T. A. Lipo, *Vector Control and Dynamics of AC Drives*. 1st Ed, Oxford University Press Inc., New York, 1996.

[36] Y. P. Yang and Y. Y. Ting, “Improved angular displacement estimation based on Hall-effect sensors for driving a brushless permanent-magnet motor,” *IEEE Trans. Ind. Electron.*, vol. 61, no. 1, pp. 504–511, Jan. 2014.

[37] M. P. Kamierkowski and L. Malesani, “Current control techniques for three-phase voltage source PWM converters: a survey,” *IEEE Trans. Ind. Electron.*, vol. 45, no. 5, pp. 691–703, Oct. 1998.

[38] F. Caricchi, F. G. Capponi, F. Crescimbini, and L. Solero, "Sinusoidal brushless drive with low-cost linear hall effect position sensors," in *Proc. IEEE Int. Conf. Power Electron. Special*, vol. 2, pp. 799–804, Jun. 2001.

[39] L. Zhong, M. F. Rahman, W. Y. Hu, and K. W. Lim, "Analysis of direct torque control in permanent magnet synchronous motor drive," *IEEE Trans. Ind. Electron.*, vol. 12, no. 3, pp. 528–536, May 1997.

[40] Y. Liu, Z. Q. Zhu, and D. Howe, "Direct torque control of brushless DC drives with reduced torque ripple," *IEEE Trans. Ind. Appl.*, vol. 41, no. 2, pp. 599–608, Mar. 2005.

[41] G. S. Buja and M. P. Kazmierkowski, "Direct torque control of PWM inverted-fed AC motors–A survey," *IEEE Trans. Ind. Electron.*, vol. 51, no. 4, pp. 744–757, Aug. 2004.

[42] D. Casadei, F. Profumo, G. Serra, and A. Tani, "FOC and DTC: Two viable schemes for induction motors torque control," *IEEE Trans. Power Electronics*, vol. 17, no. 5, pp. 779–787, Sep. 2002.

[43] G. Buja, M. Bertoluzzo, R. K. Keshri, "Torque ripple-free operation of PM BLDC drives with petal-wave current supply," *IEEE Trans. Ind. Electron.,* vol. 62, no. 7, pp. 4034–4043, Jul. 2015.

[44] C. M. Wang, S. J. Wang, S. K. Lin, and H. Y. Lin, "A novel twelve-step sensorless drive scheme for a brushless DC motor," *IEEE Trans. Magnetics*, vol. 43, no. 6, pp. 2555–2557, Jun. 2007.

[45] S. A. Kim, S. G. Lee, G, S. Choi, and Y. H. Cho, "A novel twelve-step sensor-less control for torque reduction in brushless DC motor," in *Proc. IEEE. Conf. Power mach. and Syst.*, pp. 1062–1068, Oct. 2014.

[46] D. Ishak, Z. Q. Zhu, and D. Howe, "Comparison of PM brushless motors, having either all teeth or alternate teeth wound," *IEEE Trans. Energy Conversion*, vol. 21, no. 1, pp. 95–103, 2006.

[47] P. J. Hor, Z. Q. Zhu, D. Howe, and J. R. Jones, "Minimization of cogging force in a linear permanent motor," *IEEE Trans. Magnetics*, vol. 34, no. 5, pp. 3544–3547, Sep. 1998.

[48] J. Pyrhönen, T. Jokinen, and V. Hrabovcová, *Design of Rotating Electrical Machines*, 1st Ed. John Wiley & Sons, Ltd, 2008.

[49] P. C. Sen, "Synchronous machines," in *Principles of Electric Machines and Power Electronics*. 2nd Ed., John Wiley & Sons, 1997, pp. 350–357.

[50] A. Balakrishnan, W. T. Joines, and T. G. Wilson, "Air-gap reluctance and inductance calculations for magnetic circuits using a Schwarz-Christoffel transformation," *IEEE Trans. Power Electronics*, vol. 12, no. 4, pp. 654–663, Jul. 1997.

[51] J. Mühlethaler, J. W. Kolar, and A. Ecklebe, "A novel approach for 3D air gap reluctance calculation," in *Proc. IEEE 8th ICPE, ECCE Asia,* pp. 446–452, Jun., 2011.

[52] Z. Q. Zhu and D. Howe, "Instantaneous magnetic field distribution in brushless permanent magnet dc motors, part III: Effect of stator slotting," *IEEE Trans, Magnetics*, vol. 29, no. 1, pp. 143–151, Jan. 1993.

[53] T. A. Lipo, *Analysis of Synchronous Machines.* 2nd Ed., CRC Press, 2012.

[54] J. H. J. Potgieter and M. Kamper, "Evaluation of calculation methods and the effect of end-winding inductance on the performance of non-overlapping winding PM machines," in *Proc*. *20th ICEM*, Mar. 2012, pp. 243-249.

[55] A. M. El-Refaie, Z. Q. Zhu, T. M. Jahns, and D. Howe, "Winding inductances of fractional slot surface-mounted permanent magnet brushless machine," in *Proc. IEEE IAS'*08, pp. 1–8, Oct. 2008.

[56] N. A. Al-Nuaim and H. A. Toliyat, "A novel method for modeling dynamic air-gap eccentricity in synchronous machine based on modified winding function theory," *IEEE Trans. Energy Conversion*, vol. 13, no. 2, pp. 156–162, Jun. 1998.

[57] Y. W. Zhu, S. G. Lee, K. S. Chung, and Y. H. Cho, "Investigation of auxiliary poles design criteria on reduction of end effect of detent force for PMLSM," *IEEE Trans, Magnetics*, vol. 45, no. 6, pp. 2863–2866, Jun. 2009.

[58] O. Anderson and P. Hofecker, "Advances in soft magnetic composites materials and application," in *Proc. Int. Conf. Powder Metallurgy Particulate Mater*., Las Vegas, NV, USA, 2009, pp. 1–12.

[59] E. F. Schubert, *Light-emitting diodes*. second Ed., Cambridge, 2006.

[60] OSI Optoelectronics, Photodiode Characteristics and Applications. (2013) [Online]. Available: www.osioptpelectronics.com.

[61] J. Graeme, Photodiode amplifiers. first Ed., Prentice-Hall, 1995.

[62] H. Li and K. E. Torrance, "A practical, comprehensive light reflection model," *Program of Computer Graphics*, Technical Report PCG-05-03, 2005.

[63] S. K. Nayar, K. Ikeuchi, and T. Kanade, "Surface reflection: physical and geometrical perspective," *IEEE Trans. Pattern Analysis and Machine Intelligence*, vol. 13, no. 7, pp. 611–633, Jul. 1991.

[64] T. Komine and M. Nakagawa "Fundamental analysis for visible-light communication system using LED light," *IEEE Trans. on Consumer Electronics*, vol. 50, no. 1, pp. 100–107. Feb. 2004.

[65] AVAGO Technologies, HLMP-EG08-Y2000 AllnGap LED Lamps Data Sheet, www.avagotech.com.

[66] S. K. Nayar, K. Ikeuchi, and T. Kanade, "Surface reflection: physical and geometrical perspective," *IEEE Trans. Pattern Analysis and Machine Intelligence*, vol. 13, no. 7, pp. 611–633, Jul. 1991.

[67] H. Tan and S. L. Ho, "A novel single current sensor technique suitable for BLDCM drives," in *Proc. IEEE Int. Conf. Power Electron. and Drive Sys.*, vol. 3, pp. 133–138, Jul. 1999.

[68] M. Armstrong, D. J. Atkinson, C. M. Johnson, and T. D. Abeyasekera, "Auto-calibrating dc link current sensing technique for transformerless, grid connected, H-bridge inverter systems," *IEEE Trans. Power Electronics*, vol. 21, no. 5, pp. 1385–1393, Sep. 2006.

[69] H. W. Van Der Broeck, H. C. Skudelny, and G. V. Stanke, " Analysis and realization of a pulsewidth modulatior based on voltage space vectors," *IEEE Trans. Industrial Applications*, vol. 24, no. 1, pp. 142–150, Jan. 1988.

[70] K. Zhou and D. Wang, “Relationship between space-vector modulation and three-phase carrier-based PWM: a comprehensive analysis,” *IEEE Trans. Industrial Electronics*, vol. 49, no. 49, pp. 186−196, Feb. 2002.

[71] H. W. van der Broeck, H. C. Skudelny, and G. V. Stanke, “ Analysis and realization of a pulsewidth modulator based on voltage space vectors,” *IEEE Trans. Ind. Appl.*, vol. 24, no. 1, pp. 142−150, Jan. 1988.

APPENDIX A

MECHANICAL ENGINEERING DRAWINGS

The key mechanical drawings used when machining the mechanical parts are presented in this appendix. Therefore, some sub-level drawings made in this study will not be shown in this thesis. The Photograph in Fig. 125 shows the linear motion platform with the LOP sensor.

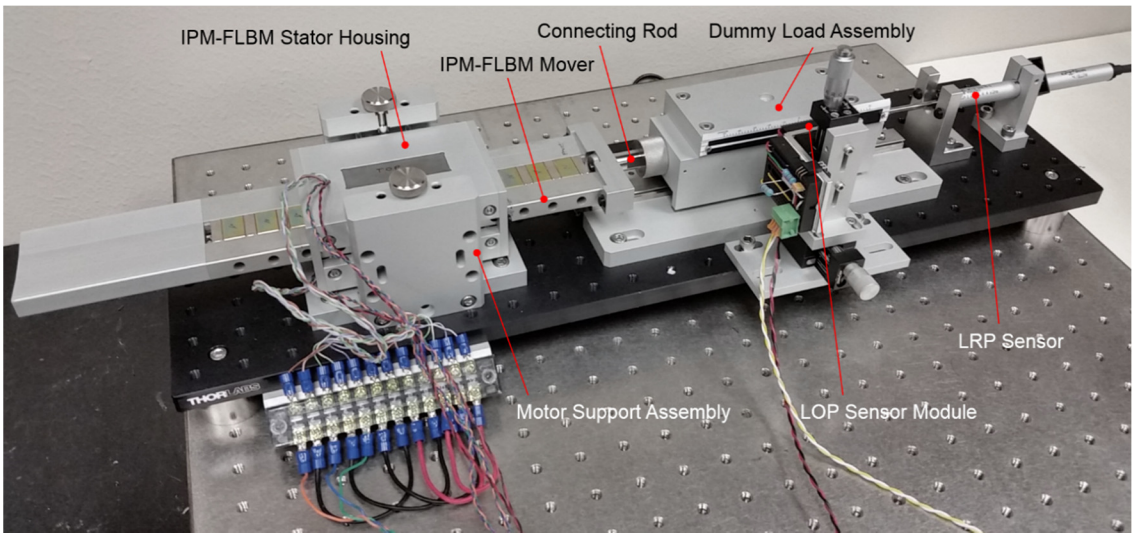

Fig. 125. The linear motion platform with LOP sensor module.

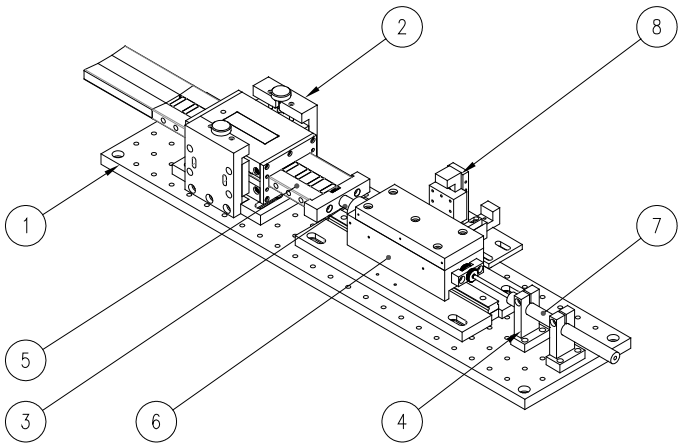

1	Optical Bread Board	5	Double-Sided IPM-FLBM
2	Motor Support Assembly	6	Dummy Load
3	Connect ing Rod	7	LRP
4	LRP Supporter	8	LOP Assembly

UNLESS OTHERWISE SPECIFIED: DIMENSIONS ARE IN MILLIMETERS SURFACE FINISH: TOLERANCES: LINEAR: ANGULAR:		FINISH:			DEBUR AND BREAK SHARP EDGES		DO NOT SCALE DRAWING	REVISION
	NAME	SIGNATURE	DATE				TITLE:	
DRAWN								
CHK'D								
APPV'D								
MFG								
Q.A				MATERIAL:			DWG NO. LinearMotionPlatform_L000	A4
				WEIGHT:			SCALE: 1:10	SHEET 1 OF 1

Fig. 126. High level components of the linear motion platform.

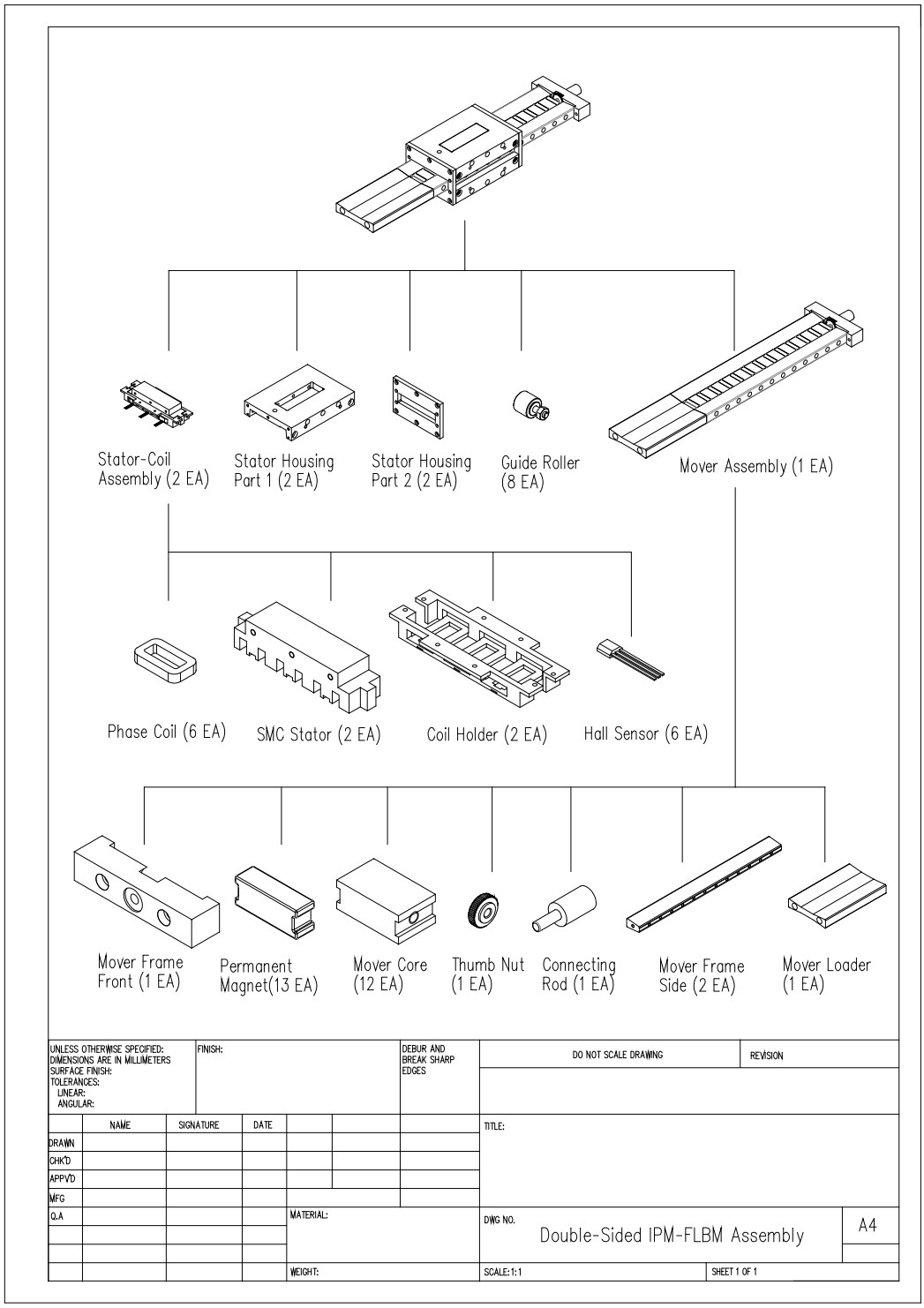

Fig. 127. Components of the double-sided IPM-FLBM assembly.

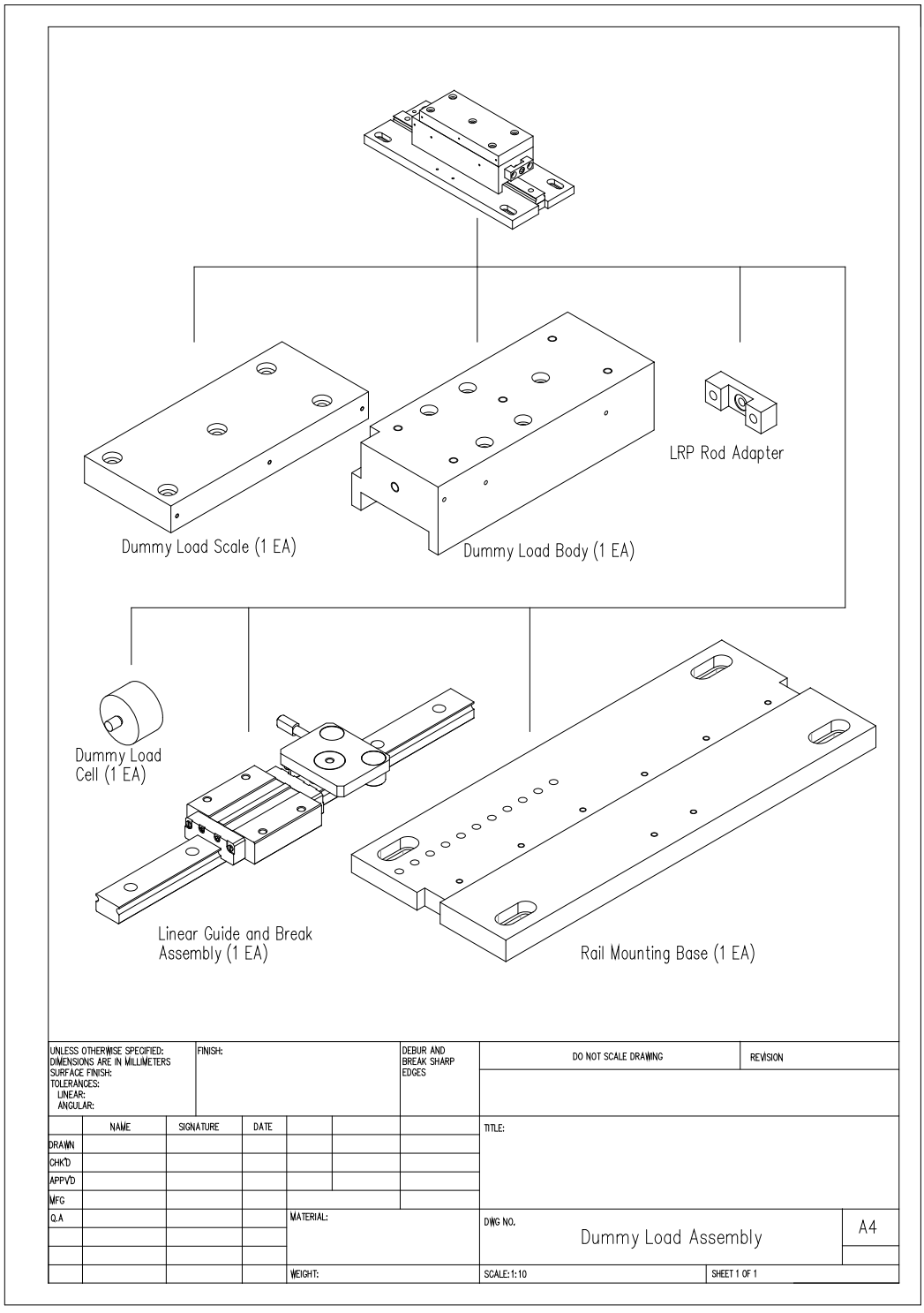

Fig. 128. Components of the dummy load assembly.

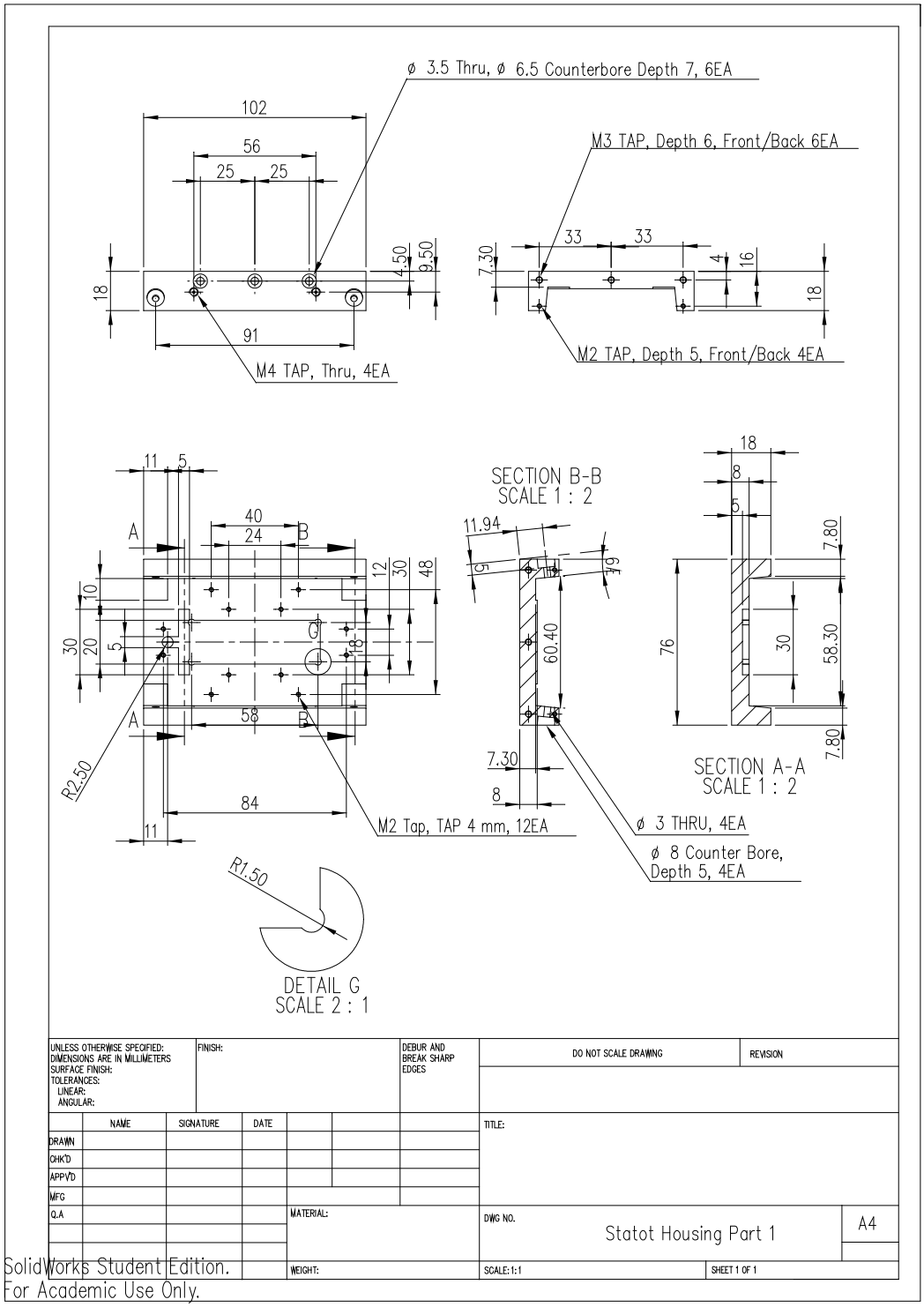

Fig. 129. Stator housing part 1.

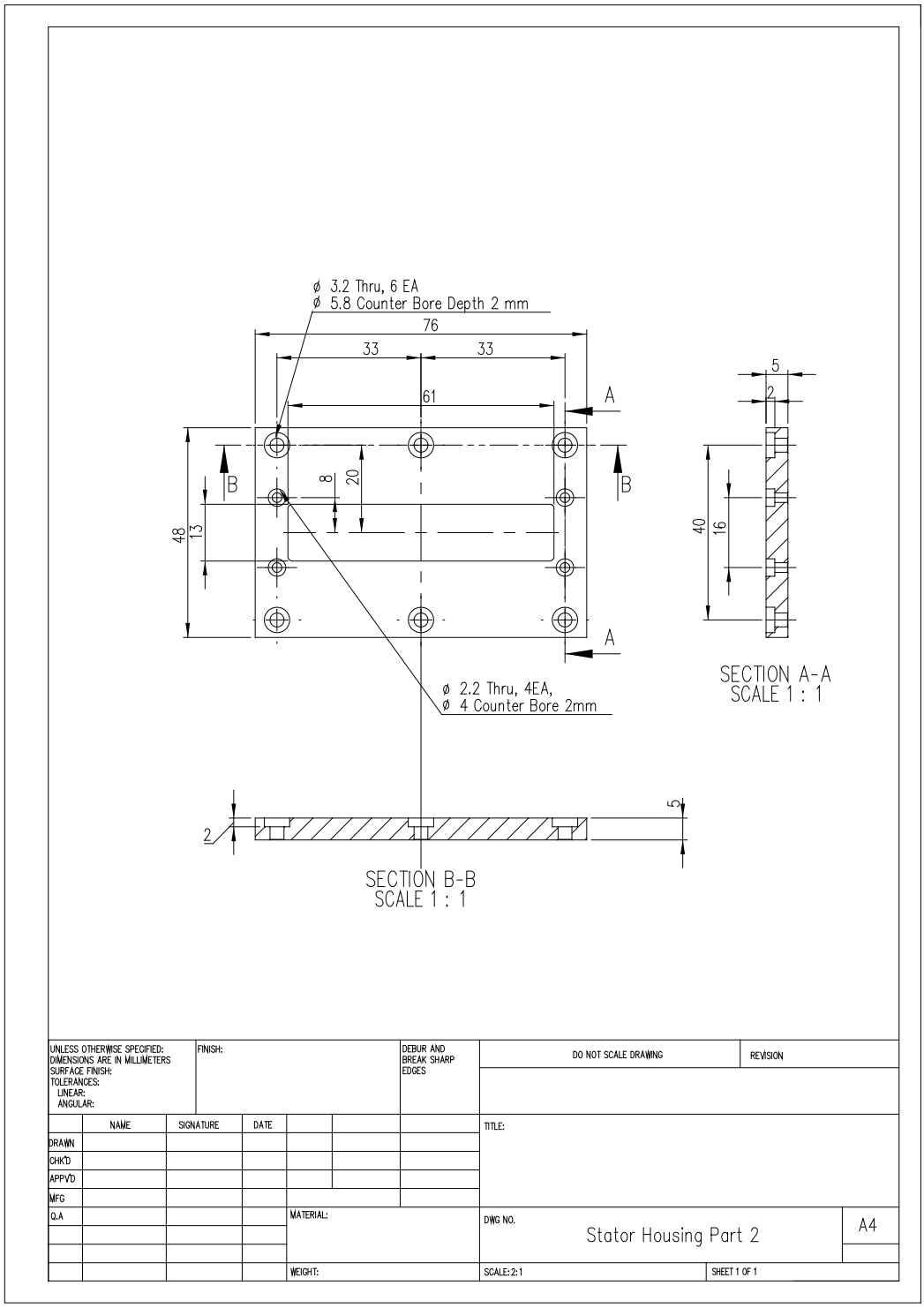

Fig. 130. Stator housing part 2.

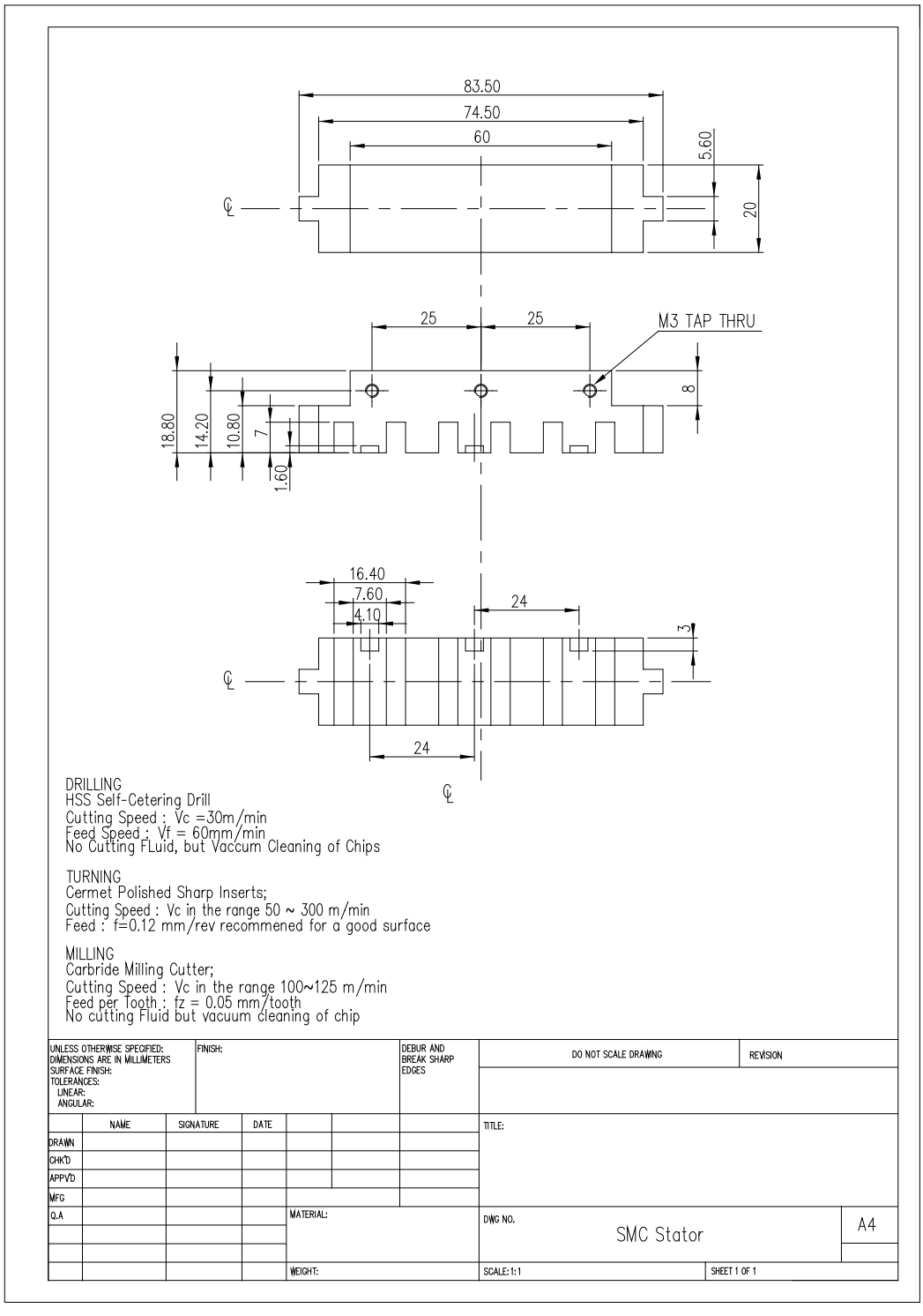

Fig. 131. SMC stator.

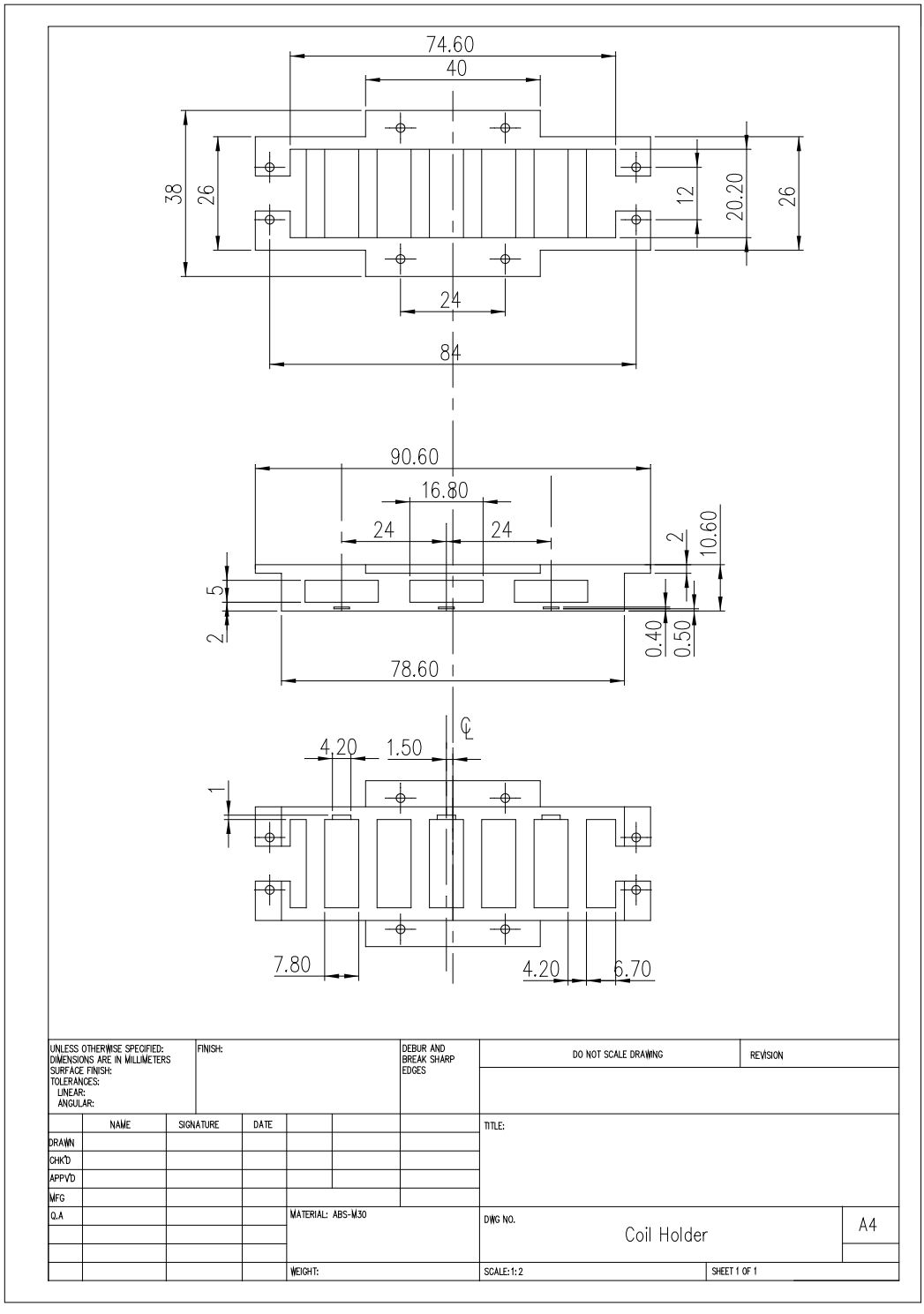

Fig. 132. Armature coil holder.

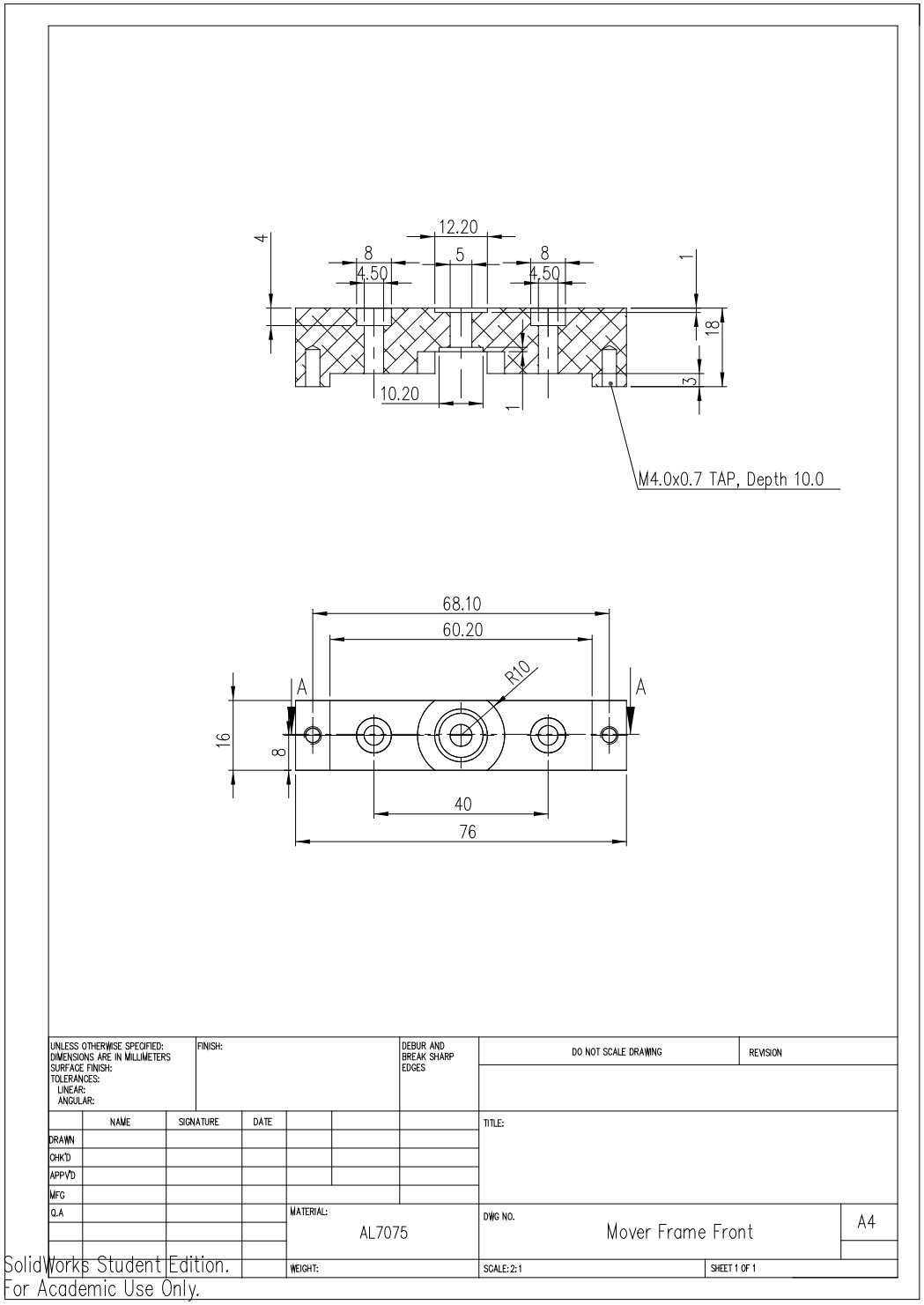

Fig. 133. Mover frame front.

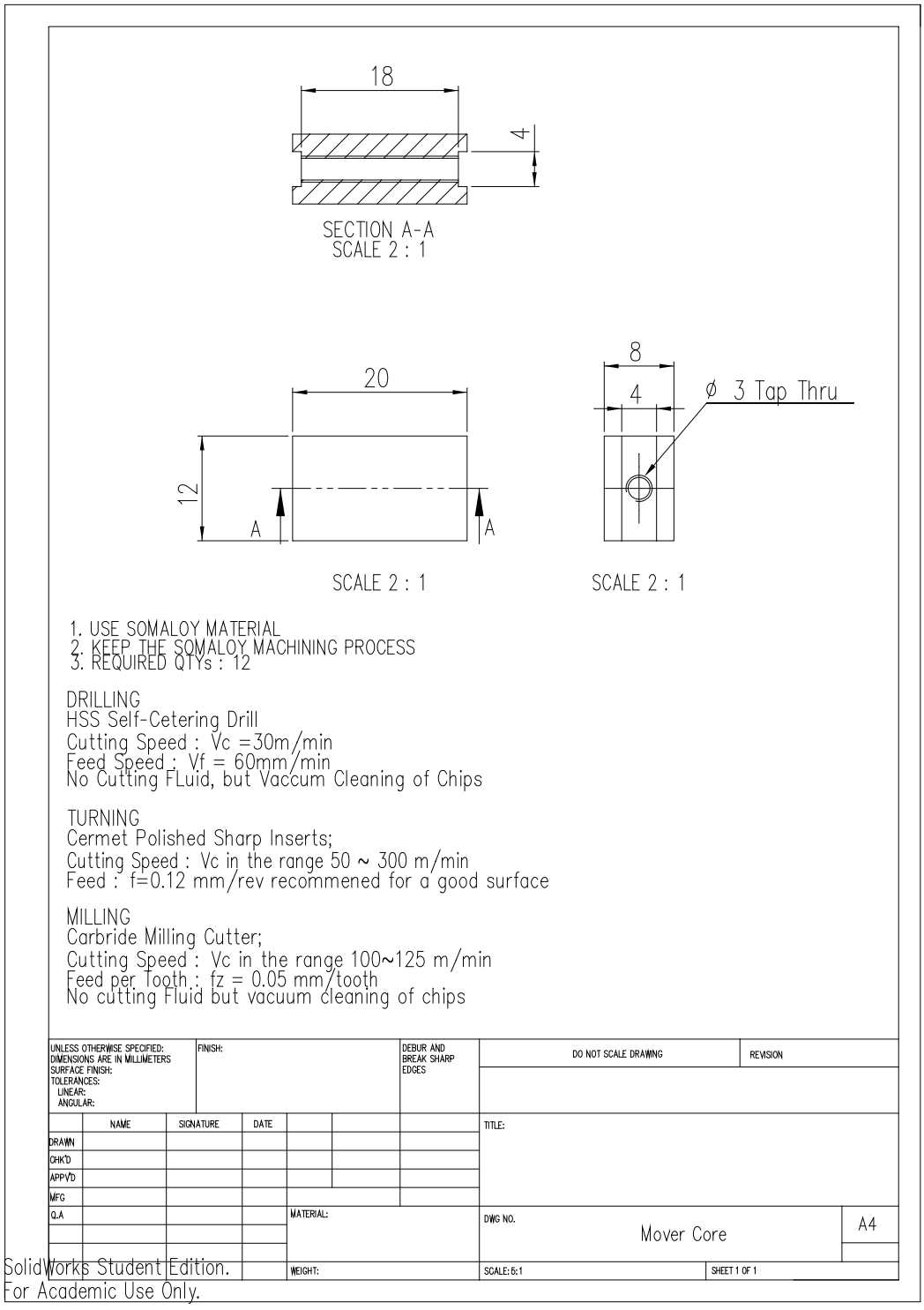

Fig. 134. Mover core.

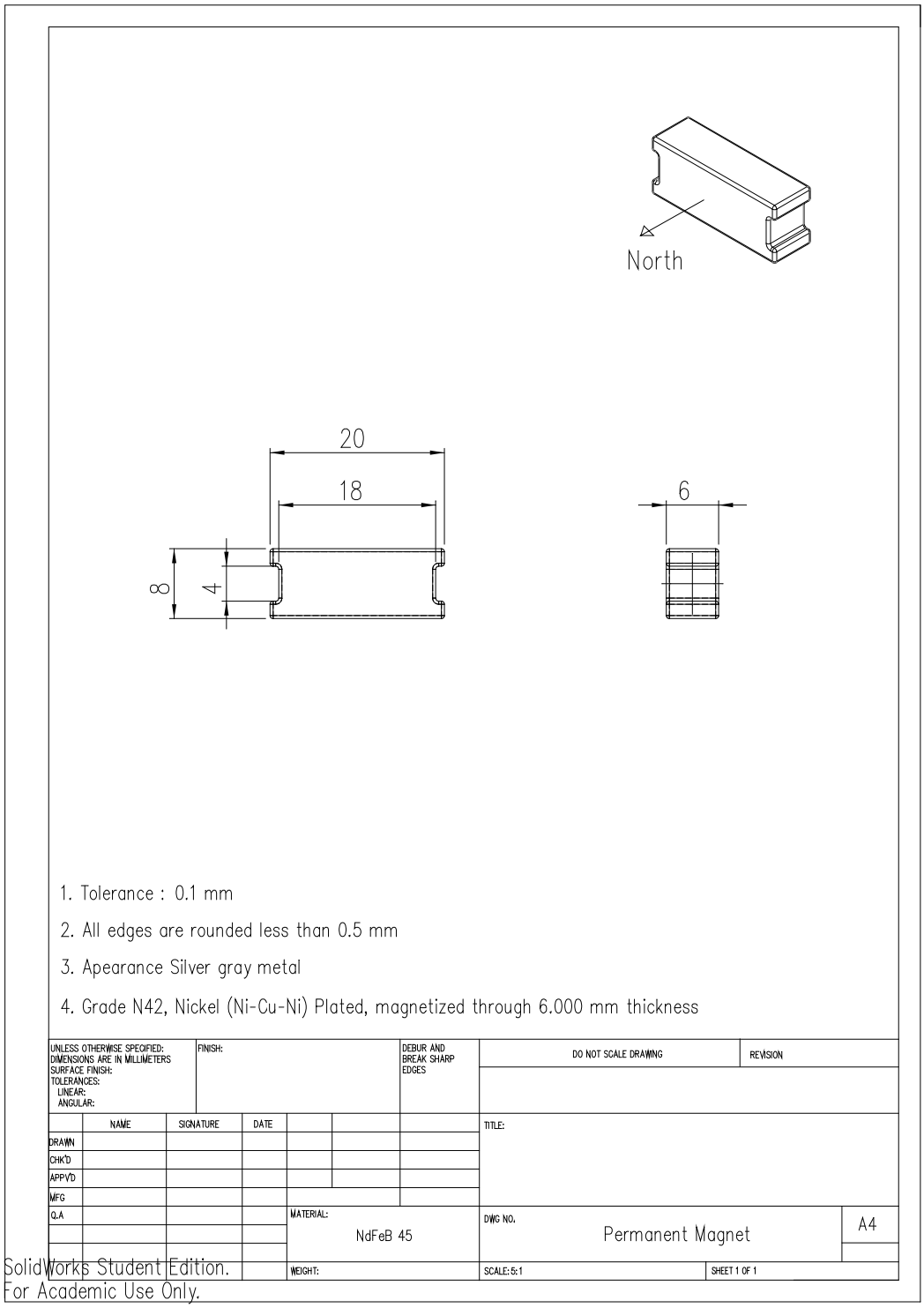

Fig. 135. Permanent magnet.

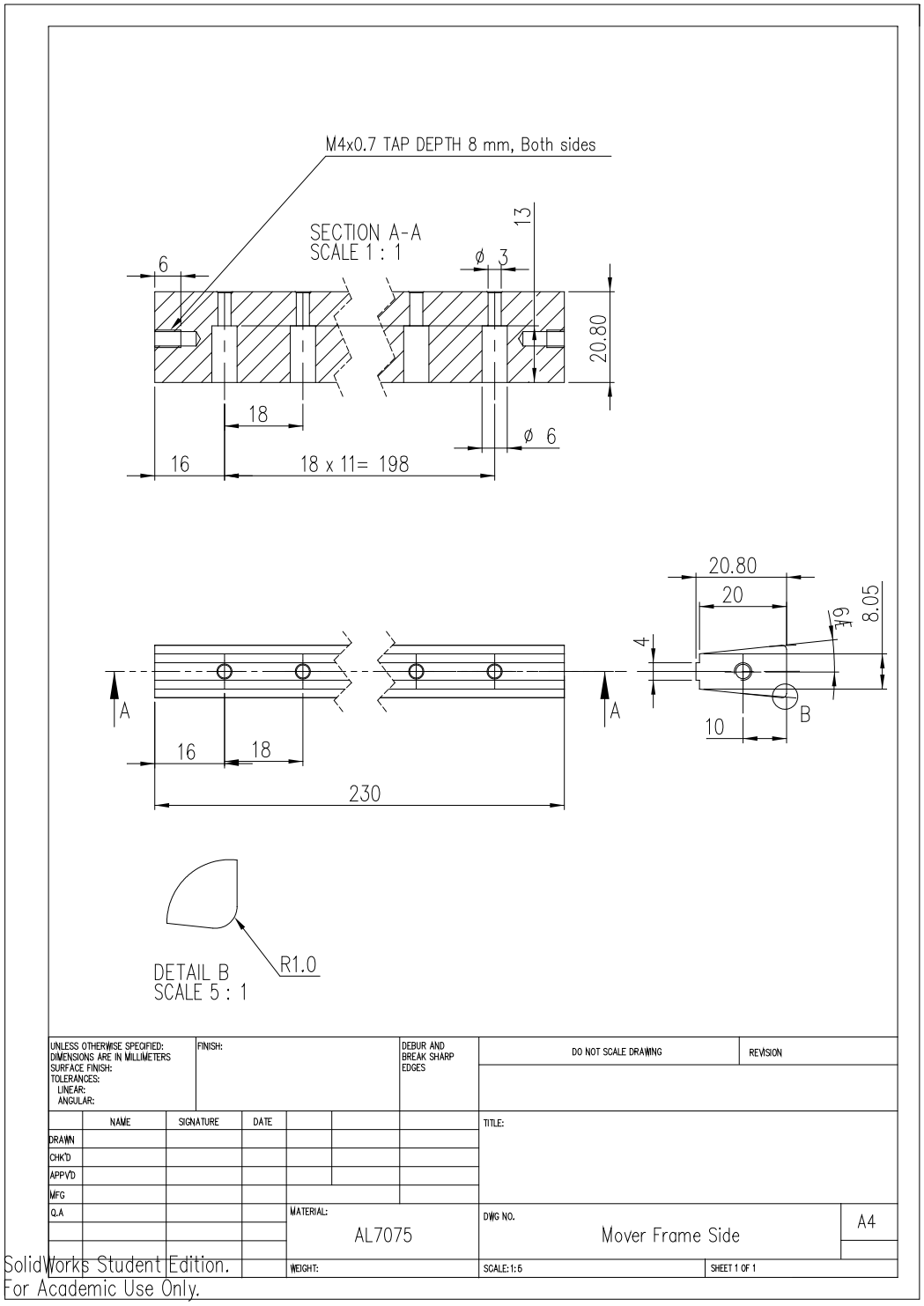

Fig. 136. Mover frame side.

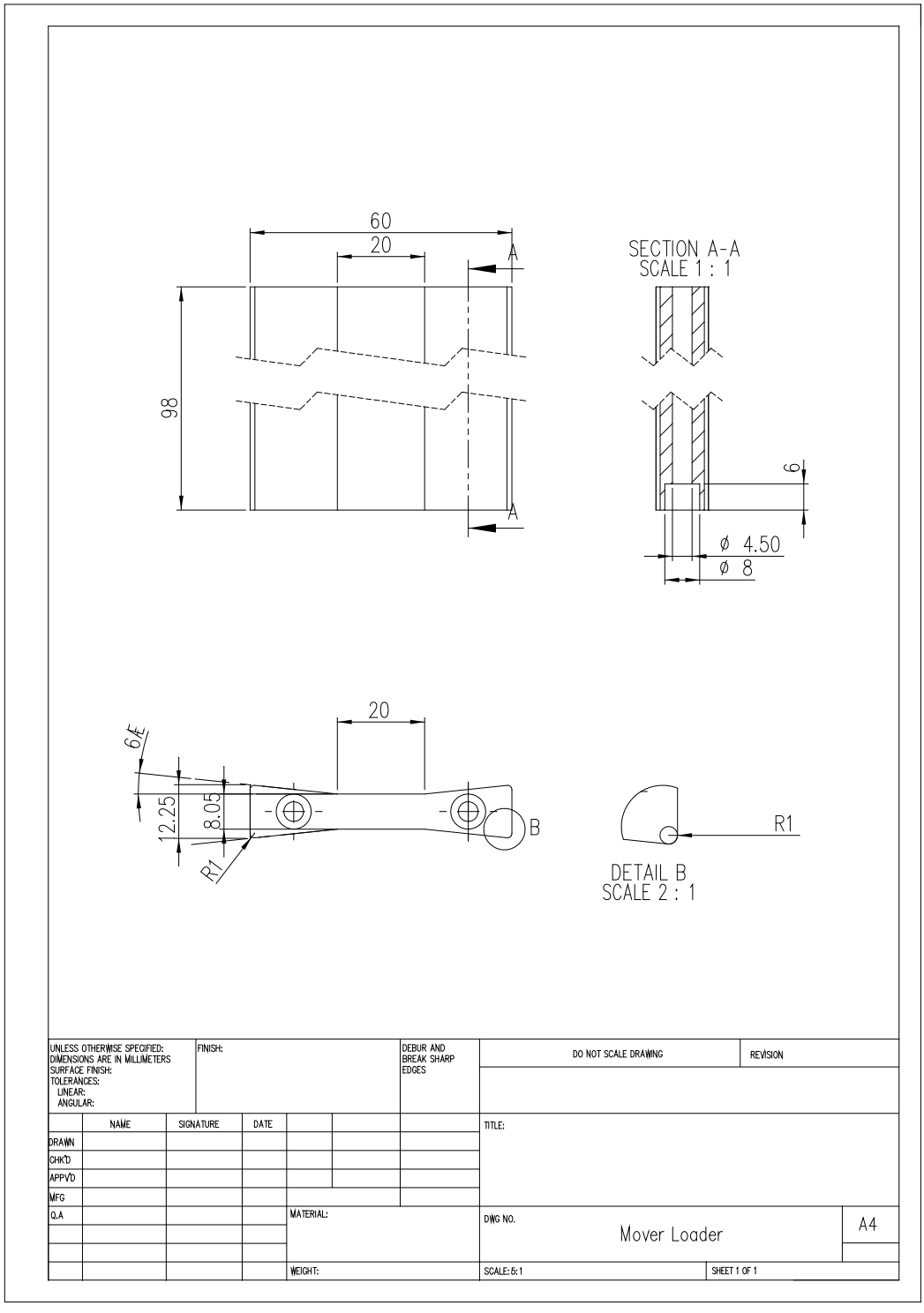

Fig. 137. Mover loader.

APPENDIX B

ELECTRICAL ENGINEERING SCHEMATICS

The controller assembly consists of four functional boards connected in a stack structure as shown in Fig. 138. These can be classified as the PWM amplifier, analog signal interface, digital signal interface, and digital signal processor boards depending on their functions. The high power (30.0 Vdc, 5.0 A) is used to produce the PWM output to drive the motor. The low power (±15.0 V, 1.0 A) is used in the analog and digital boards. The high- and low-power sources are isolated by the PCB circuit to avoid the noise interference from the PWM output. Thus, the external chassis ground is used for their common ground. All print circuit boards (PCB) has the dimension of $120 \times 80 \times 1.6$ mm^3 except for the DSP breakout board. The six layers are used for circuit fabrication, and the copper of 2 oz are used in the component and solder layers.

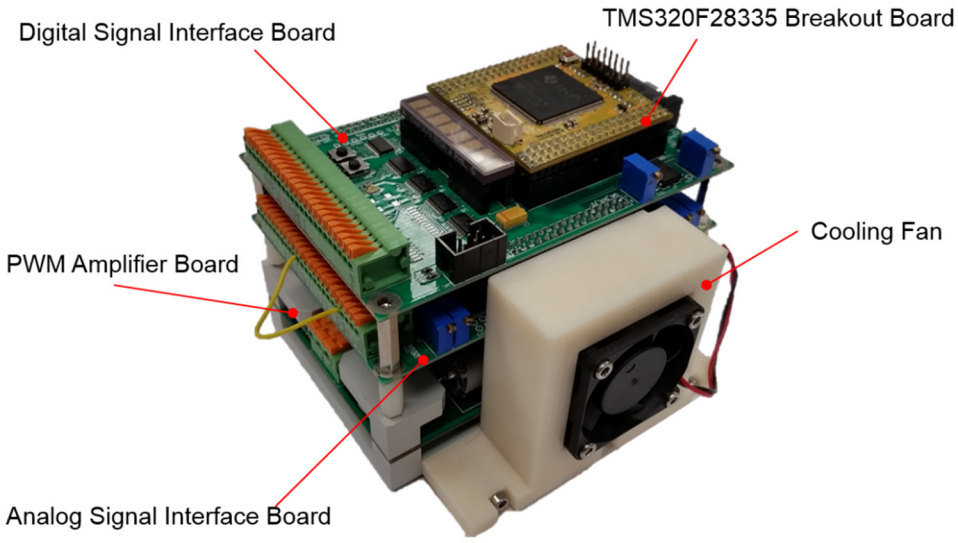

Fig. 138. Photograph of the controller assembly for the linear-motion control.

B.1. DSP Breakout Board

The cost-effective commercial TMS320F28335 (manufactured by TI instrument) DSP is used for convenience and reliability. This DSP based on the harvard BUS architecture can access various peripherial devices by using a 16- or 32-bit data bus. The operating clock up to 150 MHz can be used as a system clock. The 512 KB frash ROM and 68-KB SRAM are internally imbedded. The sixteen 12-bit ADC and six enhanced PWM channels are also included. Various serial communications are supported. The photograph in Fig. 139 shows the DSP breakout board used in this study. Table 26 and 27 describe the definitions of the external header pins.

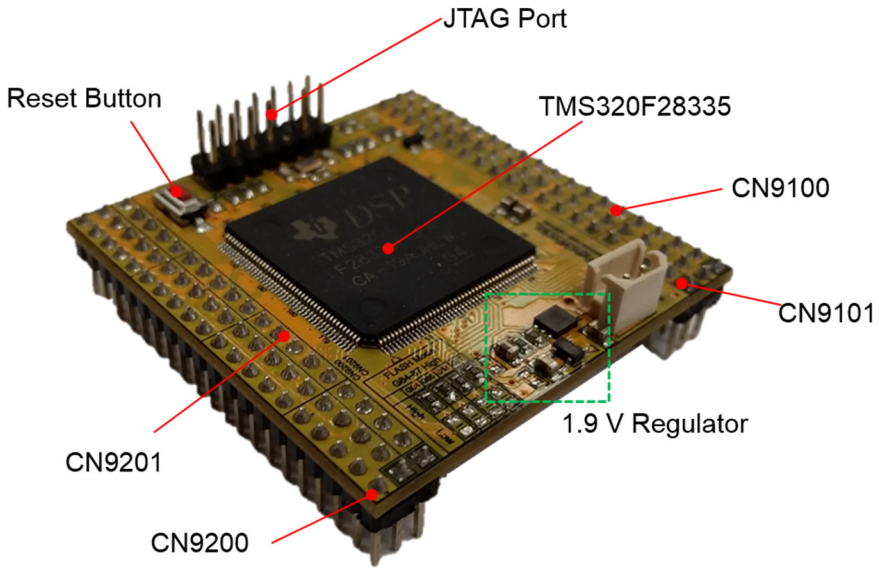

Fig. 139. Photograph of the DSP breakout board

Table 26. Pin descriptions of CN9100 and CN9101 headers

		CN9100			CN9101
1	**2**	N/C	AGND	**1**	GPIO30/CANRXA/XA18
3	**4**	ADCINA0	ADCINA1	**2**	GPIO31/CANTXA/XA17
5	**6**	ADCINA2	ADCINA3	**3**	GPIO39/XA16
7	**8**	ADCINA4	ADCINA5	**4**	GPIO87/XA15
9	**10**	ADCINA6	ADCINA7	**5**	GPIO86/XA14
11	**12**	ADCINB0	ADCINB1	**6**	GPIO85/XA13
13	**14**	ADCINB2	ADCINB3	**7**	GPIO84/XA12
15	**16**	ADCINB4	ADCINB5	**8**	GPIO83/XA11
17	**18**	ADCINB6	ADCINB7	**9**	GPIO82/XA10
19	**20**	5V	GND	**10**	GPIO81/XA9
21	**22**	GPIO28/SCIRXDA/XZCS6	GPIO33/SCLA/ADCSOCBO	**11**	GPIO80/XA8
23	**24**	/XRD	GPIO29/SCITXDA/XA19	**12**	GPIO47/XA7
25	**26**	GPIO54/SPIMOA/XD25	GPIO55/SPISOMIA/XD24	**13**	GPIO46/XA6
27	**28**	GPIO56/SPICKLA/XD23	GPIO57/SPISTES/XD22	**14**	GPIO45/XA5
29	**30**	GPIO35/SCITXDA/XR/W	GPIO36/SCIRXDA/XZCS0	**15**	GPIO44/XA4
31	**32**	GPIO19/SCIRXDB/CANTXA	GPIO18/SPICLKA/SCITXDB/CANRXA	**16**	GPIO43/X3
33	**34**	GPIO19/EQEP1S/SCITXDB	GPIO7/EPWM4B/SCAP2	**17**	GPIO42/XA2
35	**36**	GPIO23/EQEP1I/SCIRXDB	GPIO5/EPWM3B/ECAP1	**18**	GPIO41/XA1
37	**38**	GPIO20/EQEP1A/CANTXB	GPIO21/EQEP1B/CANRXB	**19**	GPIO40/XA0/XWE1
39	**40**	GPIO9/EPWM5B/SCITXDB	GPIO11/EPWM6B/SCIRXDB/ECAP4	**20**	GPIO38/XWE0

Table 27. Pin description of CN9200 and CN9201 headers

	CN9201			**CN9200**	
1	GPIO60/MCLKRB/XD19	**1**	**2**	GPIO0/EPWM1A	GPIO1/EPWM1B/ECAP6
3	GPIO61/MFSRB/XD18	**3**	**4**	GPIO2/EPWM2A	GPIO3/EPWM2B/ECAP5
5	GPIO62/SCIRXDC/XD17	**5**	**6**	GPIO4/EPWM3A	GPIO5/EPWM3B/ECAP1
7	GPIO63/SCITXDC/XD16	**7**	**8**	GPIO34/ECAP1/XREADY	GPIO37/ECAP2/XZCS7
9	GPIO64/XD15	**9**	**10**	GPIO24/ECAP1/EQEP2A/MDXB	GPIO25/ECAP2/EQEP2B
11	GPIO65/XD14	**11**	**12**	GPIO26/ECAP3/EQEP2I	GPIO27/ECAP4/EQEP2S
13	GPIO65/XD14	**13**	**14**	GPIO26/ECAP3/EQEP2I	GPIO12/TZ1/CANTXB
15	GPIO66/XD13	**15**	**16**	GPIO3/TZ2/CANRXB/MDRB	GPIO14/TZ3/XHOLD/SCITXDB
17	GPIO67/XD12	**17**	**18**	GPIO3/TZ2/CANRXB/MDRB	GPIO32/SDAA/EPWMSYNCI
19	GPIO68/XD11	**19**	**20**	GPIO6/EPWM4A/EPWMSYNCI	GPIO7/EPWM4B/MCLKRA
21	GPIO69/XD10	**21**	**22**	GPIO8/EPWM5A/ADCSOCAO	GPIO9/EPWM5B/SCITXDB
23	GPIO70/XD9	**23**	**24**	GPIO10/EPWM6A/ADCSOCBO	GPIO11/EPWM6B/SCIRXDB
25	GPIO71/XD8	**25**	**26**	GPIO17/ECAP4/EQEP2S	GPIO48/ECAP5/XD31
27	GPIO72/XD7	**27**	**28**	GPIO50/EQEP1A/XD29	GPIO51/EQEP1B/XD28
29	GPIO73/XD6	**29**	**30**	GPIO53/EQEP1I/XD26	GPIO52/EQEP1S/XD27
31	GPIO75/XD5	**31**	**32**	GPIO49/ECAP6/XD30	GPIO15/TZ4/XHOLDA/SCIRXDB
33	GPIO76/XD4	**33**	**34**	GPIO16/TZ5/SPISIMOA/CANTXB	GPIO17/TZ6/SPISOMIA/CANRXB
35	GPIO77/XD2	**35**	**36**	GPIO16/TZ5/SPISIMOA/CANTXB	GPIO33/SCLA/EPWMSYNCO
37	GPIO78/XD1	**37**	**38**	GPIO59/MFSRA/XD20	GPIO58/MCLKRA/XD21
39	GPIO79/XD0	**39**	**40**	XCLKOUT	/XRS

B.2. Digital Interface Board

The digital interface board interfaces the DSP board with the peripheral devices such as ADC, DAC, serial communication, state display, and TTL. The voltages of analog 5.0 Vdc (AVCC), digital 5.0 Vdc (DVCC), digital 3.3 Vdc (DVDD), analog 12.0 Vdc (VCC), and analog −12.0 Vdc (VSS) are used to drive the electric components. The serial communication driver chips are implemented to support the real-time serial communications such as the CAN and RS485. The 16-bit, 6-channel ADC and 14-bit, 4-channel DAC are implemented to interface with the external analog signal. These peripheral devices have their own addresses that the DSP can access. The six Hall-effect sensors can be connected at the same time. The 24-bit decoder chip is also equipped to interpret the output of the linear optical encoder (LOE). The two LOEs can be connected at the same time.

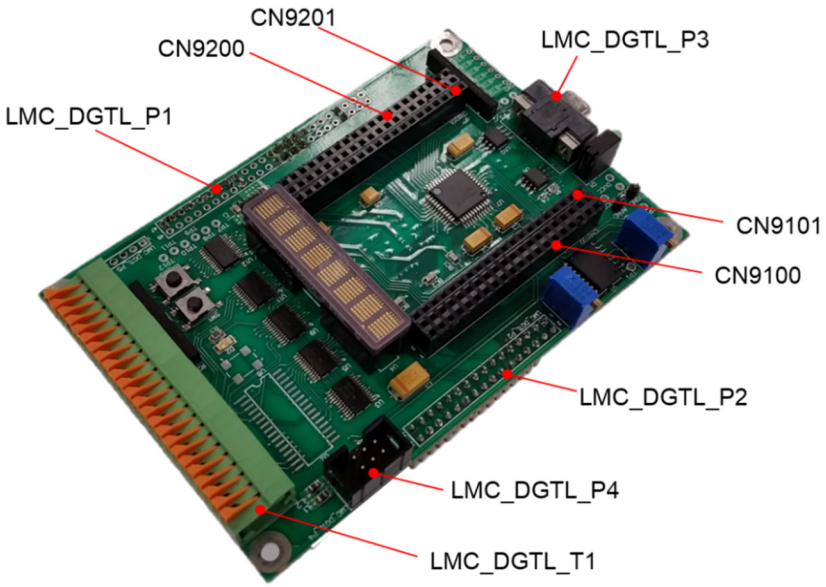

Fig. 140. Photograph of the digital interface board.

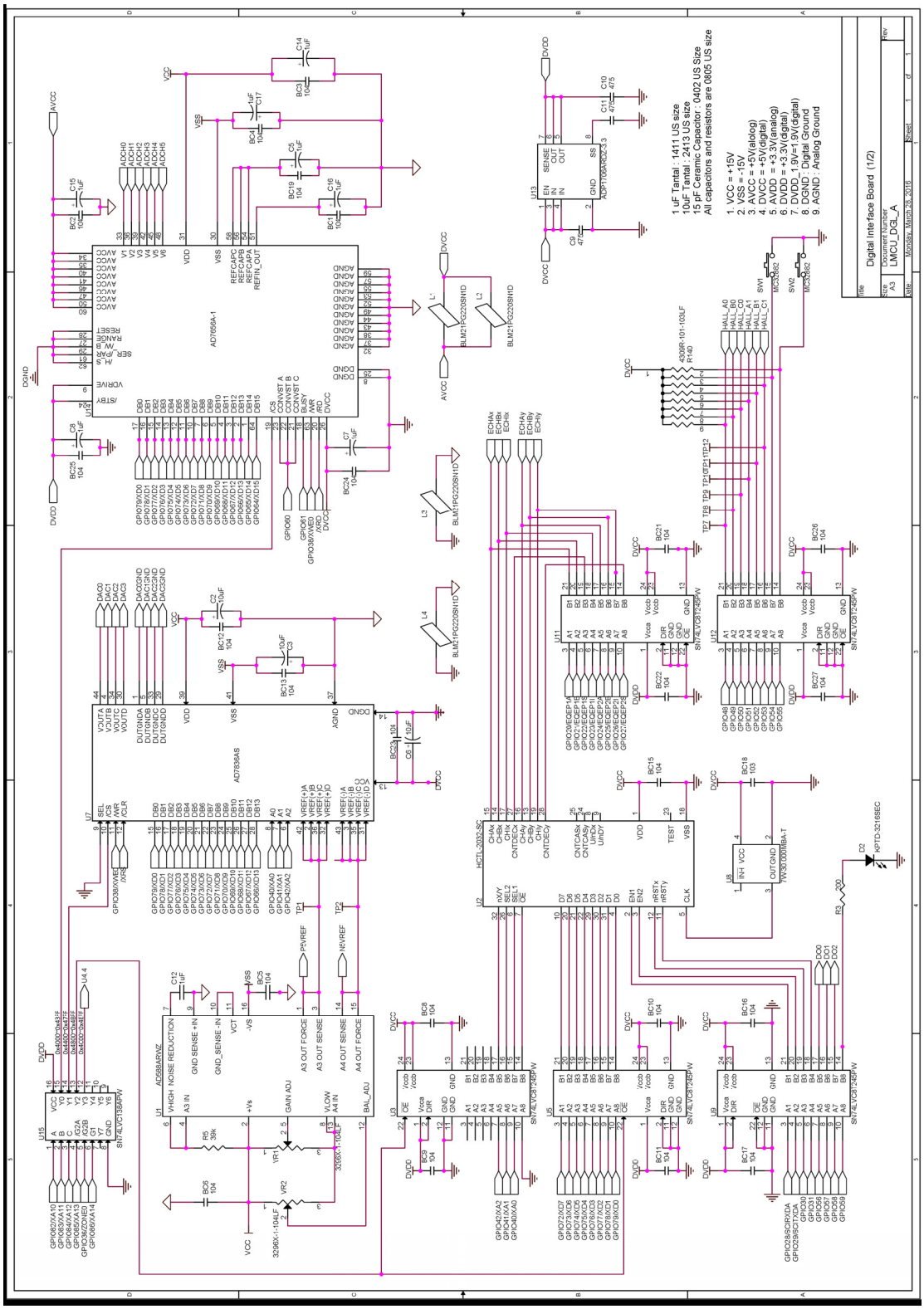

Fig. 141. Digital interface board schematic (1/2).

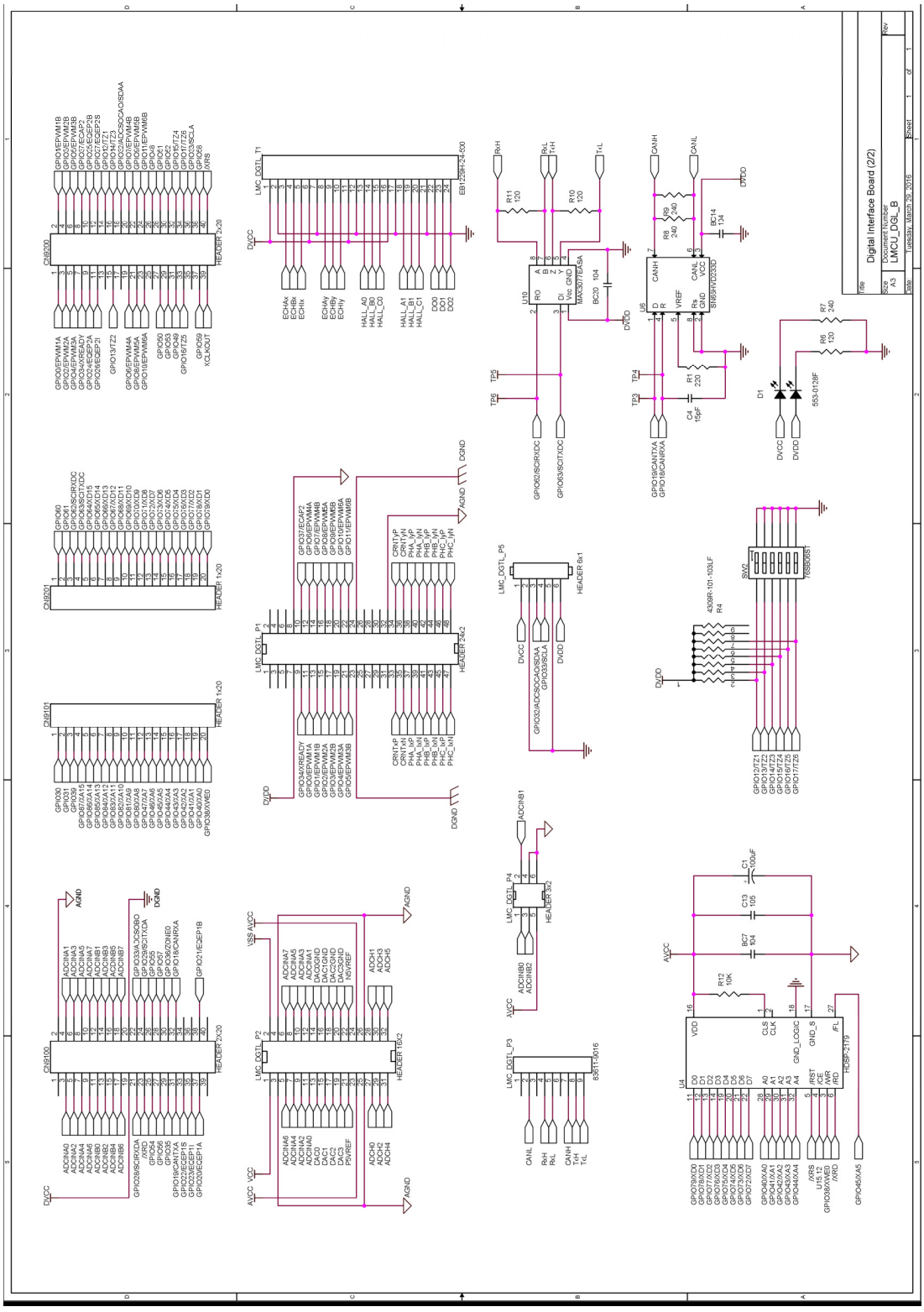

Fig. 142. Digital interface board schematic (2/2).

B.3. Analog Interface Board

The analog interface board acts as the signal conditioning board. The two functions are performed in this board: (1) to regulate the given supply voltage at the required low voltage level or generate the precision reference voltages supplied to the sensors, and (2) to attenuate the external input noise imbedded in signals using an anti-aliasing LPF, or amplifies the small signal with the desired gain. The two instrument amplifiers (INA118s) are used to amplify the low sensing voltage of the load cell, and to minimize the sensing value variation due to the potentiometer deterioration. All analog inputs passing the LPFs are fed to the external ADC input stages or the internal ADC input stages of the DSP. The gain of 100 is used for the load cell output signal.

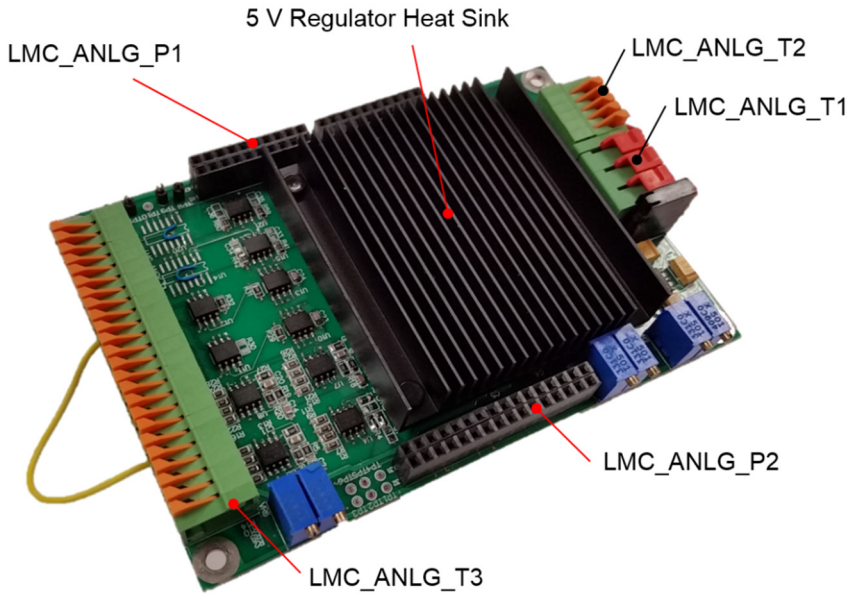

Fig. 143. Photograph of the analog interface board.

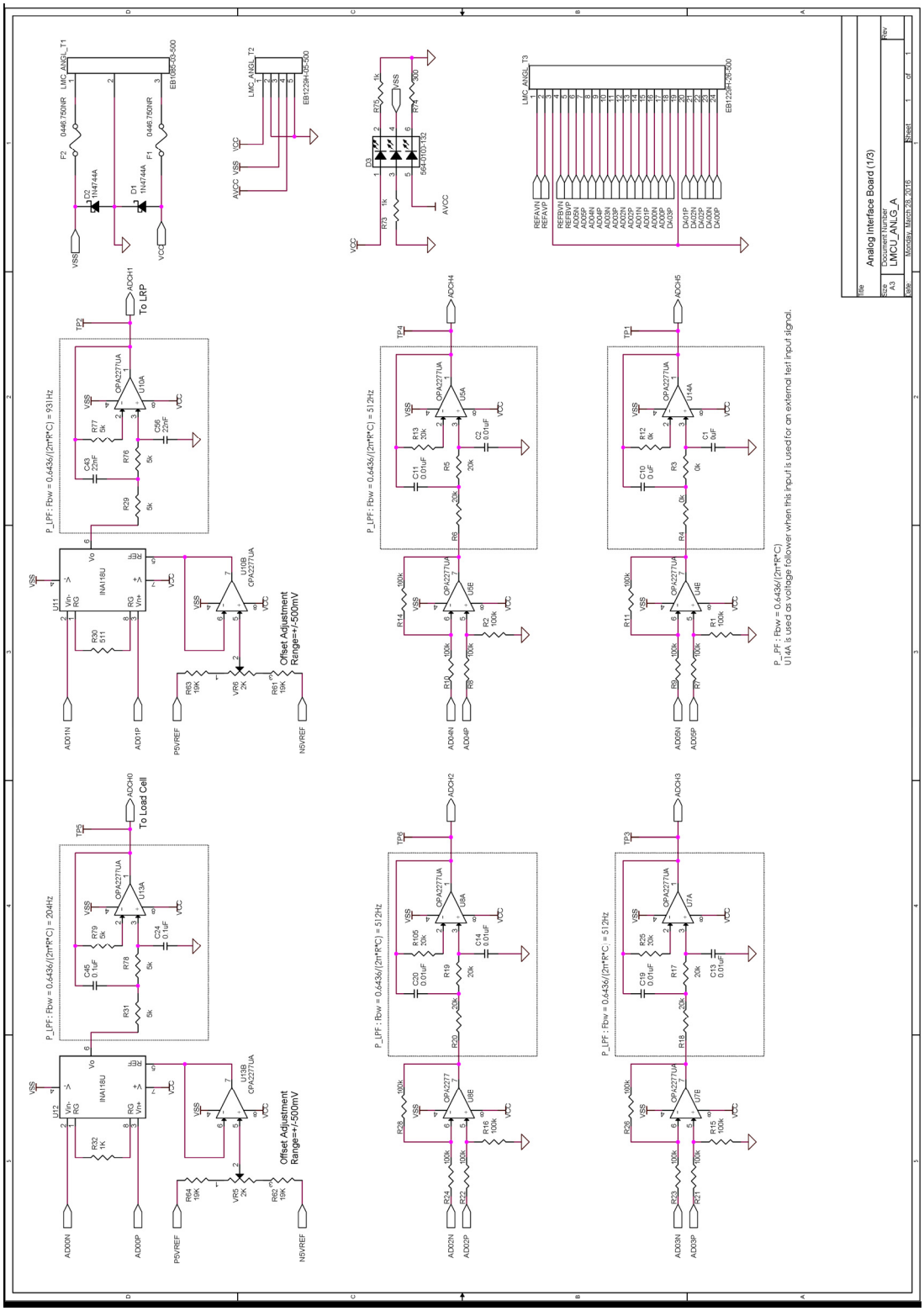

Fig. 144. Electric circuit schematic of the analog interface board (1/3).

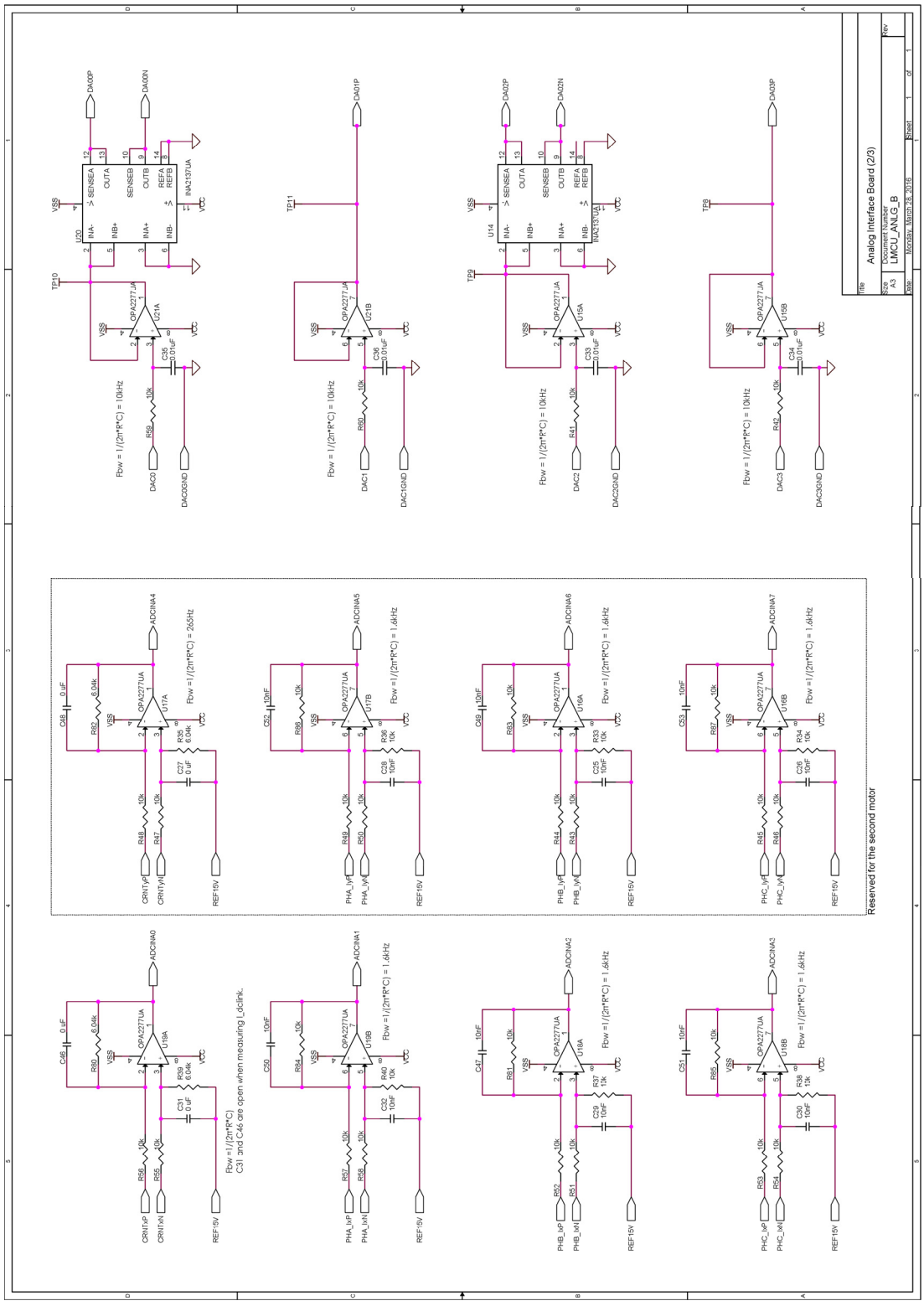

Fig. 145. Electric circuit schematic of the analog interface board (2/3).

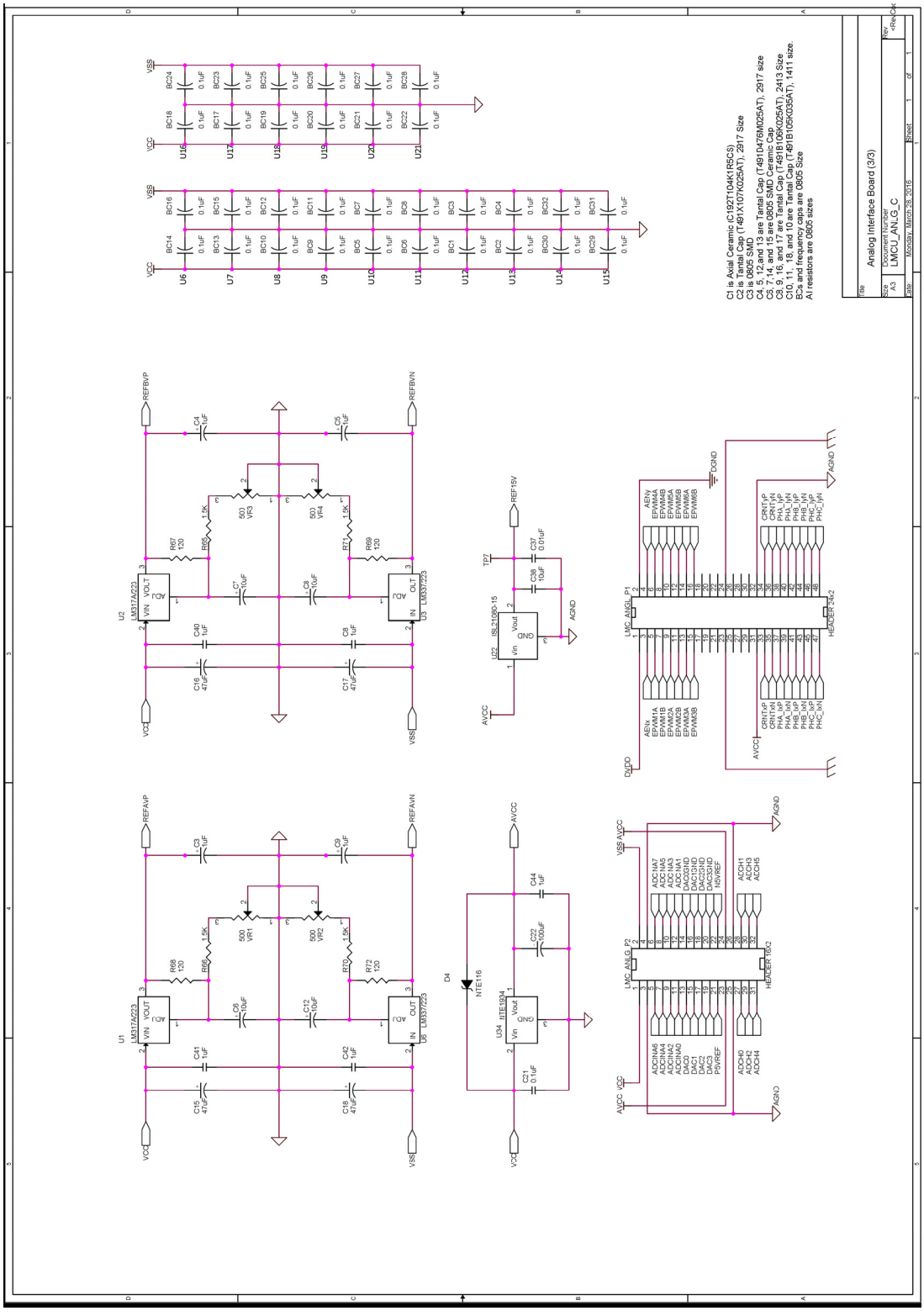

Fig. 146. Electric circuit schematic of the analog interface board (3/3)

B.4. PWM Amplifier Board

The PWM amplifier board transforms the 3.3-V PWM signals fed from the DSP into the dc-link voltage level using the six electrical switches. In this study, a hybrid IC (MSK4400U) that has the six built-in N-channel MOSFETs is used as the VSI. The isolators (HCPL-9030s) between PWM amplifier board and digital interface board are employed in order to avoid the damage or interferences caused from the high power-source fluctuations. The phase currents are measured using the contactless current sensor (MLX91205ABL) based on the Hall-effect. The dc-link current is measured using a current-sensing shunt resistor and an isolation amplifier (ACPL-79B). The maximum voltage and current of 75 V and 10 A can be supplied as the dc-link voltage The photograph in Fig. 147 shows the PWM amplifier board. Fig. 148 and 149 illustrate the schematic of the PWM amplifier board.

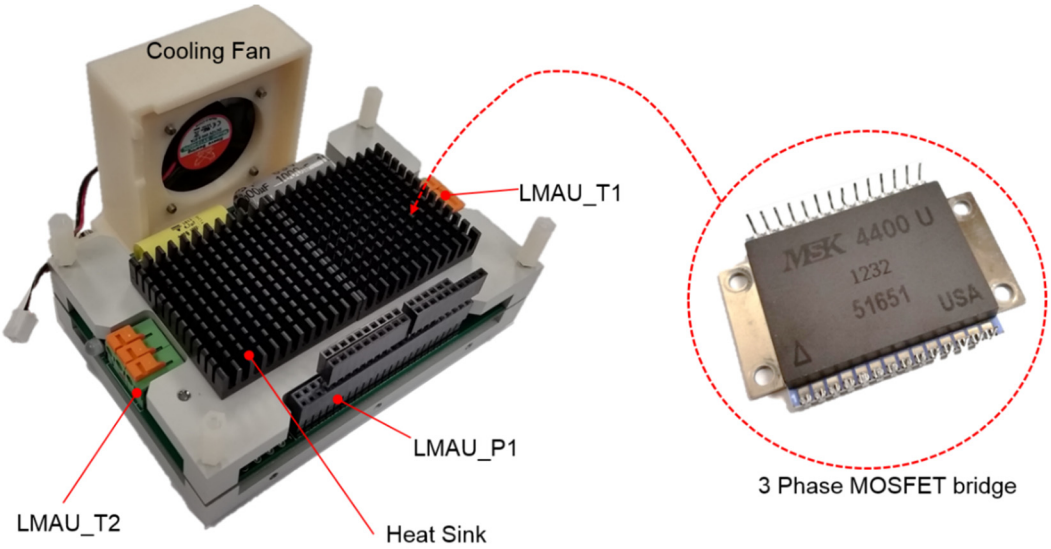

Fig. 147. Photograph of the PWM amplifier board.

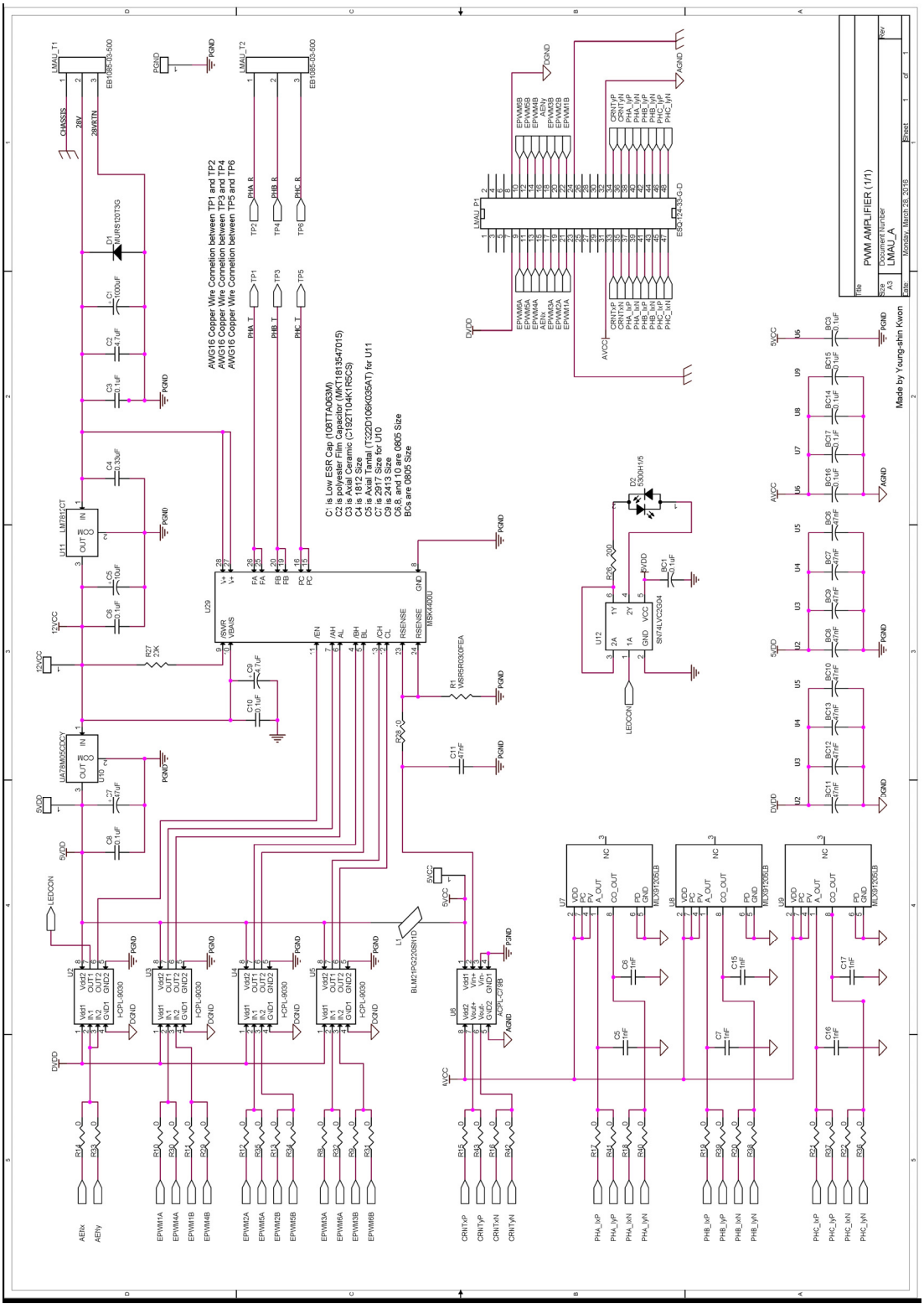

Fig. 148. Electric circuit schematic of the PWM amplifier board.

B.5. System Harness Diagram

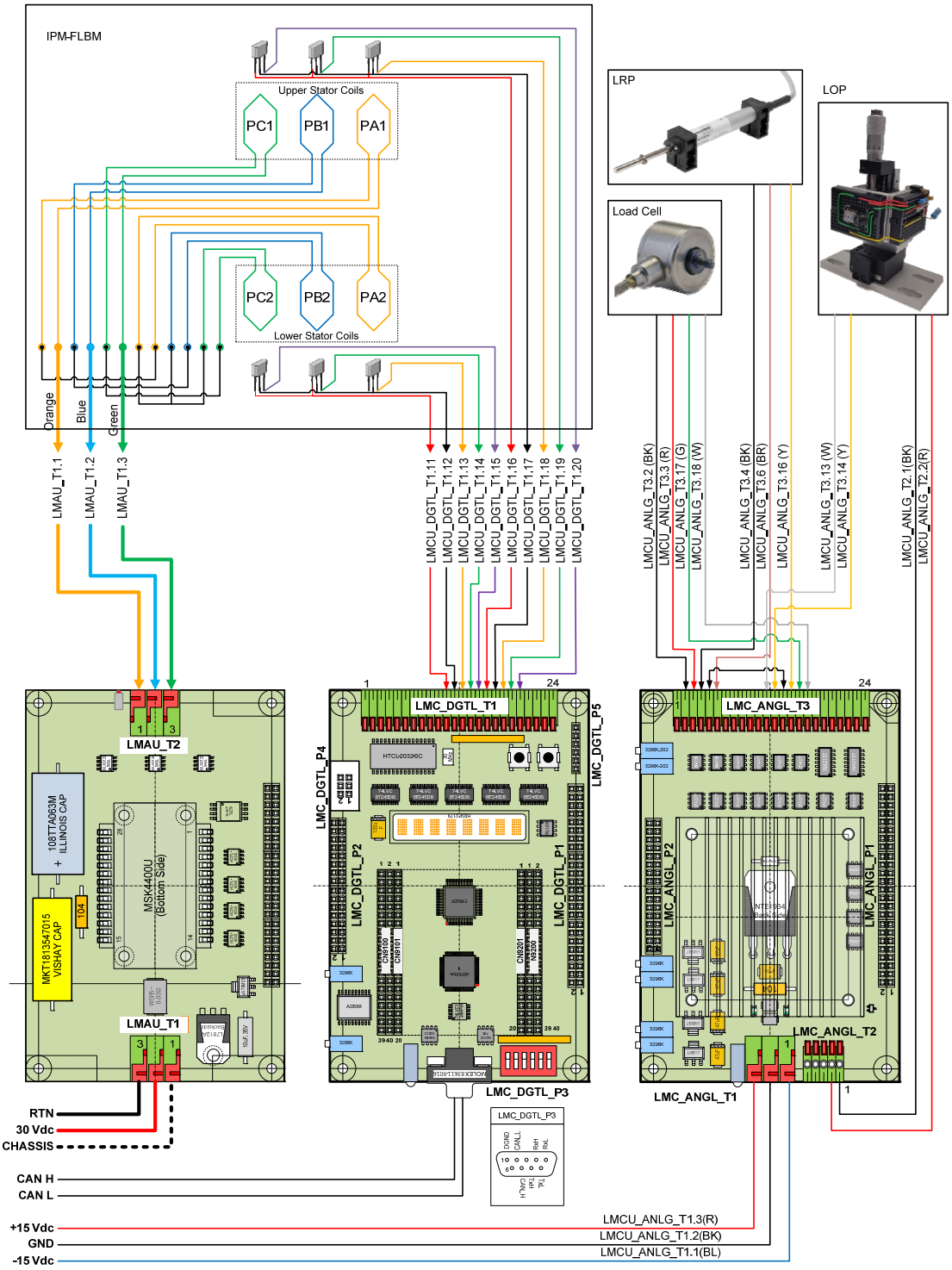

Fig. 149. Wiring diagram of the linear control system.

APPENDIX C

PROGRAM CODES

In this appendix, the C codes employed in the proportional controller with a lead compensator, the 12-step current controller scheme, and FOC scheme are presented. The real-time control code is implemented in the TMS28F335 DSP. The loop function Task300uS() is called every 300 μs using a cpu-timer interrupt built in the DSP. Based on this fundamental interrupt, the loop with a 300-μs interval is used in the current control loop for the fast response, and the loop time of 1.2 ms is employed in the position-control loop with a low control bandwidth. Every controllers designed in the continuous-time domain are transformed to be the discrete controllers using the Tustin's method. The Code Composer V5.5. of Texas Instrument is used as the debugging software tool. The general codes to access the peripheral devices such as ADC, DAC, LCD, CAN, and general purpose input-outputs (GPIOs) are not included in this appendix.

C.1. C code for the proportional controller with a lead compensator

```
//===== Set of control parameter of the P controller and lead compensator ==========
const float C51 = 3.5*10.7*(4.2*6.28*0.0012+2.0)/(45*6.28*0.0012+2.0);
const float C52 = 3.5*10.7*(4.2*6.28*0.0012-2.0)/(45*6.28*0.0012+2.0);
const float C53 = (45*6.28*0.0012-2.0)/(45*6.28*0.0012+2.0);

DeErrPs = PosCmd - PotenVolt;     // When using a feedback sensor as the LRP.
DeErrPs = PosCmd - PDPosition;    // When using a feedback sensor as the LOP.

//===== P controller and lead compensator and update of variables===== ==========
DeLeaPs = C51*DeErrPs + C52*DeErrPv - C53*DeLeaPv;
CurrentCmd = DeLeaPs;
DeErrPv = DeErrPs;
DeLpfPv = DeLpfPs;
DeLeaPv = DeLeaPs;
```

C.2. C codes for the FOC scheme

```
//========PI Current Controller Gains for the q-axis ==========================
const float C11 = (90*6.28*0.0003+2.0)/2.0;
const float C12 = (90*6.28*0.0003-2.0)/2.0;
const float C13 = 2.6;
//======== PI Current Controller Gains for the d-axis==========================
const float C21 = (110*6.28*0.0003+2.0)/2.0;
const float C22 = (110*6.28*0.0003-2.0)/2.0;
const float C23 = 1.7;

void FieldOrientedCon()
{
        if (PWMAmpBit==0)
        {
                PWMAmpInh = 0;                  // PWMAMP ON

// (STEP1) Transform the abc-frame to the alpha-beta frame ====================
                Ialpha = CurrentIb;
                Ibeta = 0.5774*(CurrentIc-CurrentIa);

// (STEP2) Transform the alpha-beta frame to d-q frame ========================
                PositionX = (0.005)*PotenVolt;      // Unit Change: Voltage to meter when using LRP
                PositionX = (0.005)*PDPosition;     // Unit Change: Voltage to meter when using LOP
                Theta_e = PI_TP*PositionX;          // Electrical angle
                CosTerm = cos(Theta_e);
                SinTerm = sin(Theta_e);
                Iq = Ialpha*CosTerm + Ibeta*SinTerm;
                Id = Ialpha*SinTerm - Ibeta*CosTerm;

// (STEP3) PI current controller ==============================================
                IqCrntErrPs = (float)(CurrentCmd - Iq);
                IqCrntIn1Ps = IqCrntIn1Pv + C11*IqCrntErrPs + C12*IqCrntErrPv;
                Vq = C13*IqCrntIn1Ps;

               IdCrntErrPs = (float)(0.0 - Id);
                IdCrntIn1Ps = IdCrntIn1Pv + C21*IdCrntErrPs + C22*IdCrntErrPv;
                Vd = C23*IdCrntIn1Ps;

                IqCrntErrPv = IqCrntErrPs;
                IqCrntIn1Pv = IqCrntIn1Ps;
                IdCrntErrPv = IdCrntErrPs;
                IdCrntIn1Pv = IdCrntIn1Ps;

// (STEP4) Inverse Transformation for the calculated Vq and Vd ================
                Valpha = Vq*CosTerm + Vd*SinTerm;
                Vbeta = Vq*SinTerm - Vd*CosTerm;
                Vref = sqrt(Valpha*Valpha + Vbeta*Vbeta);

// (STEP5) Sector Determination Algorithm =====================================
                if (Vbeta >= 0.0 )
                {
```

```
                if(Valpha >= 0.0 )
                {
                        if(Vbeta <= 1.732*Valpha) Sector = 1;
                        else Sector = 2;
                        Theta = asin(Vbeta/Vref);
                }
                else if(Valpha < 0.0)
                {
                        if(Vbeta <= -1.732*Valpha) Sector = 3;
                        else Sector = 2;
                        Theta = 3.142 - asin(Vbeta/Vref);
                }
        }
        else if (Vbeta < 0.0 )
        {
                if(Valpha <= 0.0)
                {
                        if(Vbeta >= 1.732*Valpha) Sector = 4;
                        else Sector = 5;
                        Theta = 3.142 - asin(Vbeta/Vref);
                }
                else if(Valpha > 0.0)
                {
                        if(Vbeta >= -1.732*Valpha) Sector = 6;
                        else Sector = 5;
                        Theta = 6.283 + asin(Vbeta/Vref);
                }
        }

// (STEP6) Computing the duty cycle for each high-side switch using SVM ==========
        T1 = SVMC1*Vref*sin(1.047*Sector - Theta);
        T2 = SVMC1*Vref*sin(Theta - 1.047*(Sector - 1));
        T0 = Ts - (T1 + T2);

        switch(Sector)
        {
                case 1 :
                        VasTime = 0.5*T0;
                        VbsTime = T1+T2+0.5*T0;
                        VcsTime = T1+0.5*T0;
                        break;
                case 2 :
                        VasTime = 0.5*T0;
                        VbsTime = T1+0.5*T0;
                        VcsTime = T1+T2+0.5*T0;
                        break;
                case 3 :
                        VasTime = T1+0.5*T0;
                        VbsTime = 0.5*T0;
                        VcsTime = T1+T2+0.5*T0;
                        break;
                case 4 :
                        VasTime = T1+T2+0.5*T0;
```

```
                    VbsTime = 0.5*T0;
                    VcsTime = T1+0.5*T0;
                    break;
                case 5 :
                    VasTime = T1+T2+0.5*T0;
                    VbsTime = T1+0.5*T0;
                    VcsTime = 0.5*T0;
                    break;
                case 6 :
                    VasTime = T1+0.5*T0;
                    VbsTime = T1+T2+0.5*T0;
                    VcsTime = 0.5*T0;
                    break;
                default :           break;
            }

// (STEP 7) Generating PWM signal========================== ==========
            EPwm1Regs.CMPA.half.CMPA
            = (Uint16)(EPwm1Regs.TBPRD - (EPwm1Regs.TBPRD * VasTime));
            EPwm2Regs.CMPA.half.CMPA
            = (Uint16)(EPwm2Regs.TBPRD - (EPwm1Regs.TBPRD * VbsTime));
            EPwm3Regs.CMPA.half.CMPA
            = (Uint16)(EPwm3Regs.TBPRD - (EPwm1Regs.TBPRD * VcsTime));

        }
// (STEP 7) Set to zero for PWM amp off ==================================
        else if((PWMAmpBit==1)||(CurrentCmd==0.0))
        {
            PWMAmpInh = 1;                  // PWMAMP OFF
            EPwm1Regs.CMPA.half.CMPA = (Uint16)(EPwm1Regs.TBPRD);
            EPwm2Regs.CMPA.half.CMPA = (Uint16)(EPwm2Regs.TBPRD);
            EPwm3Regs.CMPA.half.CMPA = (Uint16)(EPwm3Regs.TBPRD);

// (STEP 8) Initialization of all variables ==============================
            DutyCycle       = 0.0;
            IqCrntErrPv     = 0.0;
            IdCrntErrPv     = 0.0;
            IqCrntErrPs     = 0.0;
            IdCrntErrPs     = 0.0;
            IqCrntIn1Pv     = 0.0;
            IdCrntIn1Pv     = 0.0;
            IqCrntIn1Ps     = 0.0;
            IdCrntIn1Ps     = 0.0;
            Vq              = 0.0;
            Vd              = 0.0;
            }
        }
```

C.3 C codes for the 12-step current control scheme

```
//========PI Current Controller Gains ===================================
const float C11 = (120*6.28*0.0003+2.0)/2.0;
const float C12 = (120*6.28*0.0003-2.0)/2.0;;
const float C13 = 0.7;

void BLAC12StepCrntConV1(void)
{
        if (PWMAmpBit==0)               // PWMAMP ON
        {

// (STEP 1) Gain control according to the conduction modes ==================
                PWMAmpInh = 0;
                if (CondMode == SWITCHINGMODE3) CrntCmd12StepPs = 0.82*CurrentCmd;
                else CrntCmd12StepPs = CurrentCmd;

// (STEP 2) Calculation of the absolute error ===============================
                if ( CrntCmd12StepPs >= 0)
                {
                        CrntErrPs = (float)(CrntCmd12StepPs - DCBusCrnt);
                }
                else if ( CrntCmd12StepPs < 0)
                {
                        CrntErrPs = (float)(-1.0*CrntCmd12StepPs - DCBusCrnt);
                }

// (STEP 3) Current Control with PI-controller ==============================
                CrntIn1Ps = CrntIn1Pv + C21*CrntErrPs + C22*CrntErrPv;
                CrntCmdPs = C23*CrntIn1Ps;

// (STEP 4) Maximum duty cycle limit ========================================
                if(CrntCmdPs >= 0.0)
                {
                        DutyCycle = CrntCmdPs;
                        if(DutyCycle >= 10.0) DutyCycle = 10.0;
                }
                else if(CrntCmdPs < 0)
                {
                        DutyCycle  = 0.0;
                }

// (STEP 5) Developing the positive force for the positive command ==========
                if (CrntCmd12StepPs >= 0)
                {
                        if (Hall == 60)
                        {
                                EPwm1Regs.CMPA.half.CMPA = EPwm1Regs.TBPRD;
                                GpioDataRegs.GPASET.bit.GPIO1 = 1;
                                EPwm2Regs.CMPA.half.CMPA
        = (Uint16)(EPwm2Regs.TBPRD - (EPwm2Regs.TBPRD * DutyCycle/DMax1));
                                GpioDataRegs.GPACLEAR.bit.GPIO3 = 1;
```

```
                    EPwm3Regs.CMPA.half.CMPA = EPwm3Regs.TBPRD;
                    GpioDataRegs.GPACLEAR.bit.GPIO5 = 1;
                }
                else if (Hall == 56)
                {
                    EPwm1Regs.CMPA.half.CMPA = EPwm1Regs.TBPRD;
                    GpioDataRegs.GPASET.bit.GPIO1 = 1;
                    EPwm2Regs.CMPA.half.CMPA
= (Uint16)(EPwm2Regs.TBPRD - (EPwm2Regs.TBPRD * DutyCycle/DMax2));
                    GpioDataRegs.GPACLEAR.bit.GPIO3 = 1;
                    EPwm3Regs.CMPA.half.CMPA = EPwm3Regs.TBPRD;
                    GpioDataRegs.GPASET.bit.GPIO5 = 1;

                }
                else if (Hall == 51)
                {
                    EPwm1Regs.CMPA.half.CMPA
= (Uint16)(EPwm1Regs.TBPRD - (EPwm1Regs.TBPRD * DutyCycle/DMax1));
                    GpioDataRegs.GPACLEAR.bit.GPIO1 = 1;
                    EPwm2Regs.CMPA.half.CMPA = EPwm2Regs.TBPRD;
                    GpioDataRegs.GPACLEAR.bit.GPIO3 = 1;
                    EPwm3Regs.CMPA.half.CMPA = EPwm3Regs.TBPRD;
                    GpioDataRegs.GPASET.bit.GPIO5 = 1;
                }
                else if (Hall == 49)
                {
                    EPwm1Regs.CMPA.half.CMPA
= (Uint16)(EPwm1Regs.TBPRD - (EPwm1Regs.TBPRD * DutyCycle/DMax2));
                    GpioDataRegs.GPACLEAR.bit.GPIO1 = 1;
                    EPwm2Regs.CMPA.half.CMPA
= (Uint16)(EPwm2Regs.TBPRD - (EPwm2Regs.TBPRD * DutyCycle/DMax2));
                    GpioDataRegs.GPACLEAR.bit.GPIO3 = 1;
                    EPwm3Regs.CMPA.half.CMPA = EPwm3Regs.TBPRD;
                    GpioDataRegs.GPASET.bit.GPIO5 = 1;
                }
                else if (Hall == 48)
                {
                    EPwm1Regs.CMPA.half.CMPA = EPwm1Regs.TBPRD;
                    GpioDataRegs.GPACLEAR.bit.GPIO1 = 1;
                    EPwm2Regs.CMPA.half.CMPA
= (Uint16)(EPwm2Regs.TBPRD - (EPwm2Regs.TBPRD * DutyCycle/DMax1));
                    GpioDataRegs.GPACLEAR.bit.GPIO3 = 1;
                    EPwm3Regs.CMPA.half.CMPA = EPwm3Regs.TBPRD;
                    GpioDataRegs.GPADAT.bit.GPIO5 = 1;
                }
                else if (Hall == 35)
                {
                    EPwm1Regs.CMPA.half.CMPA
= (Uint16)(EPwm1Regs.TBPRD - (EPwm1Regs.TBPRD * DutyCycle/DMax2));
                    GpioDataRegs.GPACLEAR.bit.GPIO1 = 1;
                    EPwm2Regs.CMPA.half.CMPA = EPwm2Regs.TBPRD;
                    GpioDataRegs.GPASET.bit.GPIO3 = 1;
                    EPwm3Regs.CMPA.half.CMPA = EPwm3Regs.TBPRD;
```

```
                GpioDataRegs.GPASET.bit.GPIO5 = 1;
            }
            else if (Hall == 28)
            {
                EPwm1Regs.CMPA.half.CMPA = EPwm1Regs.TBPRD;
                GpioDataRegs.GPASET.bit.GPIO1 = 1;
                EPwm2Regs.CMPA.half.CMPA
= (Uint16)(EPwm2Regs.TBPRD - (EPwm2Regs.TBPRD * DutyCycle/DMax2));
                GpioDataRegs.GPACLEAR.bit.GPIO3 = 1;
                EPwm3Regs.CMPA.half.CMPA
= (Uint16)(EPwm3Regs.TBPRD - (EPwm3Regs.TBPRD * DutyCycle/DMax2));
                GpioDataRegs.GPACLEAR.bit.GPIO5 = 1;
            }
            else if (Hall == 15)
            {
                EPwm1Regs.CMPA.half.CMPA = EPwm1Regs.TBPRD;
                GpioDataRegs.GPACLEAR.bit.GPIO1 = 1;
                EPwm2Regs.CMPA.half.CMPA = EPwm2Regs.TBPRD;
                GpioDataRegs.GPASET.bit.GPIO3 = 1;
                EPwm3Regs.CMPA.half.CMPA
= (Uint16)(EPwm3Regs.TBPRD - (EPwm3Regs.TBPRD * DutyCycle/DMax1));
                GpioDataRegs.GPACLEAR.bit.GPIO5 = 1;
            }
            else if (Hall == 14)
            {
                EPwm1Regs.CMPA.half.CMPA = EPwm1Regs.TBPRD;
                GpioDataRegs.GPASET.bit.GPIO1 = 1;
                EPwm2Regs.CMPA.half.CMPA = EPwm2Regs.TBPRD;
                GpioDataRegs.GPASET.bit.GPIO3 = 1;
                EPwm3Regs.CMPA.half.CMPA
= (Uint16)(EPwm3Regs.TBPRD - (EPwm3Regs.TBPRD * DutyCycle/DMax2));
                GpioDataRegs.GPACLEAR.bit.GPIO5 = 1;
            }
            else if (Hall == 12)
            {
                EPwm1Regs.CMPA.half.CMPA = EPwm1Regs.TBPRD;
                GpioDataRegs.GPASET.bit.GPIO1 = 1;
                EPwm2Regs.CMPA.half.CMPA = EPwm2Regs.TBPRD;
                GpioDataRegs.GPACLEAR.bit.GPIO3 = 1;
                EPwm3Regs.CMPA.half.CMPA
= (Uint16)(EPwm3Regs.TBPRD - (EPwm3Regs.TBPRD * DutyCycle/DMax1));
                GpioDataRegs.GPACLEAR.bit.GPIO5 = 1;
            }
            else if (Hall == 7)
            {
                EPwm1Regs.CMPA.half.CMPA
= (Uint16)(EPwm1Regs.TBPRD - (EPwm1Regs.TBPRD * DutyCycle/DMax2));
                GpioDataRegs.GPACLEAR.bit.GPIO1 = 1;
                EPwm2Regs.CMPA.half.CMPA =  EPwm2Regs.TBPRD;
                GpioDataRegs.GPASET.bit.GPIO3 = 1;
                EPwm3Regs.CMPA.half.CMPA
= (Uint16)(EPwm3Regs.TBPRD - (EPwm3Regs.TBPRD * DutyCycle/DMax2));
                GpioDataRegs.GPACLEAR.bit.GPIO5 = 1;
```

```
                }
                else if (Hall == 3)
                {
                        EPwm1Regs.CMPA.half.CMPA
        = (Uint16)(EPwm1Regs.TBPRD - (EPwm1Regs.TBPRD * DutyCycle/DMax1));
                        GpioDataRegs.GPACLEAR.bit.GPIO1 = 1;
                        EPwm2Regs.CMPA.half.CMPA = EPwm2Regs.TBPRD;
                        GpioDataRegs.GPASET.bit.GPIO3 = 1;
                        EPwm3Regs.CMPA.half.CMPA = EPwm3Regs.TBPRD;
                        GpioDataRegs.GPACLEAR.bit.GPIO5 = 1;
                }
        }

// (STEP 5) Developing the positive force for the negative command ==============
        else if (CrntCmd12StepPs < 0)
        {
                if (Hall == 60)
                {
                        EPwm1Regs.CMPA.half.CMPA
        = (Uint16)(EPwm1Regs.TBPRD - (EPwm1Regs.TBPRD * DutyCycle/DMax1));
                        GpioDataRegs.GPACLEAR.bit.GPIO1 = 1;
                        EPwm2Regs.CMPA.half.CMPA = EPwm2Regs.TBPRD;
                        GpioDataRegs.GPASET.bit.GPIO3 = 1;
                        EPwm3Regs.CMPA.half.CMPA = EPwm3Regs.TBPRD;
                        GpioDataRegs.GPACLEAR.bit.GPIO5 = 1;
                }
                else if (Hall == 56)
                {
                        EPwm1Regs.CMPA.half.CMPA
        = (Uint16)(EPwm1Regs.TBPRD - (EPwm1Regs.TBPRD * DutyCycle/DMax2));
                        GpioDataRegs.GPACLEAR.bit.GPIO1 = 1;
                        EPwm2Regs.CMPA.half.CMPA = EPwm2Regs.TBPRD;
                        GpioDataRegs.GPASET.bit.GPIO3 = 1;
                        EPwm3Regs.CMPA.half.CMPA
        = (Uint16)(EPwm3Regs.TBPRD - (EPwm3Regs.TBPRD * DutyCycle/DMax2));
                        GpioDataRegs.GPACLEAR.bit.GPIO5 = 1;
                }
                else if (Hall == 51)
                {
                        EPwm1Regs.CMPA.half.CMPA = EPwm1Regs.TBPRD;
                        GpioDataRegs.GPASET.bit.GPIO1 = 1;
                        EPwm2Regs.CMPA.half.CMPA = EPwm2Regs.TBPRD;
                        GpioDataRegs.GPACLEAR.bit.GPIO3 = 1;
                        EPwm3Regs.CMPA.half.CMPA
        = (Uint16)(EPwm3Regs.TBPRD - (EPwm3Regs.TBPRD * DutyCycle/DMax1));
                        GpioDataRegs.GPACLEAR.bit.GPIO5 = 1;
                }
                else if (Hall == 49)
                {
                        EPwm1Regs.CMPA.half.CMPA = EPwm1Regs.TBPRD;
                        GpioDataRegs.GPASET.bit.GPIO1 = 1;
                        EPwm2Regs.CMPA.half.CMPA = EPwm2Regs.TBPRD;
                        GpioDataRegs.GPASET.bit.GPIO3 = 1;
```

```
                        EPwm3Regs.CMPA.half.CMPA
= (Uint16)(EPwm3Regs.TBPRD - (EPwm3Regs.TBPRD * DutyCycle/DMax2));
                        GpioDataRegs.GPACLEAR.bit.GPIO5 = 1;
                }
                else if (Hall == 48)
                {
                        EPwm1Regs.CMPA.half.CMPA = EPwm1Regs.TBPRD;
                        GpioDataRegs.GPACLEAR.bit.GPIO1 = 1;
                        EPwm2Regs.CMPA.half.CMPA = EPwm2Regs.TBPRD;
                        GpioDataRegs.GPASET.bit.GPIO3 = 1;
                        EPwm3Regs.CMPA.half.CMPA
= (Uint16)(EPwm3Regs.TBPRD - (EPwm3Regs.TBPRD * DutyCycle/DMax1));
                        GpioDataRegs.GPACLEAR.bit.GPIO5 = 1;
                }
                else if (Hall == 35)
                {
                        EPwm1Regs.CMPA.half.CMPA = EPwm1Regs.TBPRD;
                        GpioDataRegs.GPASET.bit.GPIO1 = 1;
                        EPwm2Regs.CMPA.half.CMPA
= (Uint16)(EPwm2Regs.TBPRD - (EPwm2Regs.TBPRD * DutyCycle/DMax2));
                        GpioDataRegs.GPACLEAR.bit.GPIO3 = 1;
                        EPwm3Regs.CMPA.half.CMPA
= (Uint16)(EPwm3Regs.TBPRD - (EPwm3Regs.TBPRD * DutyCycle/DMax2));
                        GpioDataRegs.GPACLEAR.bit.GPIO5 = 1;
                }
                else if (Hall == 28)
                {
                        EPwm1Regs.CMPA.half.CMPA
= (Uint16)(EPwm1Regs.TBPRD - (EPwm1Regs.TBPRD * DutyCycle/DMax2));
                        GpioDataRegs.GPACLEAR.bit.GPIO1 = 1;
                        EPwm2Regs.CMPA.half.CMPA = EPwm2Regs.TBPRD;
                        GpioDataRegs.GPASET.bit.GPIO3 = 1;
                        EPwm3Regs.CMPA.half.CMPA = EPwm3Regs.TBPRD;
                        GpioDataRegs.GPASET.bit.GPIO5 = 1;
                }
                else if (Hall == 15)
                {
                        EPwm1Regs.CMPA.half.CMPA = EPwm1Regs.TBPRD;
                        GpioDataRegs.GPACLEAR.bit.GPIO1 = 1;
                        EPwm2Regs.CMPA.half.CMPA
= (Uint16)(EPwm2Regs.TBPRD - (EPwm2Regs.TBPRD * DutyCycle/DMax1));
                        GpioDataRegs.GPACLEAR.bit.GPIO3 = 1;
                        EPwm3Regs.CMPA.half.CMPA = EPwm3Regs.TBPRD;
                        GpioDataRegs.GPASET.bit.GPIO5 = 1;
                }
                else if (Hall == 14)
                {
                        EPwm1Regs.CMPA.half.CMPA
= (Uint16)(EPwm1Regs.TBPRD - (EPwm1Regs.TBPRD * DutyCycle/DMax2));
                        GpioDataRegs.GPACLEAR.bit.GPIO1 = 1;
                        EPwm2Regs.CMPA.half.CMPA
= (Uint16)(EPwm2Regs.TBPRD - (EPwm2Regs.TBPRD * DutyCycle/DMax2));
                        GpioDataRegs.GPACLEAR.bit.GPIO3 = 1;
```

```
                    EPwm3Regs.CMPA.half.CMPA = EPwm3Regs.TBPRD;
                    GpioDataRegs.GPASET.bit.GPIO5 = 1;
                }
                else if (Hall == 12)
                {
                    EPwm1Regs.CMPA.half.CMPA
= (Uint16)(EPwm1Regs.TBPRD - (EPwm1Regs.TBPRD * DutyCycle/DMax1));
                    GpioDataRegs.GPACLEAR.bit.GPIO1 = 1;
                    EPwm2Regs.CMPA.half.CMPA = EPwm2Regs.TBPRD;
                    GpioDataRegs.GPACLEAR.bit.GPIO3 = 1;
                    EPwm3Regs.CMPA.half.CMPA = EPwm3Regs.TBPRD;
                    GpioDataRegs.GPASET.bit.GPIO5 = 1;
                }
                else if (Hall == 7)
                {
                    EPwm1Regs.CMPA.half.CMPA = EPwm1Regs.TBPRD;
                    GpioDataRegs.GPASET.bit.GPIO1 = 1;
                    EPwm2Regs.CMPA.half.CMPA
=  (Uint16)(EPwm2Regs.TBPRD - (EPwm2Regs.TBPRD * DutyCycle/DMax2));
                    GpioDataRegs.GPACLEAR.bit.GPIO3 = 1;
                    EPwm3Regs.CMPA.half.CMPA = EPwm3Regs.TBPRD;
                    GpioDataRegs.GPASET.bit.GPIO5 = 1;
                    }

                else if (Hall == 3)
                {
                    EPwm1Regs.CMPA.half.CMPA = EPwm1Regs.TBPRD;
                    GpioDataRegs.GPASET.bit.GPIO1 = 1;
                    EPwm2Regs.CMPA.half.CMPA
= (Uint16)(EPwm2Regs.TBPRD - (EPwm2Regs.TBPRD * DutyCycle/DMax1));
                    GpioDataRegs.GPACLEAR.bit.GPIO3 = 1;
                    EPwm3Regs.CMPA.half.CMPA = EPwm3Regs.TBPRD;
                    GpioDataRegs.GPACLEAR.bit.GPIO5 = 1;
                }
            }

            CrntErrPv = CrntErrPs;
            CrntIn1Pv = CrntIn1Ps;

}
else if((PWMAmpBit==1)||(CurrentCmd==0.0))              // PWMAMP OFF
{
            PWMAmpInh = 1;
            EPwm1Regs.CMPA.half.CMPA = EPwm1Regs.TBPRD;
            GpioDataRegs.GPADAT.bit.GPIO1 = 0;
            EPwm2Regs.CMPA.half.CMPA = EPwm1Regs.TBPRD;
            GpioDataRegs.GPADAT.bit.GPIO3 = 0;
            EPwm3Regs.CMPA.half.CMPA = EPwm1Regs.TBPRD;
            GpioDataRegs.GPADAT.bit.GPIO5 = 0;

            CrntCmd12StepPs         = 0.0;
            CrntErrPv               = 0.0;
            CrntErrPs               = 0.0;
```

```
                CrntIn1Pv               = 0.0;
                CrntIn1Ps               = 0.0;
                CrntCmdPs               = 0.0;
                DutyCycle               = 0.0;
        }
}
```